

**1 Proportions and metamorphic conditions of markers in
2 numerical geodynamic models of subduction**

3 Buchanan C. Kerswell¹Matthew J. Kohn¹Taras V. Gerya²

4 ¹Department of Geosciences, Boise State University, Boise, ID 83725

5 ²Department of Earth Sciences, ETH-Zurich, Sonneggstrasse 5, Zurich 8092, Switzerland

6 Key Points:

- 7** •
8 •
9 •

10 **Abstract**

11 **1 Introduction**

12 Maximum metamorphic conditions, in terms of pressure and temperature (PT),
 13 have now been estimated for hundreds of high-pressure rocks exhumed from subduction
 14 zones (Agard et al., 2018; Penniston-Dorland et al., 2015). This dataset (the *rock record*)
 15 is the only tangible record of PT conditions experienced by rocks during deformation and
 16 chemical processing in subduction systems (e.g., Agard et al., 2009). Together with geo-
 17 physical imaging (Ferris et al., 2003; Hyndman & Peacock, 2003; Naif et al., 2015; Ron-
 18 denay et al., 2008; Syracuse & Abers, 2006), surface heat flow (Currie & Hyndman, 2006;
 19 Gao & Wang, 2014; Hyndman et al., 2005; Kerswell & Kohn, 2021; Wada & Wang, 2009),
 20 and forward numerical modelling (Gerya et al., 2002, 2008; Gerya & Stöckhert, 2006; Hacker
 21 et al., 2003; McKenzie, 1969; Peacock, 1990, 1996; Sizova et al., 2010; Syracuse et al.,
 22 2010; Yamato et al., 2007, 2008), the rock record underpins contemporary views of sub-
 23 duction geodynamics (Agard et al., 2009, 2018; Bebout, 2007). However, two interest-
 24 ing observations emerge from the rock record that remain contradictory or unexplained
 25 by geophysical observations and numerical models.

26 First, temperature estimates for rocks are, on average, significantly warmer than
 27 widely cited numerical models of subduction (for a given depth, Penniston-Dorland et
 28 al., 2015). This significant temperature discrepancy implicates both geodynamic mod-
 29 elling and thermobarometry alike. Potential sources and magnitudes of uncertainty are
 30 discussed by Penniston-Dorland et al. (2015) and recapitulated by Abers et al. (2017),
 31 Kohn et al. (2018), and Keken et al. (2019) with conflicting arguments. Because sub-
 32 duction zone research relies on forward numerical modelling to generate and test hypothe-
 33 ses about temperature-dependent processes (metamorphism, mechanics, seismicity, vol-
 34 canism, and chemical fluxes), further investigation into this discrepancy is warranted.
 35 In any case, currently only one set of numerical experiments from Syracuse et al. (2010)
 36 has been systematically compared to the rock record. Comparing the rock record with
 37 other widely used geodynamic codes (e.g. I2VIS, Gerya & Yuen, 2003) may resolve or
 38 uncover recurrent and/or new incongruities.

39 Second, the probability of recovering high-pressure rocks from depths beyond 2.4
 40 GPa rapidly diminishes (Figure 1). Figure 1 implies a global recovery depth limit for

41 high-pressure rocks that is not yet understood. Perhaps coincidentally, hypotheses of com-
 42 monly thin backarcs (Currie & Hyndman, 2006) and common depths of mechanical cou-
 43 pling along the subduction interface (Furukawa, 1993; Wada & Wang, 2009) may help
 44 explain the recovery depth limit implied by Figure 1 (Kerswell et al., 2020). However,
 45 such commonalities among subduction zone thermal structure and mechanical coupling
 46 was recently scrutinized by interpolations of surface heat flow (Kerswell & Kohn, 2021).
 47 Nonetheless, if subduction zone thermal structure is related to maximum recovery depth
 48 of high-pressure rocks, explaining the curve in Figure 1 is key to understanding the tem-
 49 perature discrepancy summarized above.

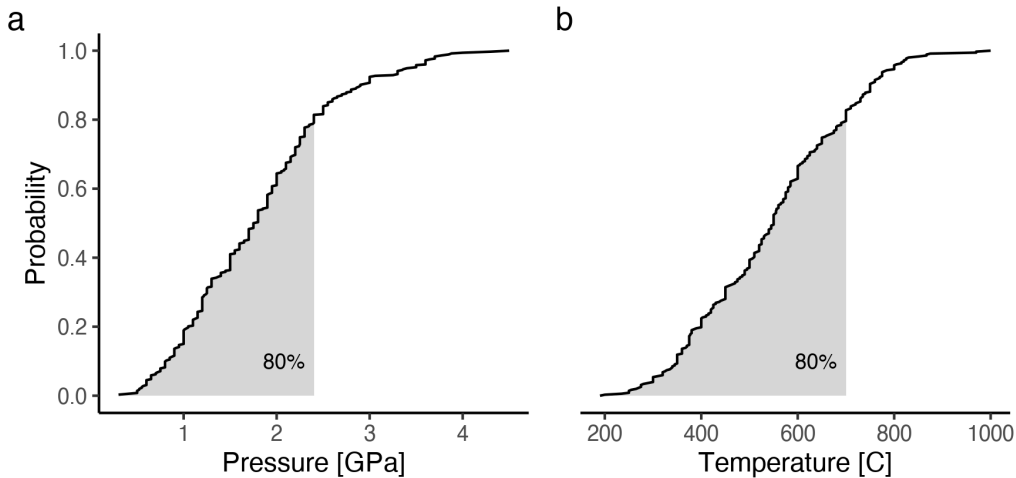


Figure 1: Cumulative probability of peak metamorphic pressures (a) and temperatures (b) for a global compilation of exhumed blueschists and eclogites. The rock record implies eighty percent (grey shaded regions) of rocks are recovered from $\leq 2.4 \text{ GPa}$ and $\leq 700 \text{ }^{\circ}\text{C}$. Note the abrupt change in slope at 2.4 GPa . Data from Penniston-Dorland et al. (2015).

50 This study attempts to answer the following questions: 1) what is the global range
 51 of maximum recovery depths and 2) maximum metamorphic conditions for subducted
 52 oceanic crust and seafloor sediments? We first collectively trace more than one million
 53 markers in geodynamic numerical models of 64 active continental margins (from Ker-
 54 swell et al., 2020) and classify recovered (vs. subducted) markers using unsupervised ma-
 55 chine learning. Next, maximum metamorphic conditions of recovered markers are cal-
 56 culated and compared to the rock record. We find that all numerical models underpre-
 57 dict the distribution of maximum marker pressures compared to the rock record. Max-
 58 imum marker temperatures are consistent with the rock record only for numerical mod-

59 els with very thin ($\leq 62 \text{ km}$) upper plate lithospheres. Finally, we calculate cumulative
60 probability curves of recovered markers and discuss (in)consistencies with the rock record
61 and their geodynamic implications.

62 2 Methods

63 This study presents a dataset of Lagrangian markers (described below) from the
 64 numerical experiments of Kerswell et al. (2020). The numerical experiments simulate
 65 64 oceanic-continental subduction systems with variable oceanic plate age, convergence
 66 velocity, and upper plate (continental) lithospheric thickness. The range of oceanic plate
 67 ages and convergence velocities broadly represent the modern global subduction system
 68 (Syracuse & Abers, 2006; Wada & Wang, 2009). Initial conditions were modified from
 69 previous studies of active margins (Gorczyk et al., 2007; Sizova et al., 2010). The code,
 70 I2VIS, models visco-plastic flow of geologic materials by solving three conservative equa-
 71 tions of mass, energy, and momentum on a fully-staggered finite difference grid with a
 72 *marker-in-cell* technique (Gerya & Yuen, 2003; Harlow & Welch, 1965). Further details
 73 about the initial setup and boundary conditions, rheologic model, metamorphic (de)hydration
 74 reactions, are in Kerswell et al. (2020). Details about the marker-in-cell technique are
 75 in Gerya & Yuen (2003) and Gerya (2019).

76 In this section we first define Lagrangian markers (now referred to as markers) and
 77 briefly elaborate on their usefulness in understanding fluid flow—including geodynamic
 78 problems like subduction. We then detail the maths and decisions involved in our marker
 79 classification algorithm, which we use to classify 1,214,757 markers from 64 numerical
 80 experiments of Kerswell et al. (2020) as either subducted or recovered based on char-
 81 acteristics of their PT paths.

82 2.1 Lagrangian markers

83 Markers are mathematical objects representing discrete parcels of fluid flowing in
 84 a continuum (Harlow, 1962, 1964). Imagine tracking millions of parcels of air as they col-
 85 lectively move around an air foil. Each marker would experience a different flow path
 86 and pressure history relative to its neighbors. For example, some parcels of air may spin
 87 off and cause turbulence, while others move orderly with their neighbors around the foil.
 88 In this analogy, knowing which parcels experience turbulence, perhaps based on some
 89 characteristic of a parcel’s flow path, is useful information for aerodynamic testing.

90 The analogy above highlights the representative advantage of markers. That is, mark-
 91 ers record physical changes to the continuum *from the perspective of the fluid* (Harlow,
 92 1962). “Tracing” markers (saving marker states through time) in a numerical geodynamic

model is useful for understanding subduction dynamics like tracing air parcels is useful for understanding aerodynamics. It is necessary, however, to first accept implicit simplifications and uncertainties (known and unknown) about the geodynamic continuum. For example, fluids like Earth's atmosphere and oceans are often modeled as incompressible fluids (Batchelor, 1953; Boussinesq, 1897). Uncertainties are especially rich in the petrologic model governing phase changes (Ito & Kennedy, 1971; Schmidt & Poli, 1998) and its effects on the highly non-linear rheologic model relating stress and strain by empirical flow laws (Hilairet et al., 2007; Karato & Wu, 1993; Ranalli, 1995; Turcotte & Schubert, 2002). See Kerswell et al. (2020) for details. Nonetheless, insofar as subducting crustal rocks on Earth behave like an incompressible visco-plastic fluid (as parameterized by Gerya, 2019; Gerya & Yuen, 2003; Kerswell et al., 2020), principled comparisons between marker PT paths and the rock record (e.g. Figure 1, Agard et al., 2018; Penniston-Dorland et al., 2015) may be made.

Markers also have a distinct numerical advantage in geodynamic cases. Unlike air parcels flowing in a relatively homogeneous atmosphere (air foil aside), markers are deforming in a partly layered, partly chaotic, visco-plastic continuum representing the interface between the top of subducting oceanic crust and the mantle it sinks into (often called the subduction interface). Current models of the subduction interface epitomize a geologic continuum with complex geometry, sharp thermal, chemical, and strain gradients, strong advection (high Peclét number), and abundant fluid flow (Agard et al., 2016, 2018; Bebout, 2007; Bebout & Barton, 2002; Gerya & Yuen, 2003; Penniston-Dorland et al., 2015; Syracuse et al., 2010). Markers greatly improve solution accuracy and stability in such cases by interpolating and updating thermal, chemical, and velocity fields during each timestep (Gerya, 2019; Gerya & Yuen, 2003; Moresi et al., 2003).

2.2 Marker classification

On average, 18,981 markers are selected from within a 760 km wide and 8 km deep section of oceanic crust and seafloor sediments (Figure 2). Tracing then proceeds for a number of timesteps $t = \{1, 2, \dots, t_{dur}\}$, where $t_{dur} = 79$. Seventy-nine timesteps is sufficient for markers to be subducted deeply (≥ 200 km) from their initial positions, regardless of subduction rate (see sec. A.1). From this set of markers, $x_i = \{x_1, x_2, \dots, x_n\}$, only markers *recovered* from the subducting slab are relevant for comparison to PT es-

124 timates of natural rocks. The main challenge, therefore, is to first classify markers as ei-
 125 ther *subducted* or *recovered* without an inherited class label.

126 At the heart of our marker classification algorithm is a finite Gaussian mixture model
 127 (GMM) fit by Expectation-Maximization (EM, Dempster et al., 1977). Please note that
 128 GMM fit by EM is a general purpose clustering algorithm broadly used in pattern recog-
 129 nition, anomaly detection, and estimating complex probability distribution functions (e.g.,
 130 Banfield & Raftery, 1993; Celeux & Govaert, 1995; Figueiredo & Jain, 2002; Fraley &
 131 Raftery, 2002; Vermeesch, 2018). We derive GMM in sec. 2.2.1 and EM in sec. 2.2.2.

132 Before deriving the details of marker classification, we hypothesize that subducted
 133 and recovered markers may be distinguished by their PTt paths. If true, clustering al-
 134 gorithms like GMM may reliably classify markers by (dis)similarity along any number
 135 of dimensions computed from marker PTt paths.

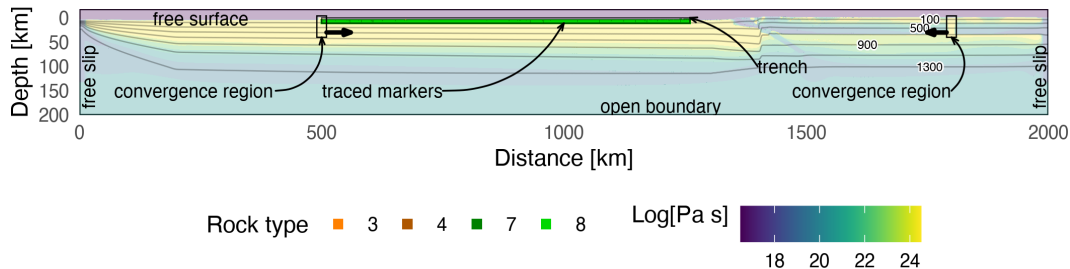


Figure 2: Initial conditions for marker tracing. Markers are selected from a 760 km wide and 8 km deep section representing 7 km of mafic oceanic crust (rock type 7 & 8) and 1 km of seafloor sediments (rock type 3 & 4). Two convergence regions far from the trench initiate and maintain subduction. On average, 18,981 markers are traced for each model. Numerical modelling details are in Kerswell et al. (2020).

136 **2.2.1 Gaussian mixture model**

137 Let the traced markers represent a d -dimensional array of n random independent
 138 variables $x_i \in \mathbb{R}$. Assume markers x_i were drawn from k discrete probability distribu-
 139 tions with parameters Φ . The probability distribution of markers x_i can be modeled with
 140 a mixture of k components:

$$p(x_i|\Phi) = \sum_{j=1}^k \pi_j p(x_i|\Theta_j) \quad (1)$$

141 where $p(x_i|\Theta_j)$ is the probability of x_i under the j^{th} mixture component and π_j
 142 is the mixture proportion representing the probability that x_i belongs to the j^{th} com-
 143 ponent ($\pi_j \geq 0; \sum_{j=1}^k \pi_j = 1$).

144 Assuming Θ_j describes a Gaussian probability distributions with mean μ_j and co-
 145 variance Σ_j , Equation 1 becomes:

$$p(x_i|\Phi) = \sum_{j=1}^k \pi_j \mathcal{N}(x_i|\mu_j, \Sigma_j) \quad (2)$$

146 where

$$\mathcal{N}(x_i|\mu_j, \Sigma_j) = \frac{\exp\{-\frac{1}{2}(x_i - \mu_j)(x_i - \mu_j)^T \Sigma_j^{-1}\}}{\sqrt{\det(2\pi\Sigma_j)}} \quad (3)$$

147 The parameters μ_j and Σ_j , representing the center and shape of each cluster, are
 148 estimated by maximizing the log of the likelihood function, $L(x_i|\Phi) = \prod_{i=1}^n p(x_i|\Phi)$:

$$\log L(x_i|\Phi) = \log \prod_{i=1}^n p(x_i|\Phi) = \sum_{i=1}^n \log \left[\sum_{j=1}^k \pi_j p(x_i|\Theta_j) \right] \quad (4)$$

149 Taking the derivative of Equation 4 with respect to each parameter, π , μ , Σ , set-
 150 ting the equation to zero, and solving for each parameter gives the Maximum Likelihood
 151 Estimators (MLE):

$$\begin{aligned}
N_j &= \sum_{i=1}^n \omega_{ij} \\
\pi_j &= \frac{N_j}{n} \\
\mu_j &= \frac{1}{N_j} \sum_{i=1}^n \omega_{ij} x_i \\
\Sigma_j &= \frac{1}{N_j} \sum_{i=1}^n \omega_{ij} (x_i - \mu_j)(x_i - \mu_j)^T
\end{aligned} \tag{5}$$

where ω_{ij} ($\omega_{ij} \geq 0; \sum_{j=1}^k \omega_{ij} = 1$) are membership weights representing the probability of an observation x_i belonging to the j^{th} Gaussian and N_j represents the number of observations belonging to the j^{th} Gaussian. Please note that ω_{ij} is unknown for unlabelled datasets, like the unclassified markers, so MLE cannot be computed with Equation 5. The solution to this problem is derived in sec. 2.2.2.

General purpose functions in the R package **Mclust** (Scrucca et al., 2016) are used to fit Gaussian mixutre models. After Banfield & Raftery (1993), covariance matrices Σ in **Mclust** are parameterized to be flexible in their shape, volume, and orientation (Scrucca et al., 2016):

$$\Sigma_j = \lambda_j D_j A_j D_j^T \tag{6}$$

where D_j is the orthogonal eigenvector matrix, A_j and λ_j are diagonal matrices of values proportional to the eigenvalues. This implementation allows fixing one, two, or three geometric elements of the covariance matrices. That is, the volume λ_j , shape A_j , and orientation D_j of Gaussian clusters can change or be fixed among all k clusters (e.g., Celeux & Govaert, 1995; Fraley & Raftery, 2002). Fourteen parameterizations of Equation 6 are tried, representing different geometric combinations of the covariance matrices Σ (see Scrucca et al., 2016) and the Bayesian Information Criterion (BIC, Schwarz & others, 1978) is computed. The best parameterization for Equation 6 is chosen by BIC.

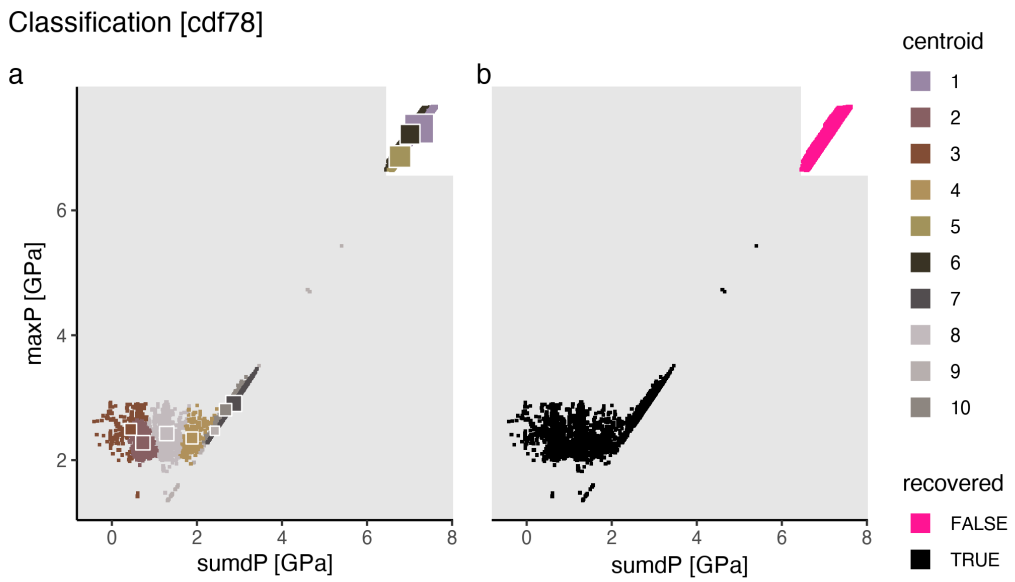


Figure 3: Marker classification for model cdf78. GMM groups 18,934 markers into ten clusters according to each marker's maximum pressure and sum of all pressure changes along its PTt path (a). If a cluster's centroid is below the median $sumdP$ or $maxP$ of all markers (within the grey shaded region), it is classified as recovered (b). The size of centroid squares are proportional to the number of markers in a cluster.

169 **2.2.2 Expectation-Maximization fitting of Gaussian Mixtures**

170 The EM algorithm estimates GMM parameters by initializing k Gaussians with pa-
 171 rameters (π_j, μ_j, Σ_j) , then iteratively computing membership weights with Equation 7
 172 (E-step) and updating Gaussian parameters with Equation 5 (M-step) until convergence
 173 (Dempster et al., 1977).

174 The *expectation* (E-)step involves a “latent” multinomial variable $z_{ij} \in \{1, 2, \dots, k\}$
 175 representing the unknown classifications of x_i with a joint distribution $p(x_i, z_{ij}) = p(x_i|z_{ij})p(z_j)$.
 176 Membership weights ω_{ij} are equivalent to the conditional probability $p(z_{ij}|x_i)$, which rep-
 177 resents the probability of observation x_i belonging to the j^{th} Gaussian. Given initial guesses
 178 for k sets of Gaussian parameters π_j, μ_j, Σ_j , membership weights are computed using
 179 Bayes Theorem (E-step):

$$p(z_{ij}|x_i) = \frac{p(x_i|z_{ij})p(z_{ij})}{p(x_i)} = \frac{\pi_j \mathcal{N}(\mu_j, \Sigma_j)}{\sum_{j=1}^k \pi_j \mathcal{N}(\mu_j, \Sigma_j)} = \omega_{ij} \quad (7)$$

180 and new Gaussian estimates are computed with ω_{ij} (Equation 5) during the *max-*
 181 *imization* (M-)step.

182 **2.2.3 Feature selection and final decision**

183 EM is sensitive to local optima and initialization (Figueiredo & Jain, 2002), so a
 184 number of features were computed from marker PTt paths and tested in combination.
 185 Redundant or useless features (e.g., Dy & Brodley, 2004) were filtered out. We settled
 186 on two features:

$$\begin{aligned} maxP &\leftarrow \max_{1 \leq t \leq t} P \\ sumdP &\leftarrow \sum_1^{t_{dur}} dP \end{aligned} \quad (8)$$

187 where $maxP$ and $sumdP$ represent the maximum pressure attained each marker’s
 188 PTt path and the sum total of all pressure changes along each marker’s PTt path, re-
 189 spectively. Up to ten Gaussian components are fit to the bivariate mixture model de-
 190 scribed by Equation 2 and Equation 8 using EM (Equations 7, 5). This clustering step
 191 gives markers x_i class labels $z_i \in \{1, \dots, k\}$ representing assignment to one of k clus-
 192 ters (Figure 3a).

193 A final decision is made to classify a cluster, and all of its markers, as either *sub-*
 194 *ducted* or *recovered* by comparing cluster centroids (μ_j , Equation 5) to the overall dis-
 195 tribution of *maxP* and *sumdP*. Clusters with centroids μ_j below the median in either
 196 *maxP* or *sumdP* dimensions, classify as *recovered* (Figure 3b).

197 **3 Results**

198 **3.1 Classification variance and error**

199 Typical measures of classification accuracy, like confusion matrices (Stehman, 1997),
 200 bootstrap (Efron & Tibshirani, 1994), and cross-validation (Kohavi & others, 1995), lever-
 201 age *a priori* information (class labels y_i) about the data x_i to validate clustering results.
 202 Generally speaking, these methods compare classes predicted by clustering z_i with ac-
 203 tual classes y_i to quantify type I (false positive—classified as recovered but was subducted)
 204 and type II (false negative—classified as subducted but was recovered) errors. However,
 205 our markers are unlabelled (no y_i) so *true* validation is not possible by these methods
 206 or similar. Instead, we use a straight-forward resampling approach to assess variance in
 207 our clustering results. First, all markers x_i from all numerical models are classified one-
 208 hundred times. Summary statistics for each numerical model (mean and standard de-
 209 viation) are then computed from the one-hundred classifications (Table 1).

Table 1: Summary of subduction parameters and marker tracing results

z_{cpl} [km]	z_{1100} [km]	age [Ma]	\vec{v}_{conv} [$\frac{km}{Ma}$]	n_{marx}	n_{rec}	σ_{rec}	n_{sub}	σ_{sub}	$\frac{n_{rec}}{n_{marx}}$	$\sigma_{\frac{n_{rec}}{n_{marx}}}$
66	46	33	40	18802	4777	0	14025	0	0.25	0
74	46	33	66	18913	4987	199	13926	199	0.26	0.011
69	46	33	80	18921	5109	254	13812	254	0.27	0.013
67	46	33	100	18912	4048	3	14864	3	0.21	0
72	46	55	40	18760	4480	2	14280	2	0.24	0
78	46	55	66	18782	3905	32	14877	32	0.21	0.002
78	46	55	80	18794	4852	569	13942	569	0.26	0.03
59	46	55	100	18812	4505	144	14307	144	0.24	0.008
80	46	85	40	18719	2690	0	16029	0	0.14	0
70	46	85	66	18750	5211	12	13539	12	0.28	0.001

z_{cpl} [km]	z_{1100} [km]	age [Ma]	\vec{v}_{conv} [$\frac{\text{km}}{\text{Ma}}$]	n_{marx}	n_{rec}	σ_{rec}	n_{sub}	σ_{sub}	$\frac{n_{rec}}{n_{marx}}$	$\sigma_{\frac{n_{rec}}{n_{marx}}}$
58	46	85	80	18760	4115	16	14645	16	0.22	0.001
65	46	85	100	18779	3314	91	15465	91	0.18	0.005
79	46	110	40	18739	4427	89	14312	89	0.24	0.005
70	46	110	66	18769	4933	103	13836	103	0.26	0.005
68	46	110	80	18764	4231	0	14533	0	0.23	0
64	46	110	100	18771	3842	46	14929	46	0.2	0.002
80	62	33	40	18942	5861	2	13081	2	0.31	0
79	62	33	66	19034	4839	0	14195	0	0.25	0
78	62	33	80	19036	4599	1	14437	1	0.24	0
77	62	33	100	19028	4016	0	15012	0	0.21	0
87	62	55	40	18770	5232	81	13538	81	0.28	0.004
82	62	55	66	18836	3733	0	15103	0	0.2	0
75	62	55	80	18843	3658	0	15185	0	0.19	0
70	62	55	100	18852	3239	1	15613	1	0.17	0
91	62	85	40	18775	4666	0	14109	0	0.25	0
77	62	85	66	18839	3612	0	15227	0	0.19	0
72	62	85	80	18850	3140	2	15710	2	0.17	0
67	62	85	100	18866	2945	153	15921	153	0.16	0.008
88	62	110	40	18829	4328	0	14501	0	0.23	0
77	62	110	66	18889	2643	0	16246	0	0.14	0
74	62	110	80	18908	3480	0	15428	0	0.18	0
75	62	110	100	18908	3902	170	15006	170	0.21	0.009
87	78	33	40	19228	3729	0	15499	0	0.19	0
94	78	33	66	19326	3257	0	16069	0	0.17	0
97	78	33	80	19324	2538	25	16786	25	0.13	0.001
97	78	33	100	19338	2373	59	16965	59	0.12	0.003
90	78	55	40	18942	4226	0	14716	0	0.22	0
90	78	55	66	18934	3080	0	15854	0	0.16	0
88	78	55	80	18945	3080	2	15865	2	0.16	0
85	78	55	100	18960	2847	2	16113	2	0.15	0
97	78	85	40	18860	4186	0	14674	0	0.22	0

z_{cpl} [km]	z_{1100} [km]	age [Ma]	\vec{v}_{conv} [$\frac{\text{km}}{\text{Ma}}$]	n_{marx}	n_{rec}	σ_{rec}	n_{sub}	σ_{sub}	$\frac{n_{rec}}{n_{marx}}$	$\sigma_{\frac{n_{rec}}{n_{marx}}}$
91	78	85	66	18911	2861	0	16050	0	0.15	0
84	78	85	80	18909	2658	1	16251	1	0.14	0
77	78	85	100	18910	2663	28	16247	28	0.14	0.001
78	78	110	40	18885	3397	0	15488	0	0.18	0
87	78	110	66	18935	3362	74	15573	74	0.18	0.004
85	78	110	80	18944	2813	0	16131	0	0.15	0
78	78	110	100	18940	2685	2	16255	2	0.14	0
95	94	33	40	19634	2634	1	17000	1	0.13	0
101	94	33	66	19701	2895	3	16806	3	0.15	0
108	94	33	80	19722	2445	0	17277	0	0.12	0
113	94	33	100	19732	3118	28	16614	28	0.16	0.001
100	94	55	40	19169	2957	14	16212	14	0.15	0.001
104	94	55	66	19166	2530	1	16636	1	0.13	0
104	94	55	80	19190	2626	1	16564	1	0.14	0
104	94	55	100	19220	2364	5	16856	5	0.12	0
101	94	85	40	18996	3108	0	15888	0	0.16	0
102	94	85	66	19003	2580	0	16423	0	0.14	0
101	94	85	80	19001	2585	1	16416	1	0.14	0
107	94	85	100	19008	2670	15	16338	15	0.14	0.001
106	94	110	40	19011	3098	0	15913	0	0.16	0
102	94	110	66	18997	2382	0	16615	0	0.13	0
98	94	110	80	18988	2590	17	16398	17	0.14	0.001
108	94	110	100	18976	2944	0	16032	0	0.16	0

210 Type I and type II errors, qualitatively assessed by visualizing the geodynamic evolution
 211 and marker metamorphic conditons of each model (see sec. A.2), show consistently
 212 low prevalence of type I error and variable amounts of type II error. Note that type II
 213 error is analogous to a biased rock record only the proportion of recovered rocks that are
 214 exhumed to Earth's surface may be sampled. Therefore, some principled comparisons
 215 may still be made between the rock record and models with abundant type II error. The
 216 same is not true for type I error. Rocks do not generally record anomalously high PT

217 conditions if demonstrably absent of disequilibrium (kinetic) textures. The only exam-
 218 ple of excessive type I error is shown in Figures 4, A.147, A.146, A.145. Type I error is
 219 especially apparent in Figure 4b with eighty percent of markers being recovered from pres-
 220 sures of $\leq 6 \text{ GPa}$. Model cdm46 notwithstanding, the prevalence of type I error is low
 221 and overall and the shapes of cumulative probability curves for all other models are neg-
 222 ligibly affected.

Excessive type I error

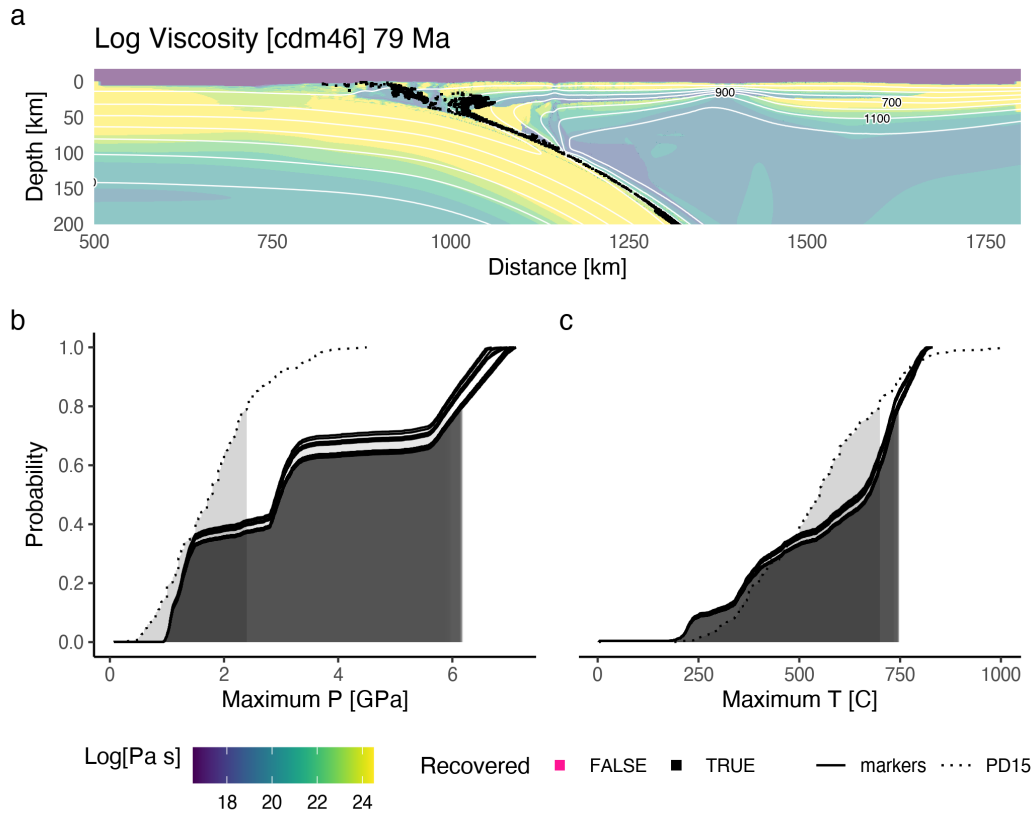


Figure 4: Example of excessive type I error.

223

3.2 Marker motions

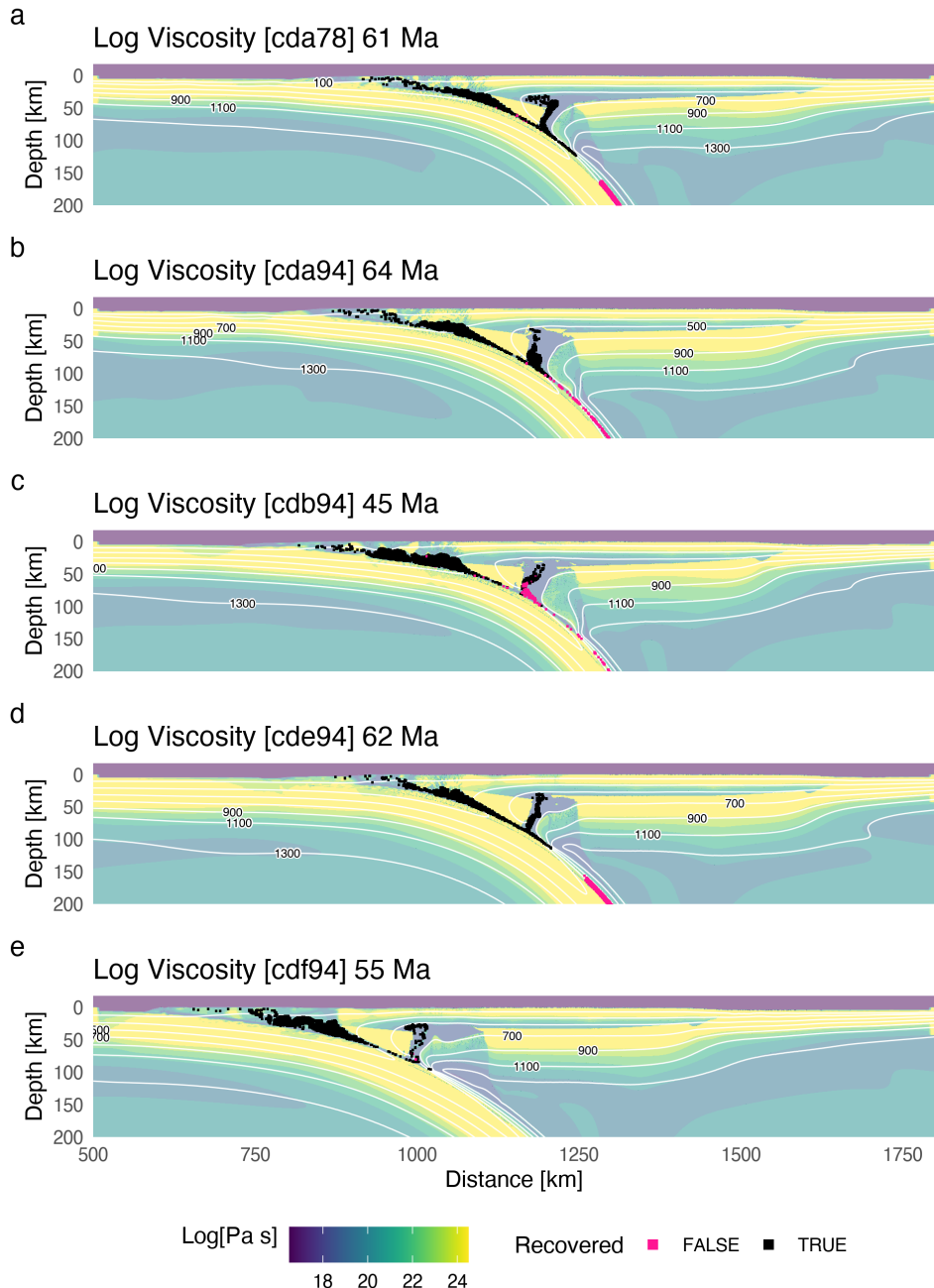


Figure 5: Examples of mantle wedge diapirs.

224

3.3 Marker proportions

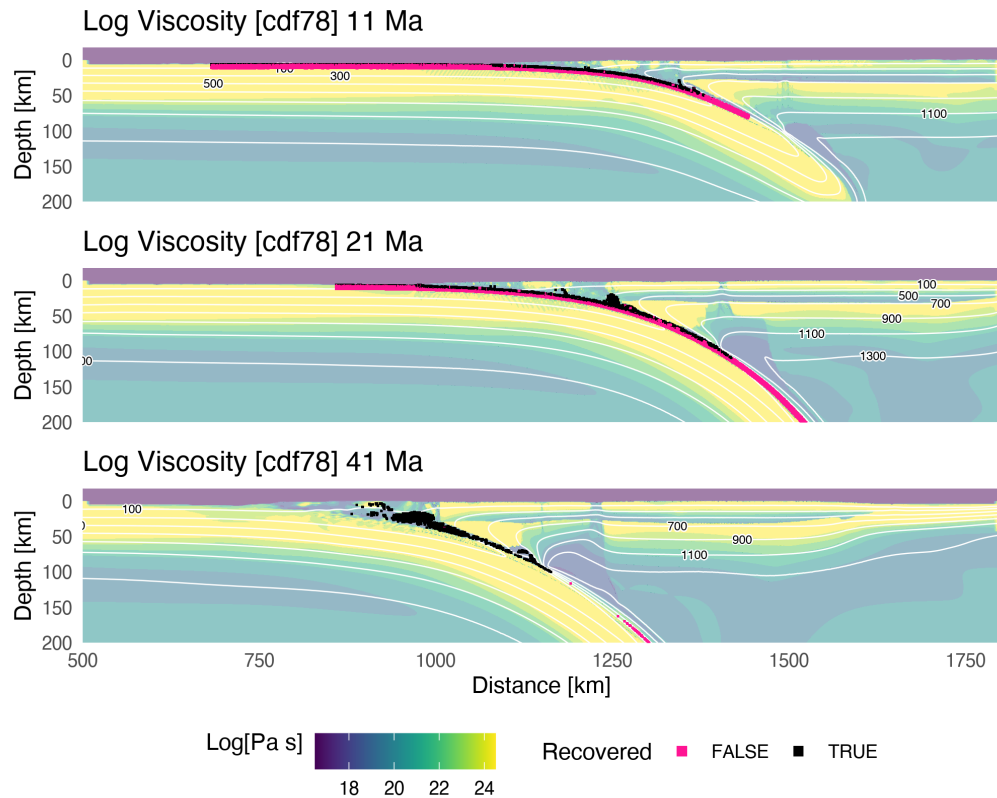


Figure 6: Geodynamic evolution for model cdf78.

225

3.4 Maximum recovery depths

Metamorphic conditions [cdf78]

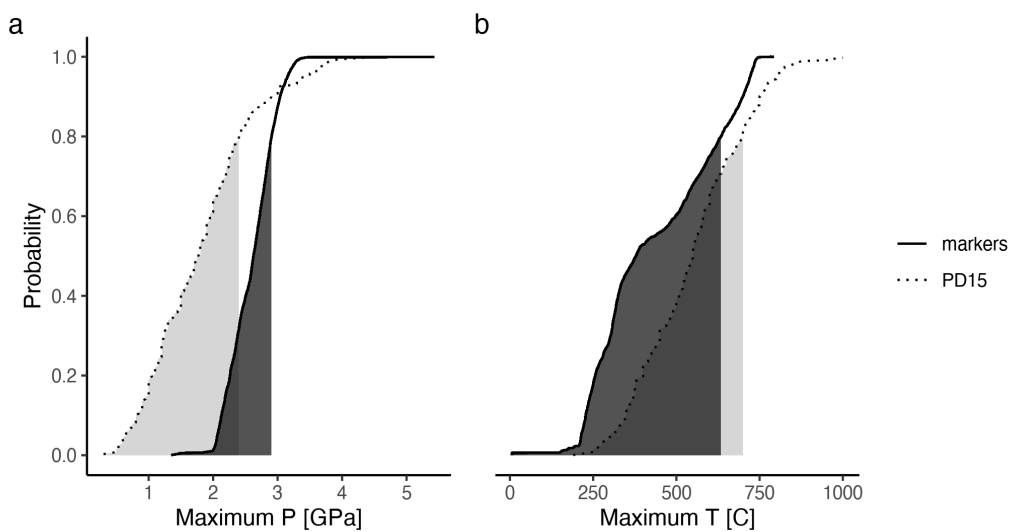


Figure 7: Maximum metamorphic conditons for markers recovered from model cdf78. Maximum pressures for recovered markers (solid curves) range from 1.4 to 2.9 (a) and only marginally overlap with the rock record (dotted curves). However, maximum temperatures for recovered markers range from 6 to 634 (b) and show better agreement with the rock record than (a). PD15 dataset from Penniston-Dorland et al. (2015).

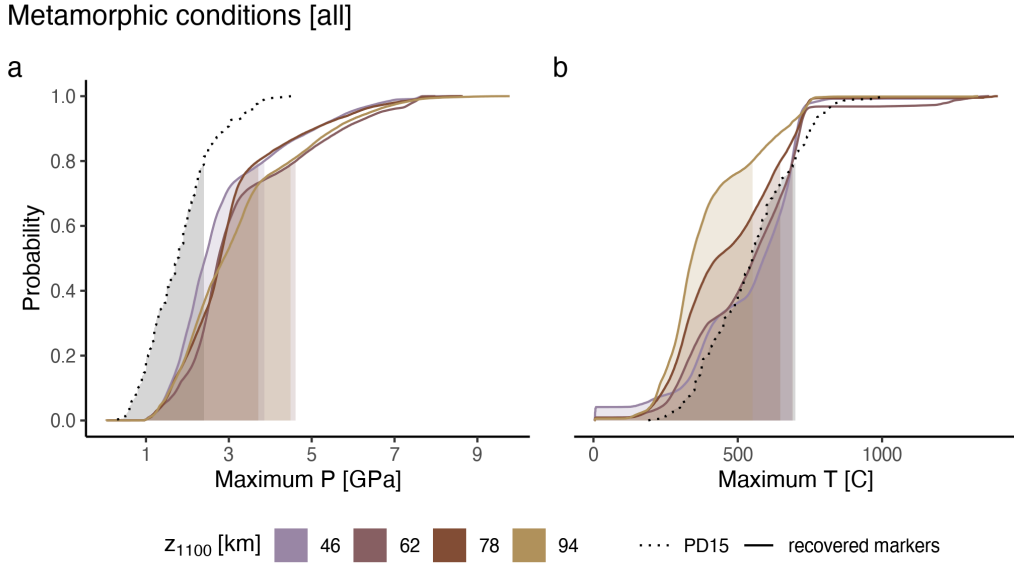
226 **4 Discussion**227 **4.1 Cold nose geometry**228 **4.2 Diapirs**229 **4.3 Metamorphic conditions of rocks and markers**

Figure 8: Metamorphic conditions of markers grouped by models with different upper plate lithospheric thicknesses z_{1100} . Eighty percent (shaded regions under curves) of recovered markers (solid curves) reach maximum pressures between 0.1 and 4.4 with ostensibly no markers reaching maximum pressures of less than one gigapascal (a). In general, markers are recovered from lower maximum pressures for models with thin upper plates ($z_{1100} \leq 62$ km) compared to models with thicker upper plates ($z_{1100} > 62$ km) due to differences in coupling depths between the oceanic plate and upper plate (see Kerswell et al., 2020). Eighty percent of recovered markers reach maximum temperatures between 8 and 551 (b). With respect to temperature, models with thin upper plates ($z_{1100} \leq 62$ km) show better agreement with the rock record (dotted line) compared to models with thicker upper plates ($z_{1100} > 62$ km). The rock record does not significantly overlap with maximum metamorphic conditions of markers regardless of model parameterization. PD15 dataset from Penniston-Dorland et al. (2015)

230 **5 Conclusion**231 **6 Open Research**

232 **Acknowledgments**

233 We gratefully acknowledge high-performance computing support of the Borah com-
234 pute cluster (DOI: [10.18122/oit/3/boisestate](https://doi.org/10.18122/oit/3/boisestate)) provided by Boise State University's
235 Research Computing Department. This work was supported by the National Science Foun-
236 dation grant OIA1545903 to M. Kohn, S. Penniston-Dorland, and M. Feineman.

237 **A Appendix**238 **A.1 Marker tracing duration**

239 Spontaneous sinking motion of the oceanic plate, as opposed to a fixed subduction
 240 rate (e.g., Syracuse et al., 2010; Wada & Wang, 2009), induces right-to-left plate motions
 241 as the sinking oceanic plate (the *slab*) provides a leftward horizontal force (known as *slab*
 242 *rollback*). Slab rollback eventually leads to mechanical interference (collision) between
 243 trench sediments and the stationary convergence region centered at 500 km from the left
 244 boundary (Figure 2). The fixed, high-viscosity, convergence region acts as a barrier to
 245 the incoming sediments, deforming the accretionary wedge into a rapidly thickening pile.
 246 The sudden change in accretionary wedge geometry flattens the slab, causing intense man-
 247 tle circulation and crustal deformation in the forearc and backarc regions. We consider
 248 the dynamics after interference begins unrepresentative of natural buoyancy-driven slab
 249 motion. Therefore, marker PTt paths are also increasingly meaningless after mechani-
 250 cal interference begins.

251 Although our classification algorithm uses a constant tracing duration $t_{dur} = 79$
 252 for classification (see sec. 2), we define another duration t_{max} , which is the maximum
 253 timestep used for calculating PTt paths. t_{max} is chosen automatically for each model
 254 by computing the topographic surface profile through time. The timestep when the sed-
 255 iment pile deforming against the convergence region becomes the overall topographic high
 256 is selected to be t_{max} , usually within one or two timesteps after interference. Marker PTt
 257 paths from different models, therefore, represent approximately the same amount of to-
 258 tal convergence in km, but different subduction durations.

259

A.2 Visualizations

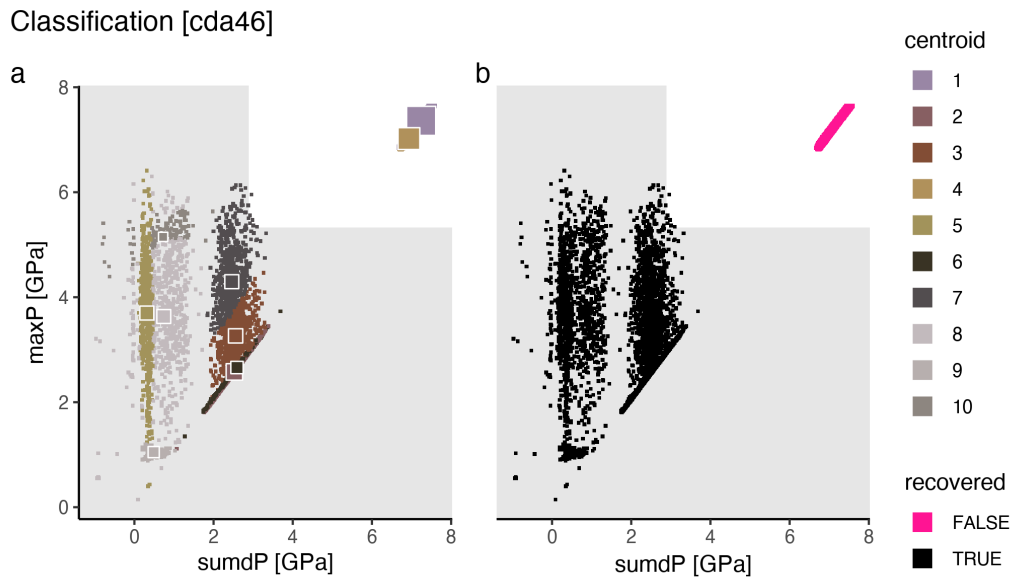


Figure A.1: Marker classification for model cda46.

Metamorphic conditions [cda46]

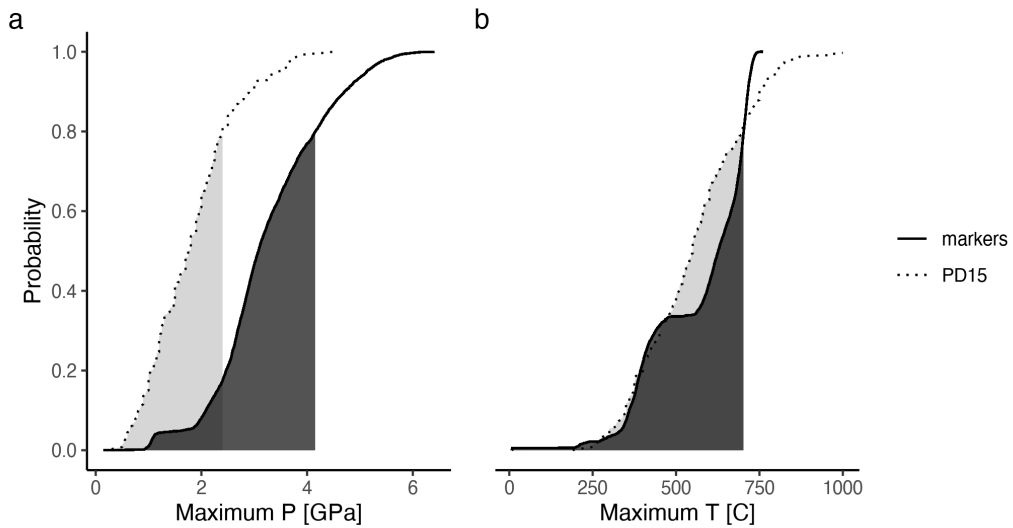


Figure A.2: Metamorphic conditions of markers recovered from model cda46.

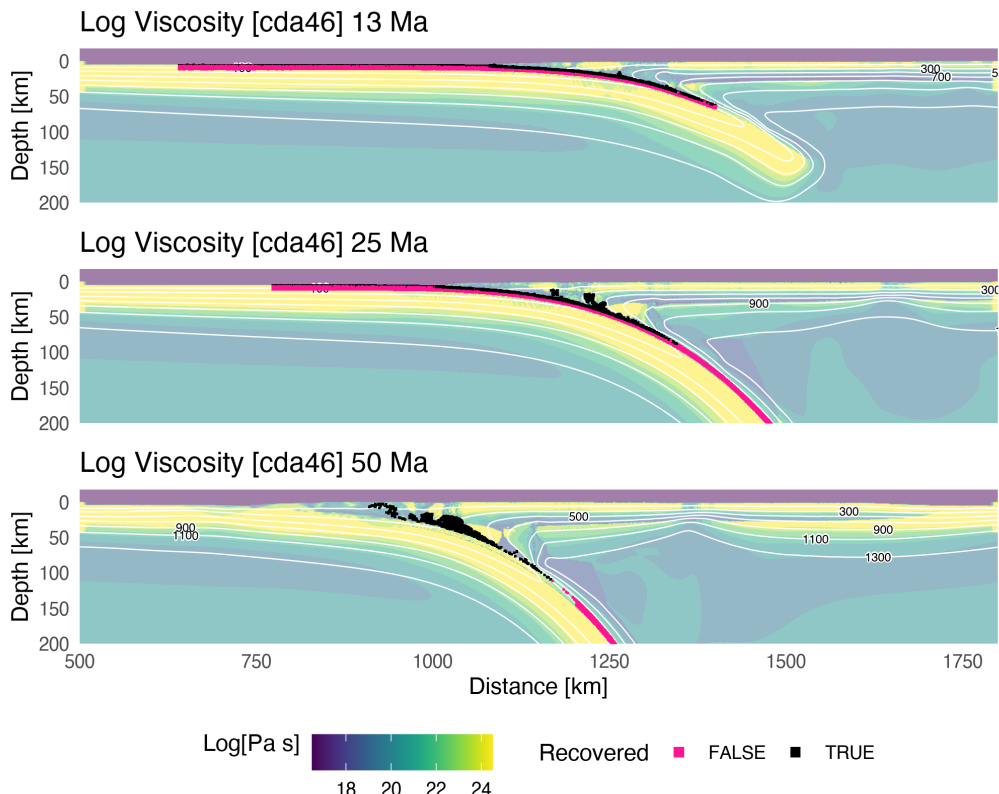


Figure A.3: Geodynamic evolution of model cda46.

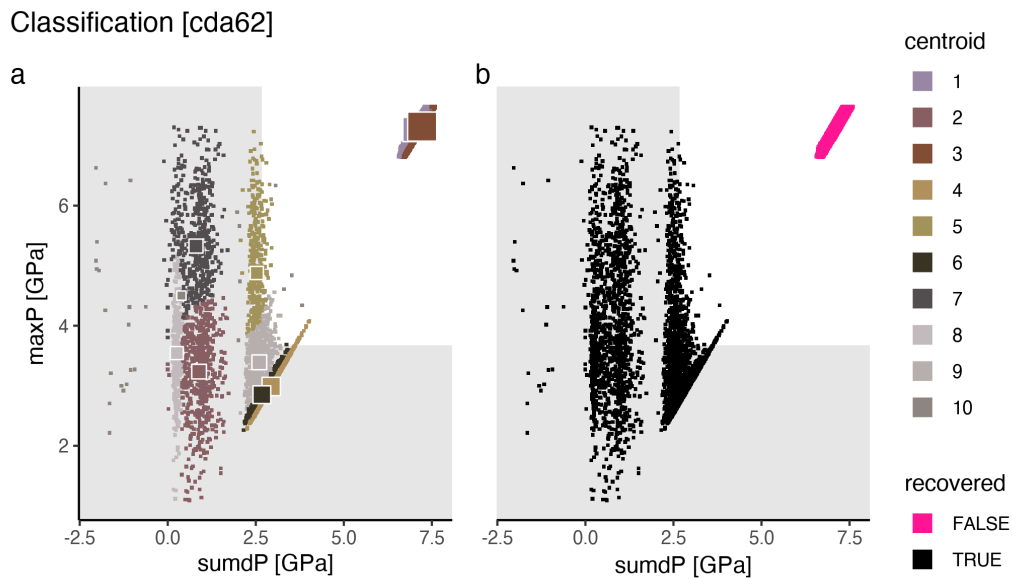


Figure A.4: Marker classification for model cda62.

Metamorphic conditions [cda62]

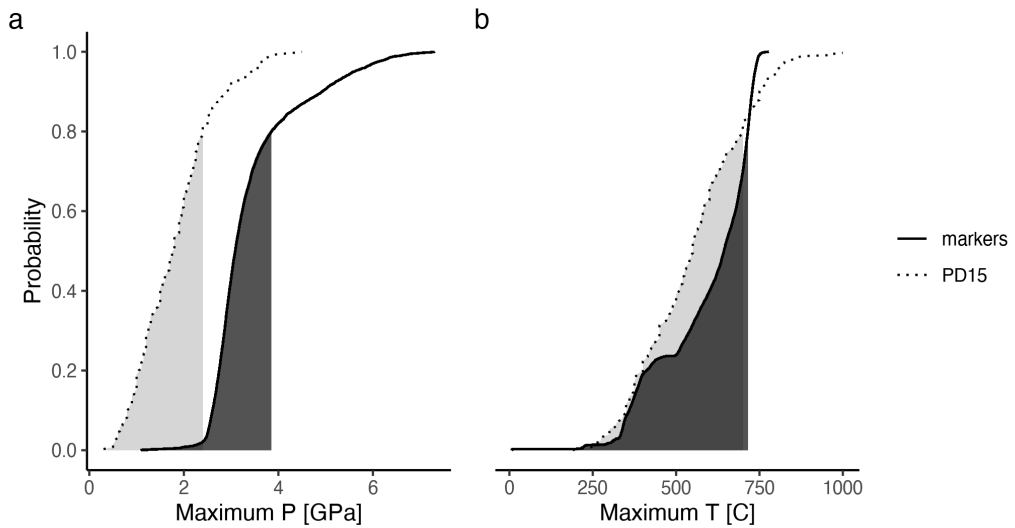


Figure A.5: Metamorphic conditions of markers recovered from model cda62.

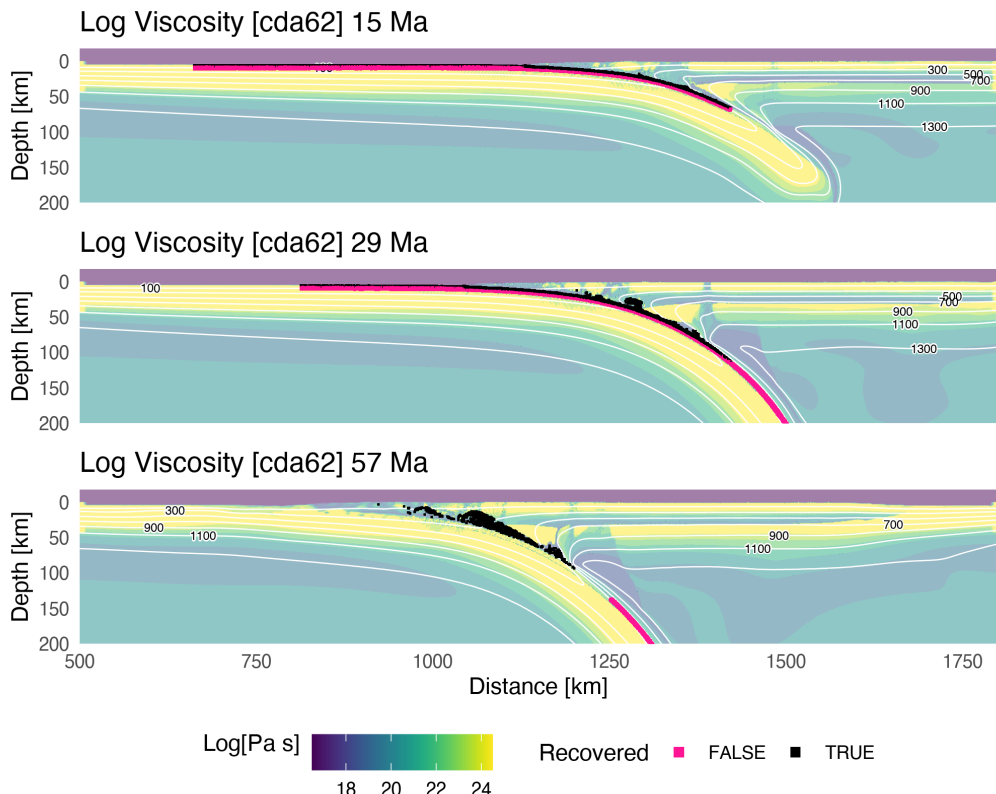


Figure A.6: Geodynamic evolution of model cda62.

Classification [cda78]

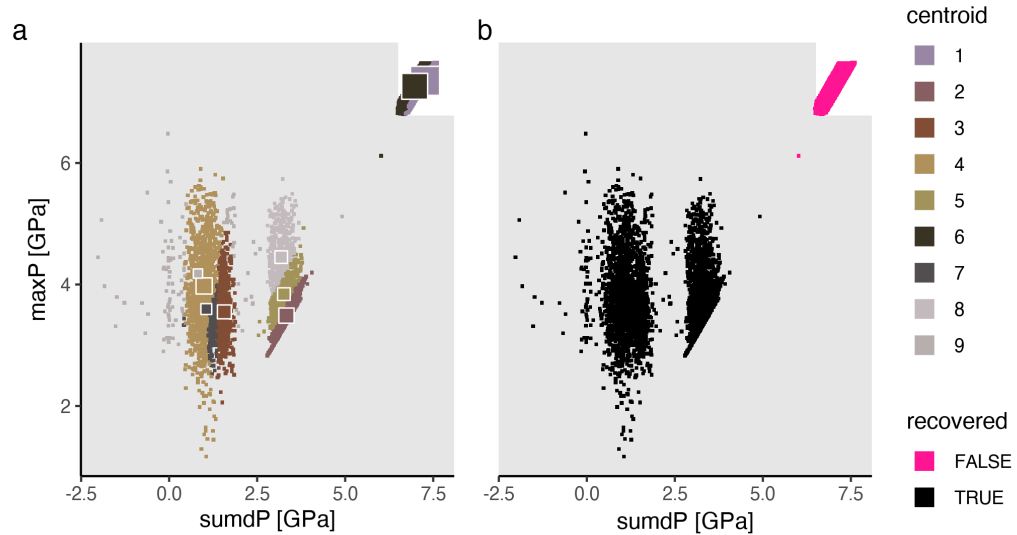


Figure A.7: Marker classification for model cda78.

Metamorphic conditions [cda78]

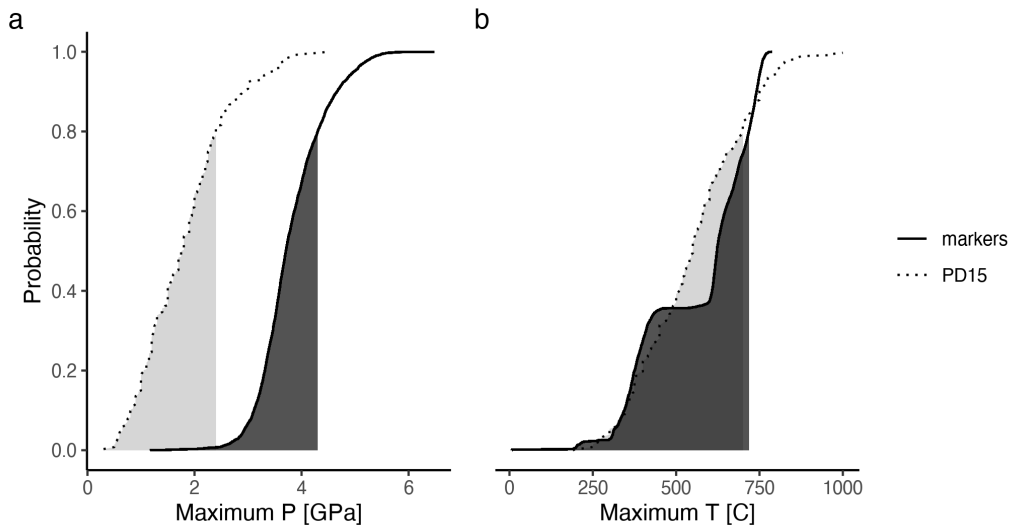


Figure A.8: Metamorphic conditions of markers recovered from model cda78.

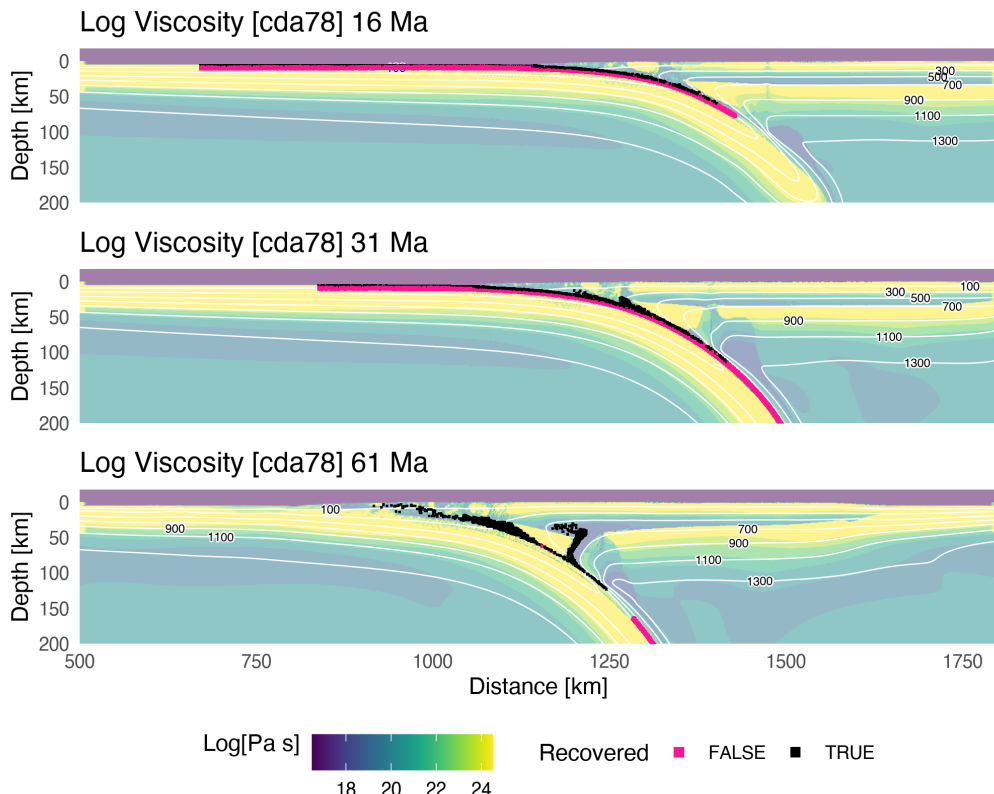


Figure A.9: Geodynamic evolution of model cda78.

Classification [cda94]

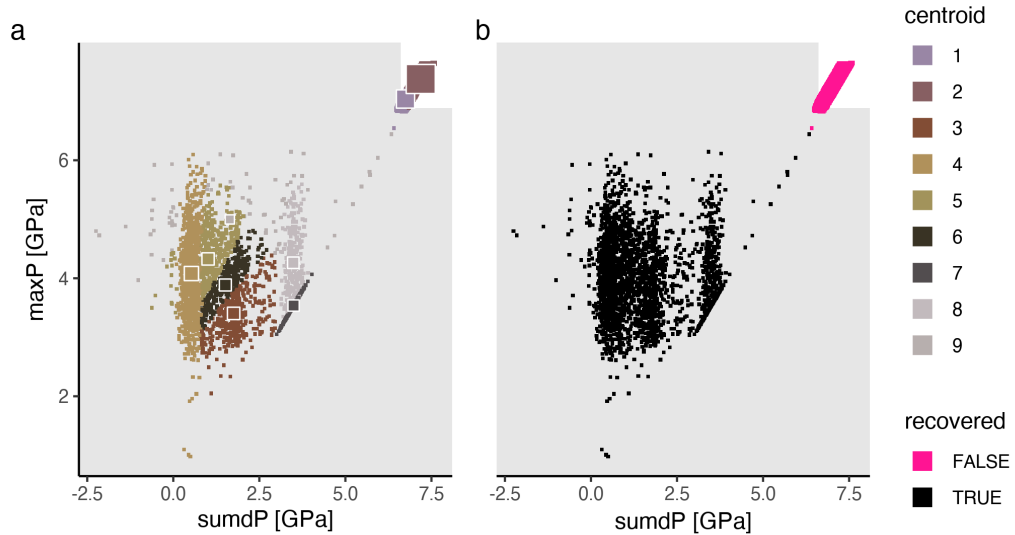


Figure A.10: Marker classification for model cda94.

Metamorphic conditions [cda94]

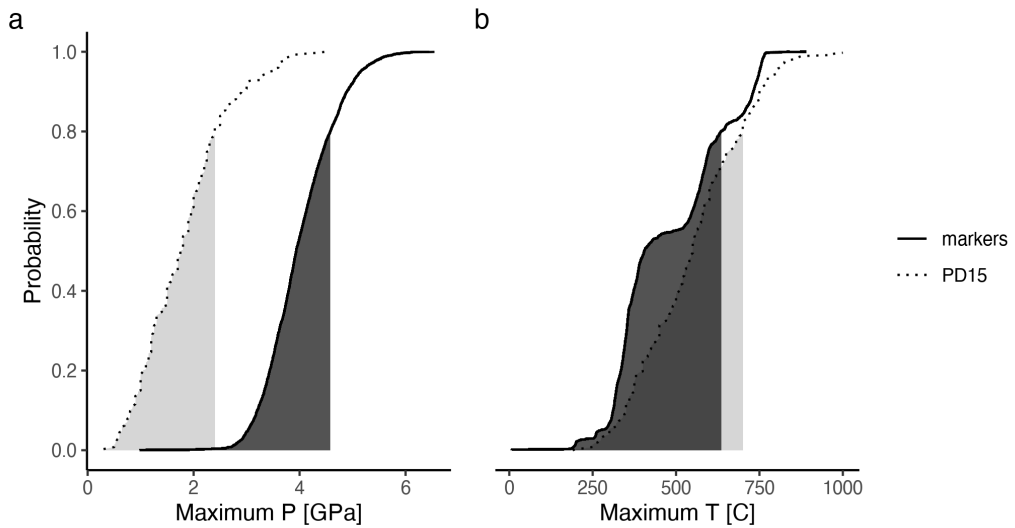


Figure A.11: Metamorphic conditions of markers recovered from model cda94.

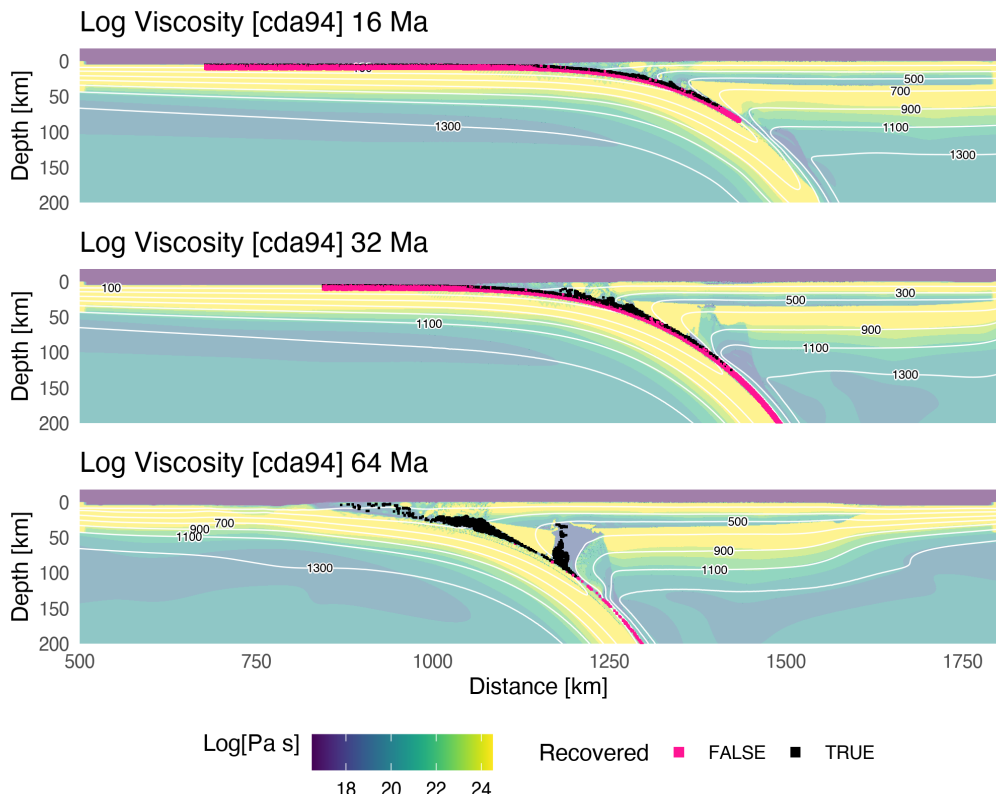


Figure A.12: Geodynamic evolution of model cda94.

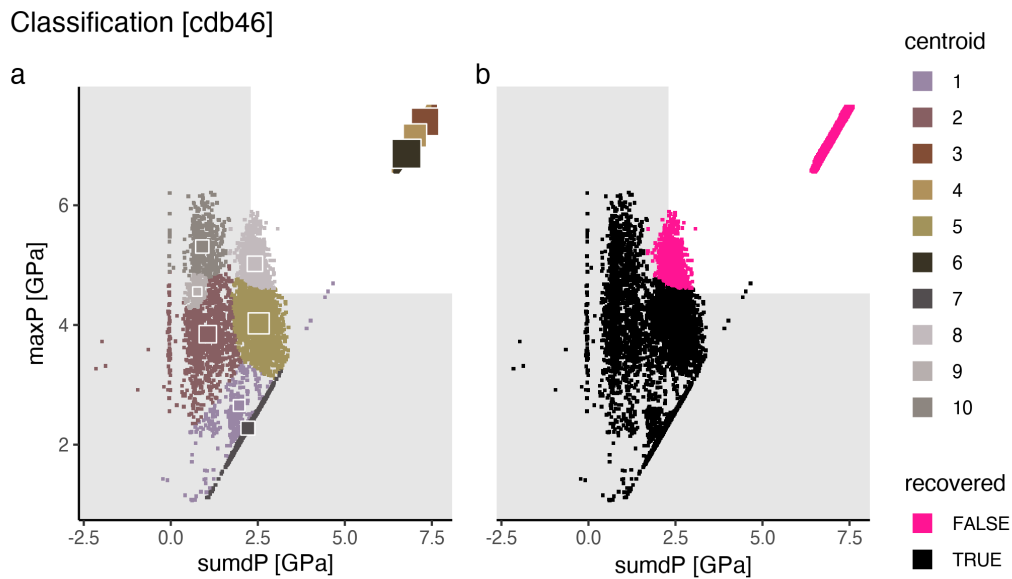


Figure A.13: Marker classification for model cdb46.

Metamorphic conditions [cdb46]

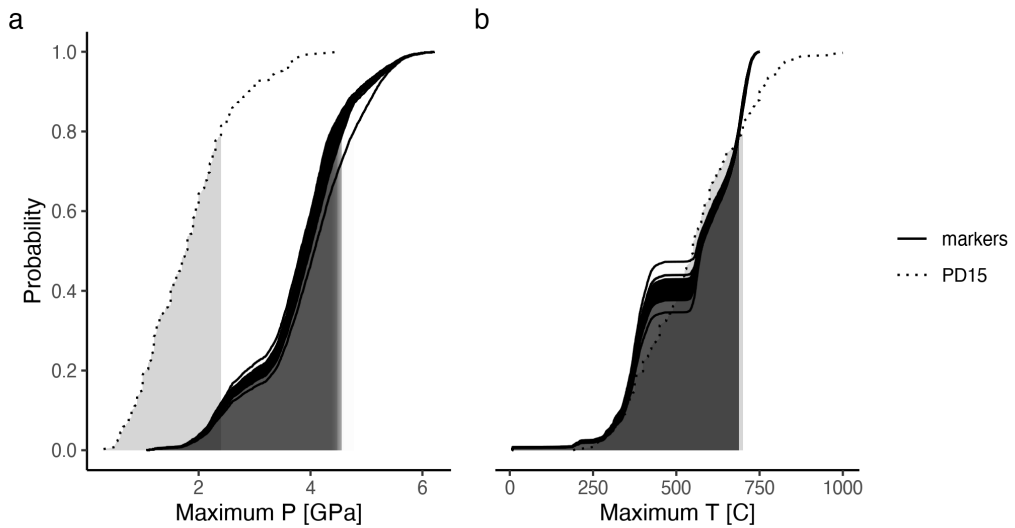


Figure A.14: Metamorphic conditions of markers recovered from model cdb46.

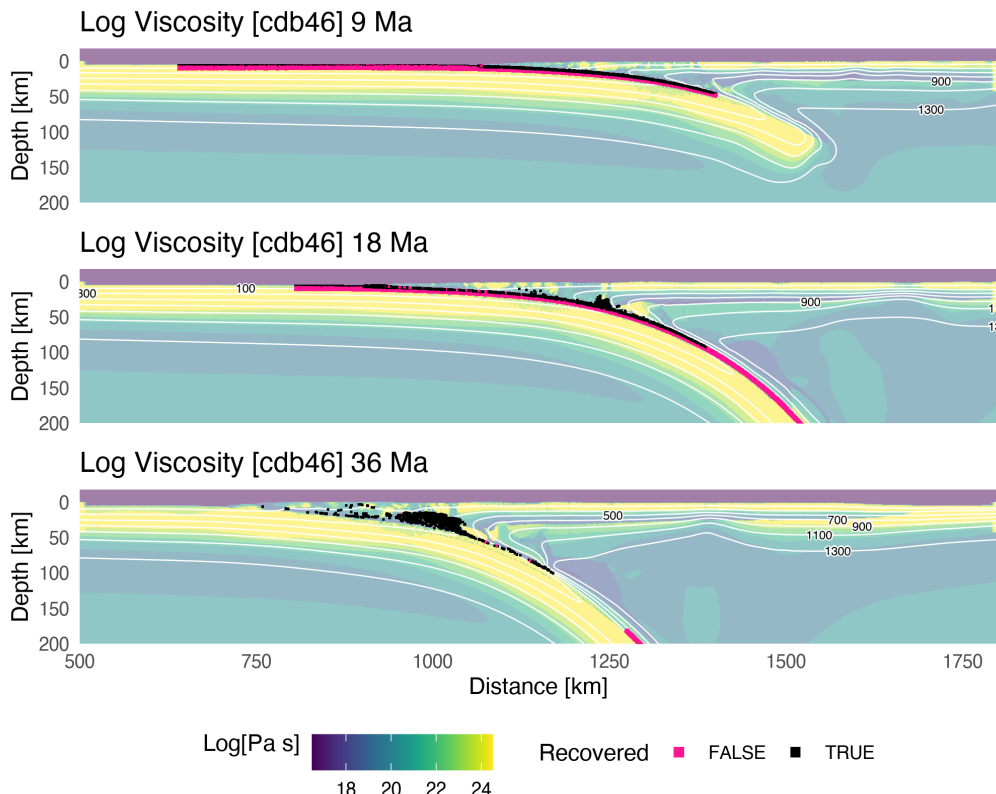


Figure A.15: Geodynamic evolution of model cdb46.

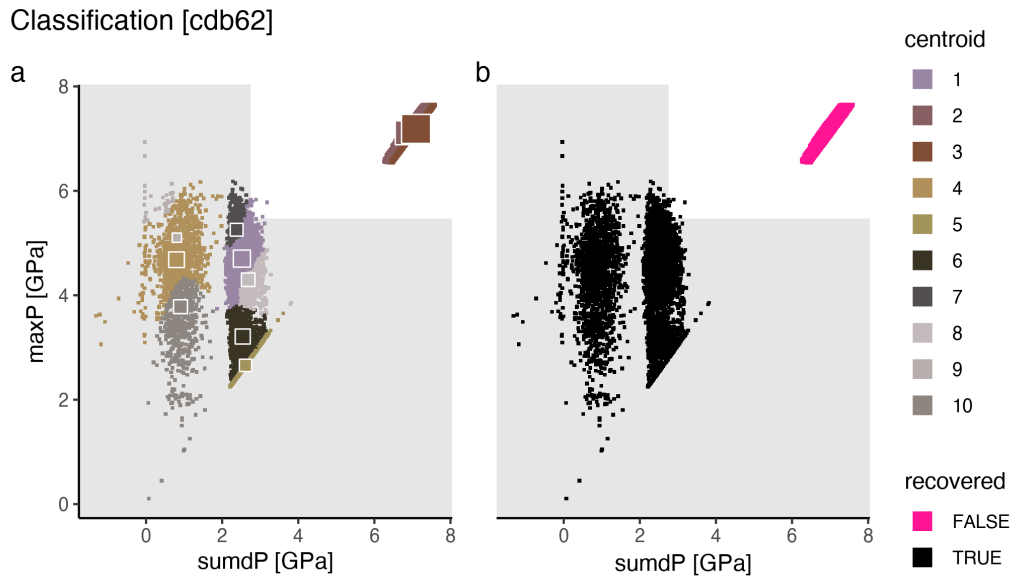


Figure A.16: Marker classification for model cdb62.

Metamorphic conditions [cdb62]

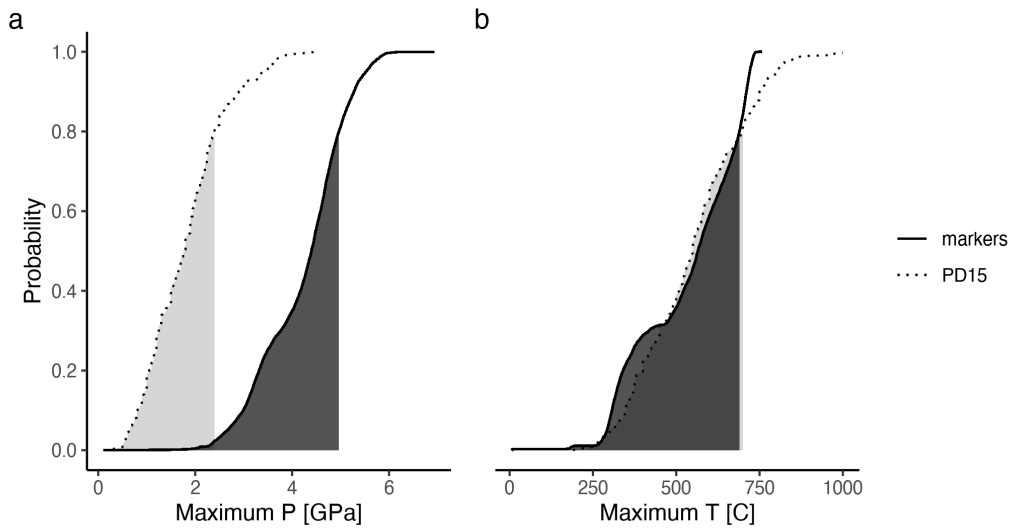


Figure A.17: Metamorphic conditions of markers recovered from model cdb62.

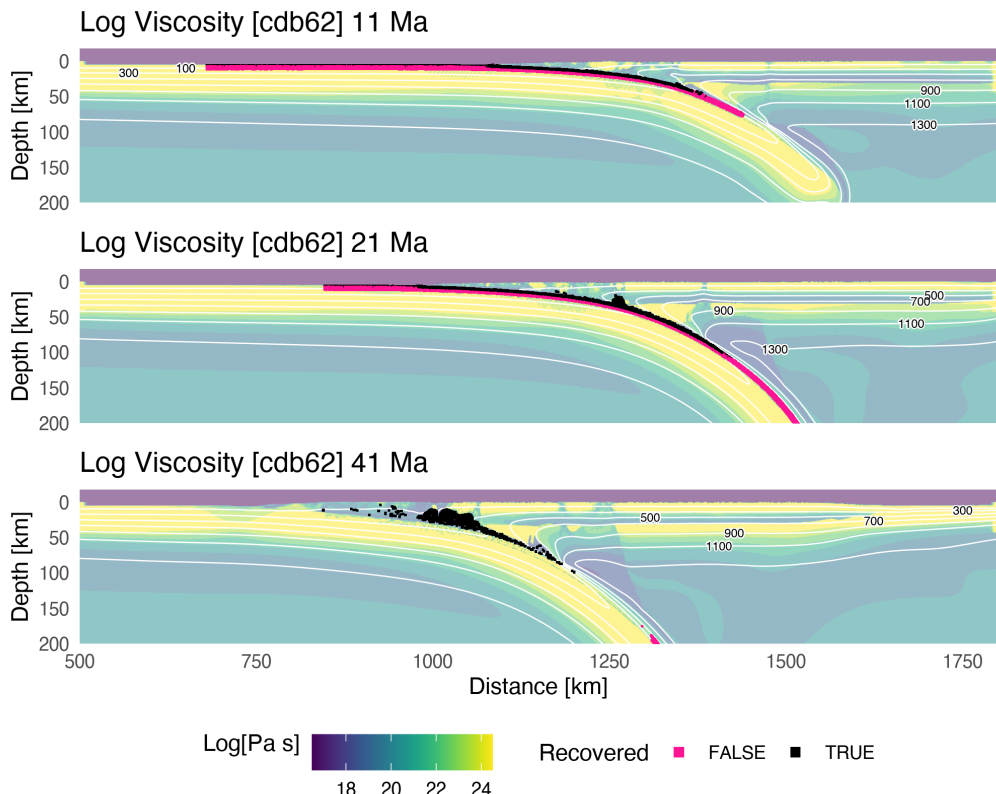


Figure A.18: Geodynamic evolution of model cdb62.

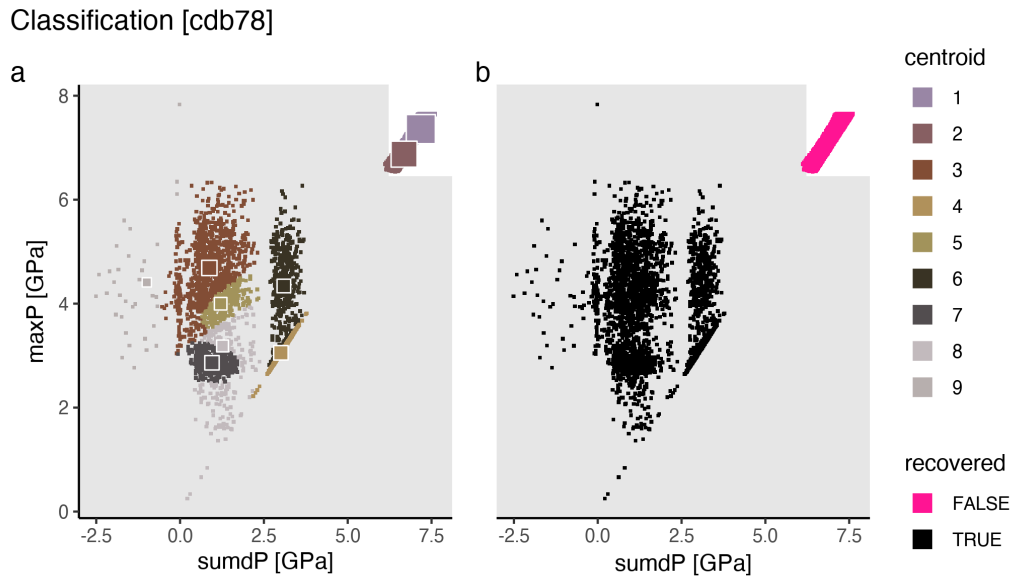


Figure A.19: Marker classification for model cdb78.

Metamorphic conditions [cdb78]

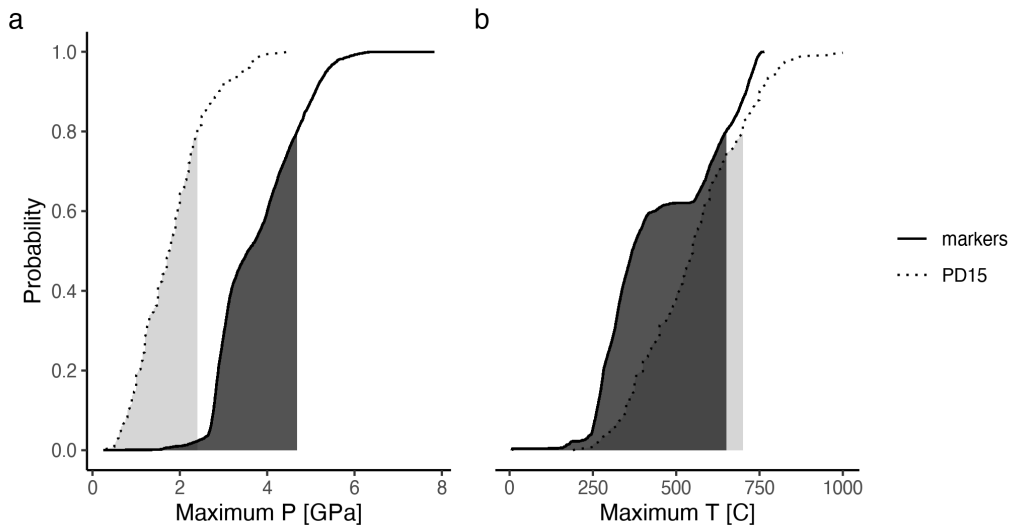


Figure A.20: Metamorphic conditions of markers recovered from model cdb78.

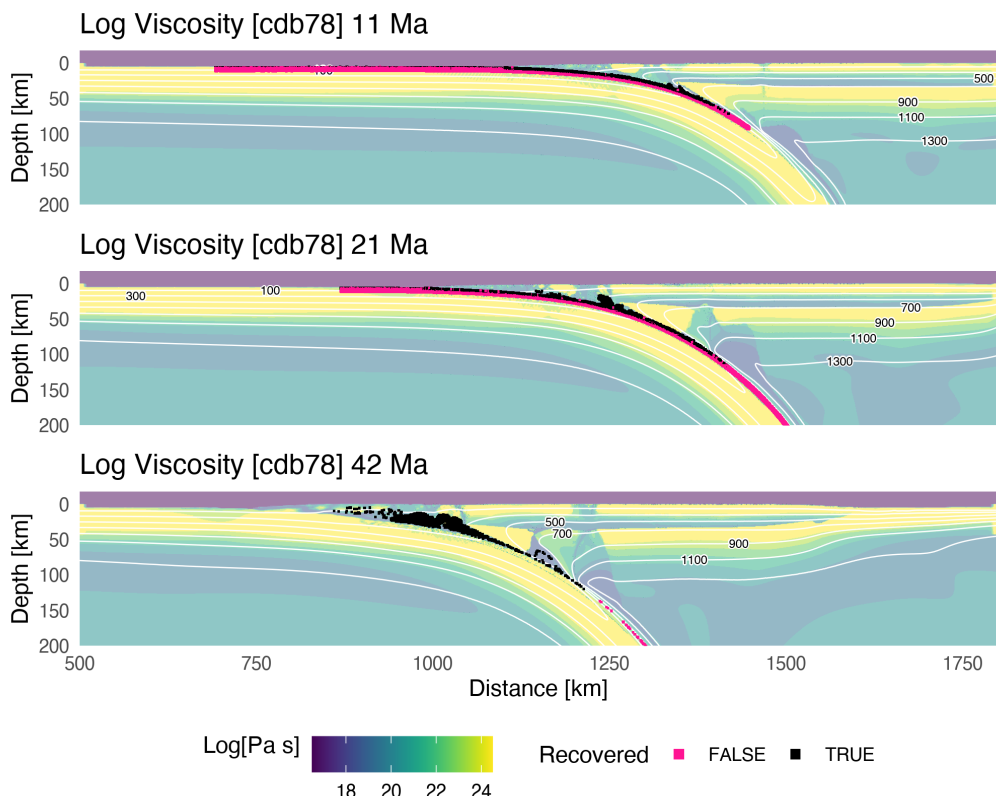


Figure A.21: Geodynamic evolution of model cdb78.

Classification [cdb94]

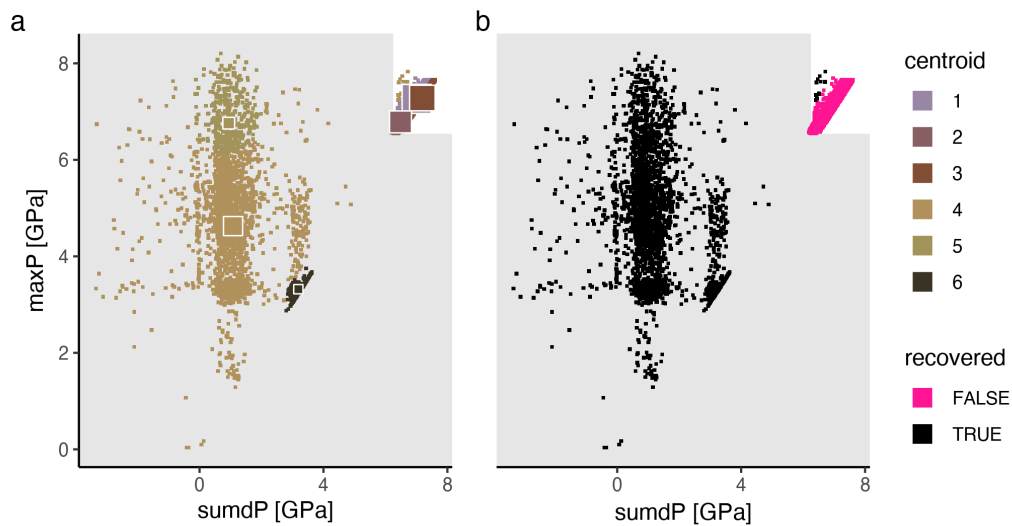


Figure A.22: Marker classification for model cdb94.

Metamorphic conditions [cdb94]

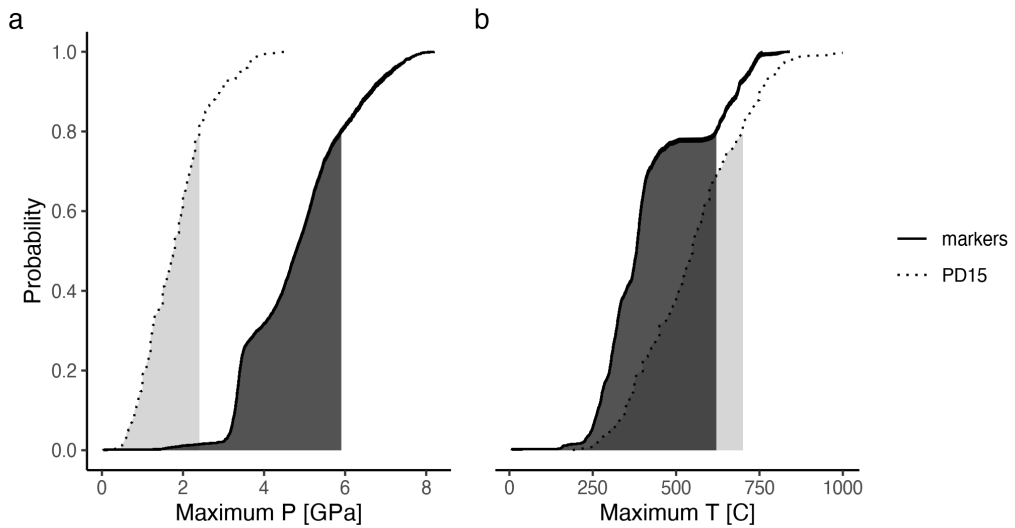


Figure A.23: Metamorphic conditions of markers recovered from model cdb94.

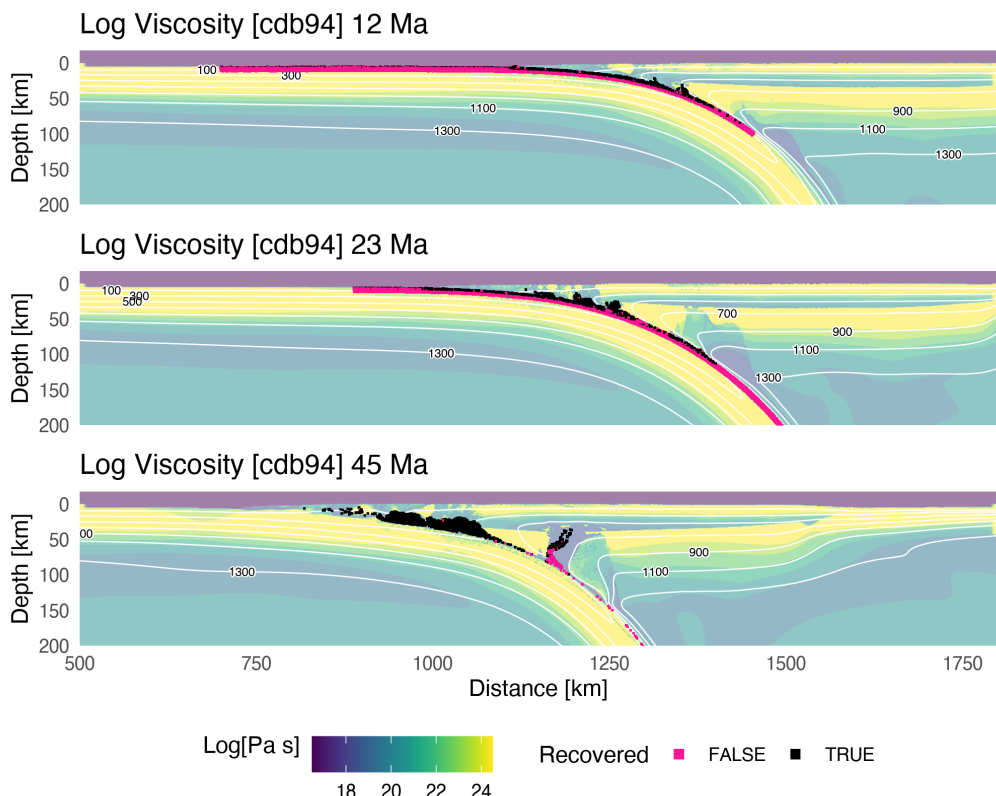


Figure A.24: Geodynamic evolution of model cdb94.

Classification [cdc46]

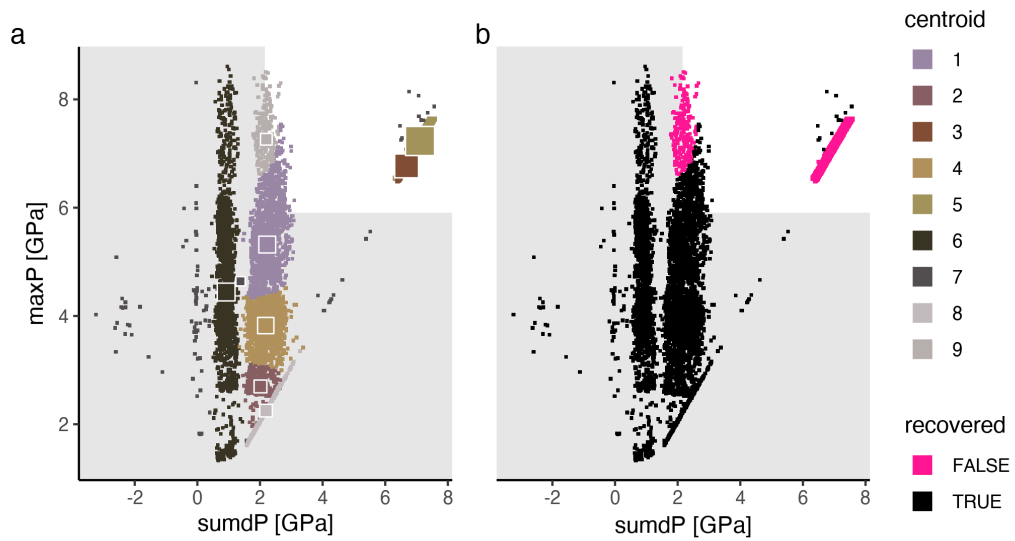


Figure A.25: Marker classification for model cdc46.

Metamorphic conditions [cdc46]

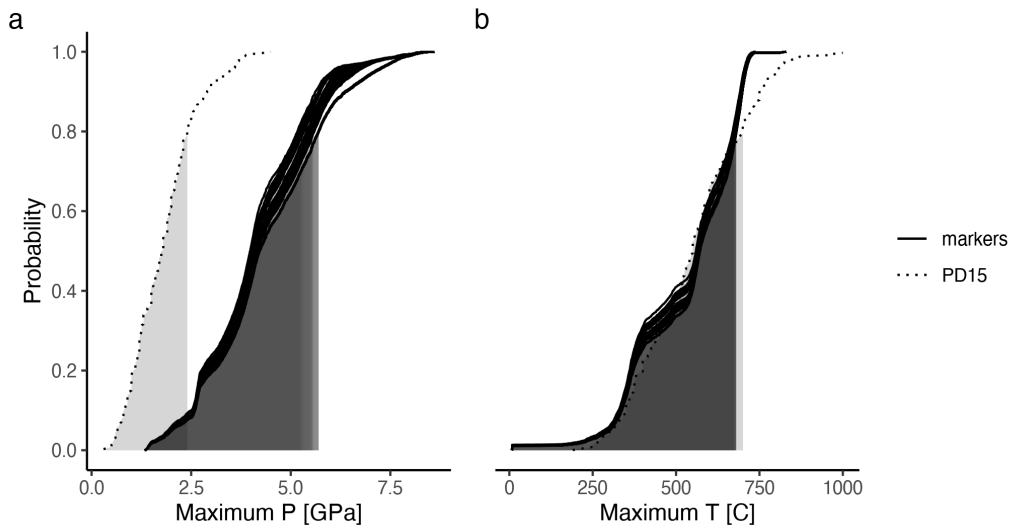


Figure A.26: Metamorphic conditions of markers recovered from model cdc46.

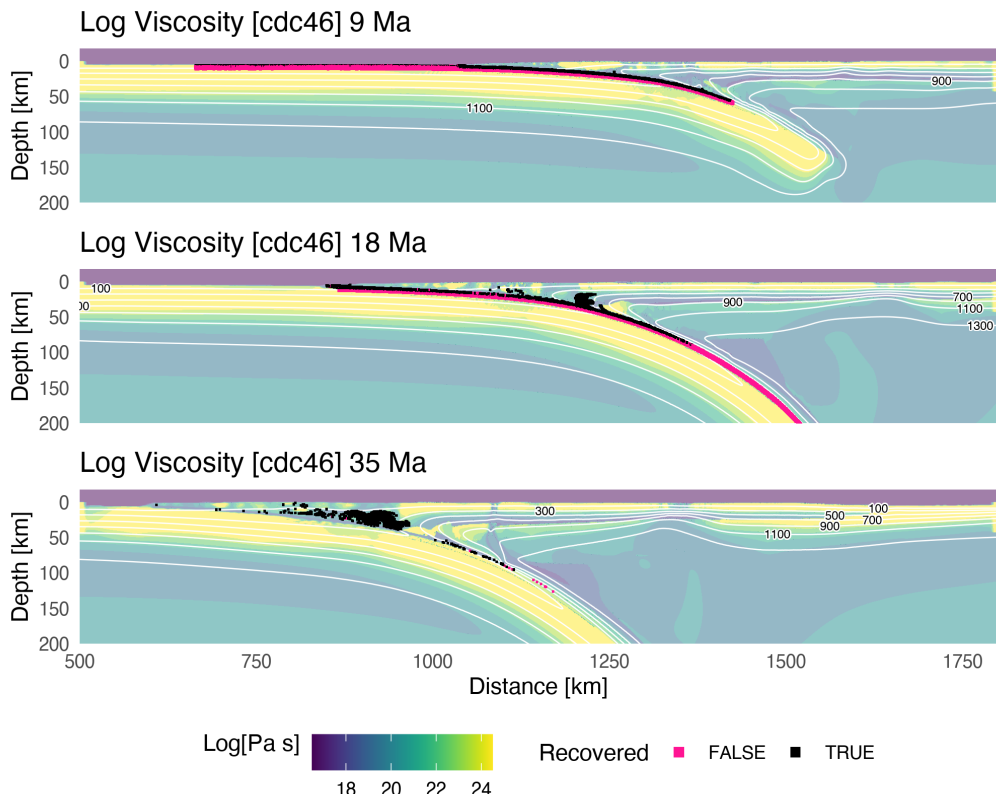


Figure A.27: Geodynamic evolution of model cdc46.

Classification [cdc62]

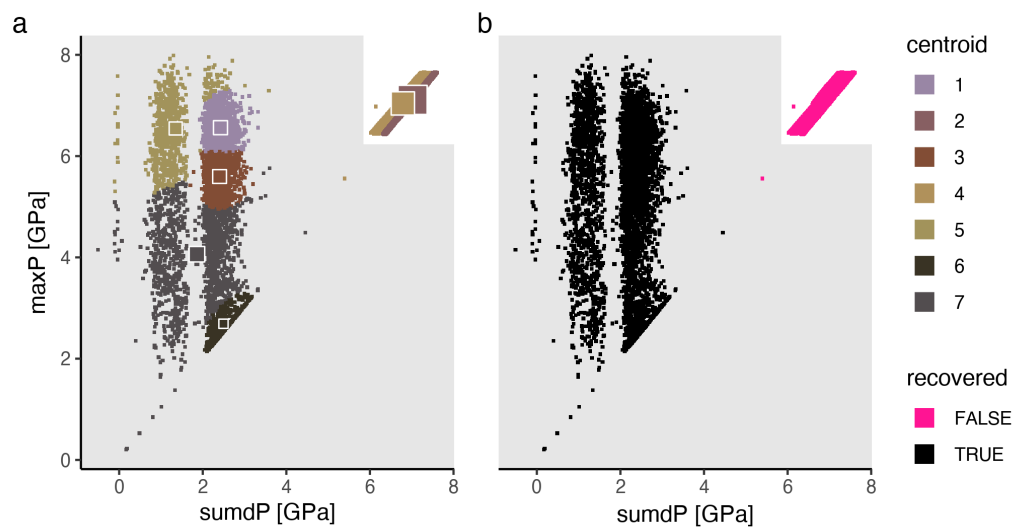


Figure A.28: Marker classification for model cdc62.

Metamorphic conditions [cdc62]

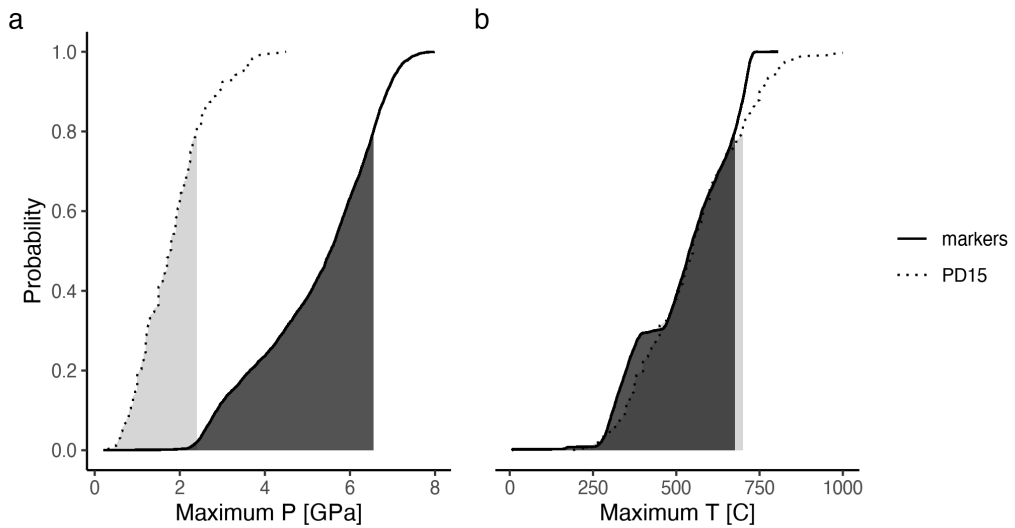


Figure A.29: Metamorphic conditions of markers recovered from model cdc62.

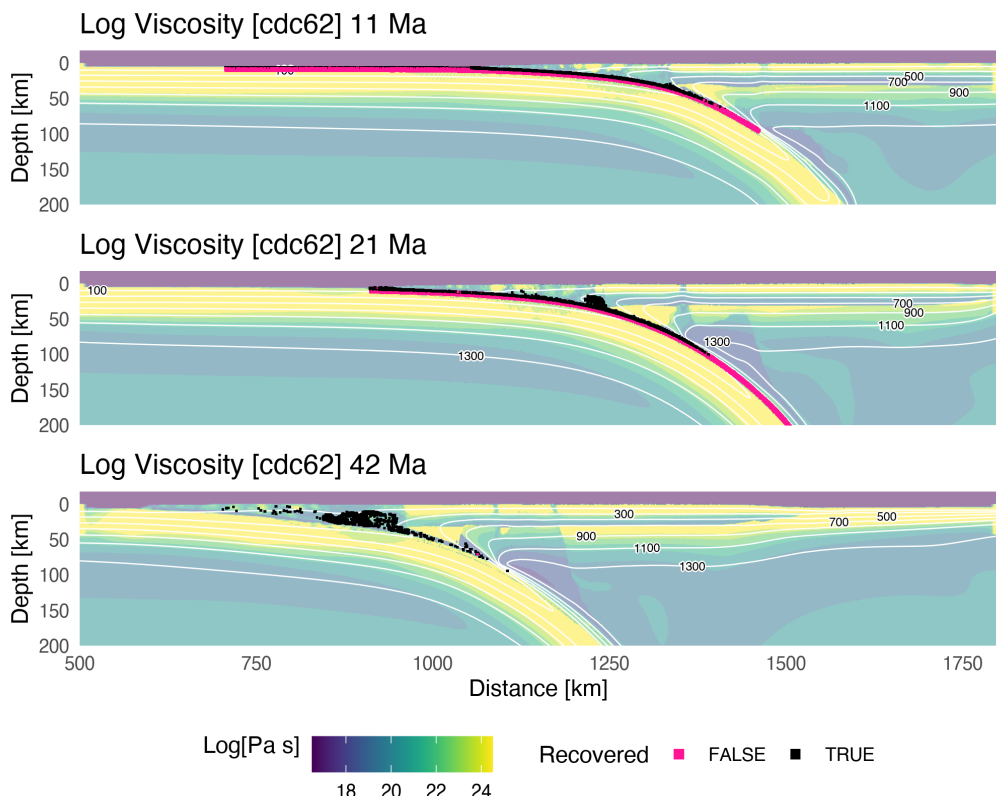


Figure A.30: Geodynamic evolution of model cdc62.

Classification [cdc78]

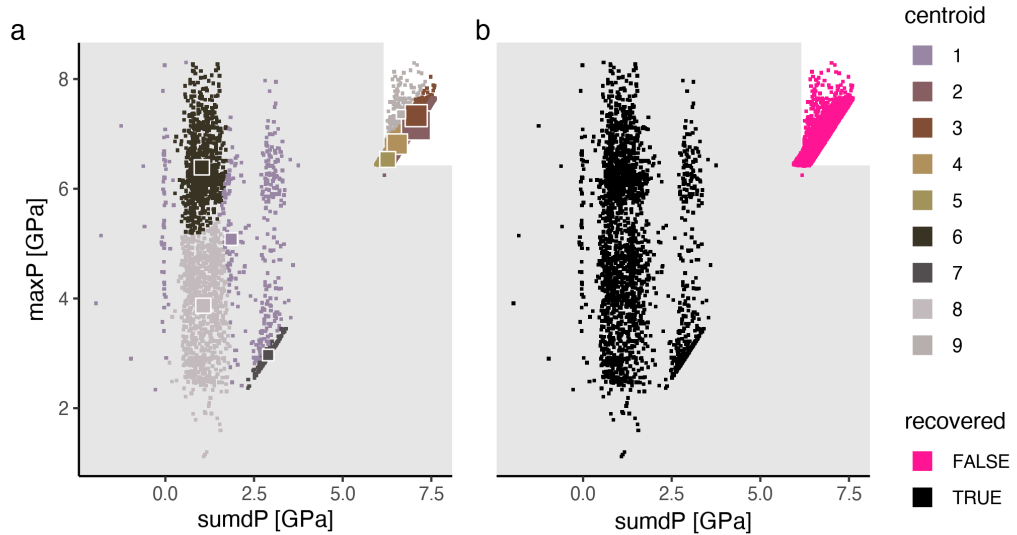


Figure A.31: Marker classification for model cdc78.

Metamorphic conditions [cdc78]

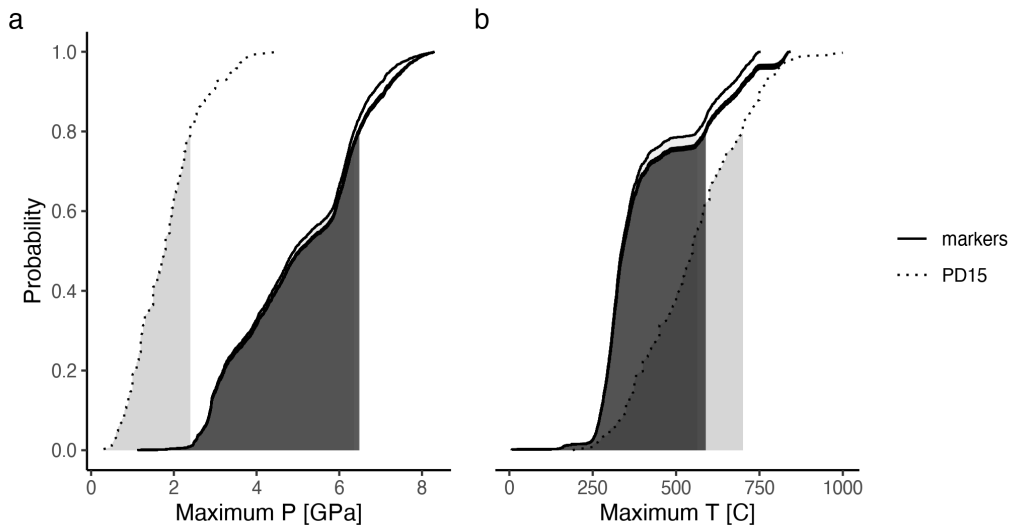


Figure A.32: Metamorphic conditions of markers recovered from model cdc78.

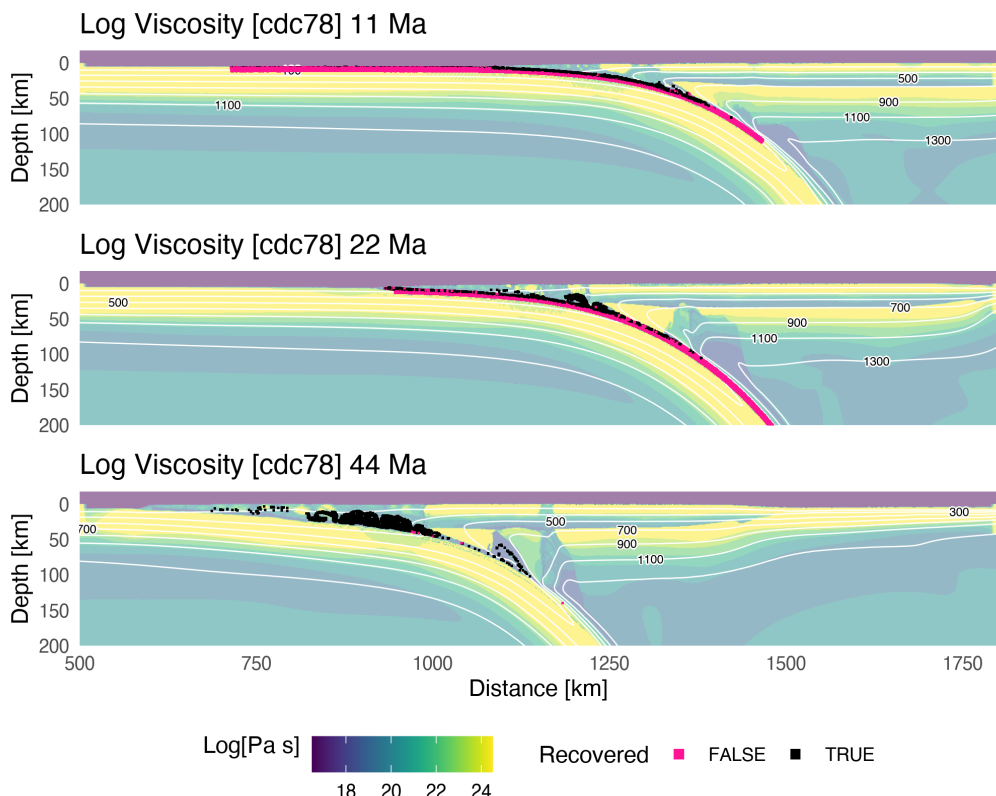


Figure A.33: Geodynamic evolution of model cdc78.

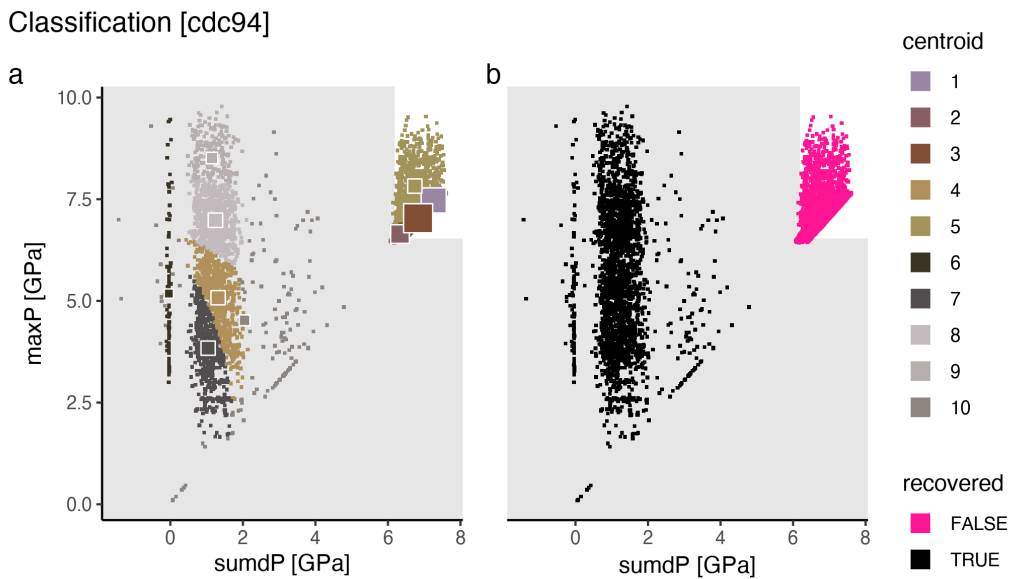


Figure A.34: Marker classification for model cdc94.

Metamorphic conditions [cdc94]

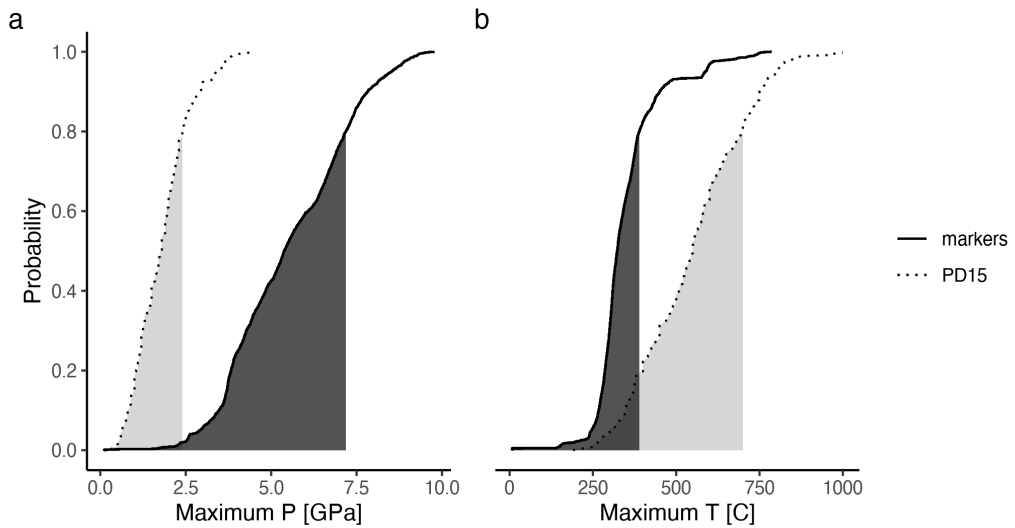


Figure A.35: Metamorphic conditions of markers recovered from model cdc94.

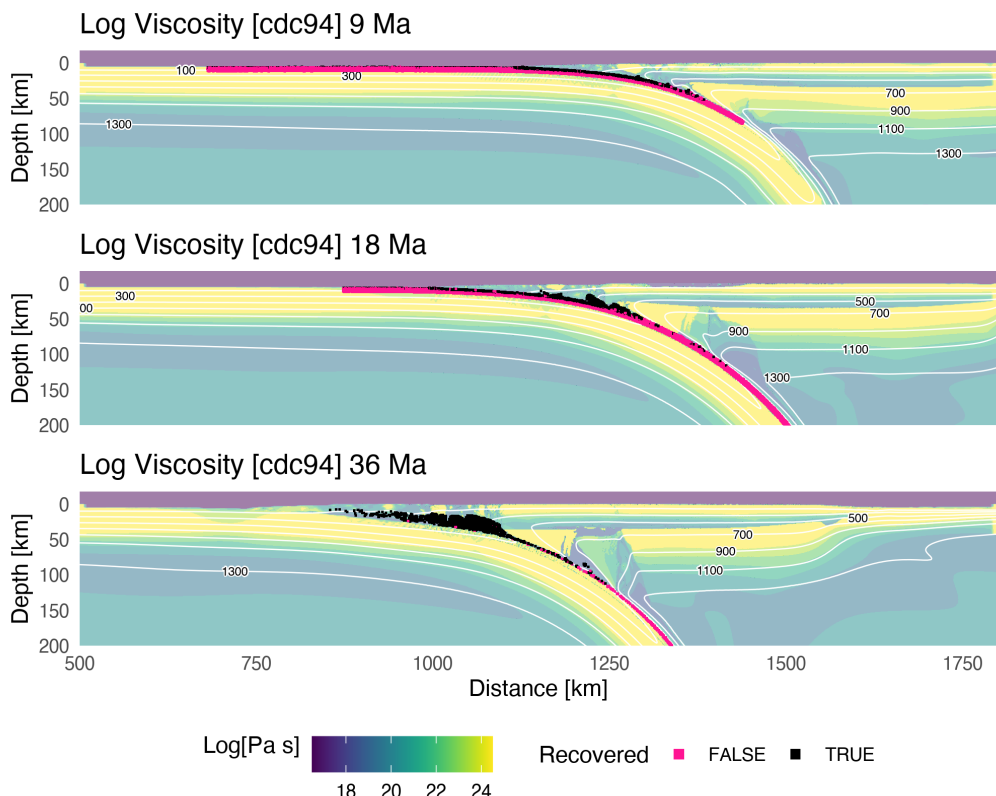


Figure A.36: Geodynamic evolution of model cdc94.

Classification [cdd46]

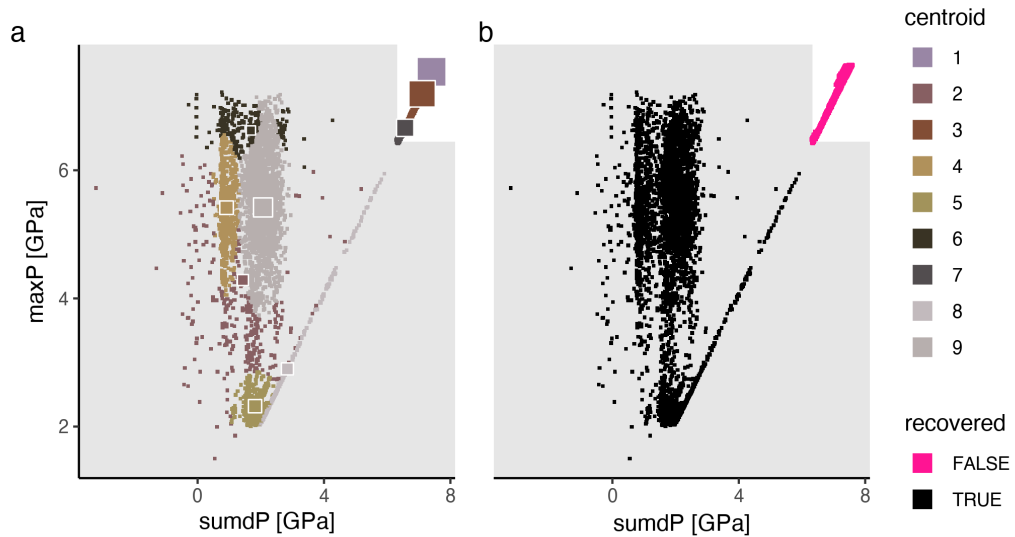


Figure A.37: Marker classification for model cdd46.

Metamorphic conditions [cdd46]

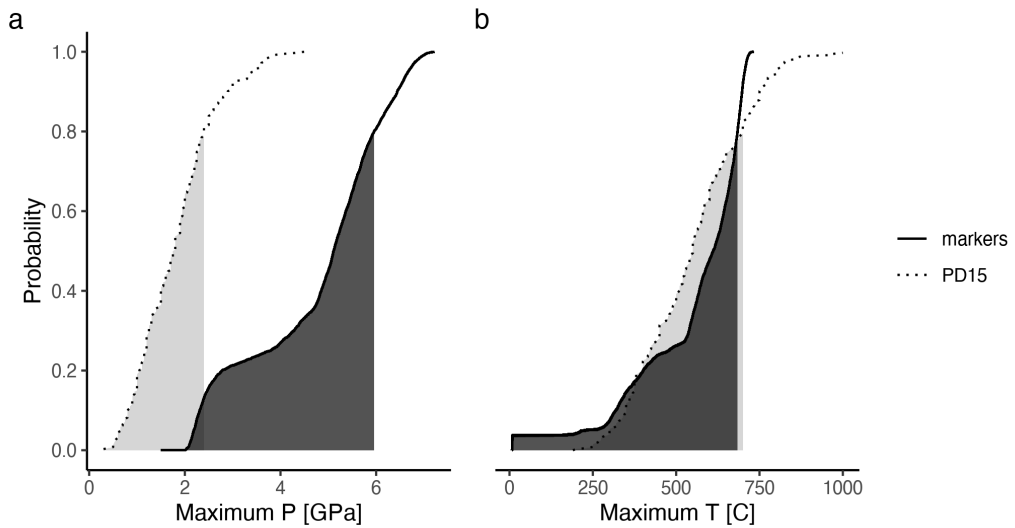


Figure A.38: Metamorphic conditions of markers recovered from model cdd46.

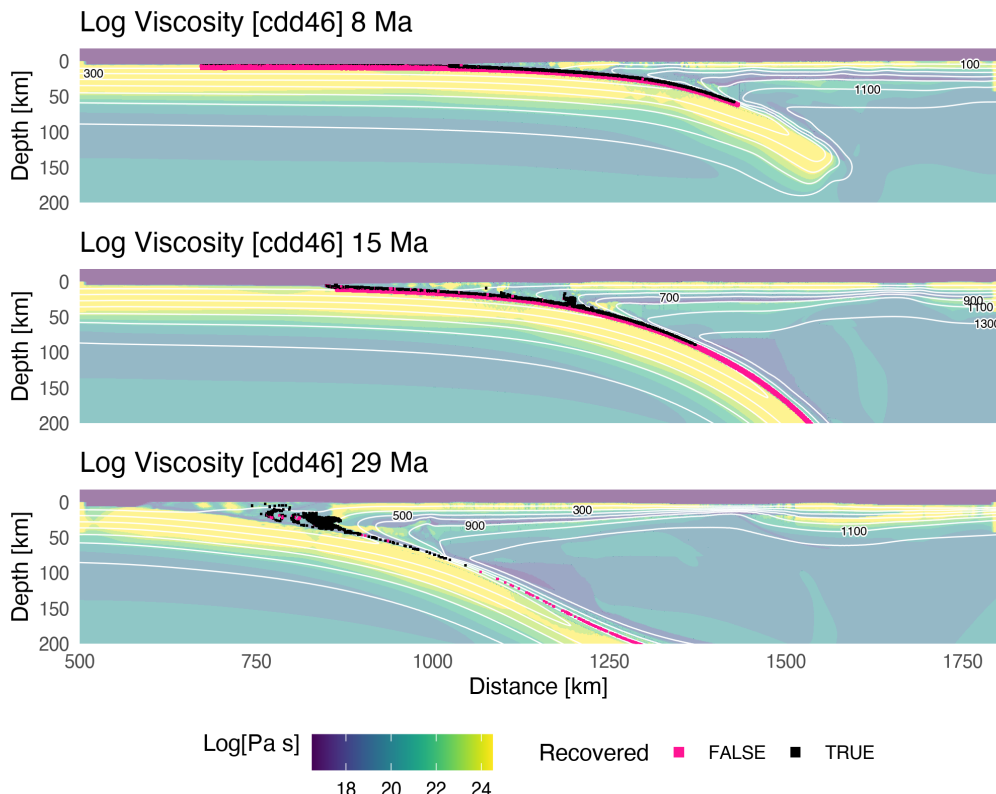


Figure A.39: Geodynamic evolution of model cdd46.

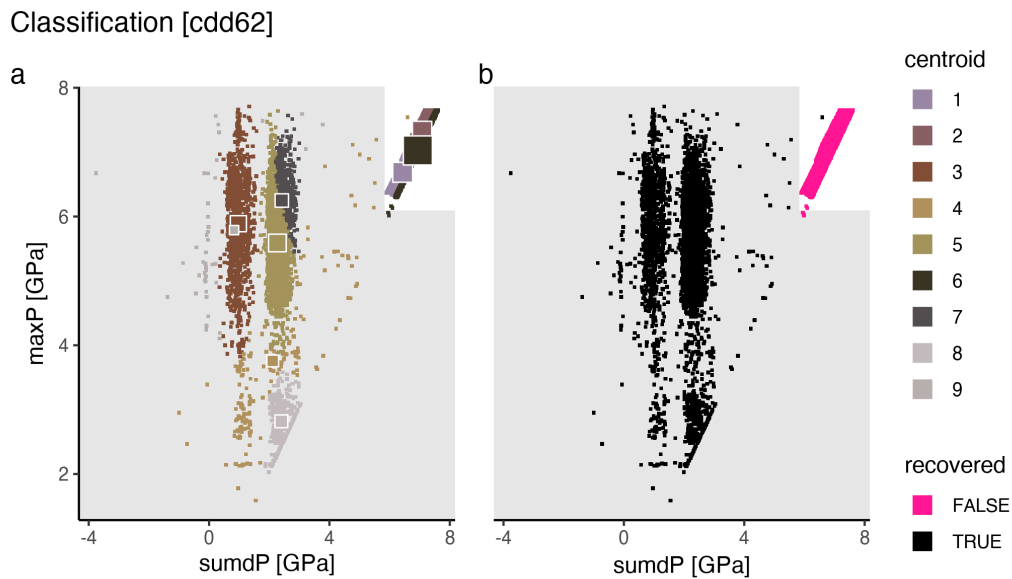


Figure A.40: Marker classification for model cdd62.

Metamorphic conditions [cdd62]

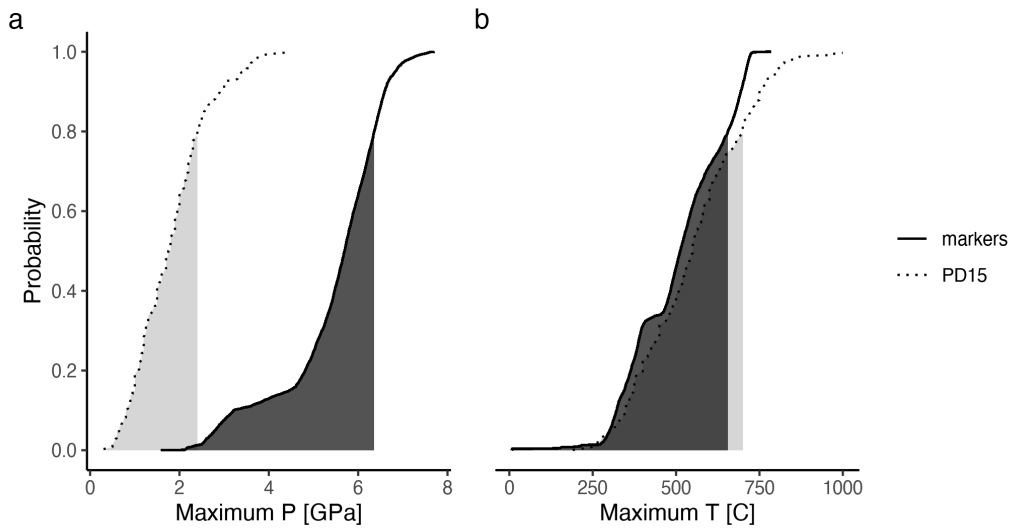


Figure A.41: Metamorphic conditions of markers recovered from model cdd62.

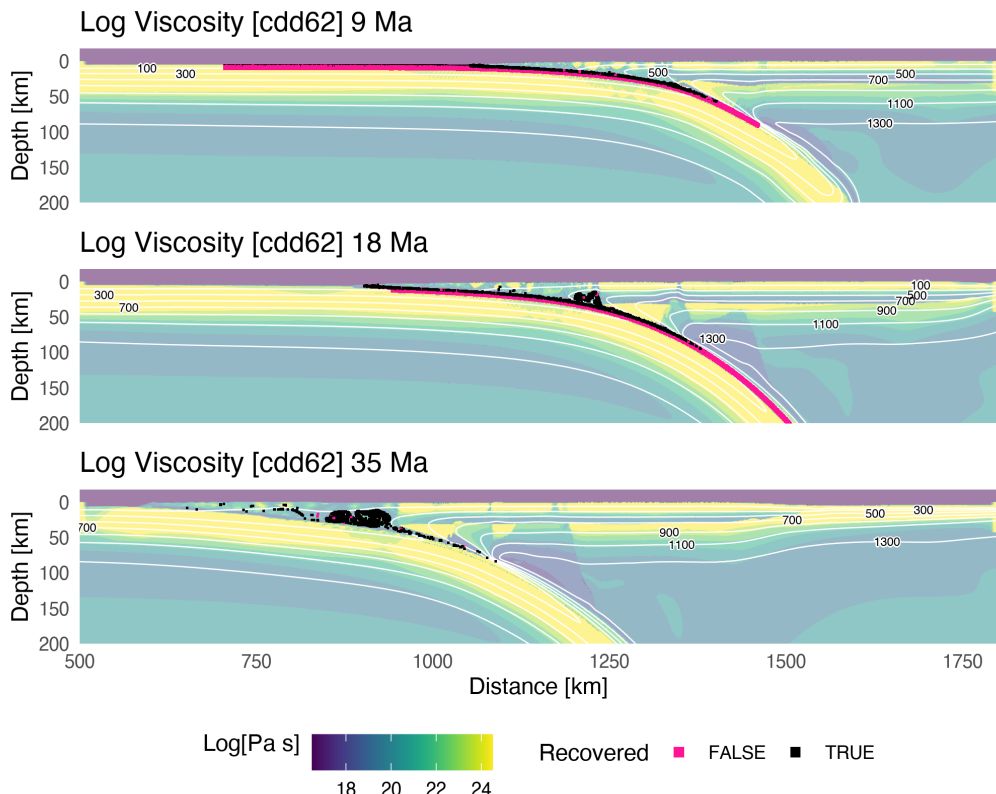


Figure A.42: Geodynamic evolution of model cdd62.

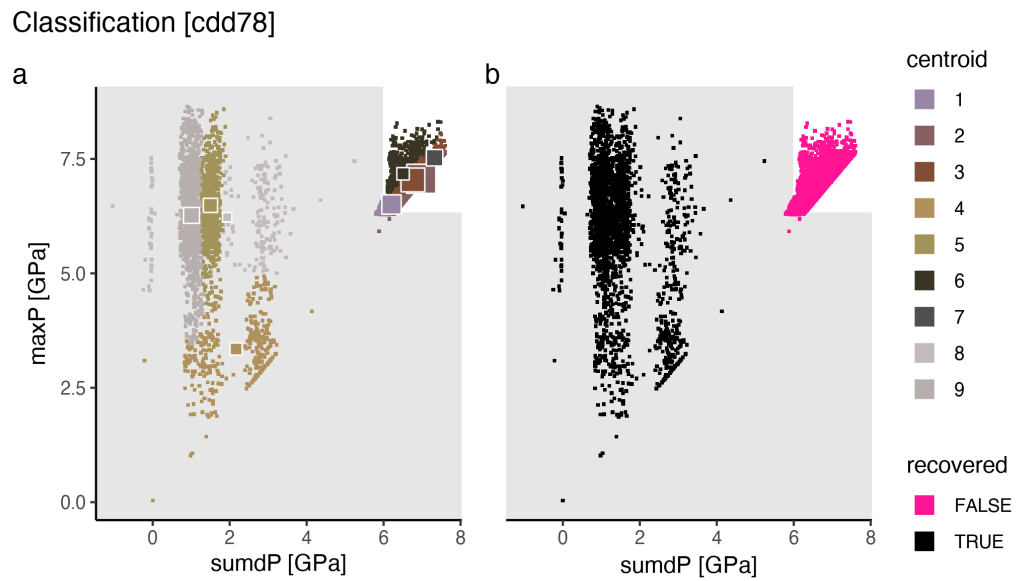


Figure A.43: Marker classification for model cdd78.

Metamorphic conditions [cdd78]

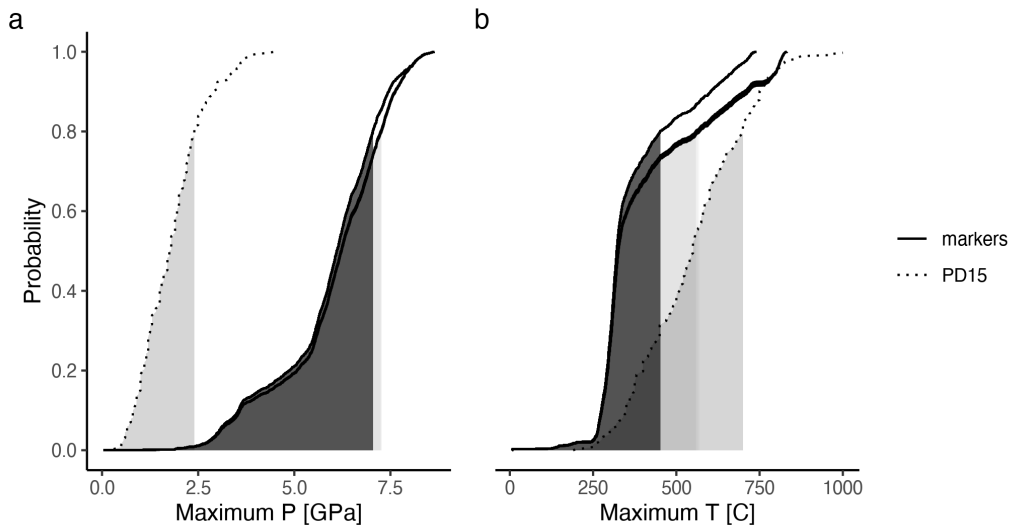


Figure A.44: Metamorphic conditions of markers recovered from model cdd78.

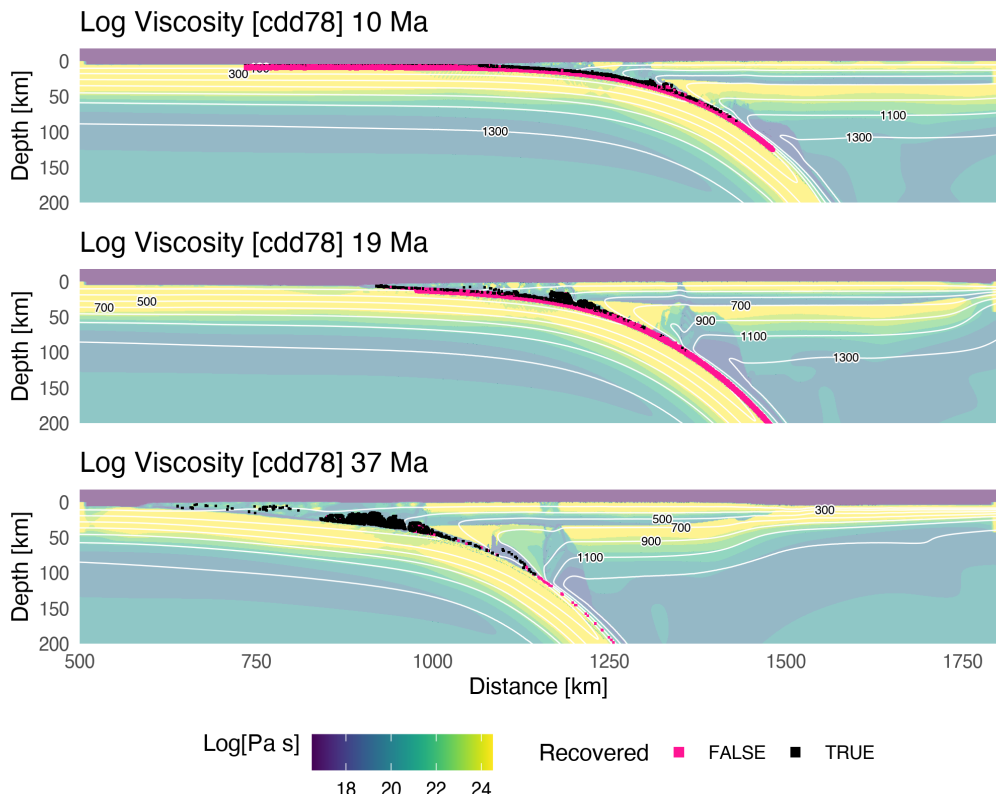


Figure A.45: Geodynamic evolution of model cdd78.

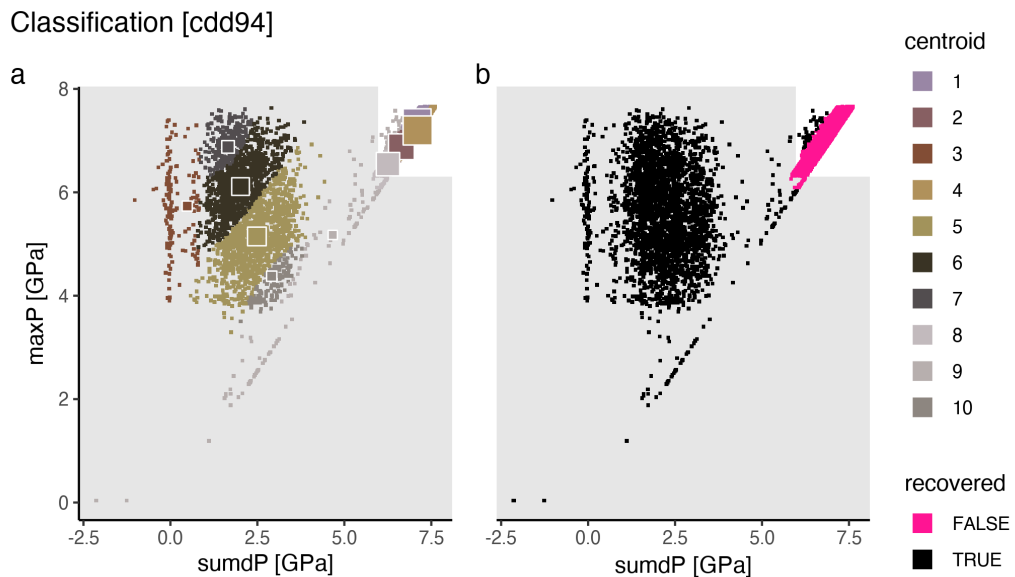


Figure A.46: Marker classification for model cdd94.

Metamorphic conditions [cdd94]

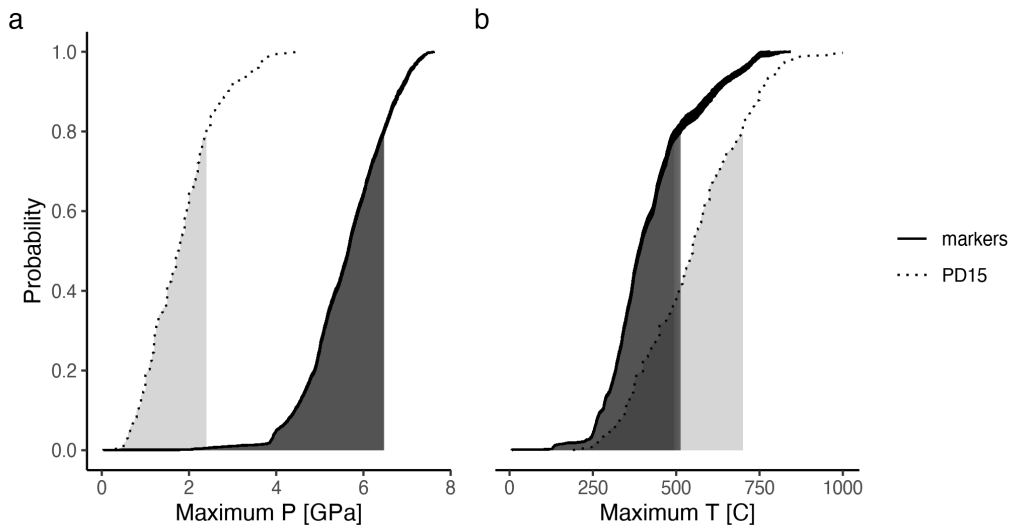


Figure A.47: Metamorphic conditions of markers recovered from model cdd94.

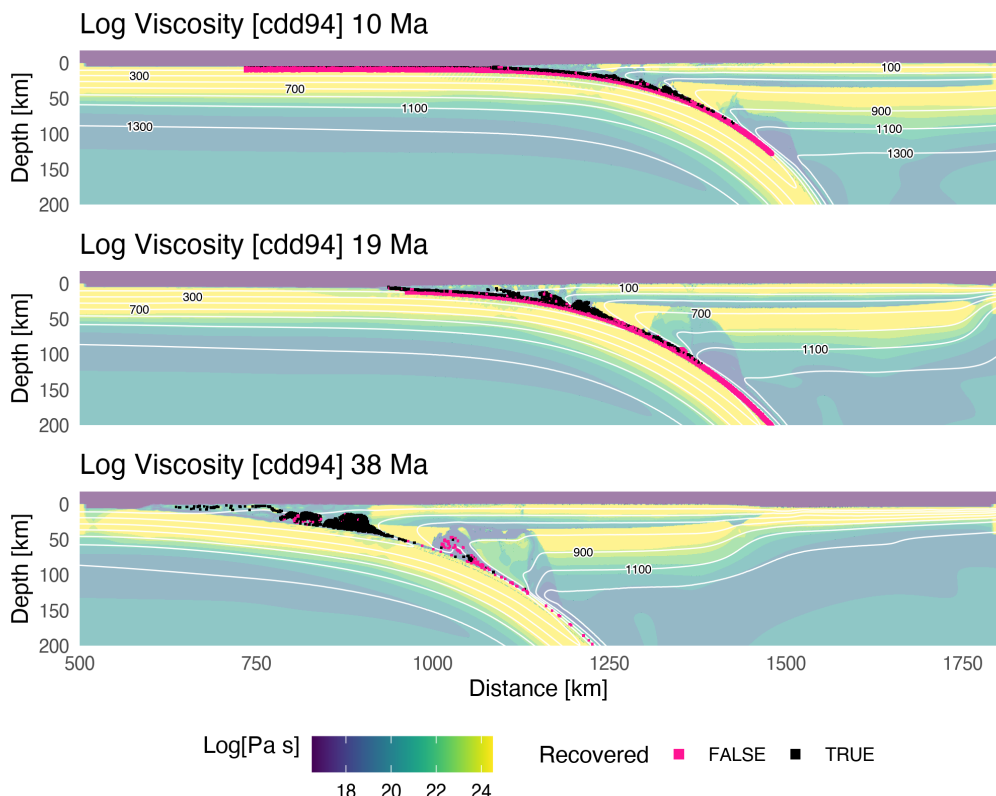


Figure A.48: Geodynamic evolution of model cdd94.

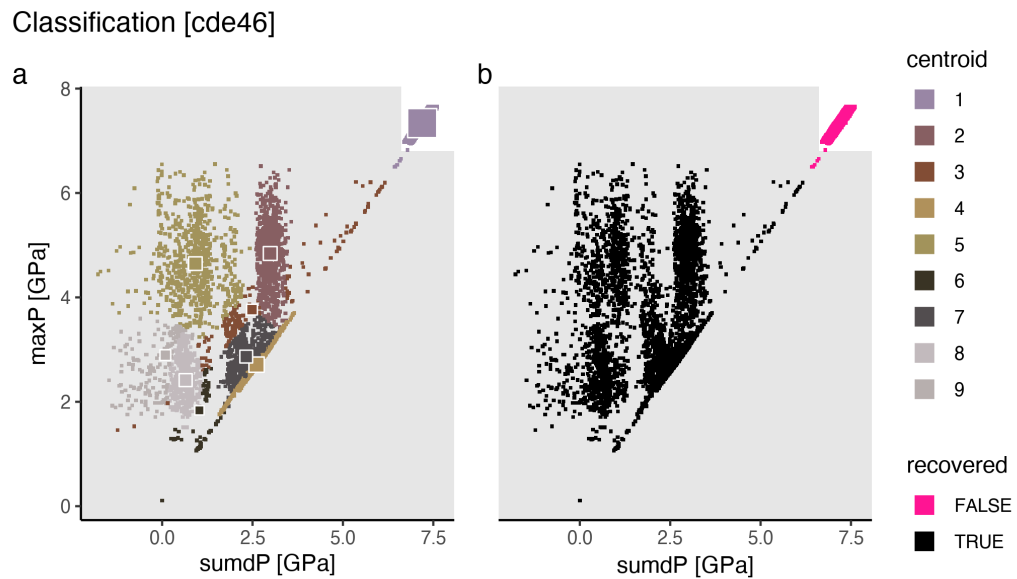


Figure A.49: Marker classification for model cde46.

Metamorphic conditions [cde46]

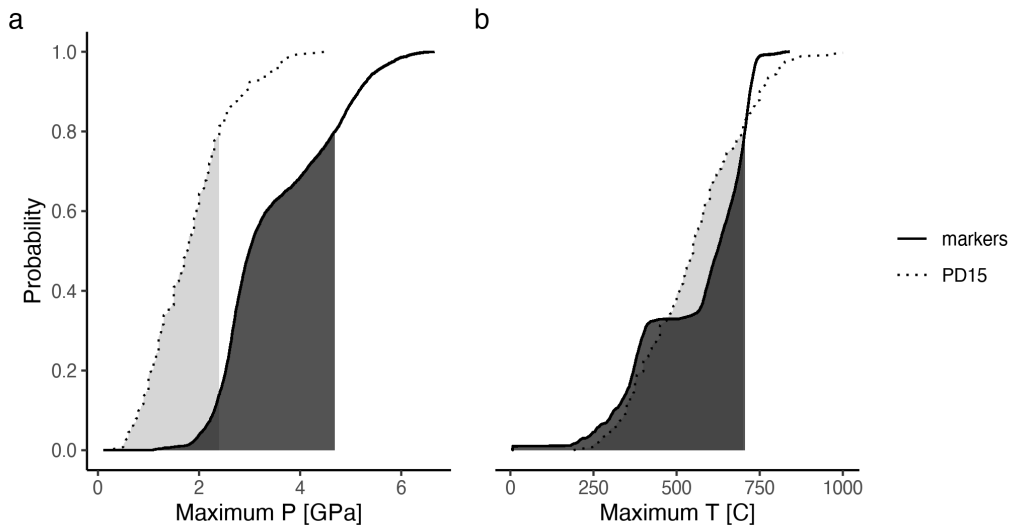


Figure A.50: Metamorphic conditions of markers recovered from model cde46.

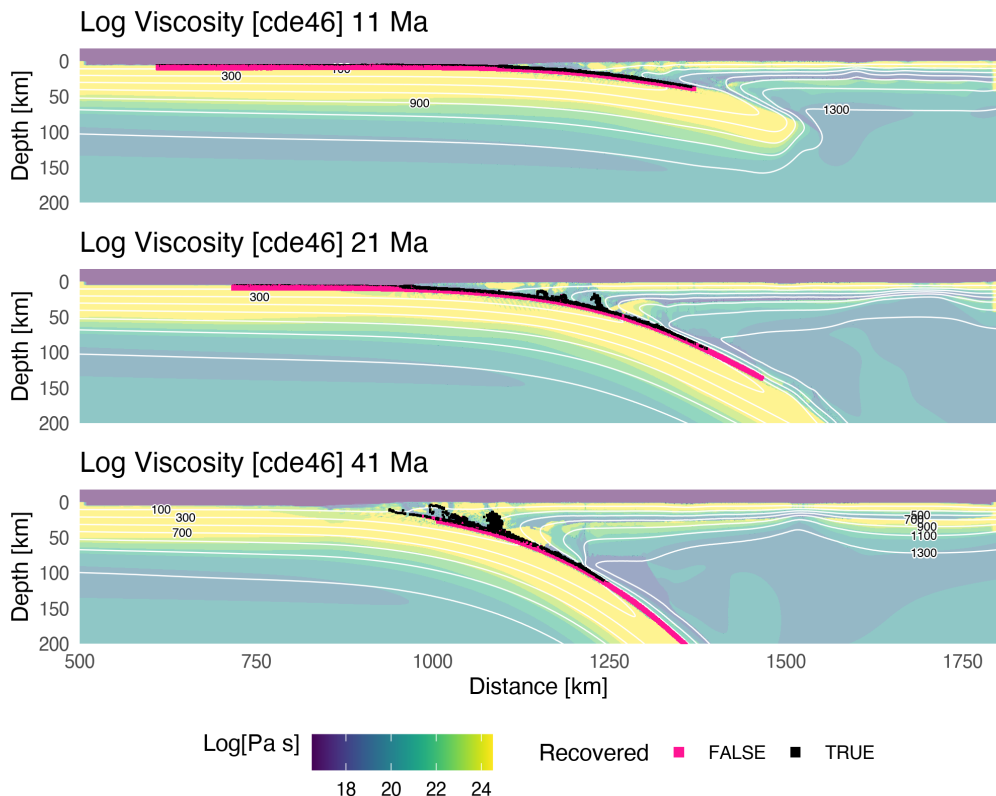


Figure A.51: Geodynamic evolution of model cde46.

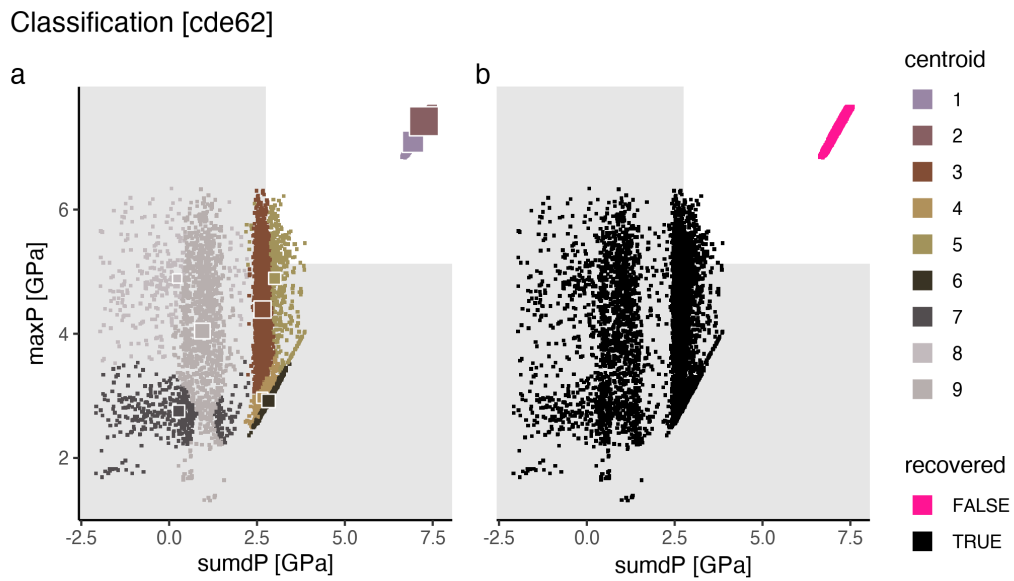


Figure A.52: Marker classification for model cde62.

Metamorphic conditions [cde62]

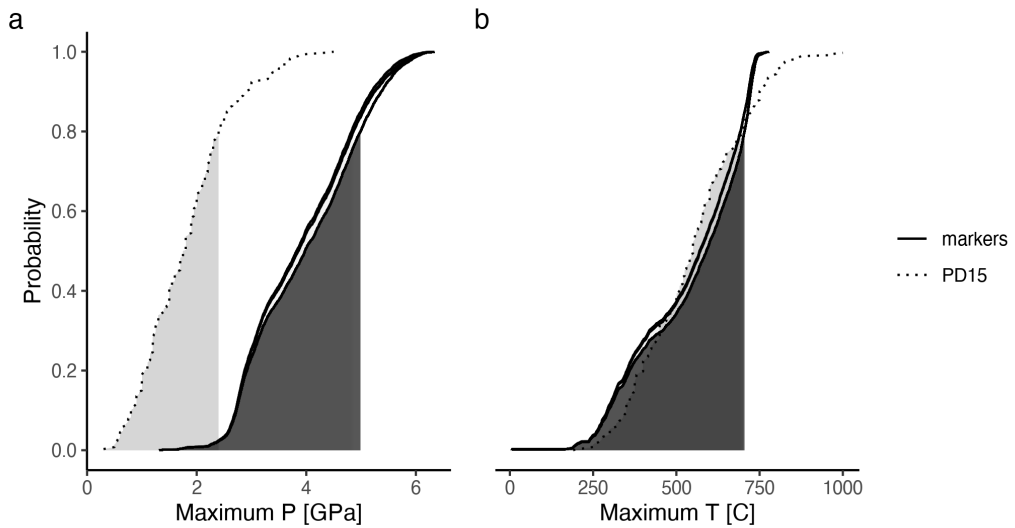


Figure A.53: Metamorphic conditions of markers recovered from model cde62.

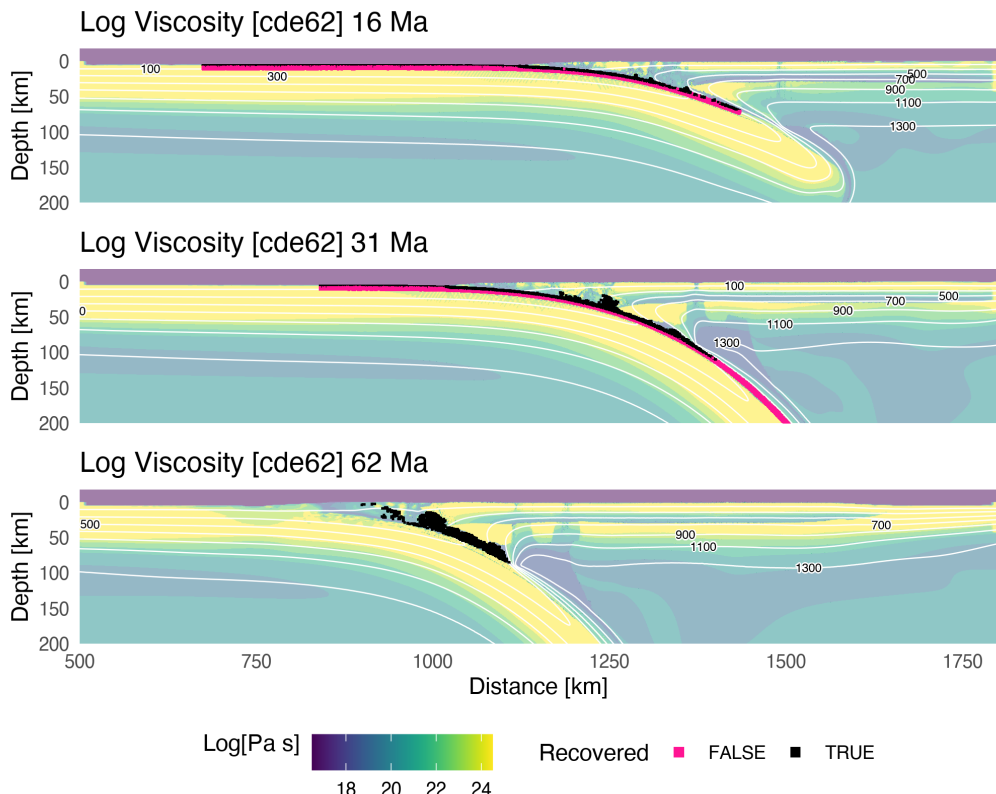


Figure A.54: Geodynamic evolution of model cde62.

Classification [cde78]

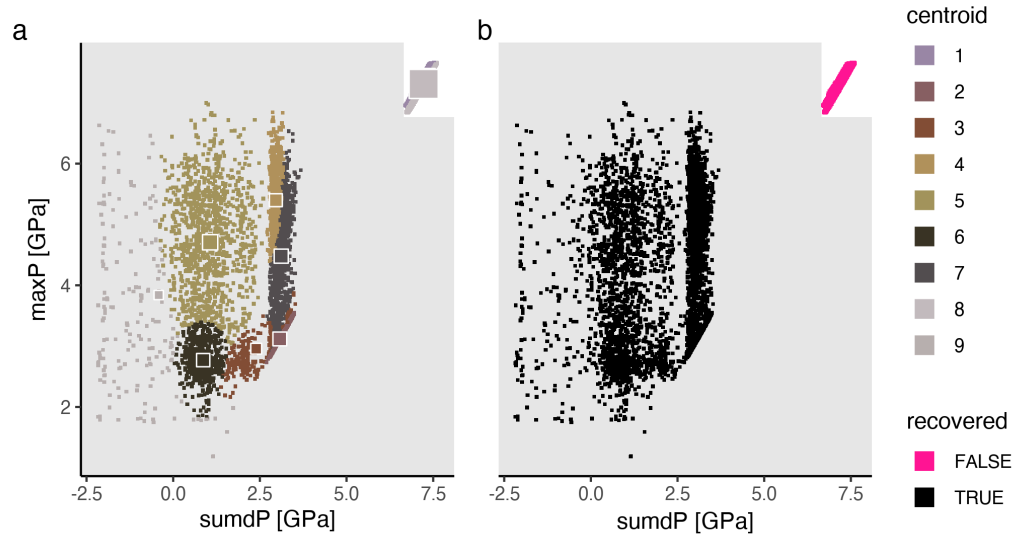


Figure A.55: Marker classification for model cde78.

Metamorphic conditions [cde78]

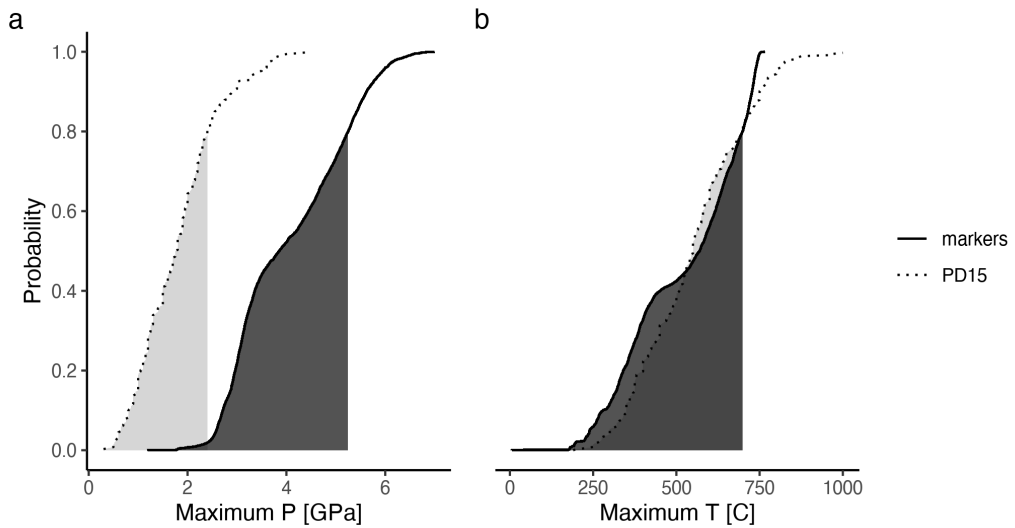


Figure A.56: Metamorphic conditions of markers recovered from model cde78.

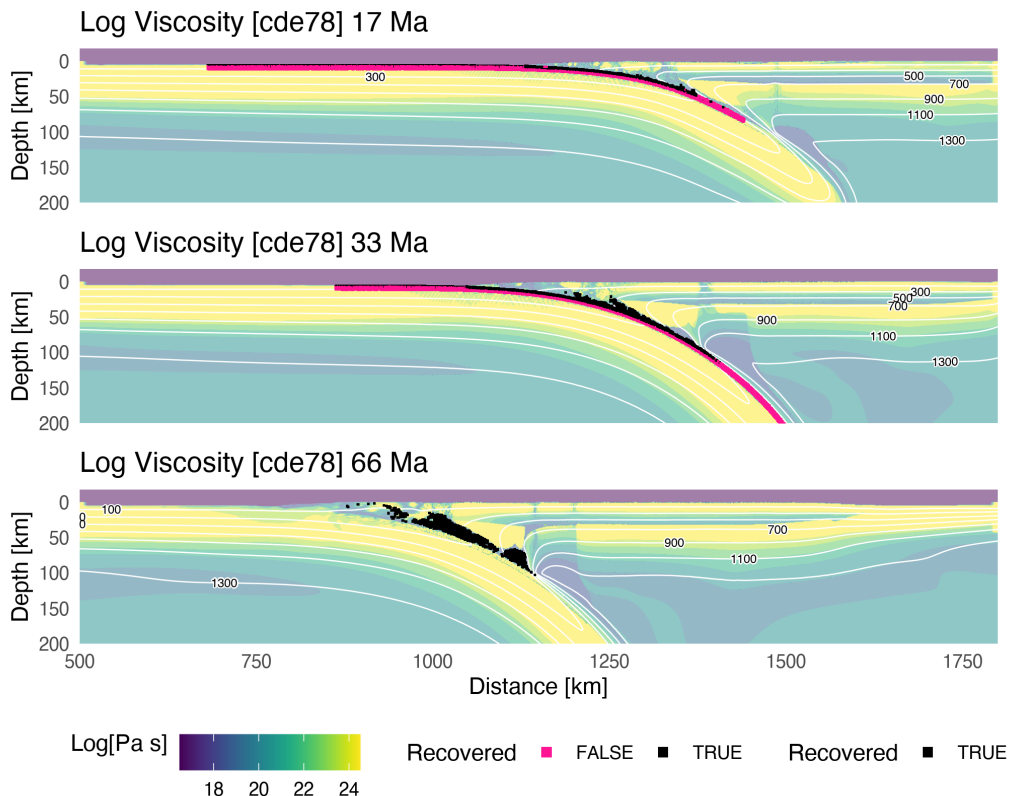


Figure A.57: Geodynamic evolution of model cde78.

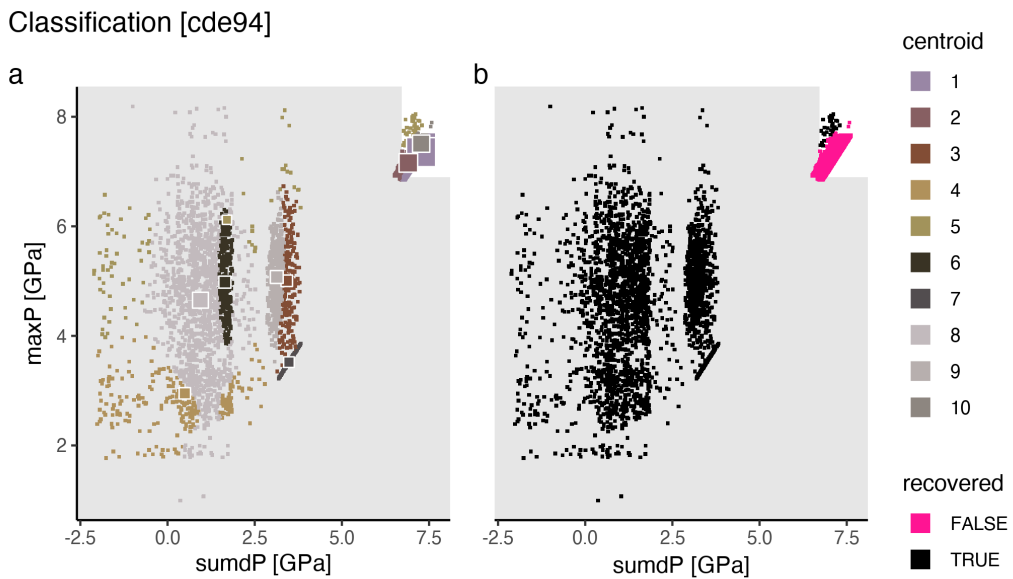


Figure A.58: Marker classification for model cde94.

Metamorphic conditions [cde94]

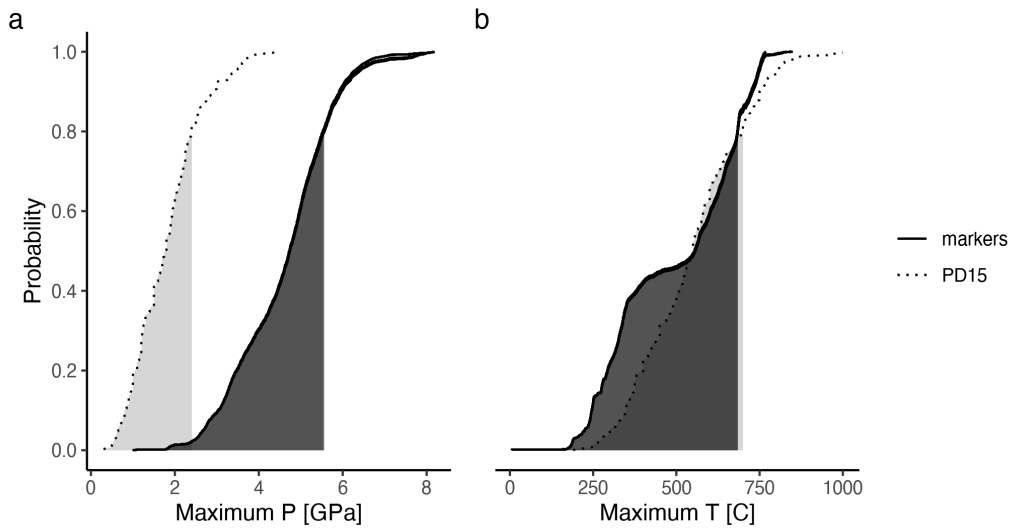


Figure A.59: Metamorphic conditions of markers recovered from model cde94.

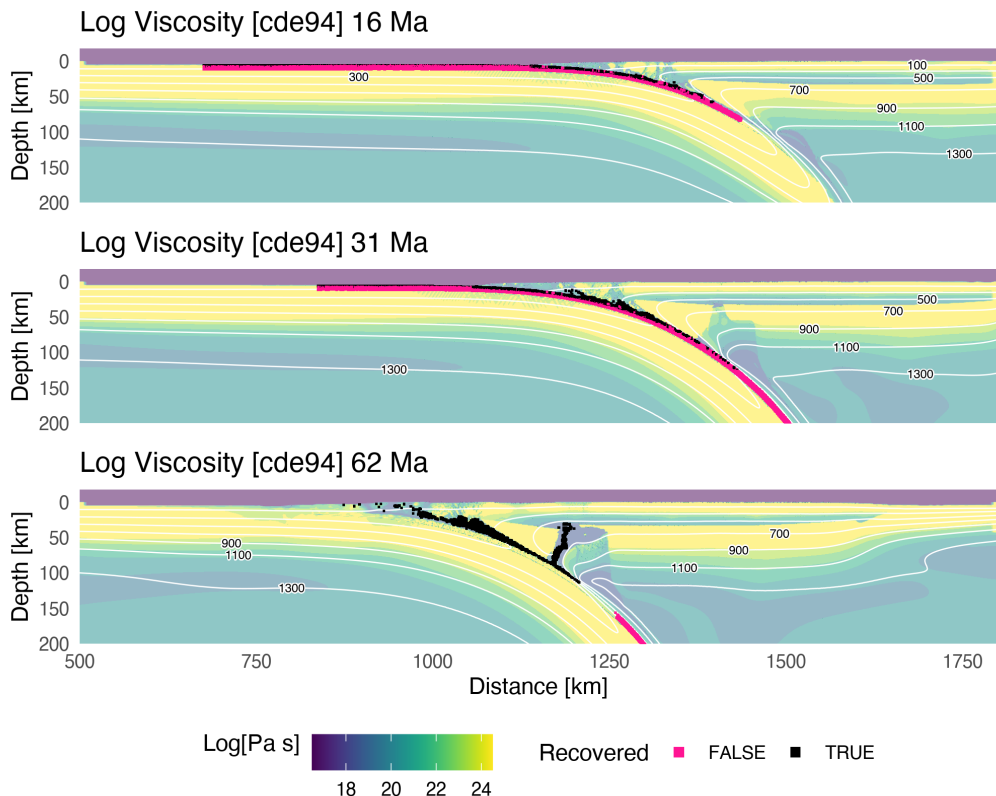


Figure A.60: Geodynamic evolution of model cde94.

Classification [cdf46]

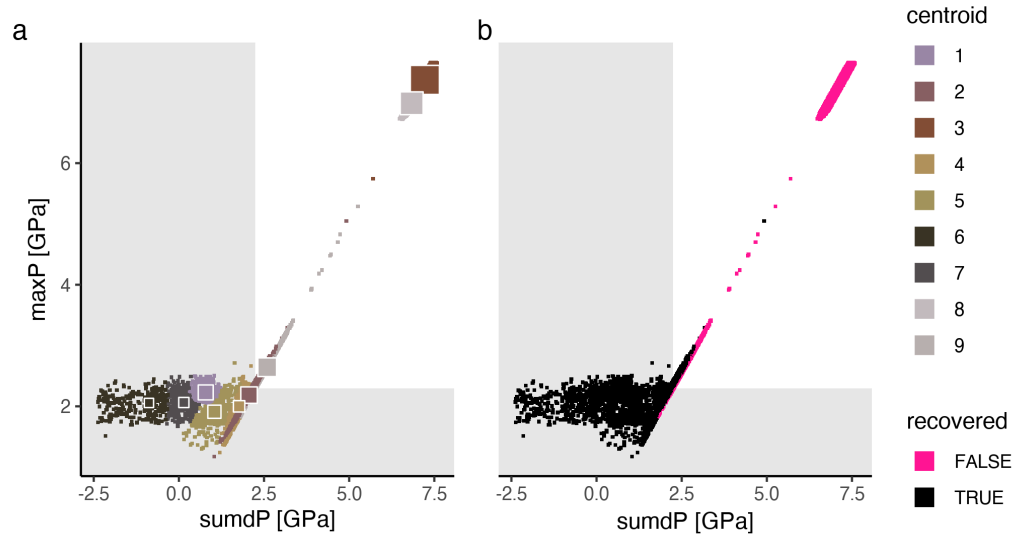


Figure A.61: Marker classification for model cdf46.

Metamorphic conditions [cdf46]

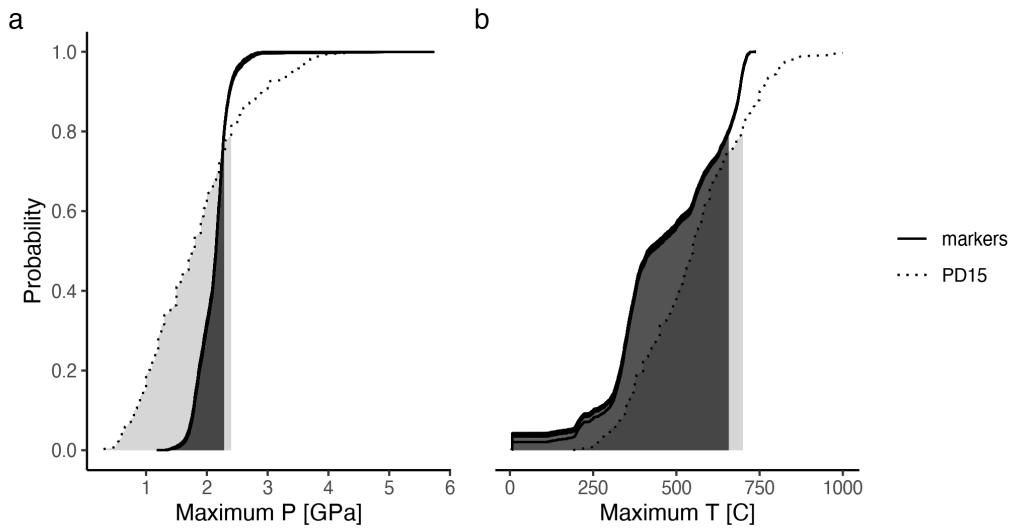


Figure A.62: Metamorphic conditions of markers recovered from model cdf46.

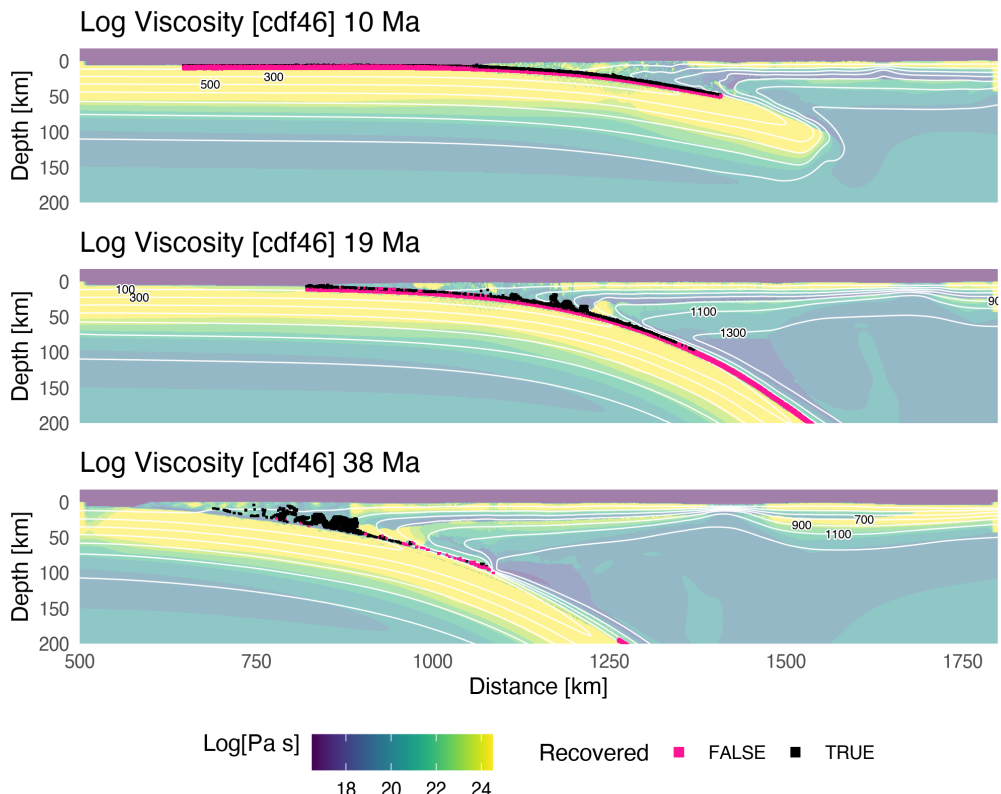


Figure A.63: Geodynamic evolution of model cdf46.

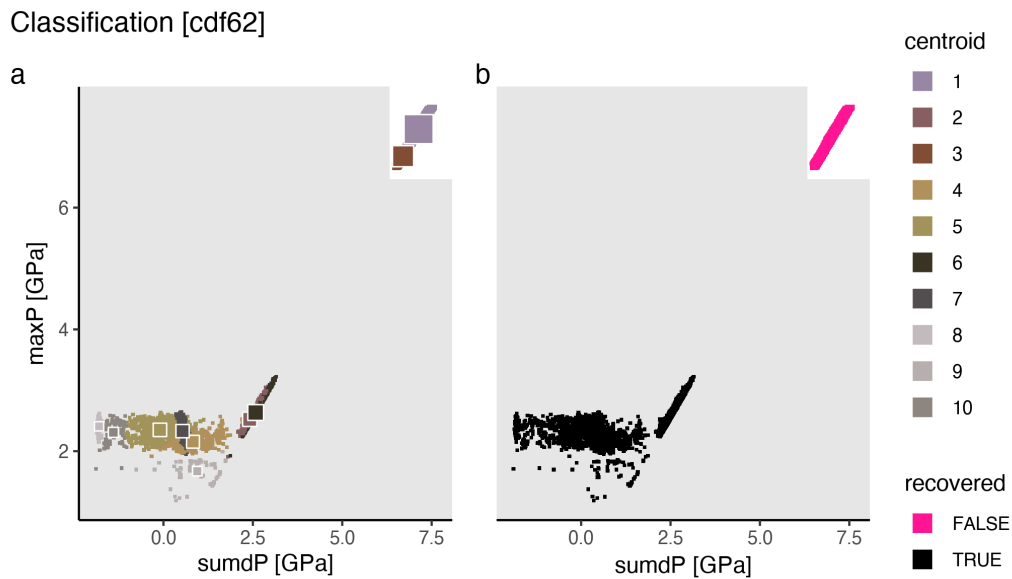


Figure A.64: Marker classification for model cdf62.

Metamorphic conditions [cdf62]

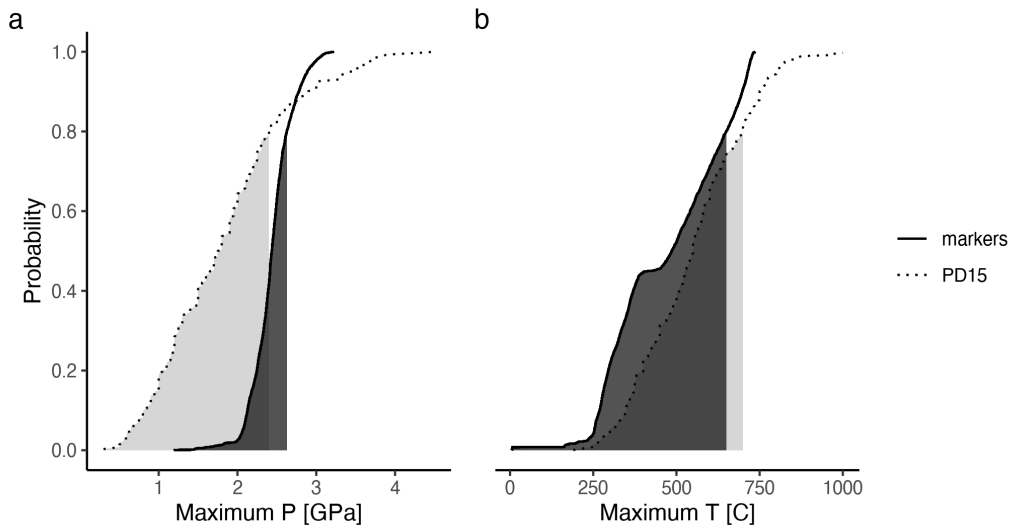


Figure A.65: Metamorphic conditions of markers recovered from model cdf62.

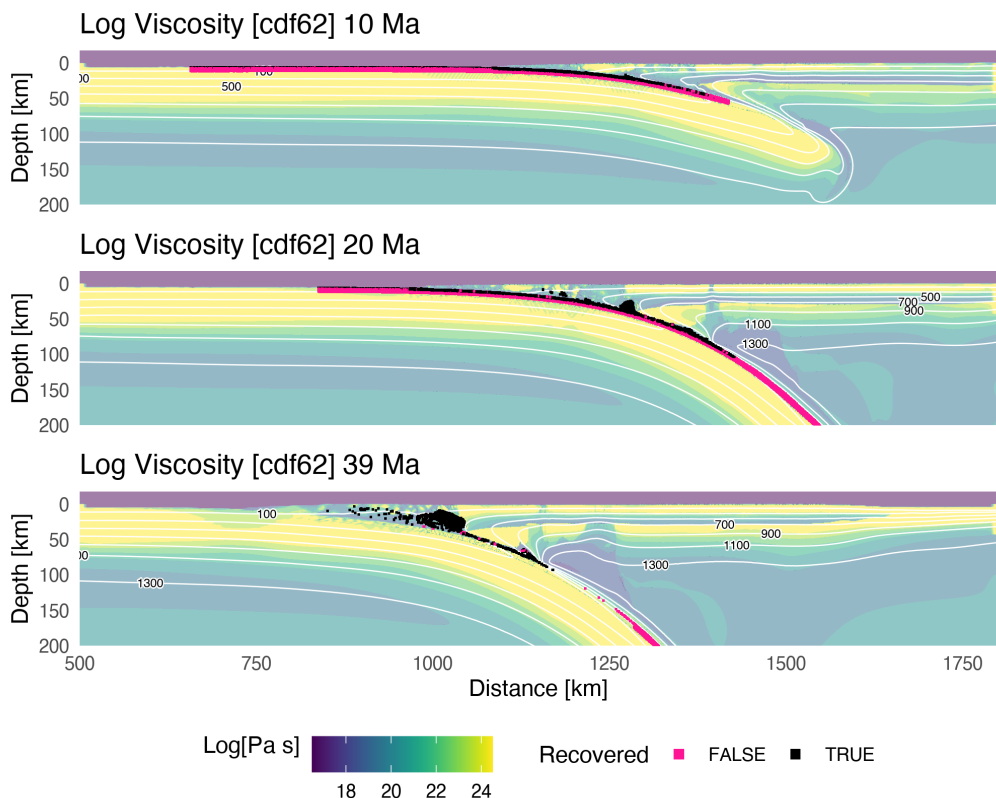


Figure A.66: Geodynamic evolution of model cdf62.

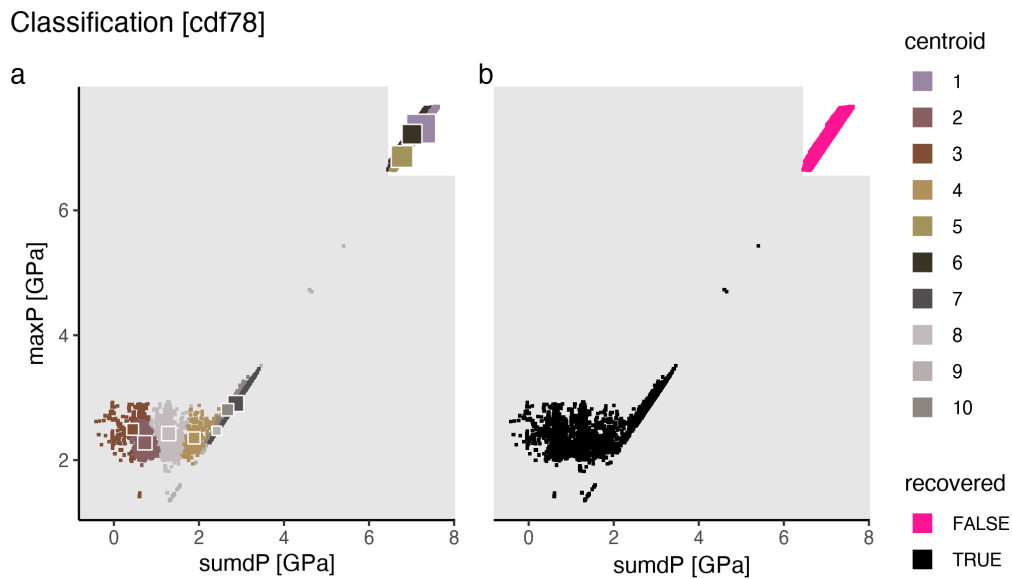


Figure A.67: Marker classification for model cdf78.

Metamorphic conditions [cdf78]

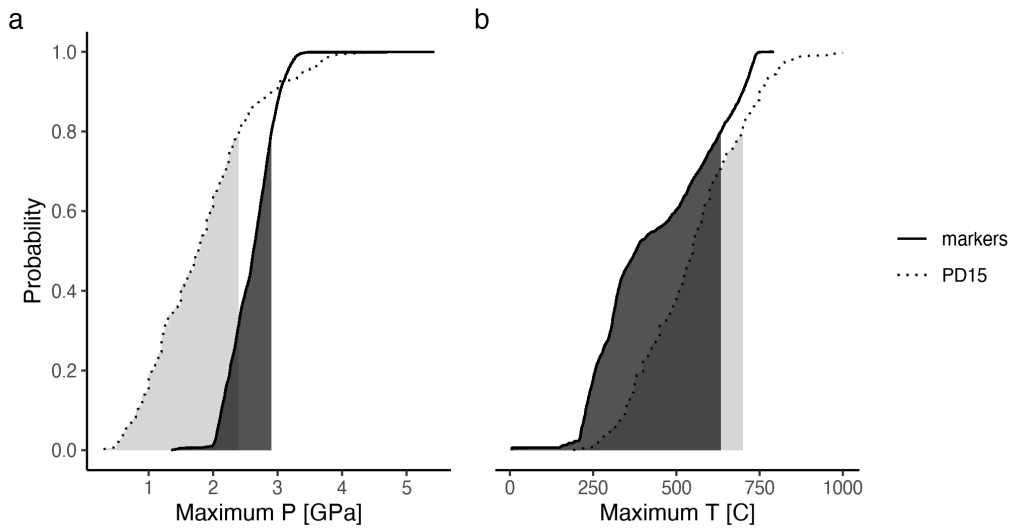


Figure A.68: Metamorphic conditions of markers recovered from model cdf78.

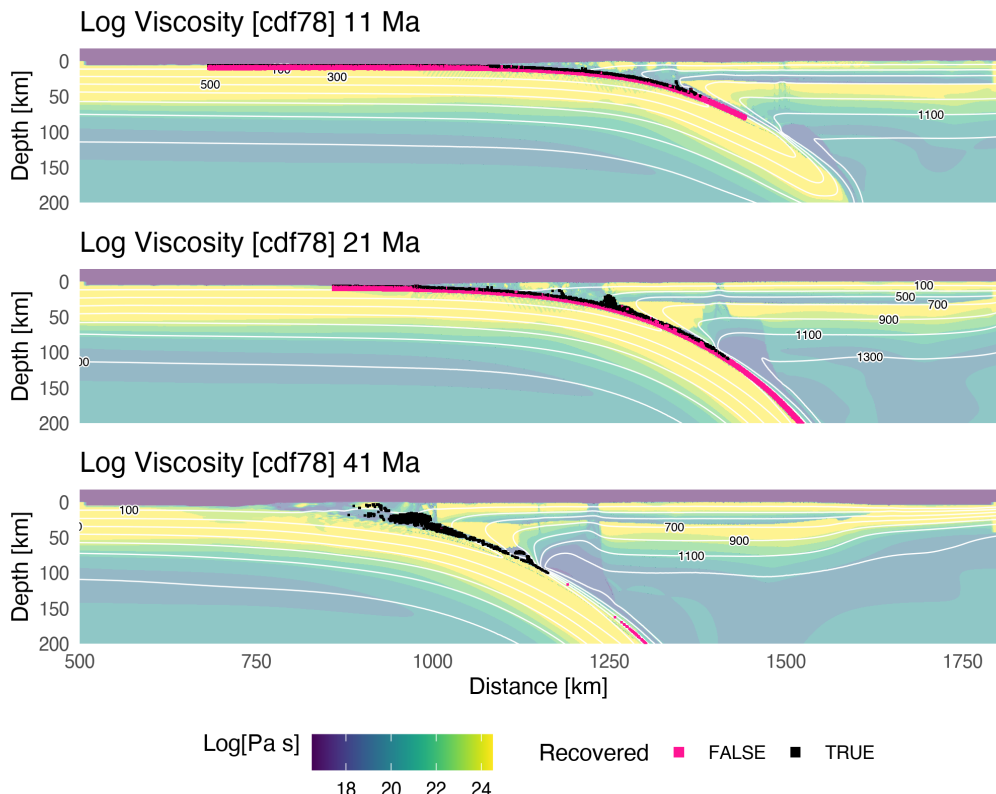


Figure A.69: Geodynamic evolution of model cdf78.

Classification [cdf94]

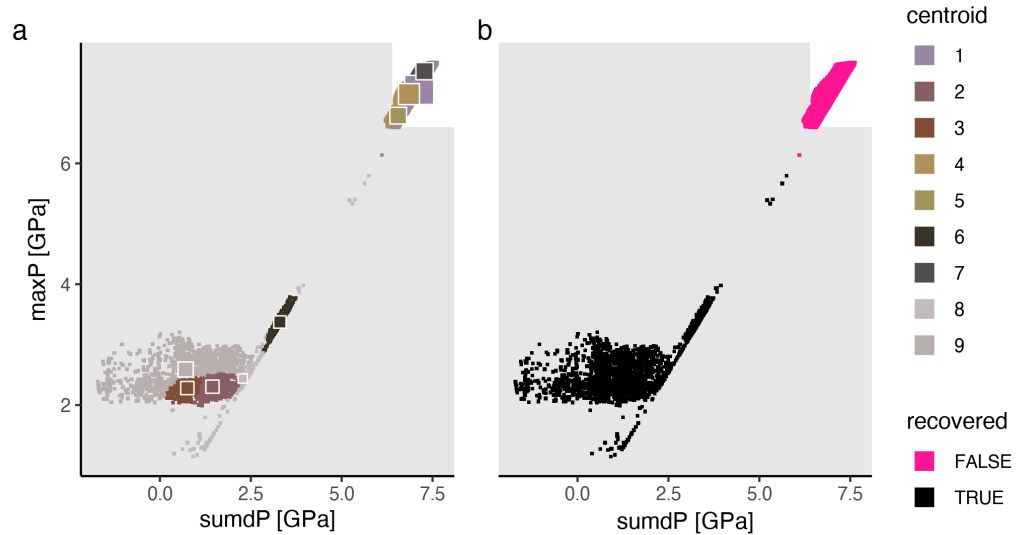


Figure A.70: Marker classification for model cdf94.

Metamorphic conditions [cdf94]

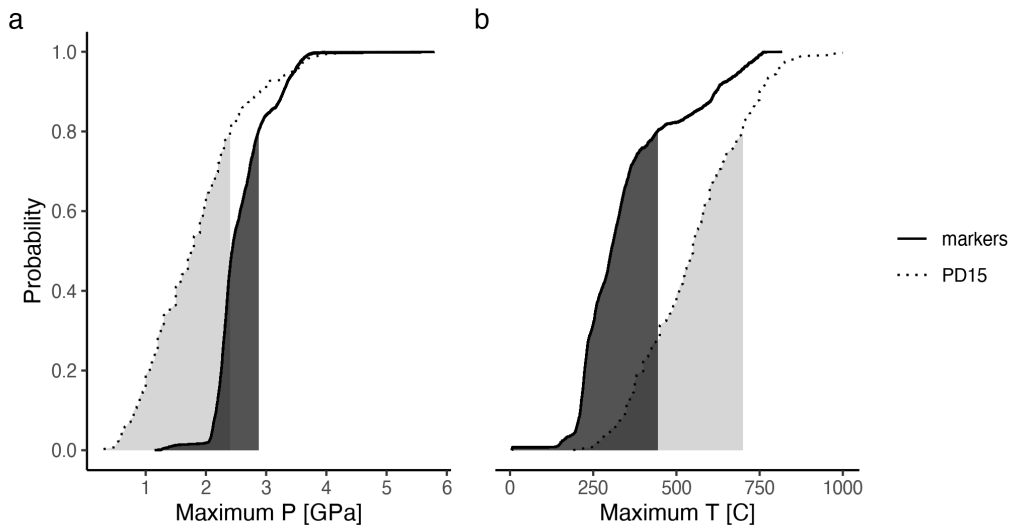


Figure A.71: Metamorphic conditions of markers recovered from model cdf94.

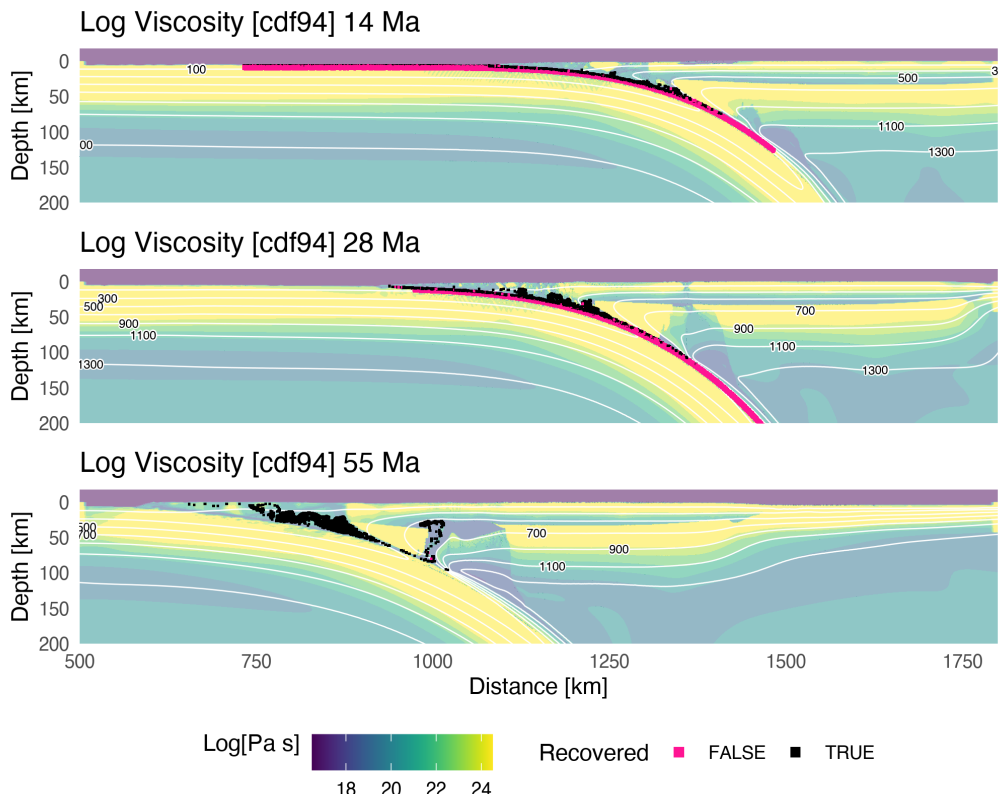


Figure A.72: Geodynamic evolution of model cdf94.

Classification [cdg46]

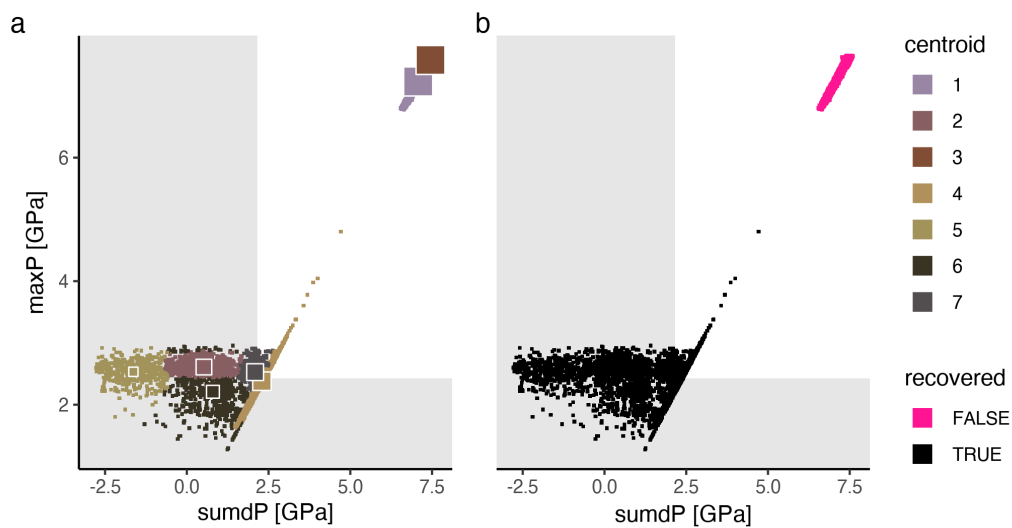


Figure A.73: Marker classification for model cdg46.

Metamorphic conditions [cdg46]

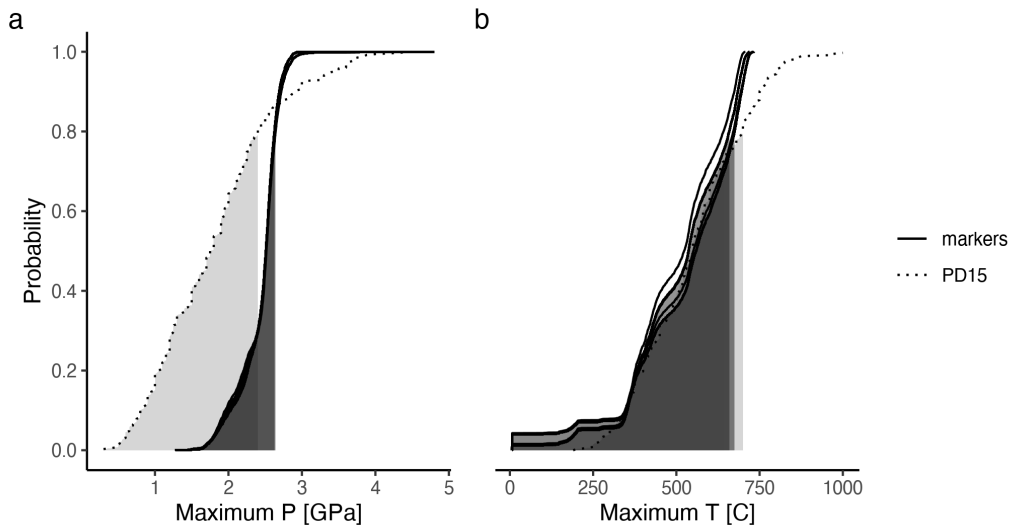


Figure A.74: Metamorphic conditions of markers recovered from model cdg46.

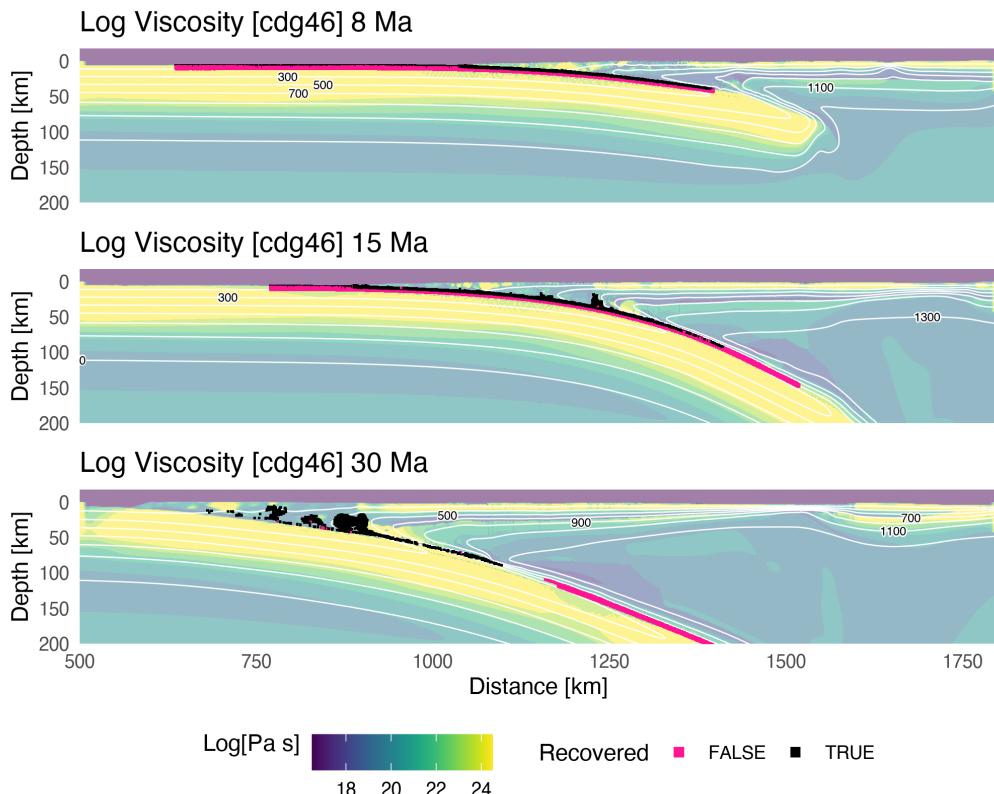


Figure A.75: Geodynamic evolution of model cdg46.

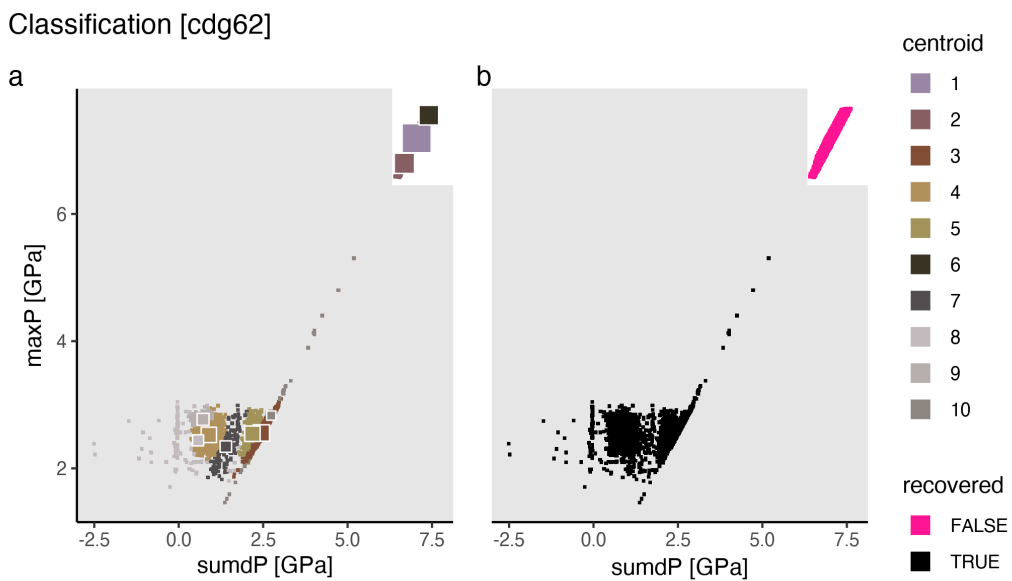


Figure A.76: Marker classification for model cdg62.

Metamorphic conditions [cdg62]

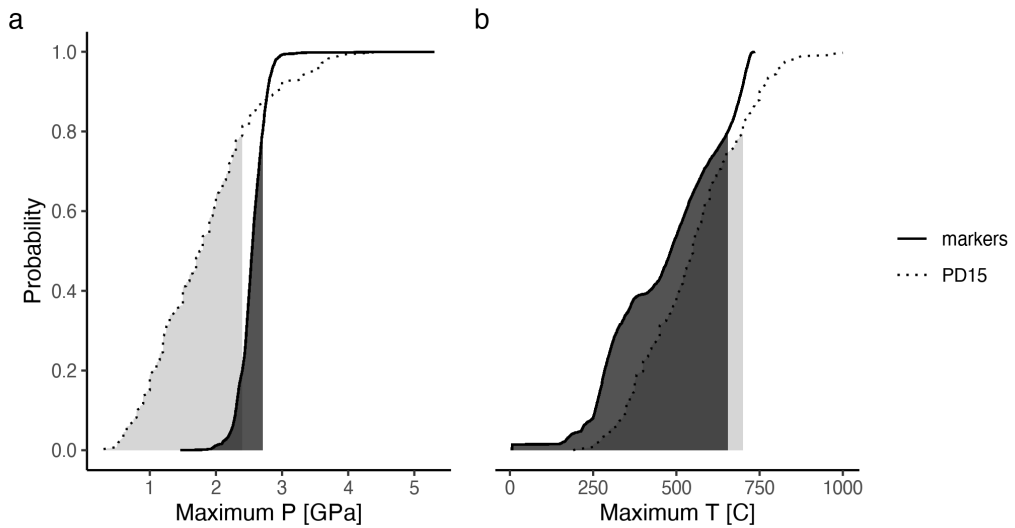


Figure A.77: Metamorphic conditions of markers recovered from model cdg62.

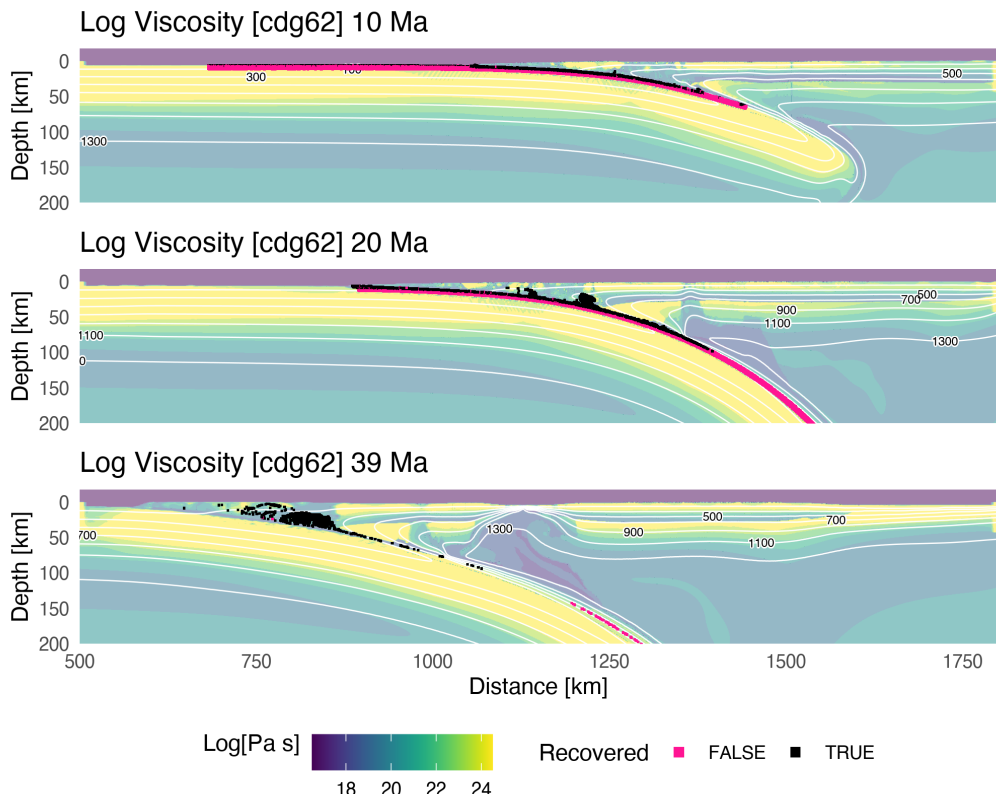


Figure A.78: Geodynamic evolution of model cdg62.

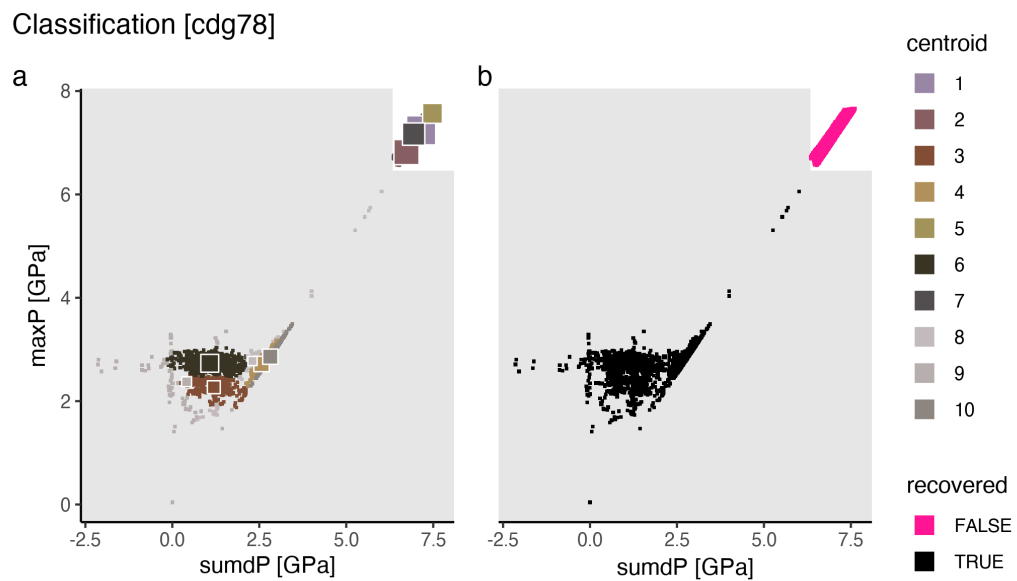


Figure A.79: Marker classification for model cdg78.

Metamorphic conditions [cdg78]

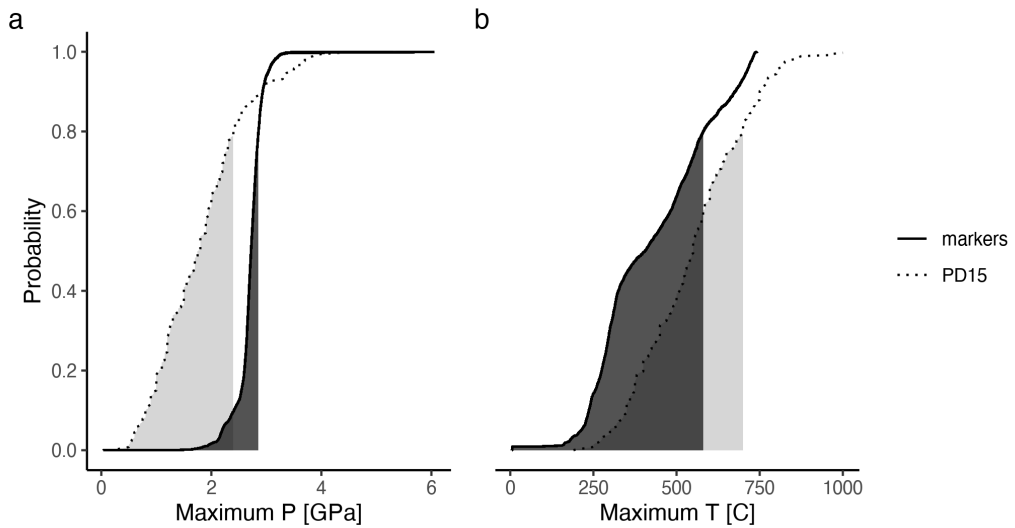


Figure A.80: Metamorphic conditions of markers recovered from model cdg78.

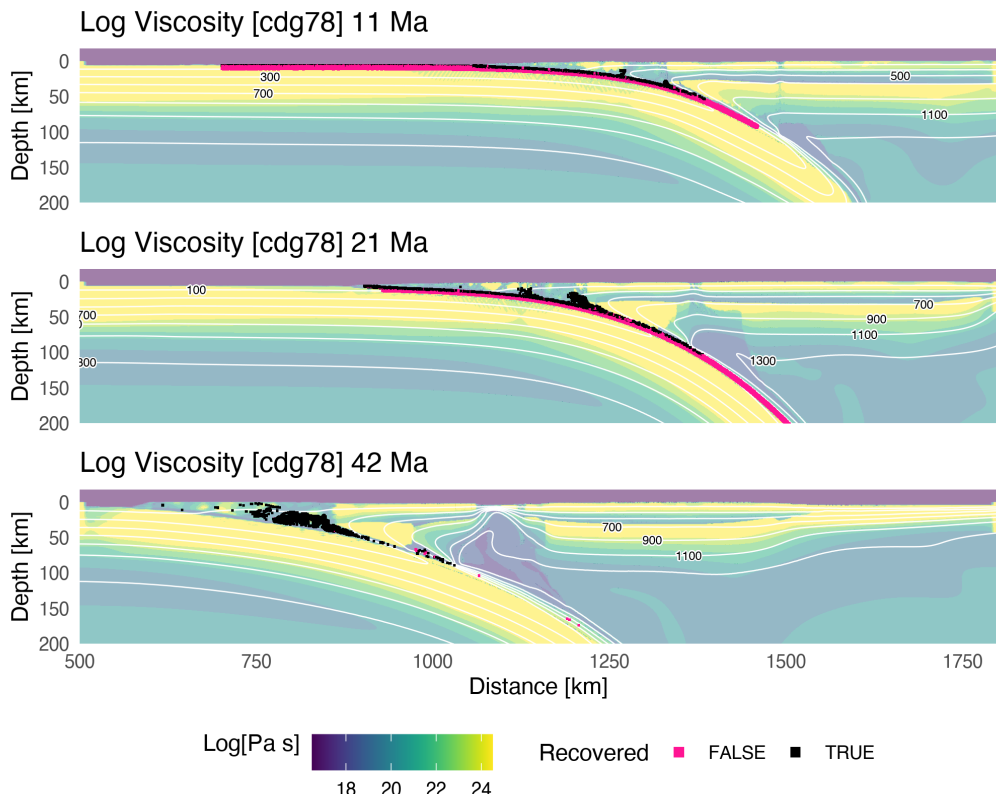


Figure A.81: Geodynamic evolution of model cdg78.

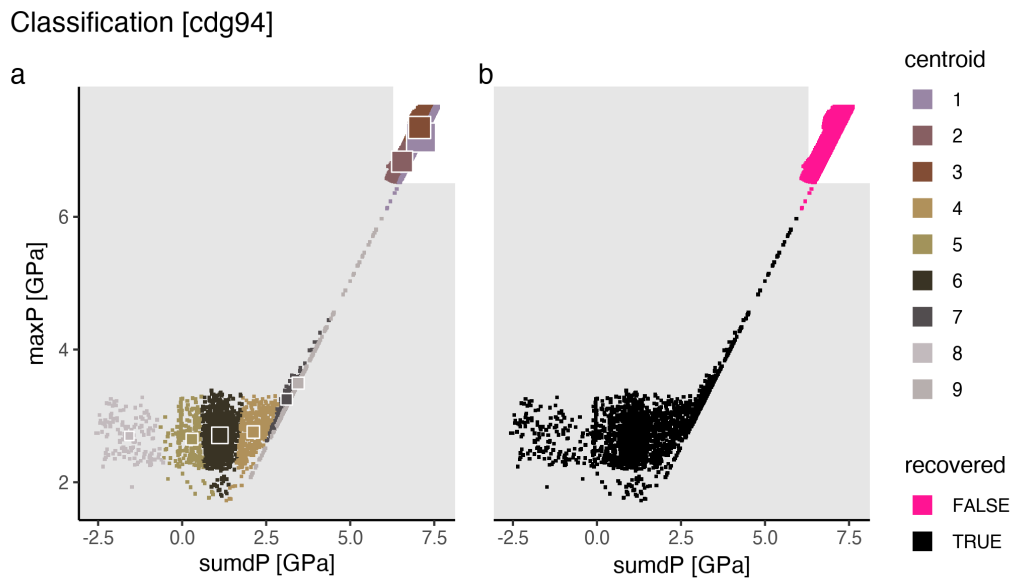


Figure A.82: Marker classification for model cdg94.

Metamorphic conditions [cdg94]

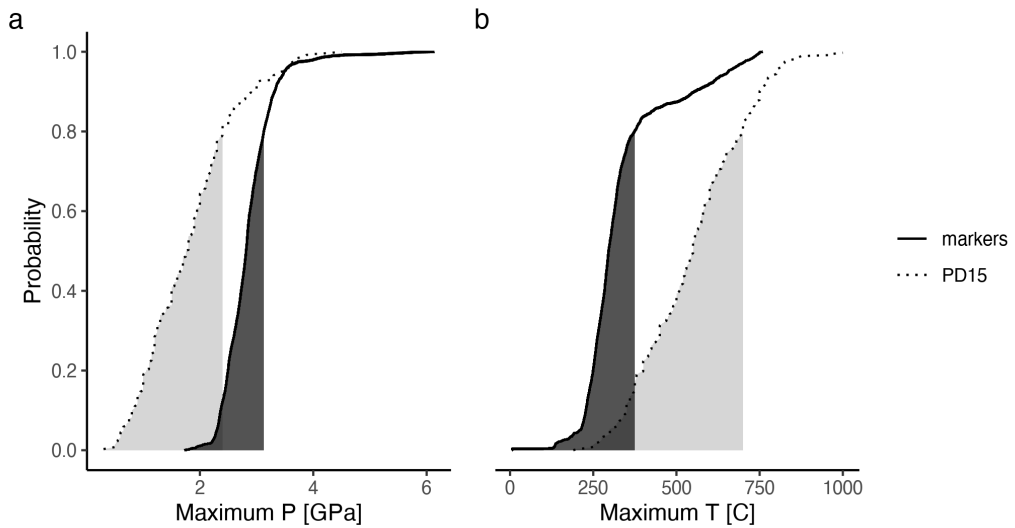


Figure A.83: Metamorphic conditions of markers recovered from model cdg94.

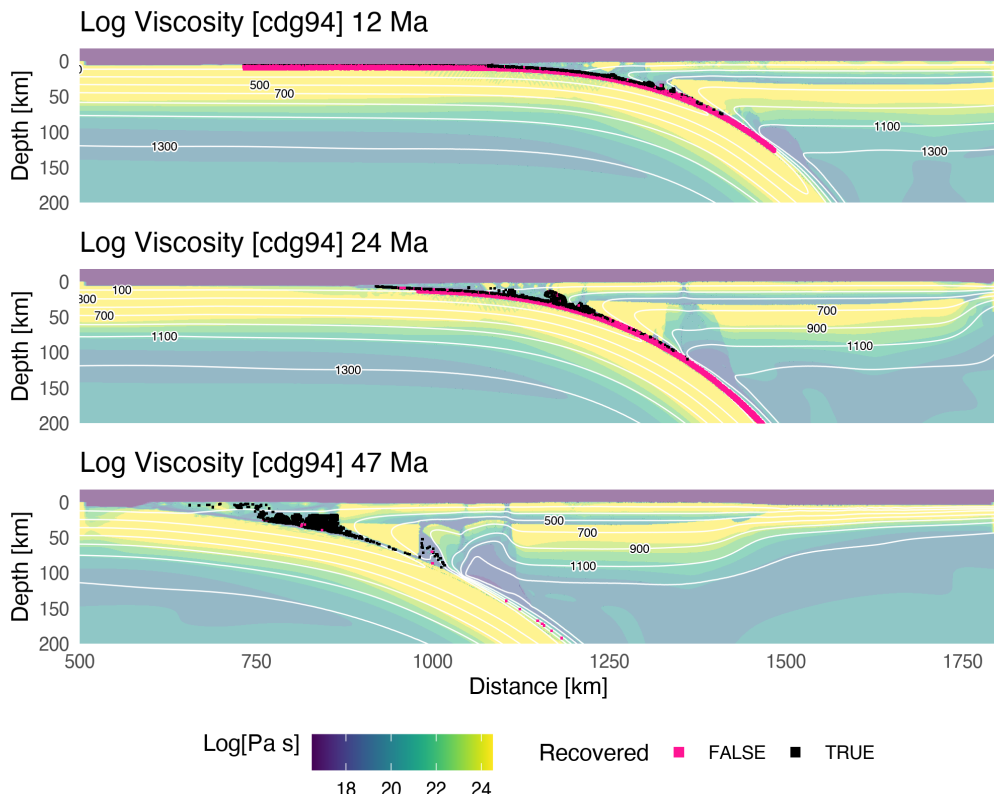


Figure A.84: Geodynamic evolution of model cdg94.

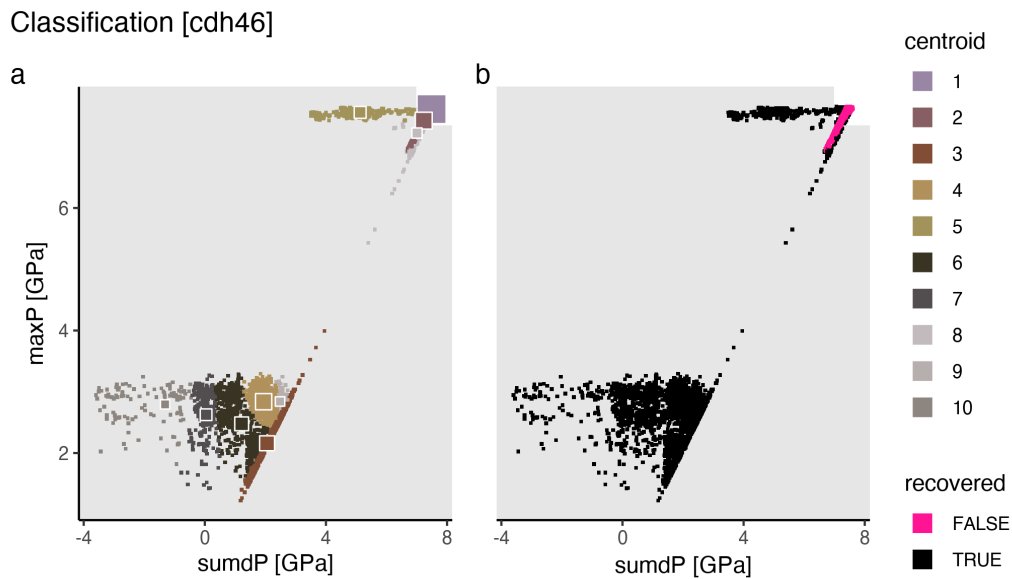


Figure A.85: Marker classification for model cdh46.

Metamorphic conditions [cdh46]

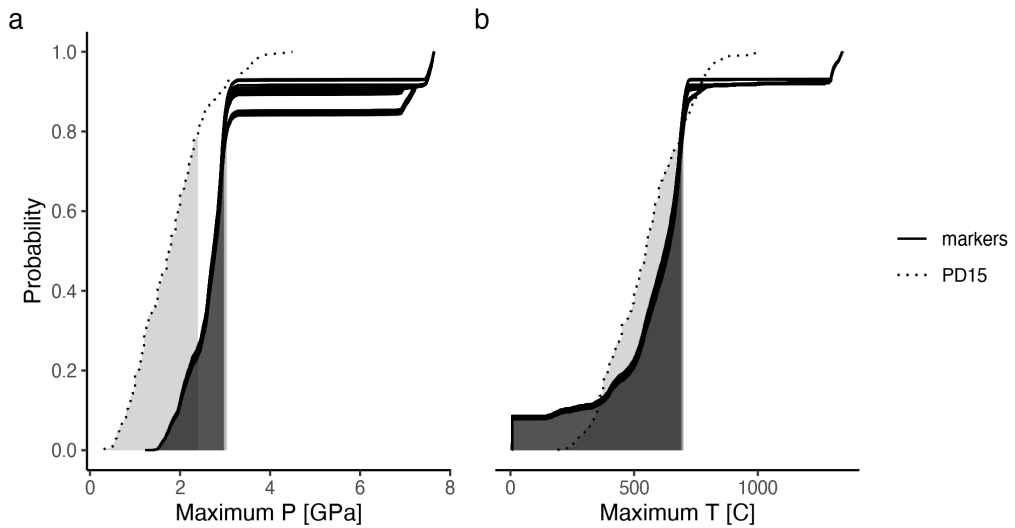


Figure A.86: Metamorphic conditions of markers recovered from model cdh46.

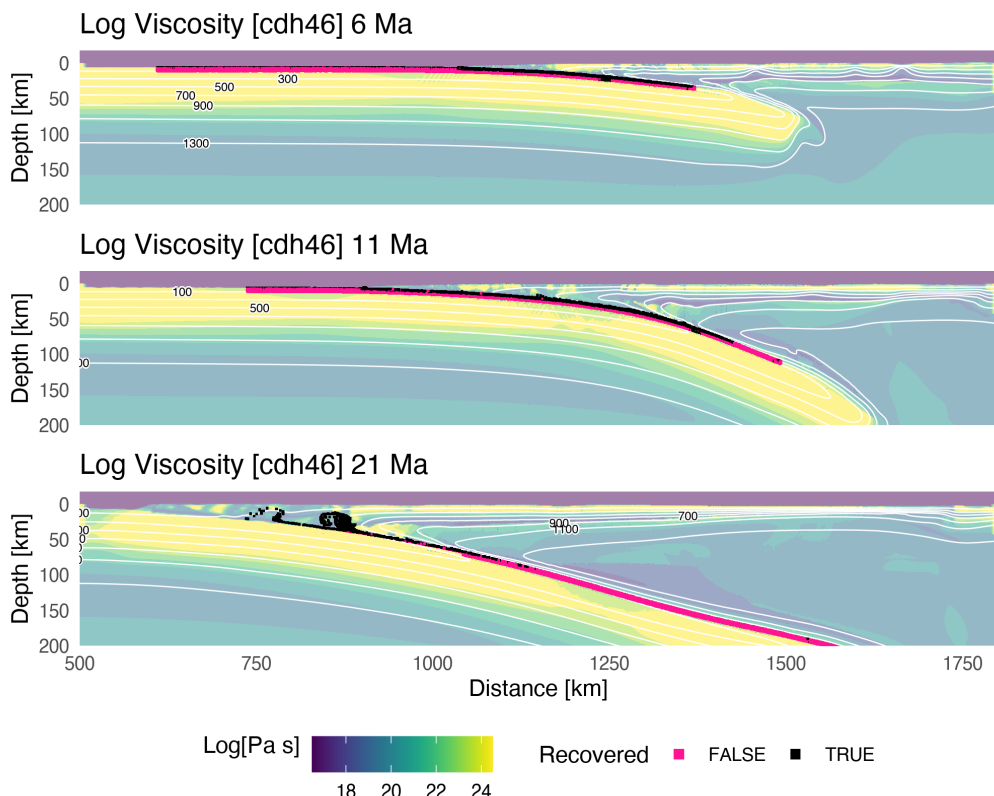


Figure A.87: Geodynamic evolution of model cdh46.

Classification [cdh62]

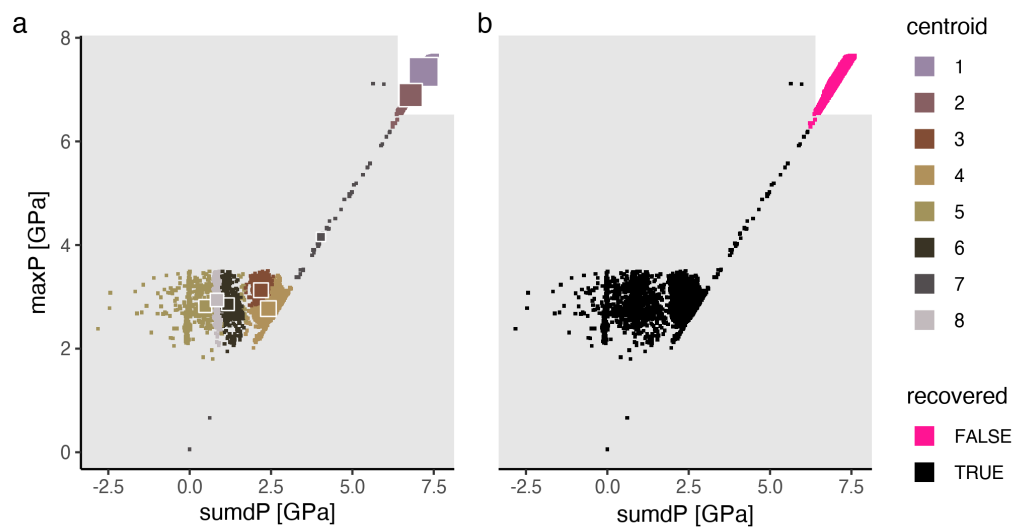


Figure A.88: Marker classification for model cdh62.

Metamorphic conditions [cdh62]

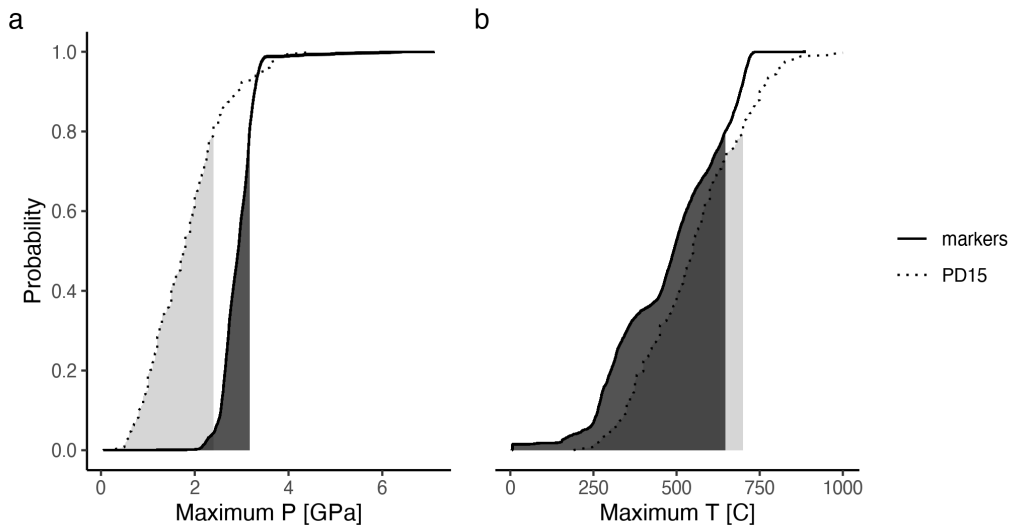


Figure A.89: Metamorphic conditions of markers recovered from model cdh62.

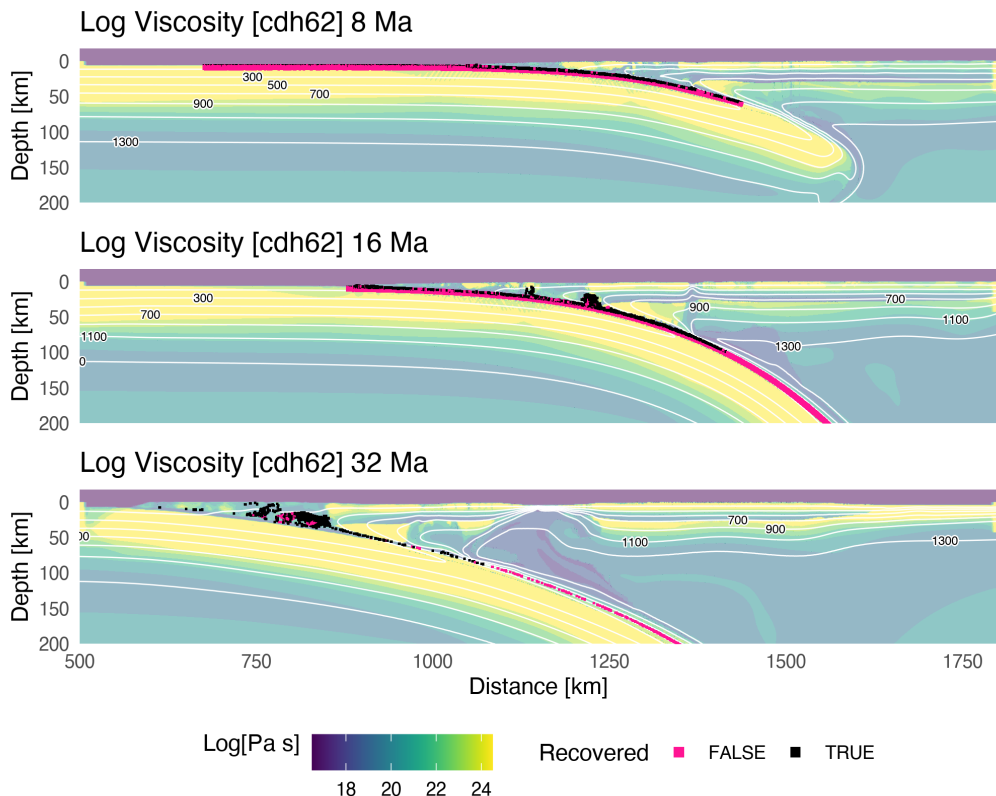


Figure A.90: Geodynamic evolution of model cdh62.

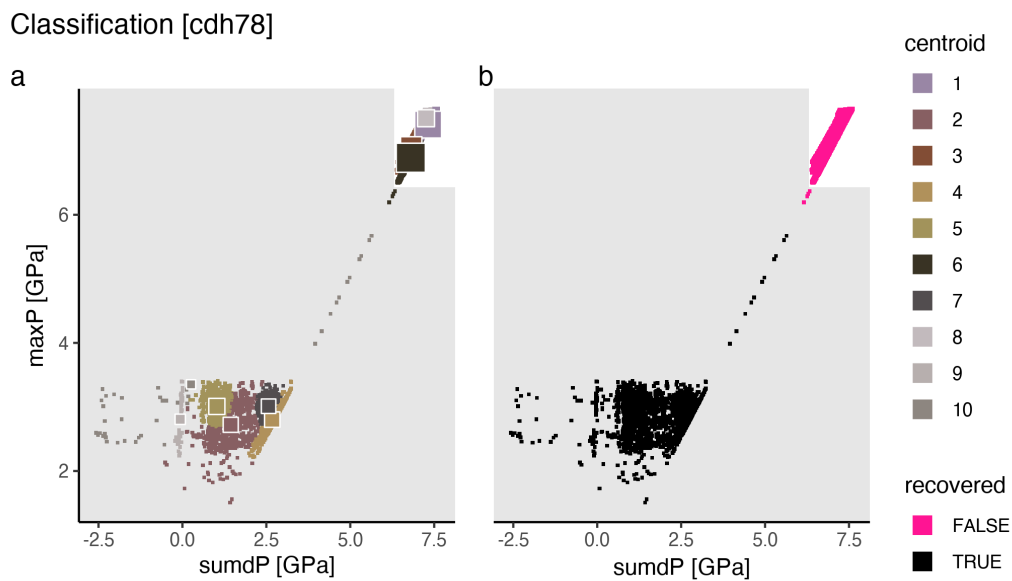


Figure A.91: Marker classification for model cdh78.

Metamorphic conditions [cdh78]

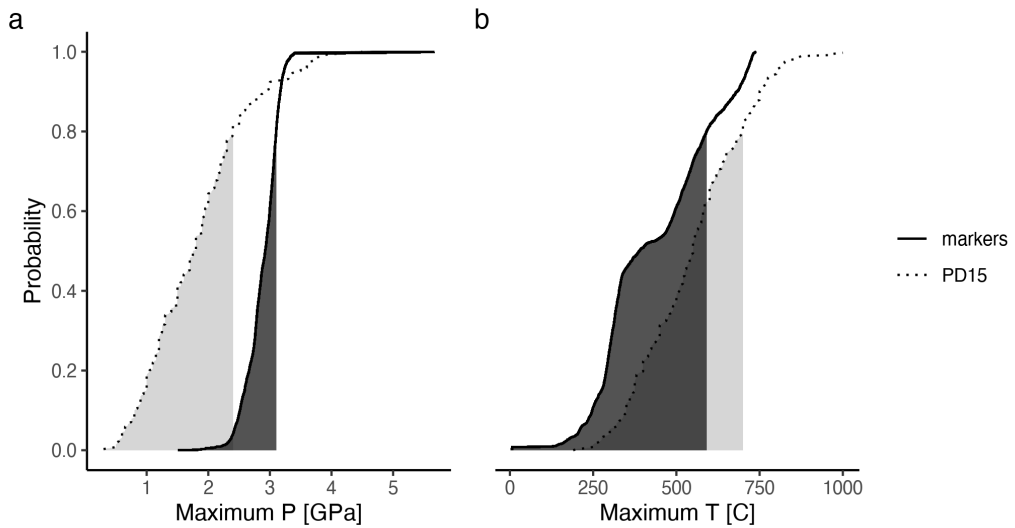


Figure A.92: Metamorphic conditions of markers recovered from model cdh78.

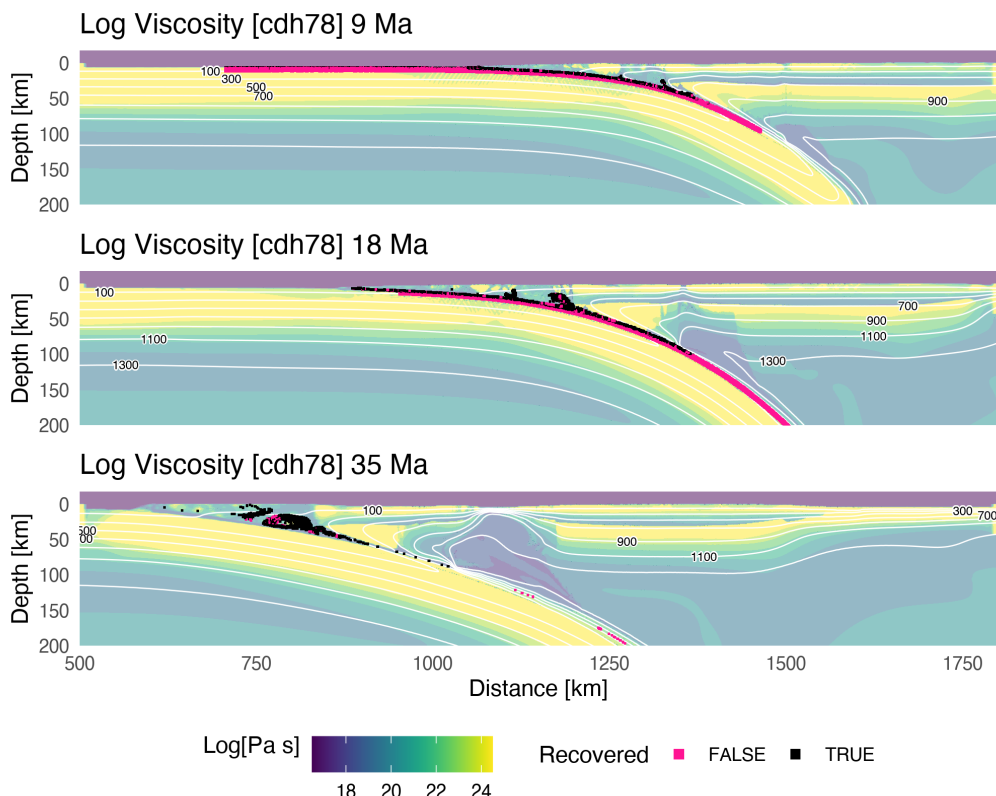


Figure A.93: Geodynamic evolution of model cdh78.

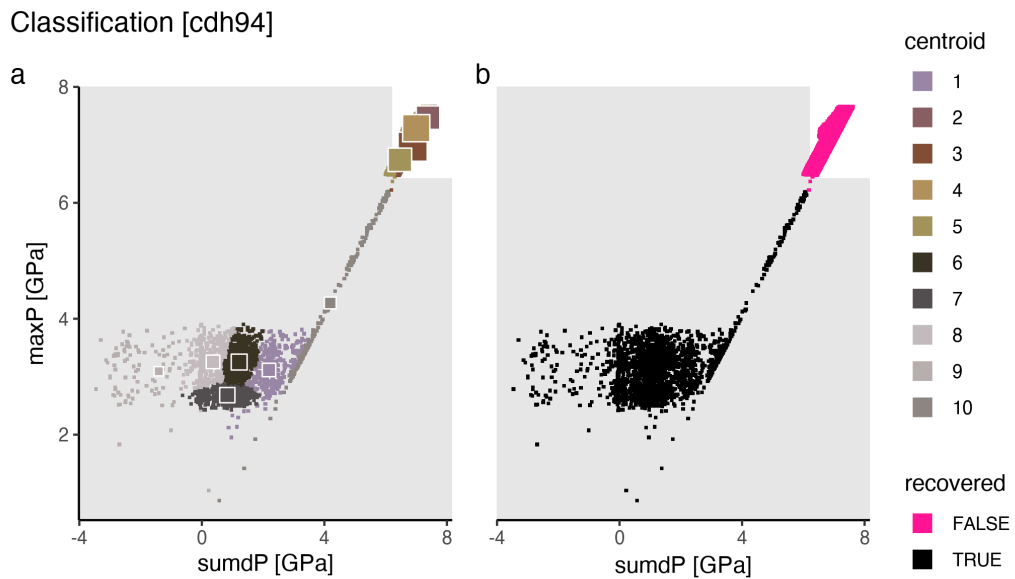


Figure A.94: Marker classification for model cdh94.

Metamorphic conditions [cdh94]

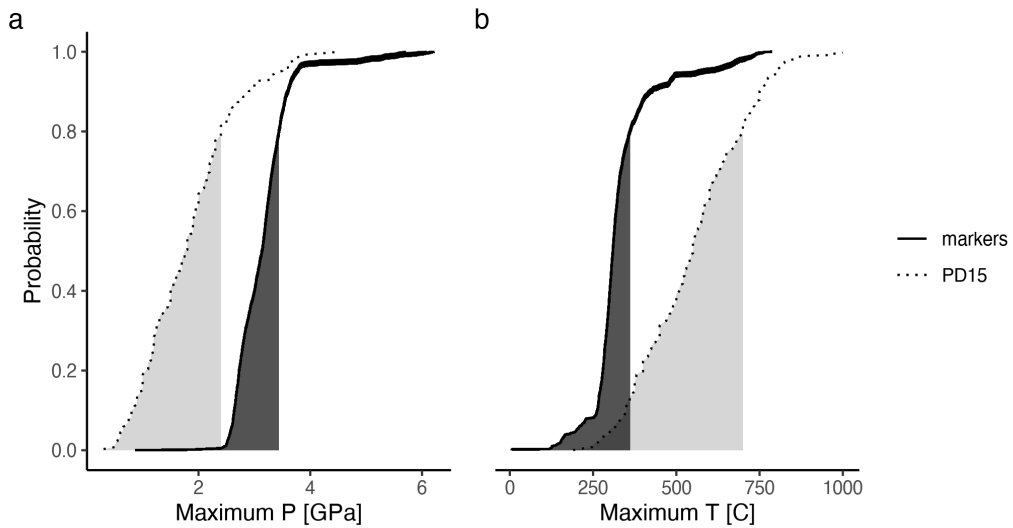


Figure A.95: Metamorphic conditions of markers recovered from model cdh94.

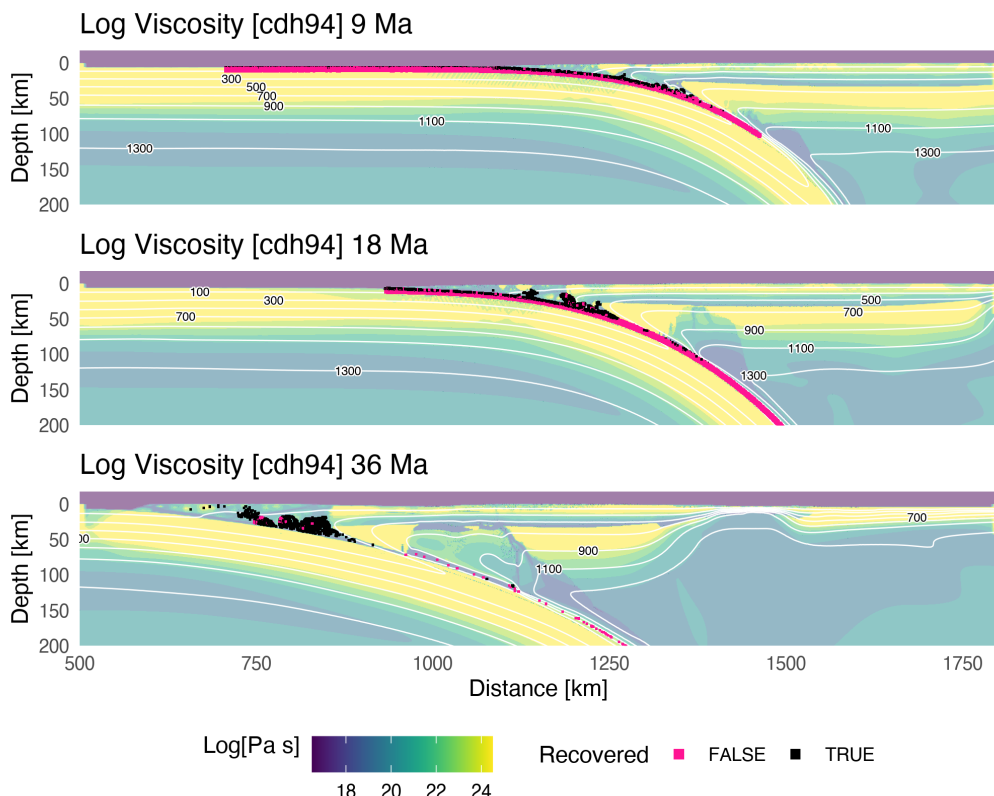


Figure A.96: Geodynamic evolution of model cdh94.

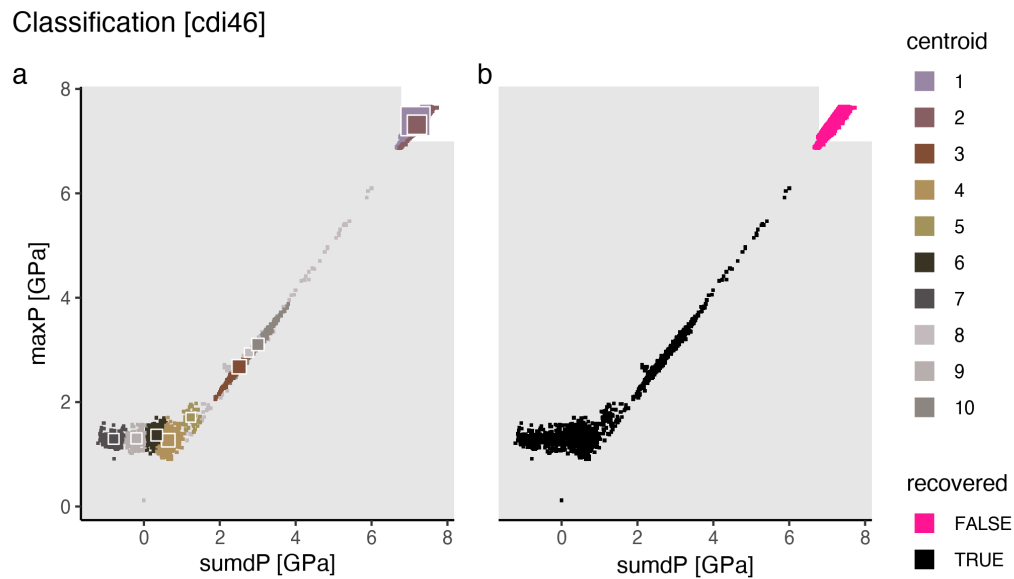


Figure A.97: Marker classification for model cdi46.

Metamorphic conditions [cdi46]

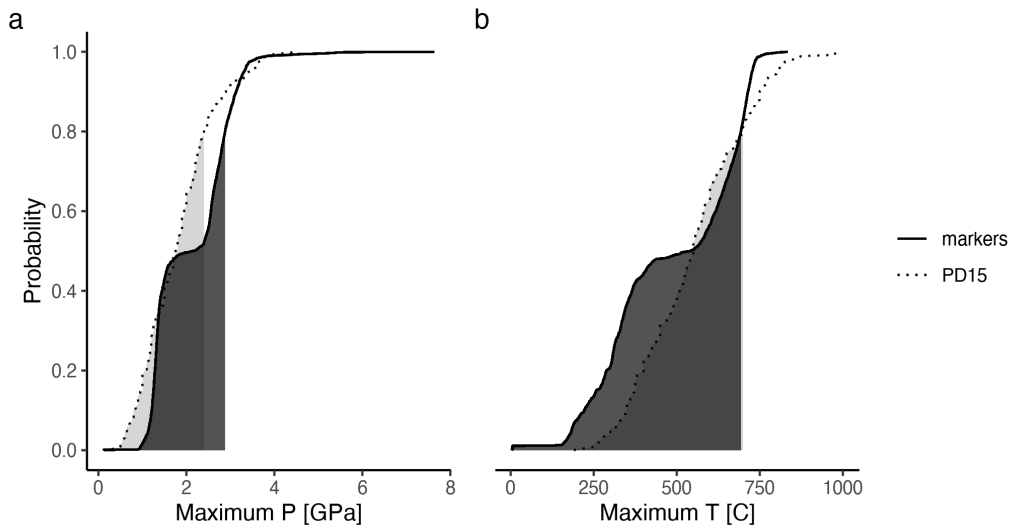


Figure A.98: Metamorphic conditions of markers recovered from model cdi46.

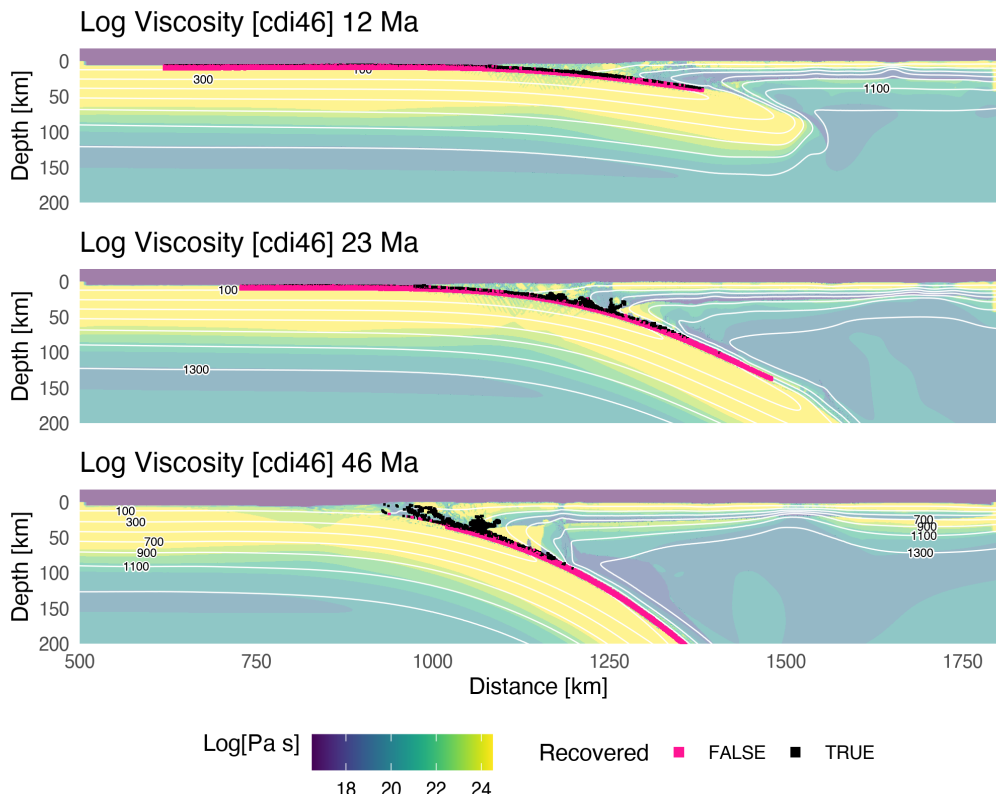


Figure A.99: Geodynamic evolution of model cdi46.

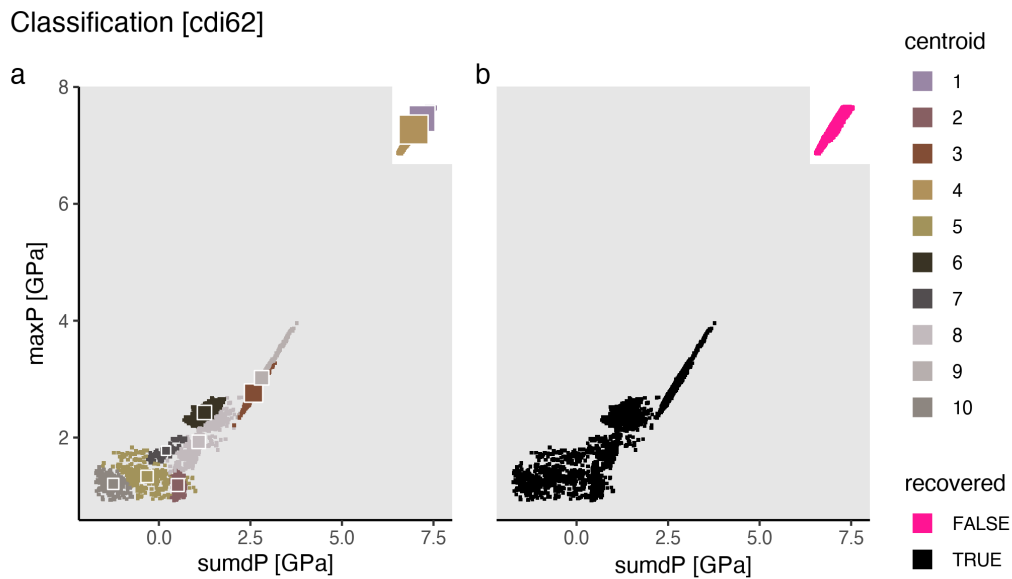


Figure A.100: Marker classification for model cdi62.

Metamorphic conditions [cdi62]

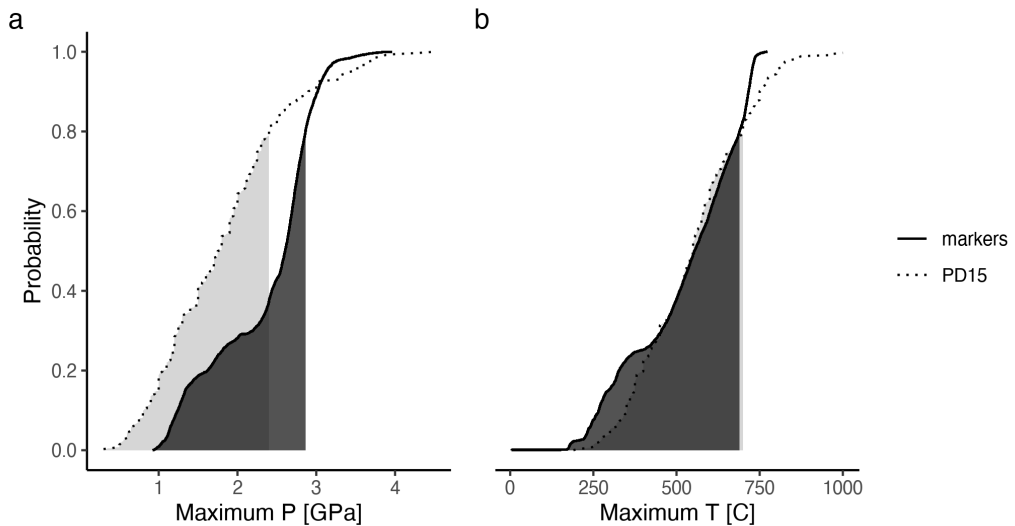


Figure A.101: Metamorphic conditions of markers recovered from model cdi62.

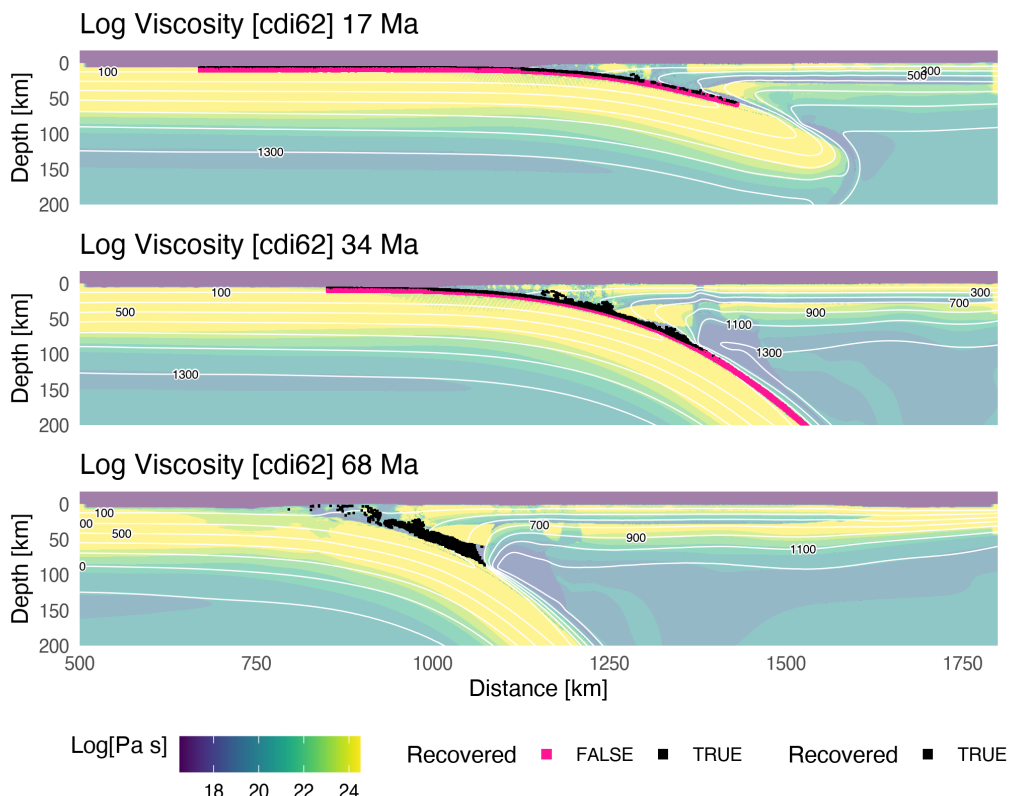


Figure A.102: Geodynamic evolution of model cdi62.

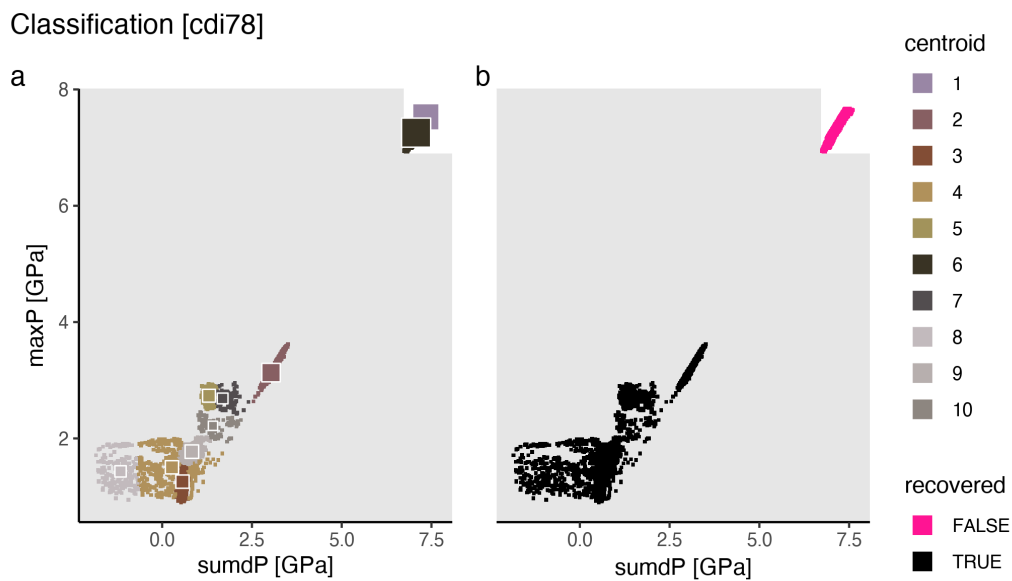


Figure A.103: Marker classification for model cdi78.

Metamorphic conditions [cdi78]

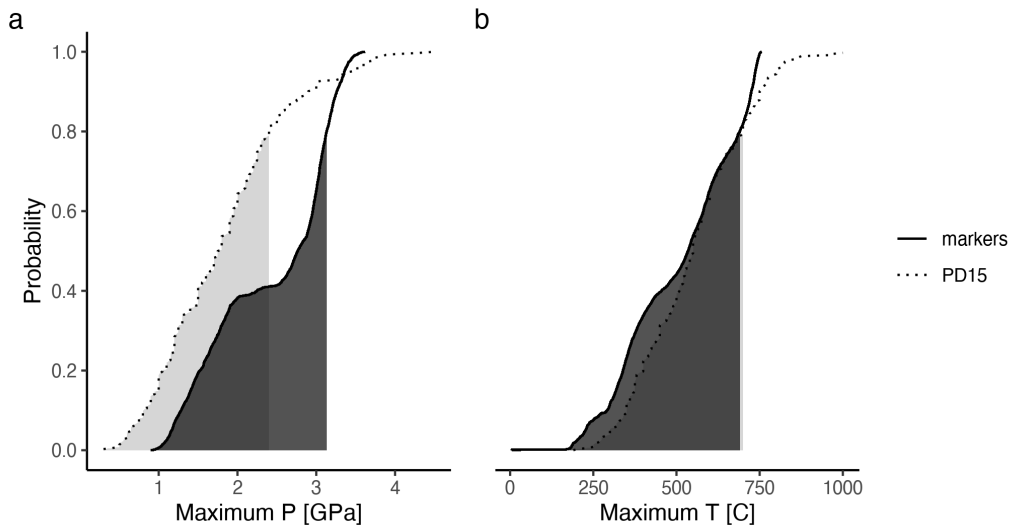


Figure A.104: Metamorphic conditions of markers recovered from model cdi78.

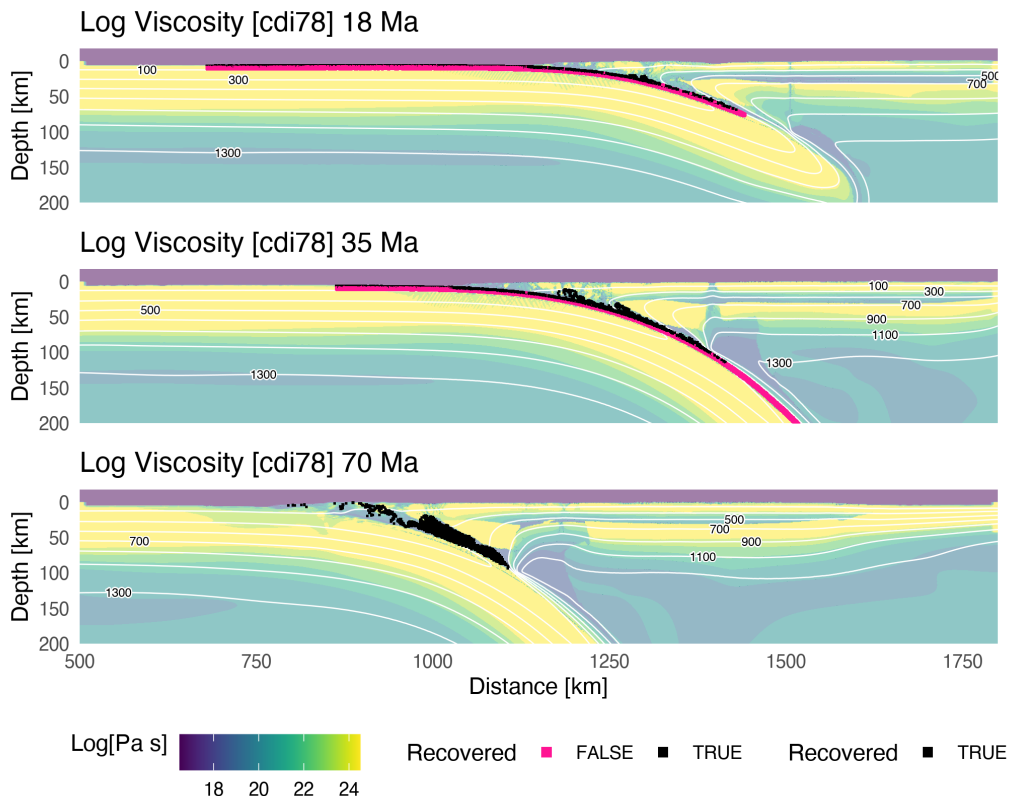


Figure A.105: Geodynamic evolution of model cdi78.

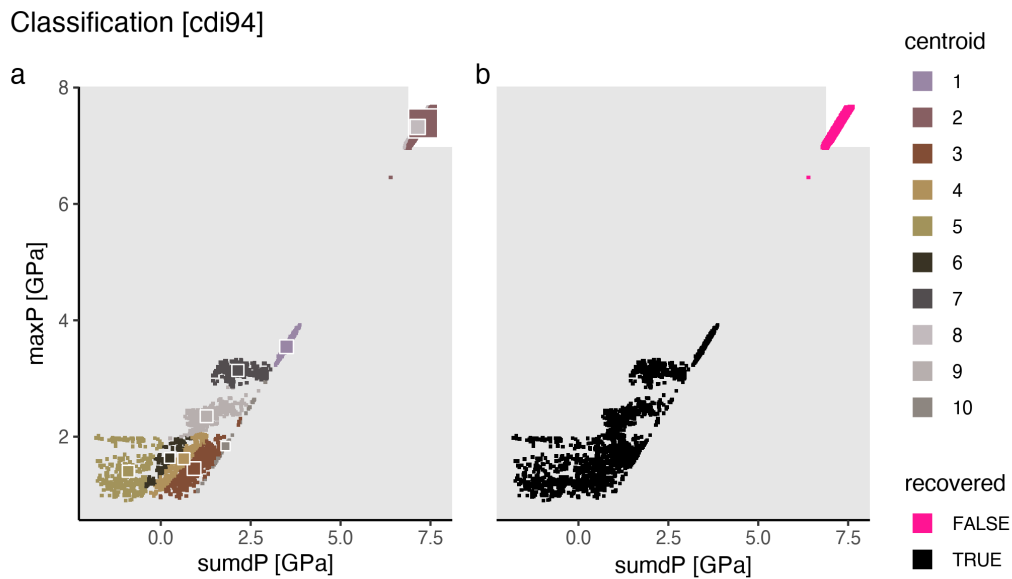


Figure A.106: Marker classification for model cdi94.

Metamorphic conditions [cdi94]

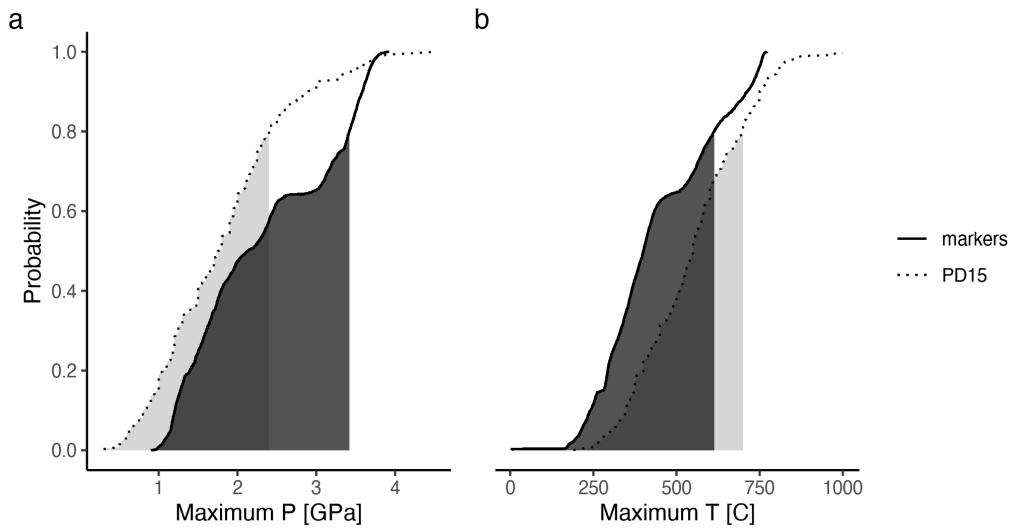


Figure A.107: Metamorphic conditions of markers recovered from model cdi94.

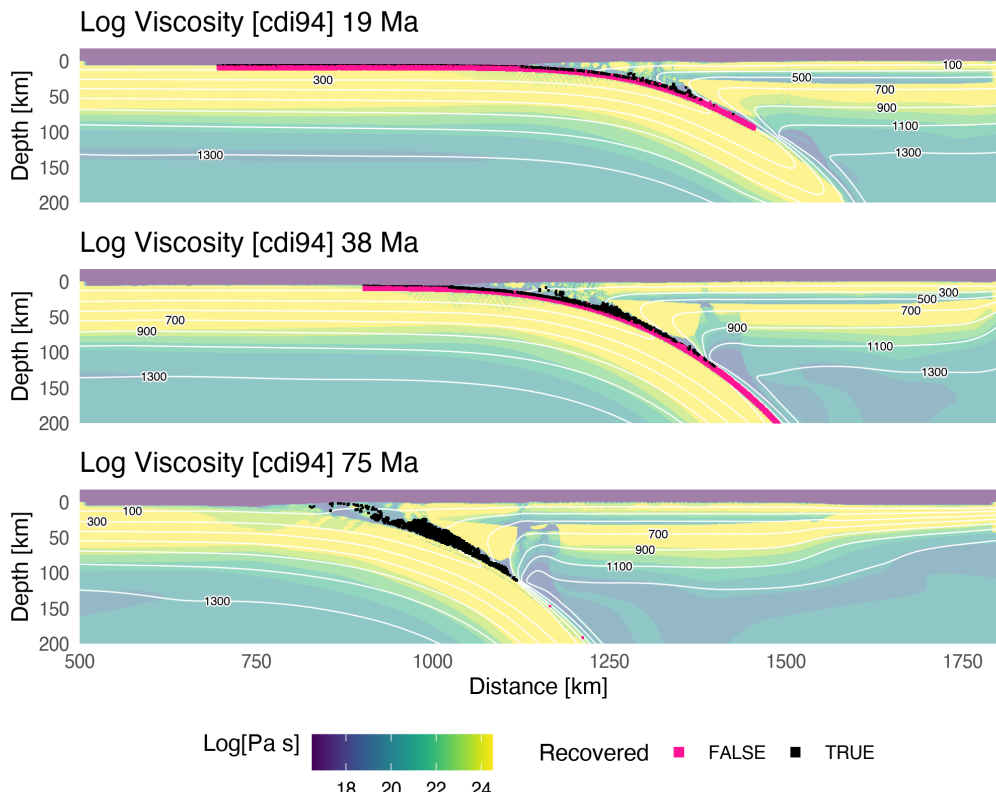


Figure A.108: Geodynamic evolution of model cdi94.

Classification [cdj46]

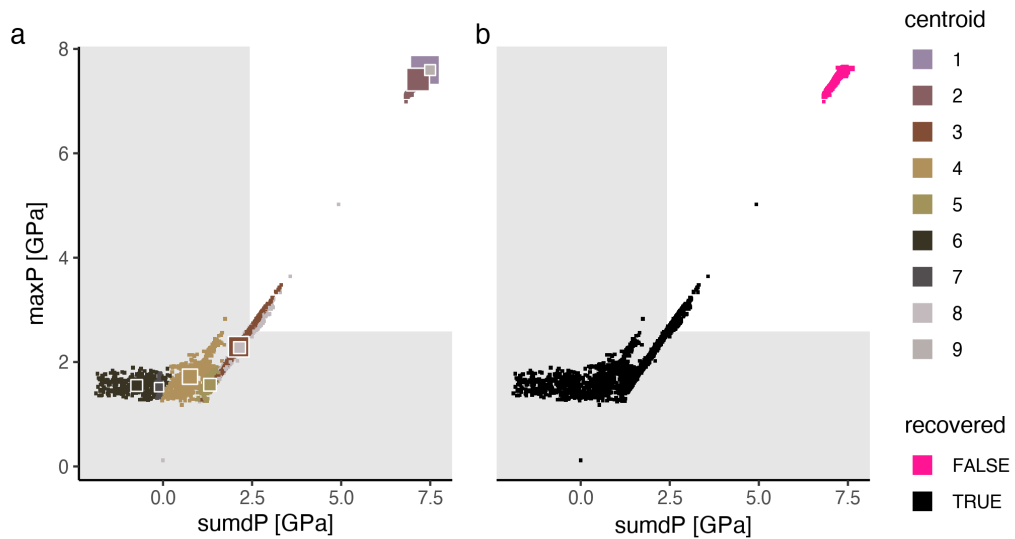


Figure A.109: Marker classification for model cdj46.

Metamorphic conditions [cdj46]

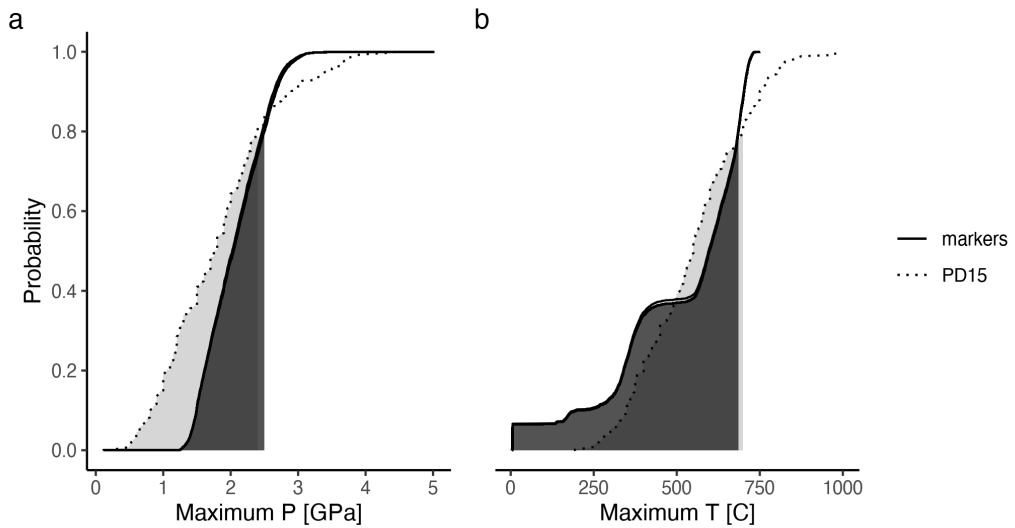


Figure A.110: Metamorphic conditions of markers recovered from model cdj46.

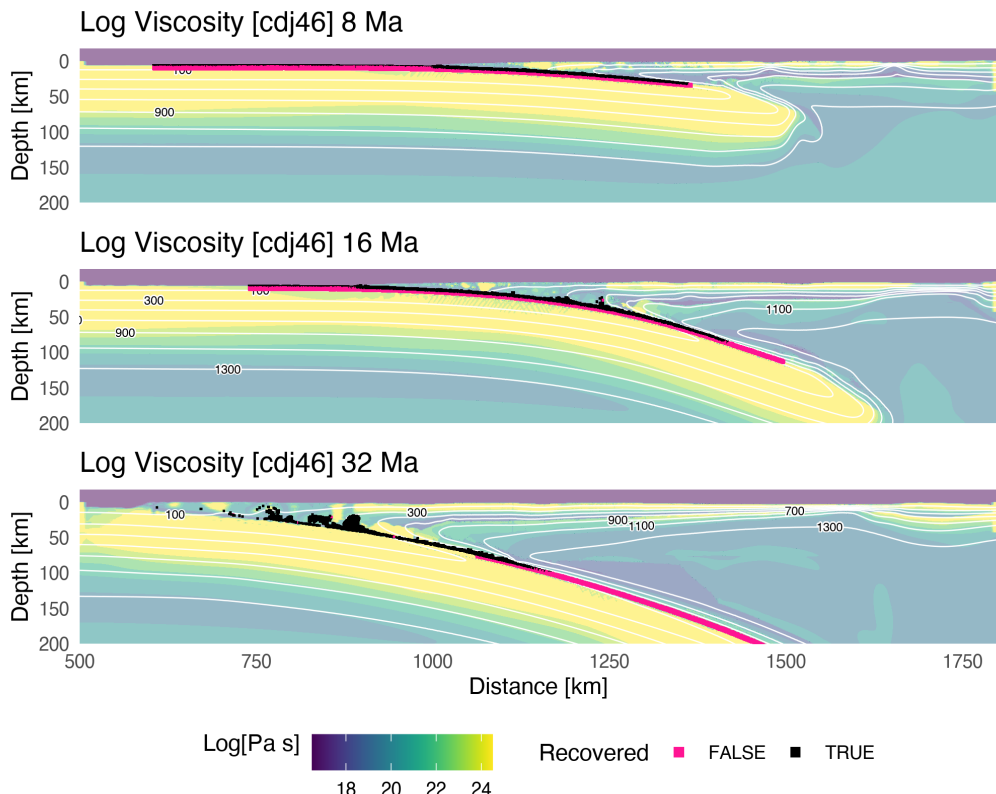


Figure A.111: Geodynamic evolution of model cdj46.

Classification [cdj62]

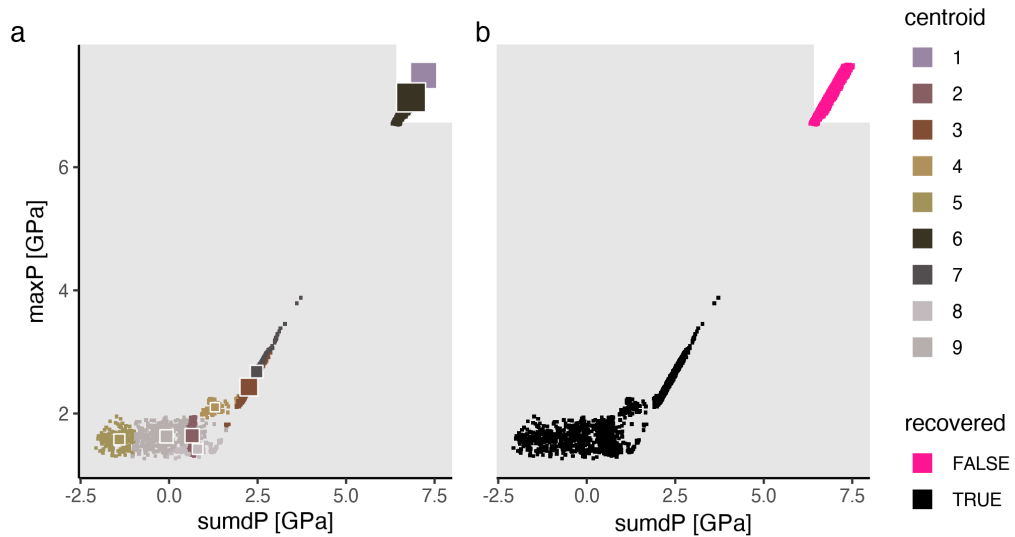


Figure A.112: Marker classification for model cdj62.

Metamorphic conditions [cdj62]

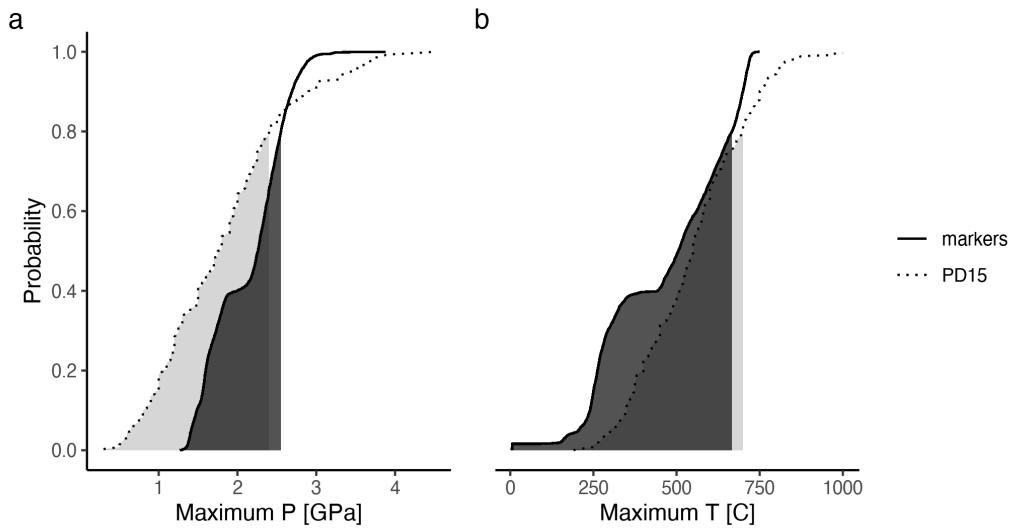


Figure A.113: Metamorphic conditions of markers recovered from model cdj62.

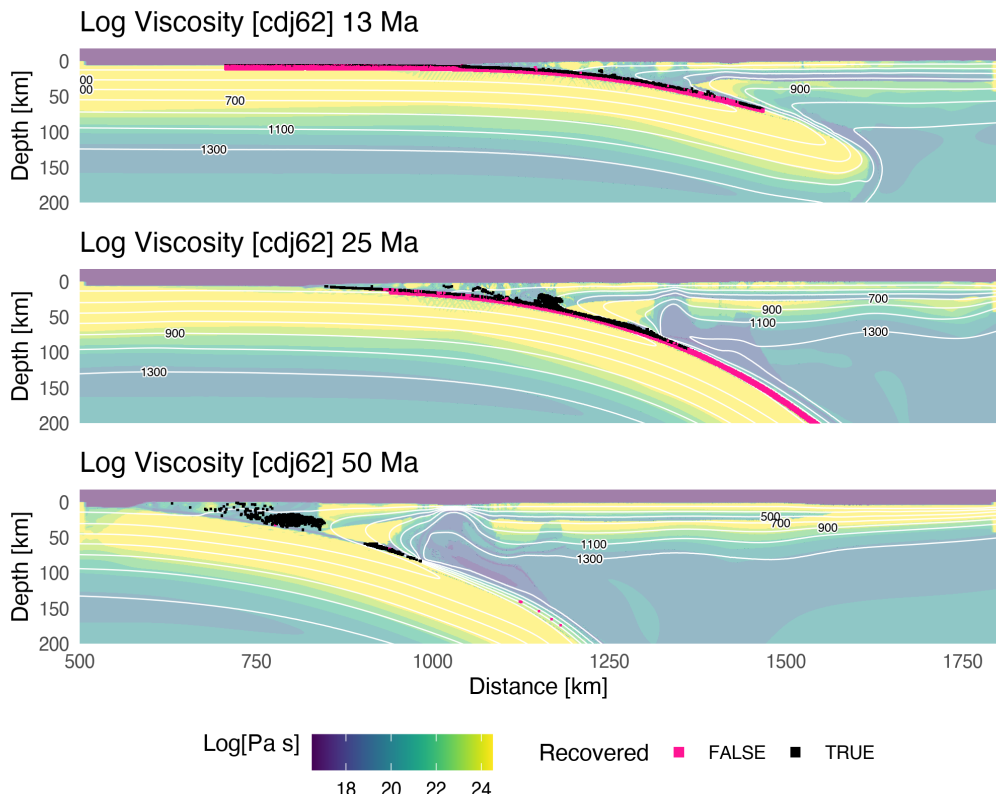


Figure A.114: Geodynamic evolution of model cdj62.

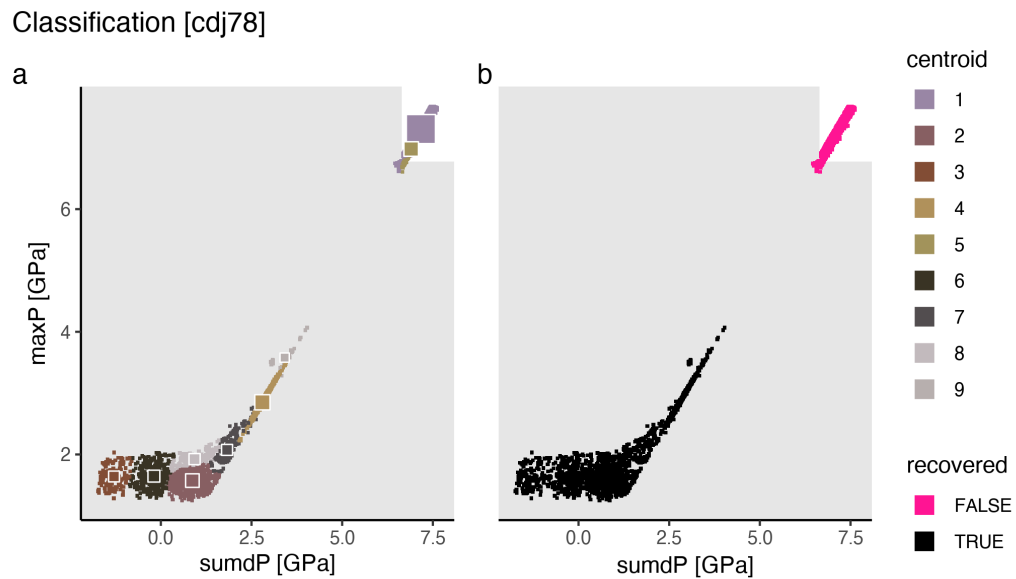


Figure A.115: Marker classification for model cdj78.

Metamorphic conditions [cdj78]

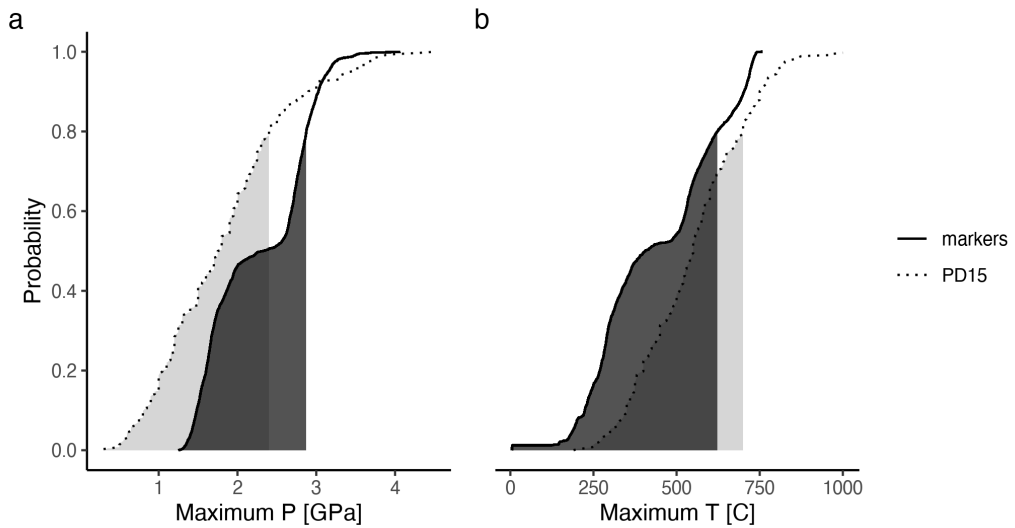


Figure A.116: Metamorphic conditions of markers recovered from model cdj78.

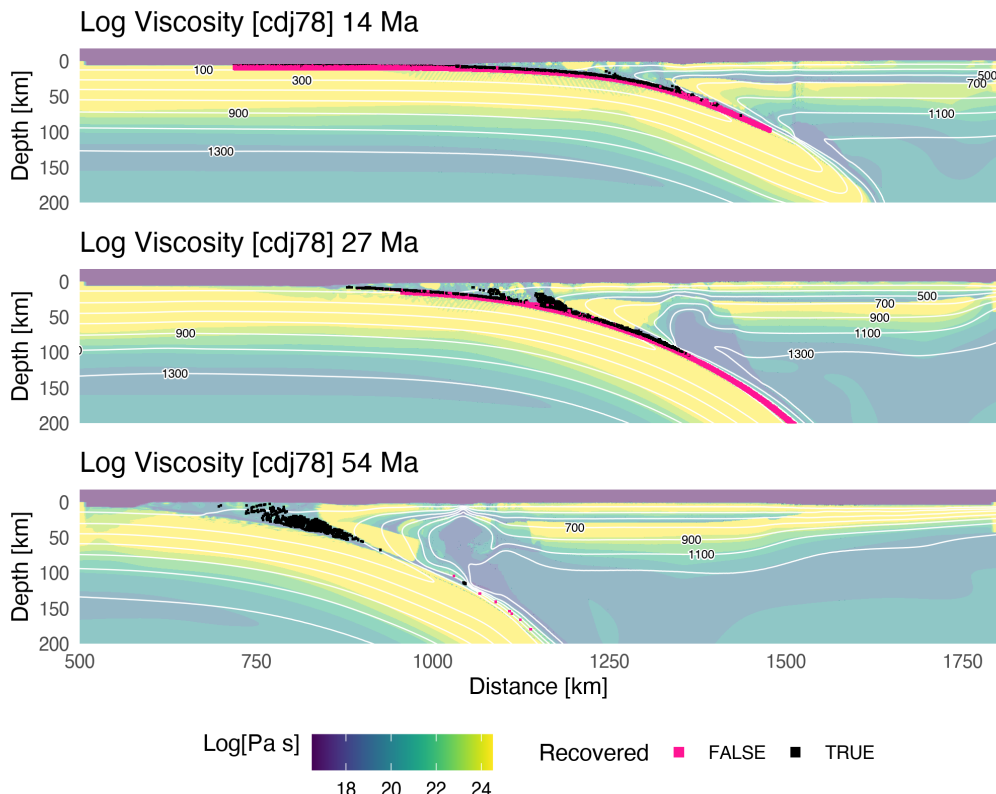


Figure A.117: Geodynamic evolution of model cdj78.

Classification [cdj94]

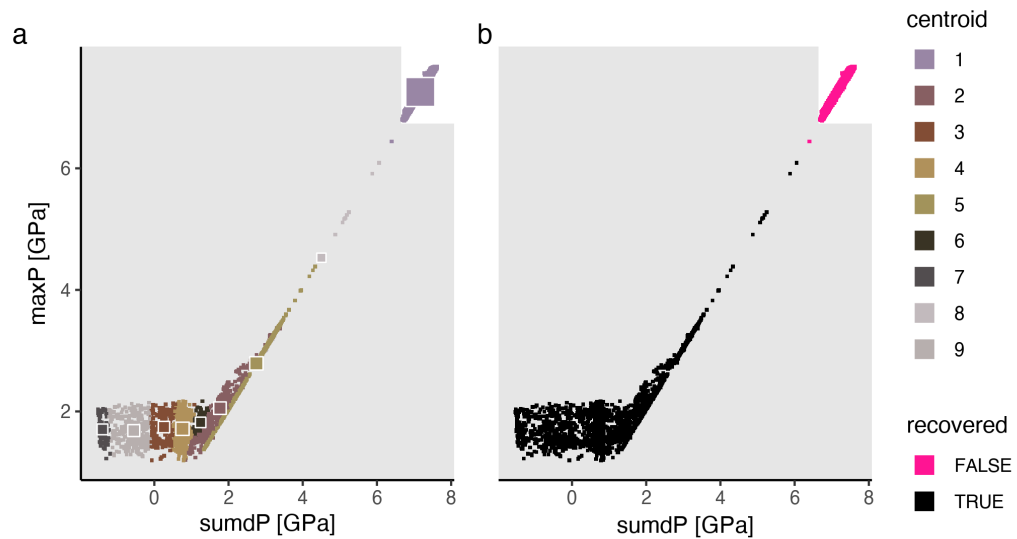


Figure A.118: Marker classification for model cdj94.

Metamorphic conditions [cdj94]

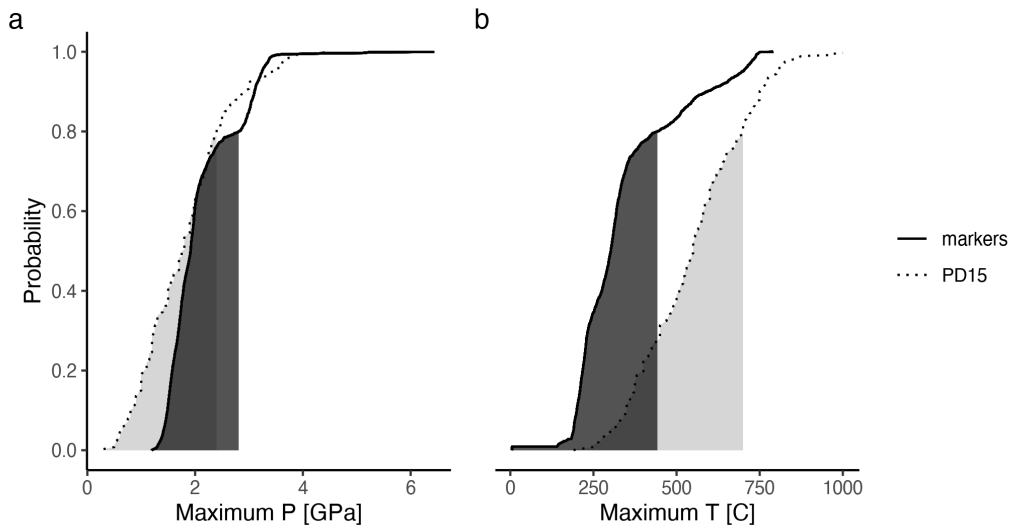


Figure A.119: Metamorphic conditions of markers recovered from model cdj94.

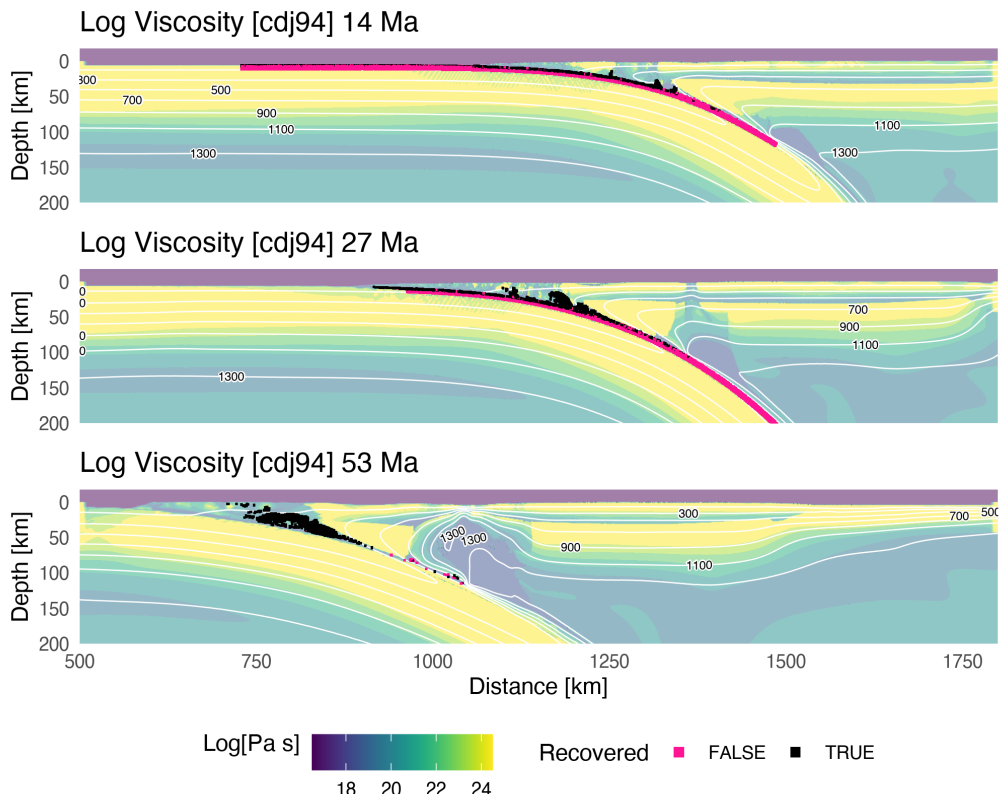


Figure A.120: Geodynamic evolution of model cdj94.

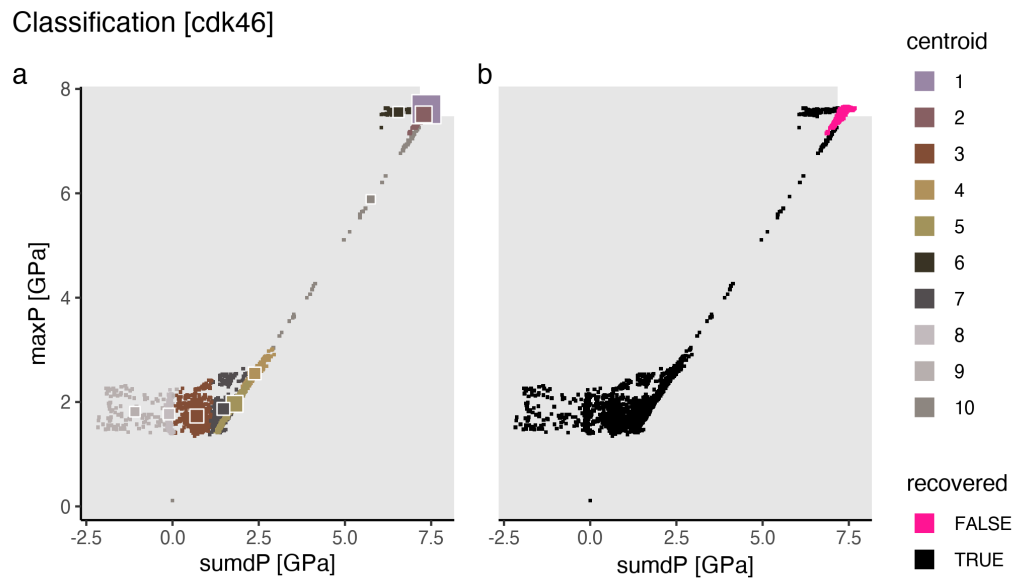


Figure A.121: Marker classification for model cdk46.

Metamorphic conditions [cdk46]

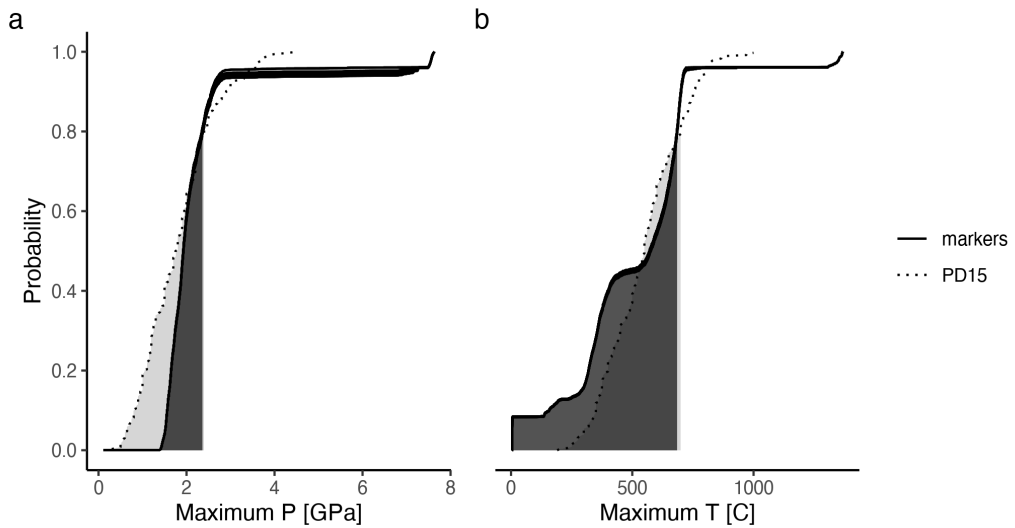


Figure A.122: Metamorphic conditions of markers recovered from model cdk46.

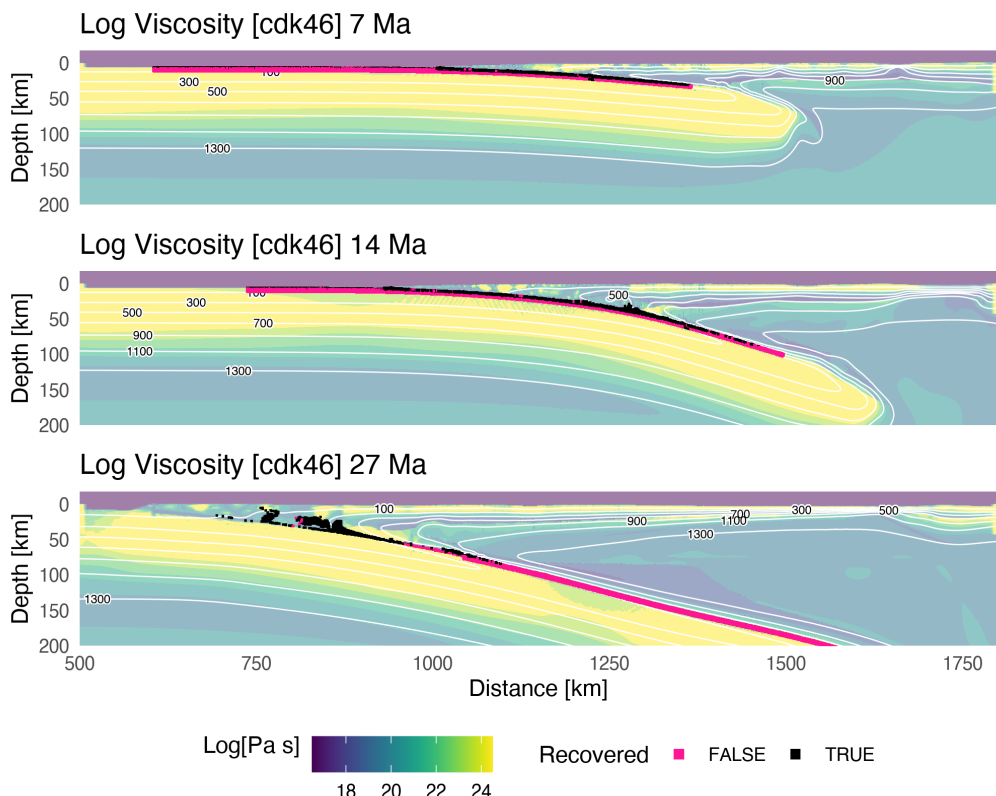


Figure A.123: Geodynamic evolution of model cdk46.

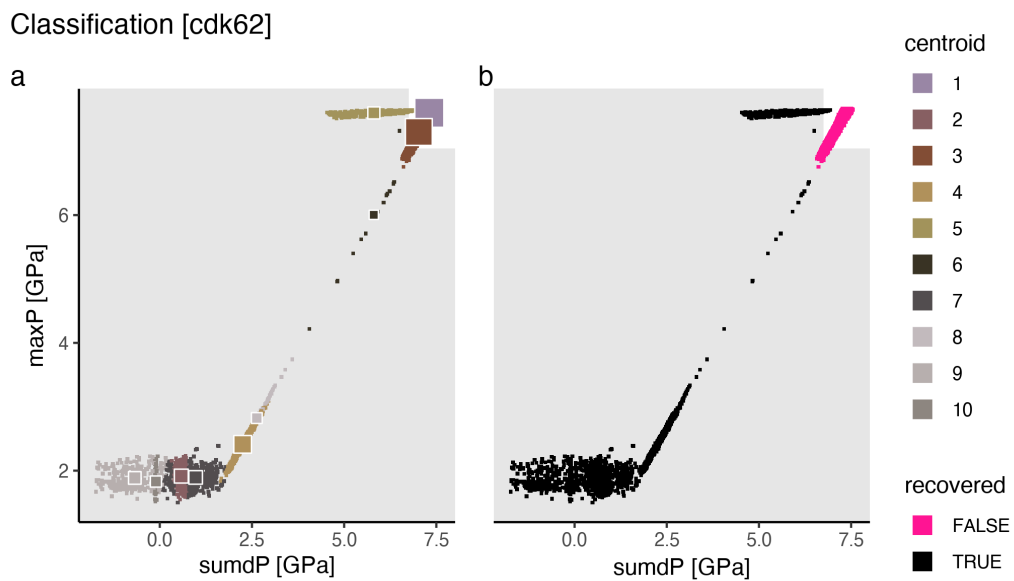


Figure A.124: Marker classification for model cdk62.

Metamorphic conditions [cdk62]

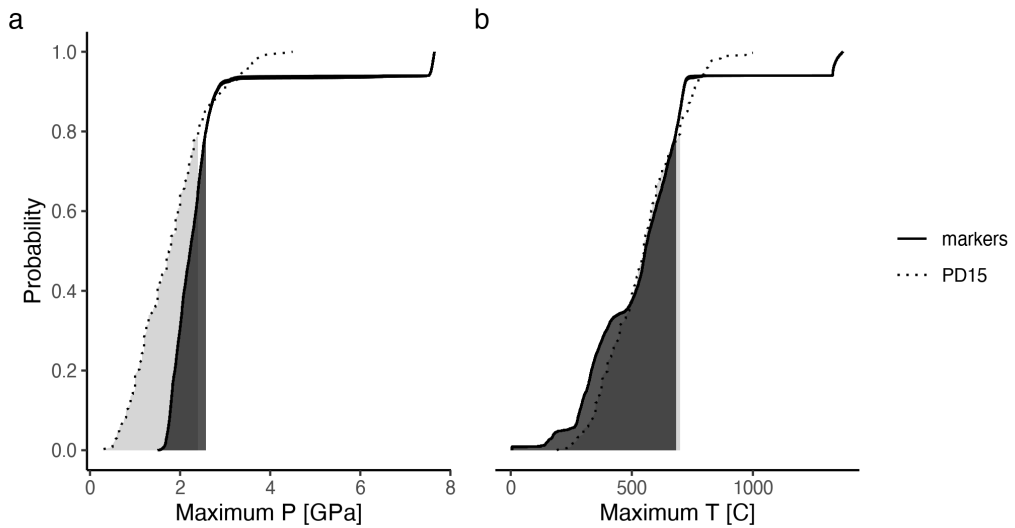


Figure A.125: Metamorphic conditions of markers recovered from model cdk62.

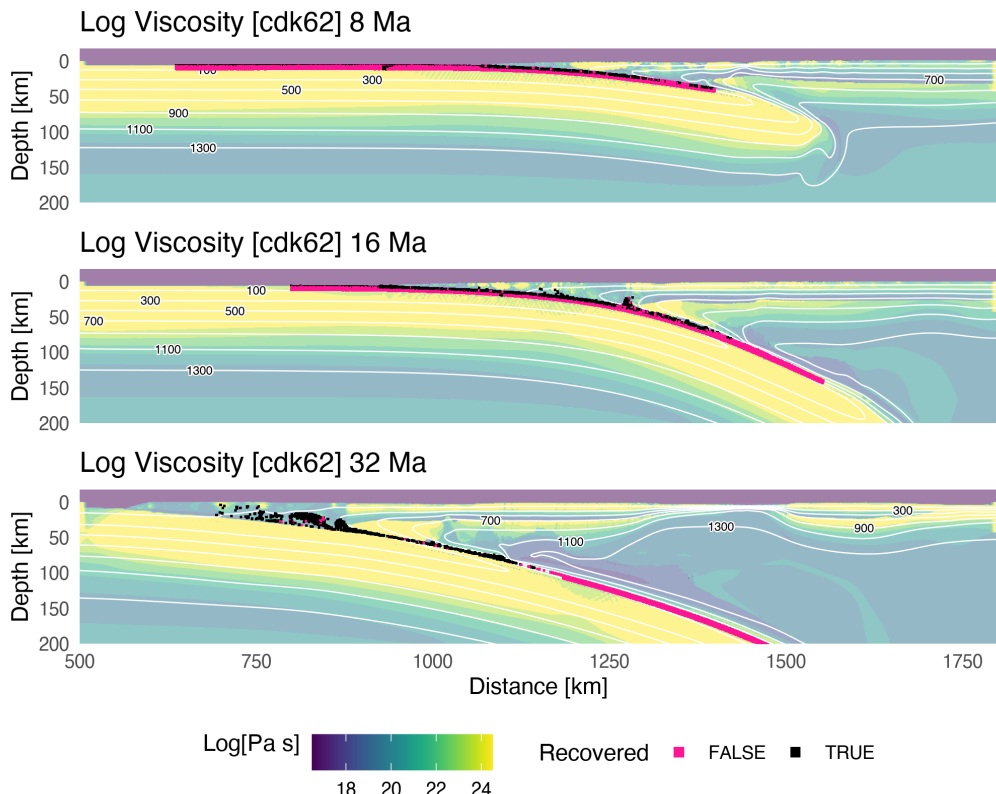


Figure A.126: Geodynamic evolution of model cdk62.

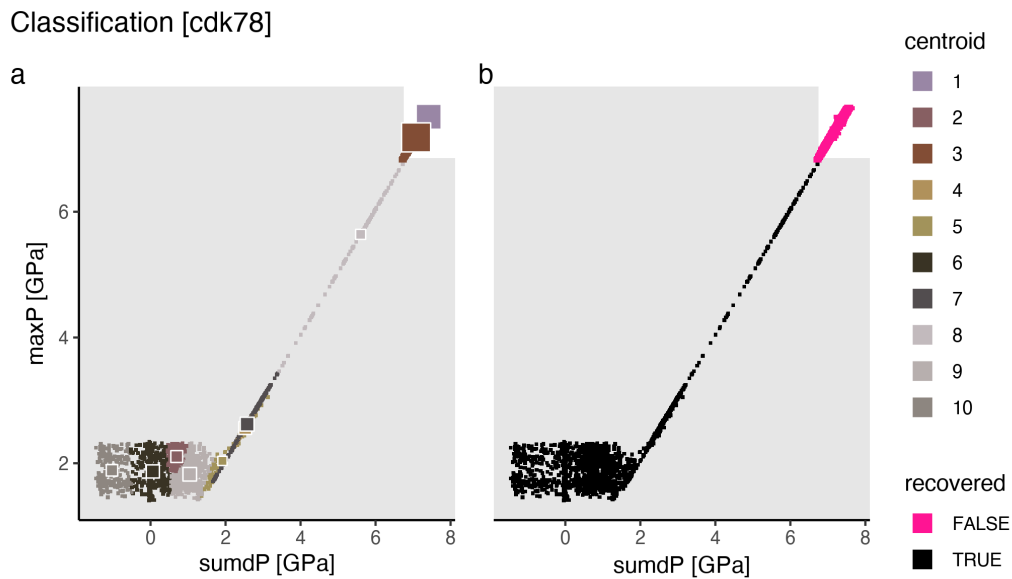


Figure A.127: Marker classification for model cdk78.

Metamorphic conditions [cdk78]

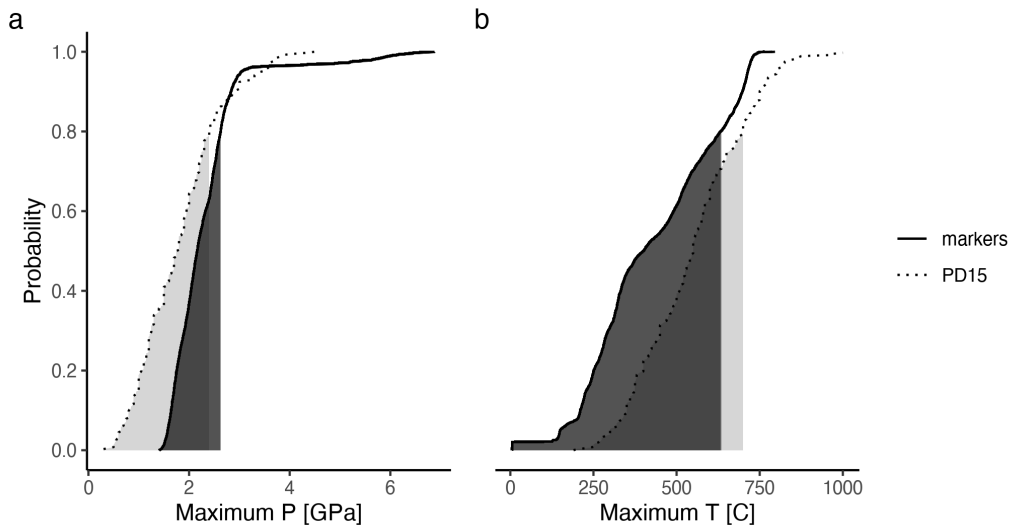


Figure A.128: Metamorphic conditions of markers recovered from model cdk78.

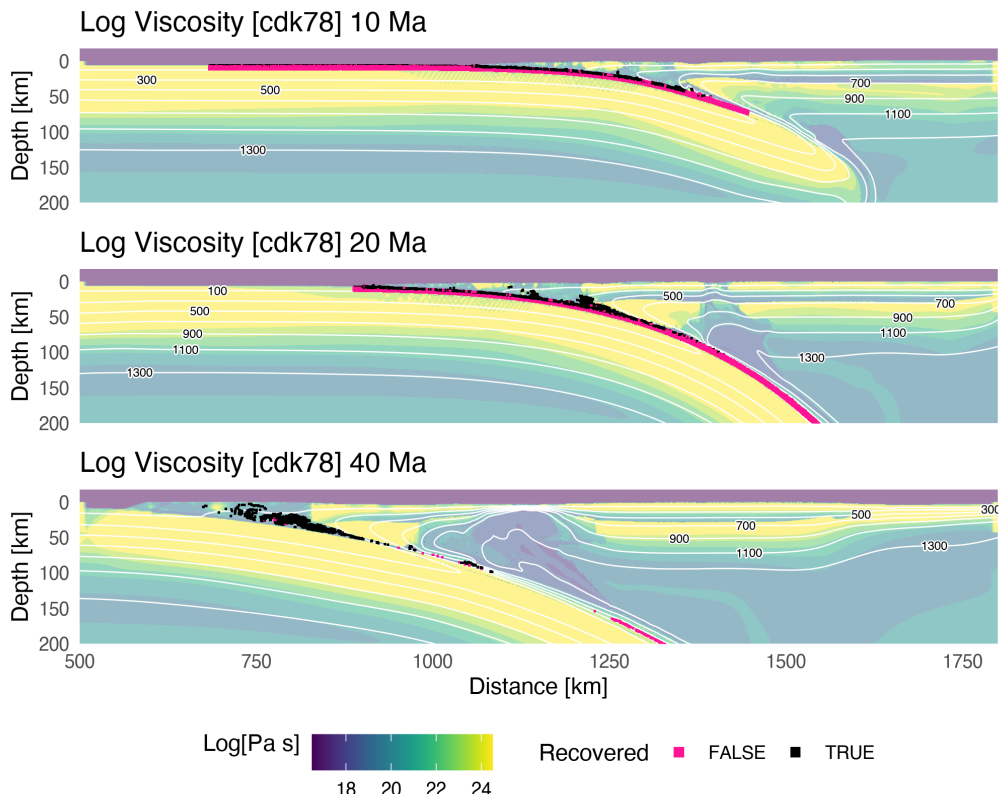


Figure A.129: Geodynamic evolution of model cdk78.

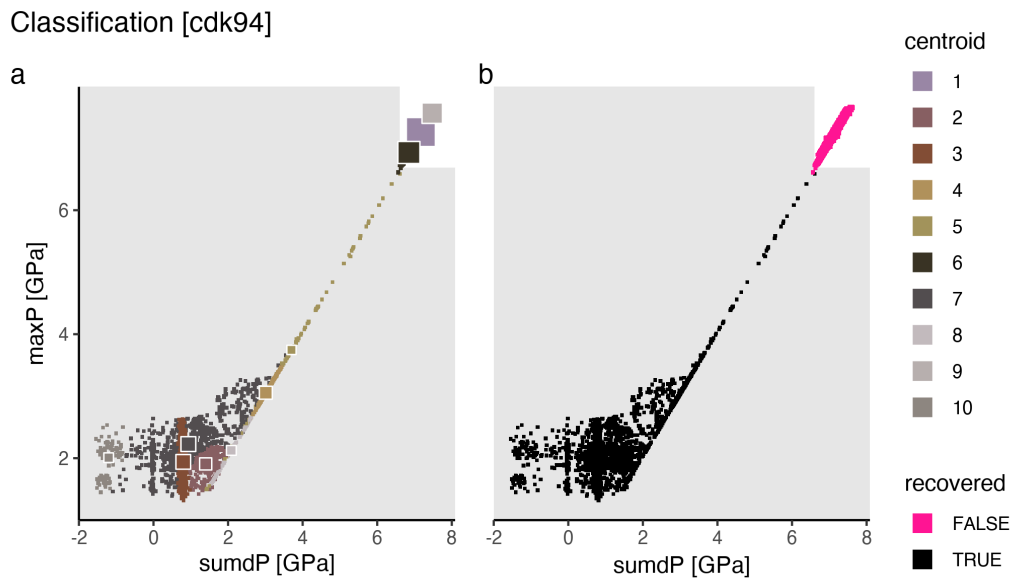


Figure A.130: Marker classification for model cdk94.

Metamorphic conditions [cdk94]

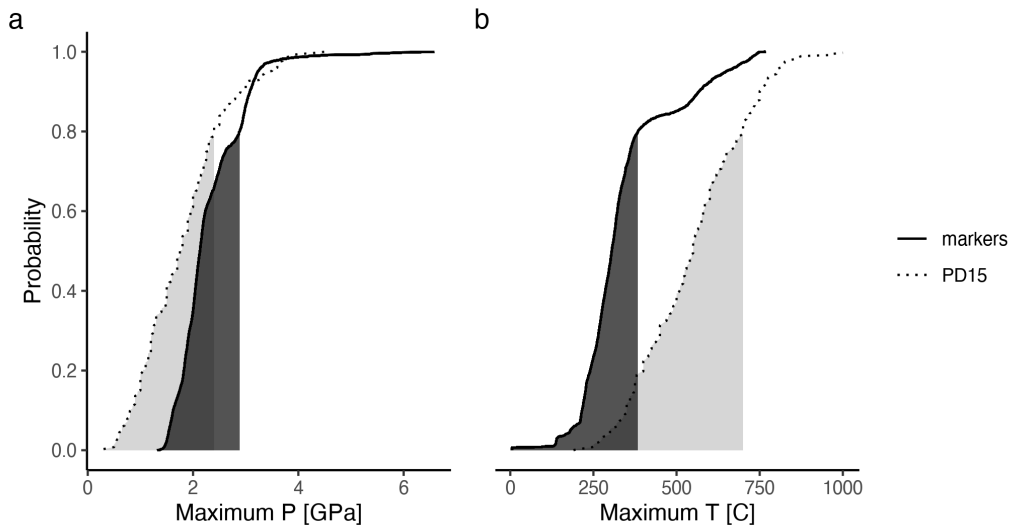


Figure A.131: Metamorphic conditions of markers recovered from model cdk94.

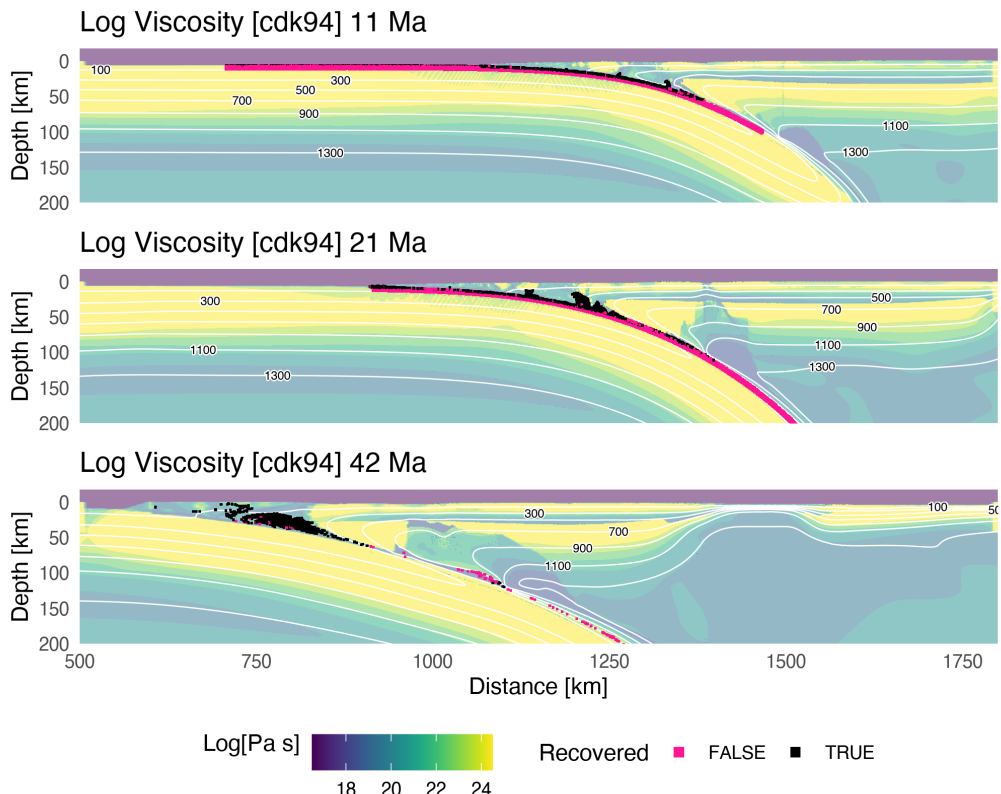


Figure A.132: Geodynamic evolution of model cdk94.

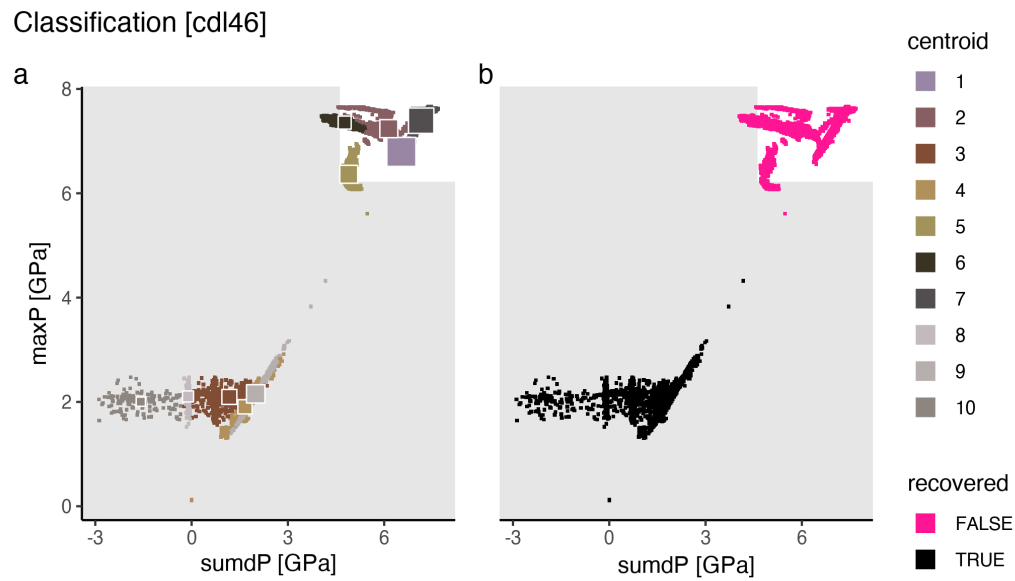


Figure A.133: Marker classification for model cdl46.

Metamorphic conditions [cdl46]

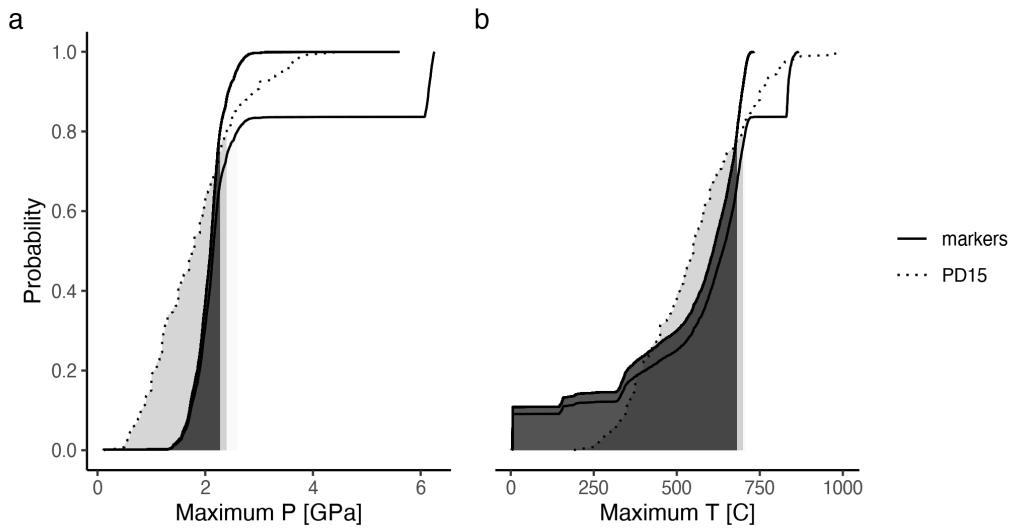


Figure A.134: Metamorphic conditions of markers recovered from model cdl46.

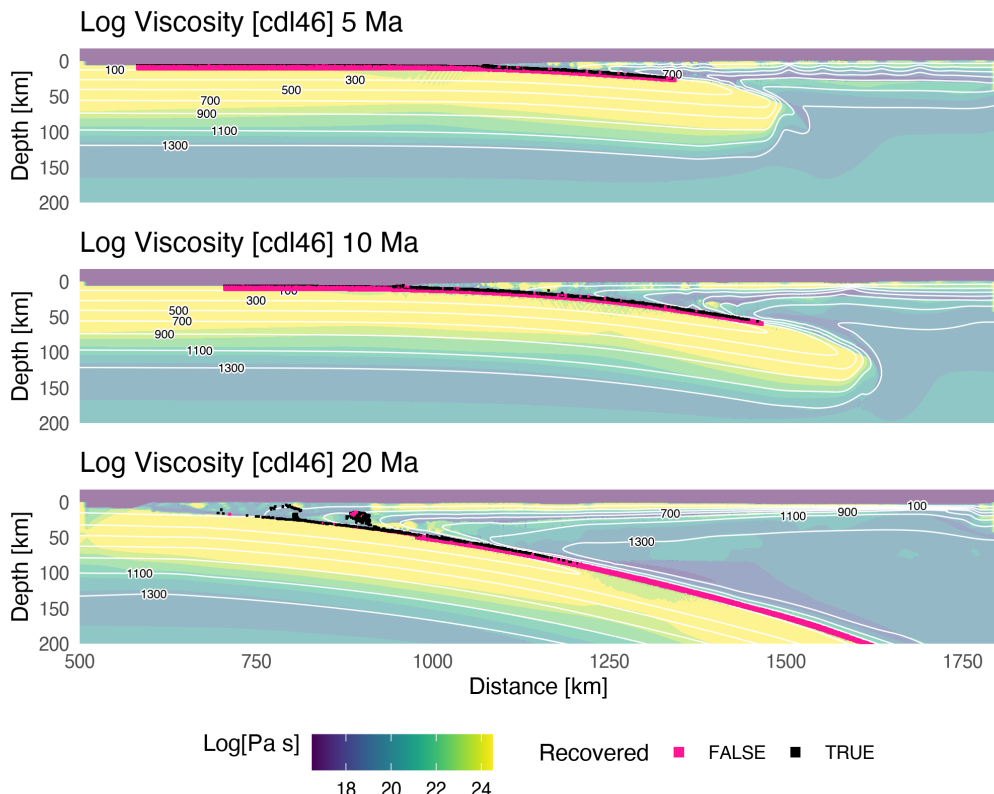


Figure A.135: Geodynamic evolution of model cdl46.

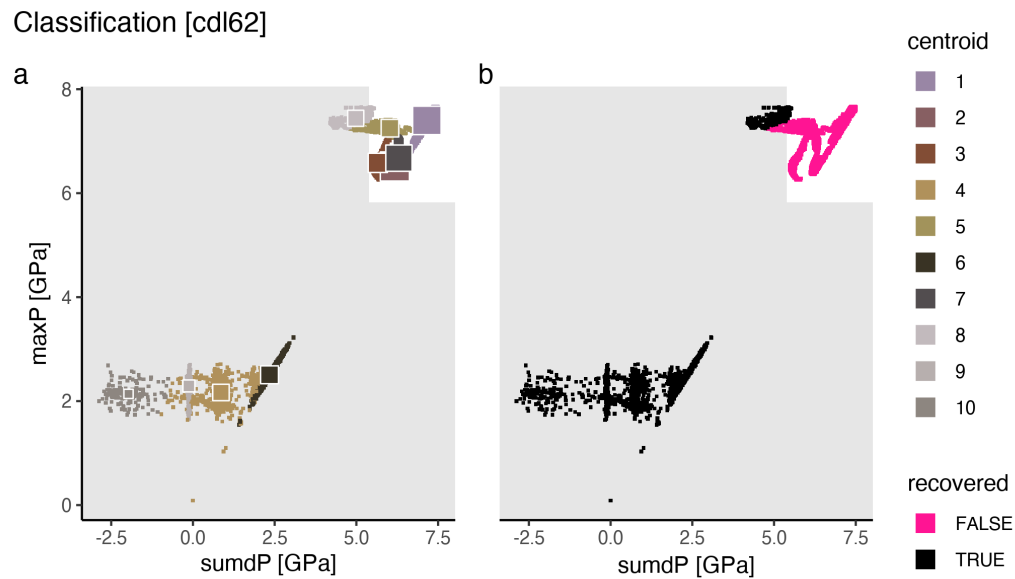


Figure A.136: Marker classification for model cdl62.

Metamorphic conditions [cdl62]

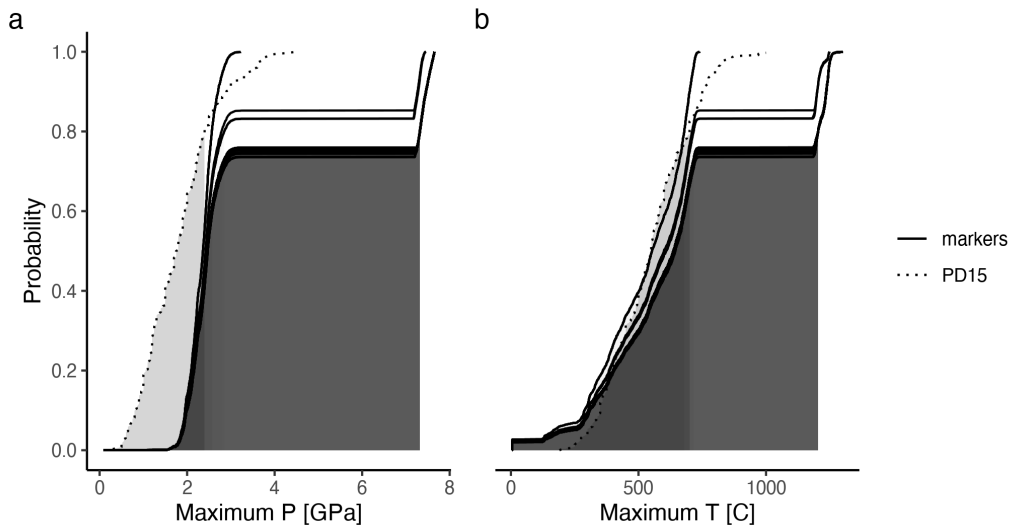


Figure A.137: Metamorphic conditions of markers recovered from model cdl62.

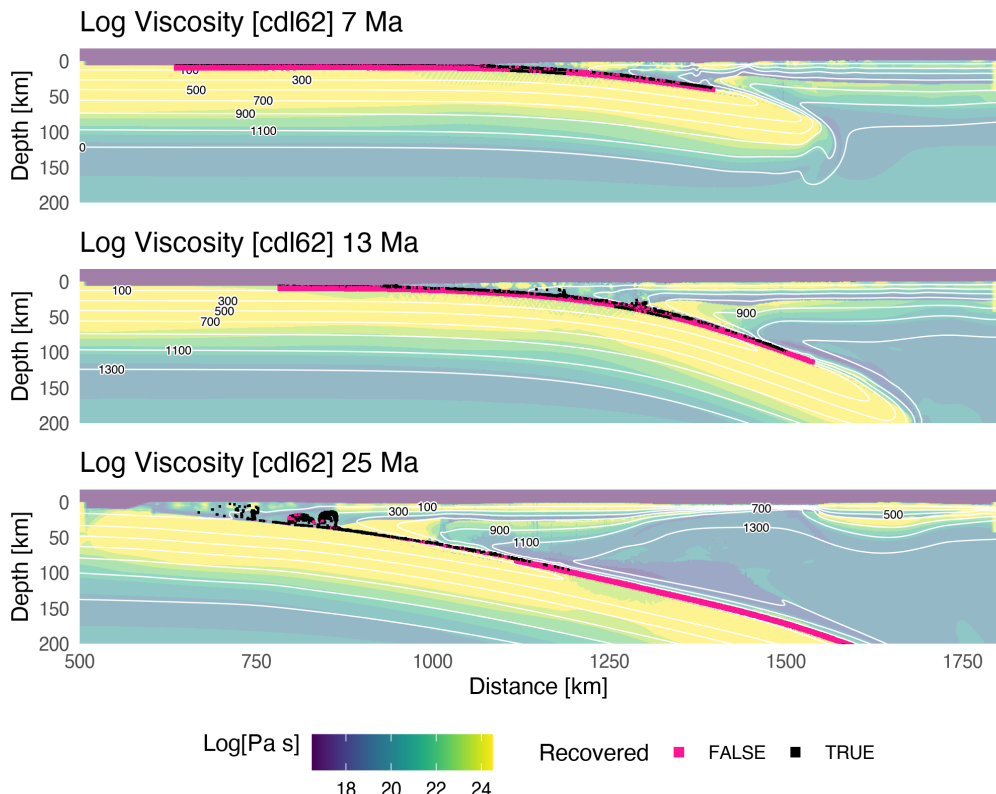


Figure A.138: Geodynamic evolution of model cdl62.

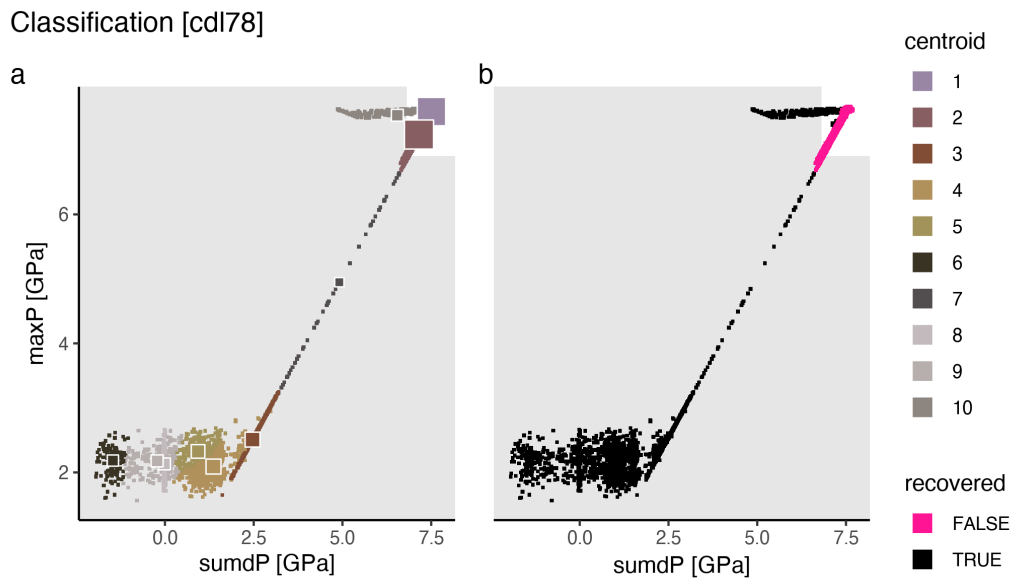


Figure A.139: Marker classification for model cdl78.

Metamorphic conditions [cdl78]

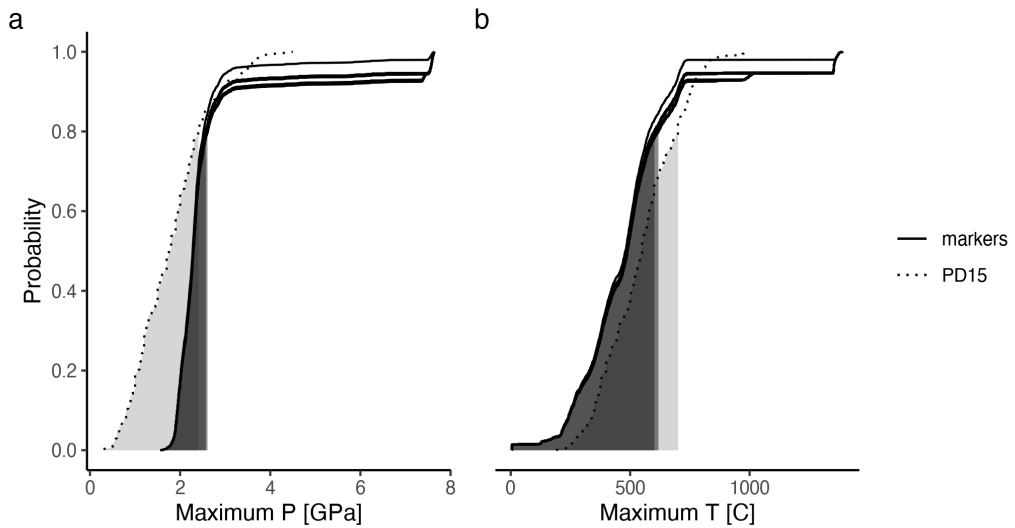


Figure A.140: Metamorphic conditions of markers recovered from model cdl78.

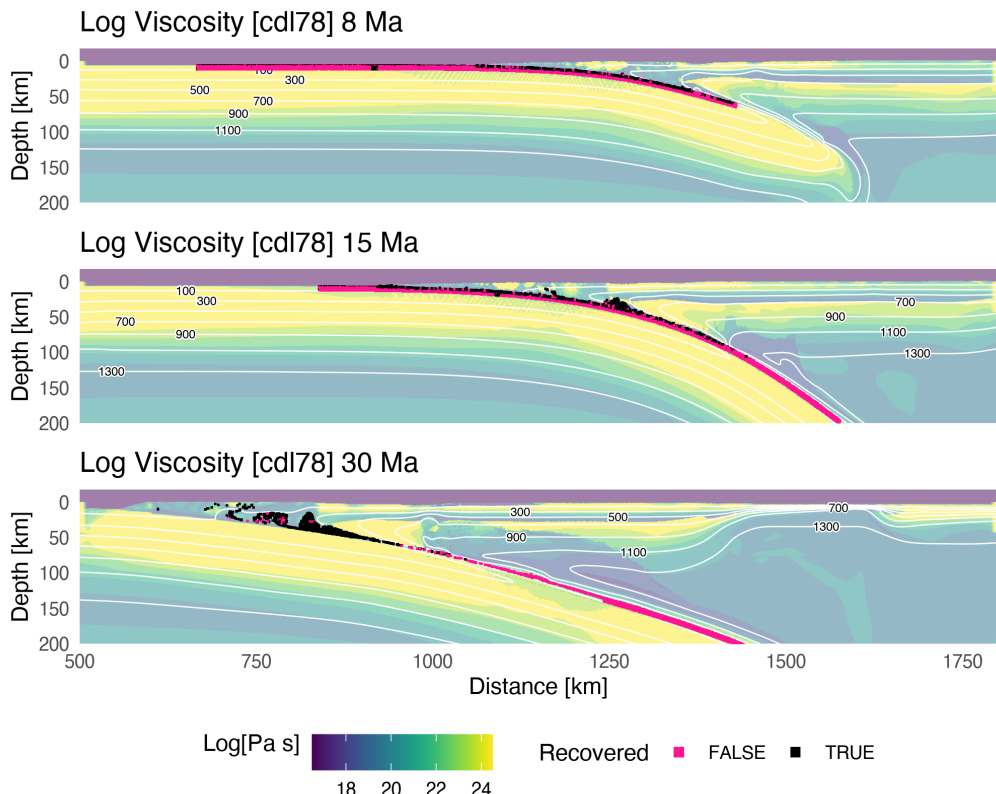


Figure A.141: Geodynamic evolution of model cdl78.

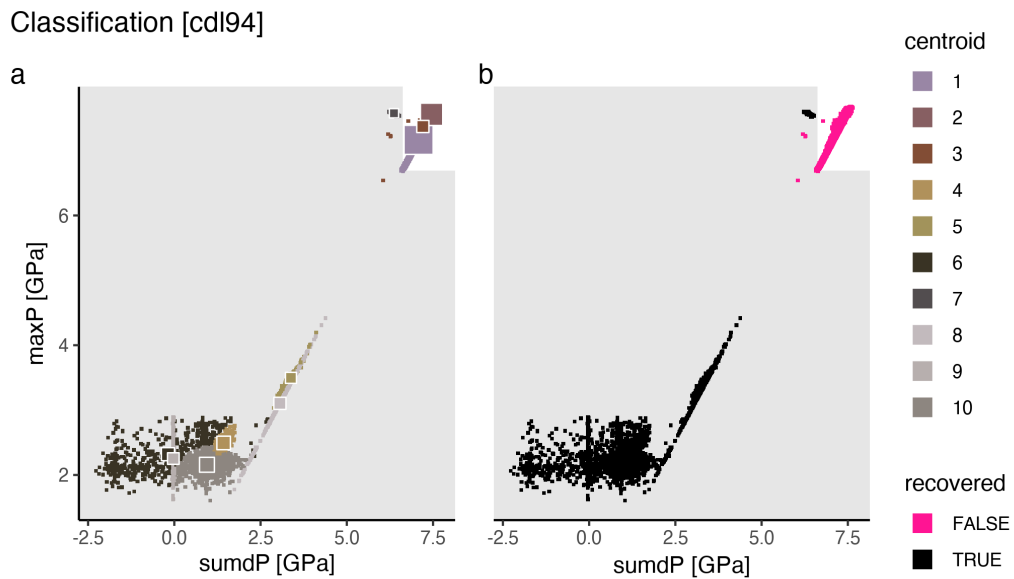


Figure A.142: Marker classification for model cdl94.

Metamorphic conditions [cdl94]

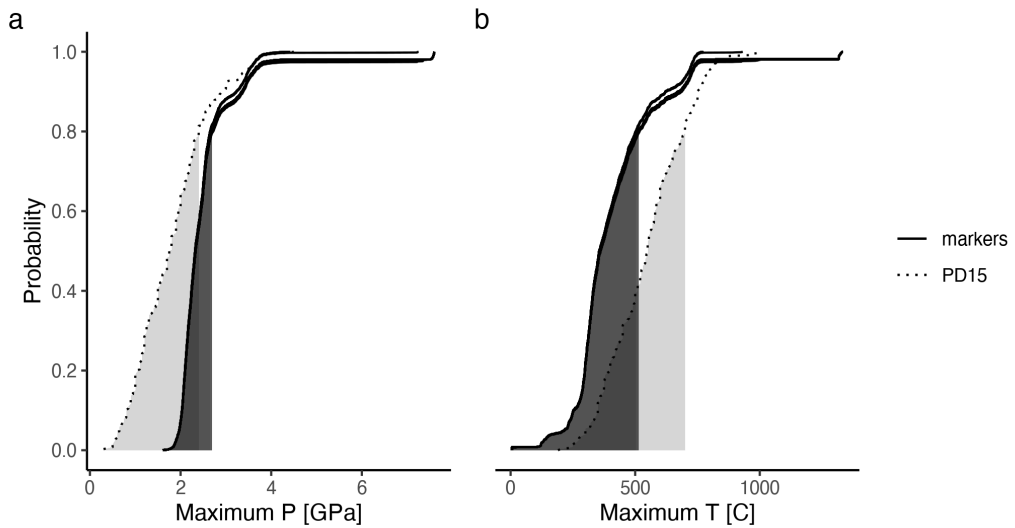


Figure A.143: Metamorphic conditions of markers recovered from model cdl94.

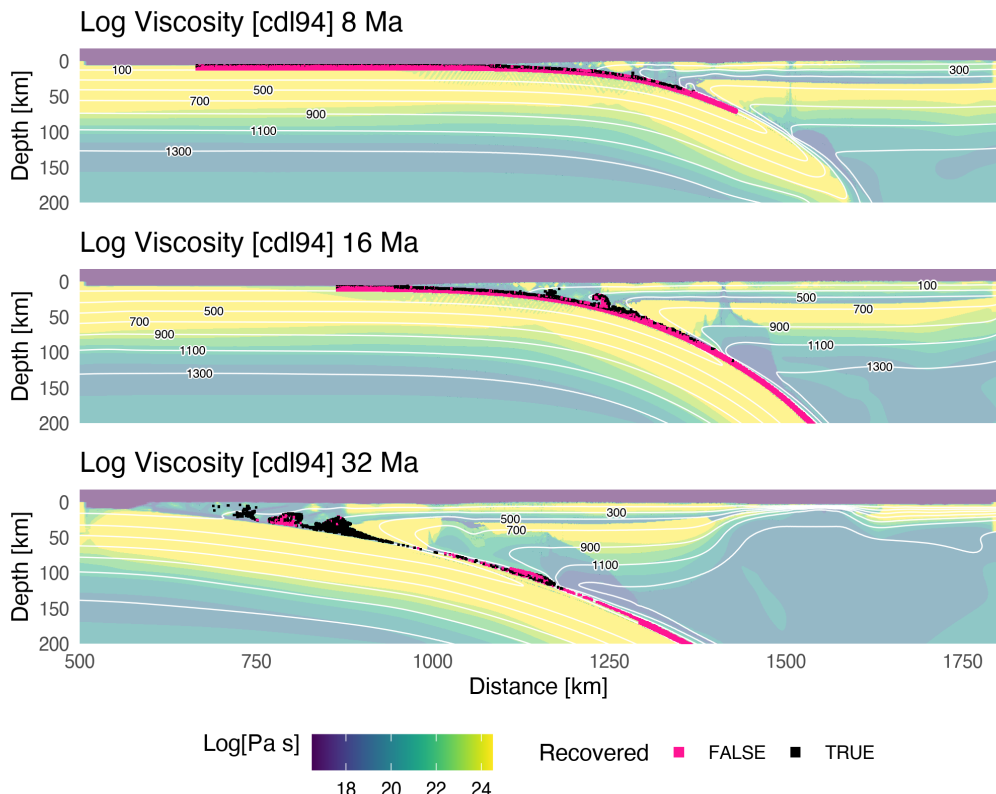


Figure A.144: Geodynamic evolution of model cdl94.

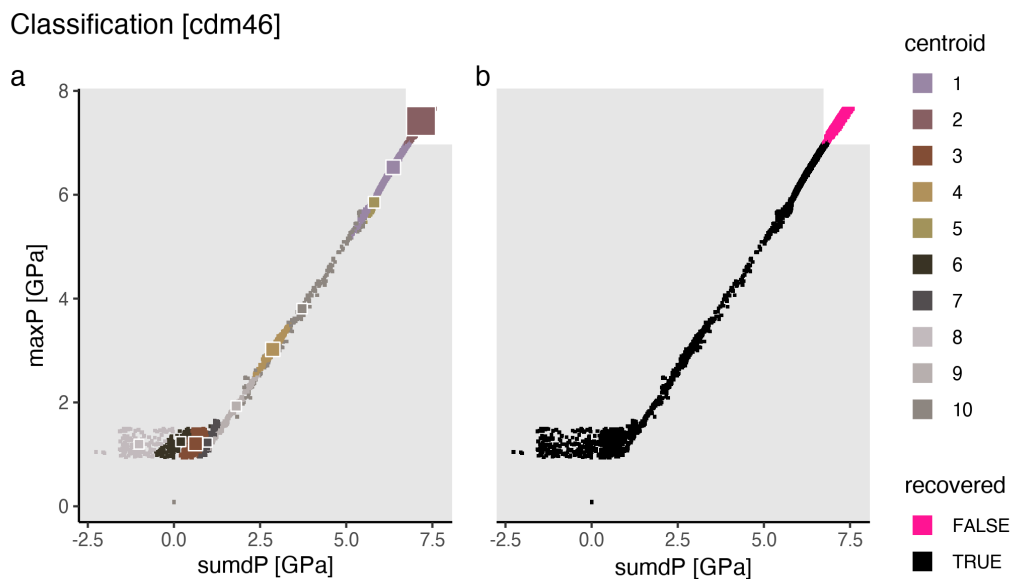


Figure A.145: Marker classification for model cdm46.

Metamorphic conditions [cdm46]

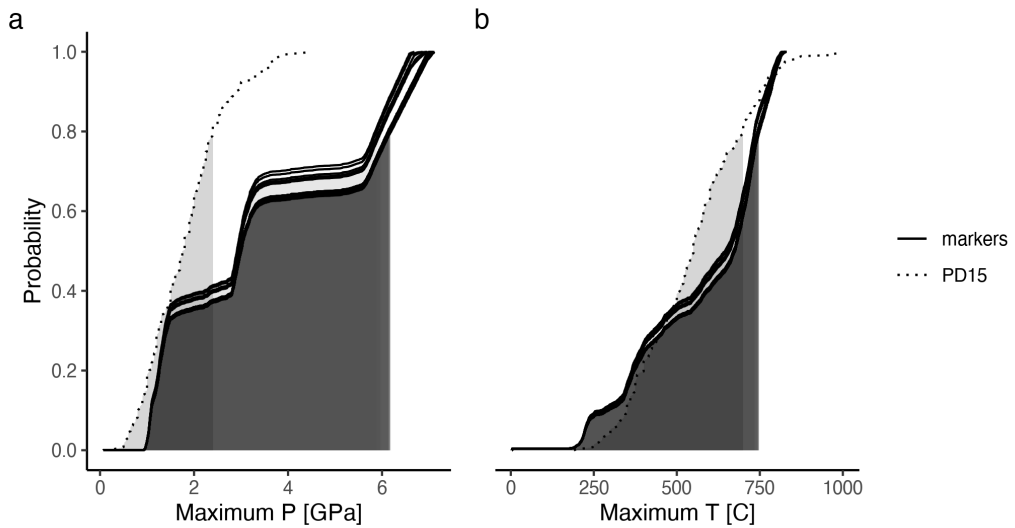


Figure A.146: Metamorphic conditions of markers recovered from model cdm46.

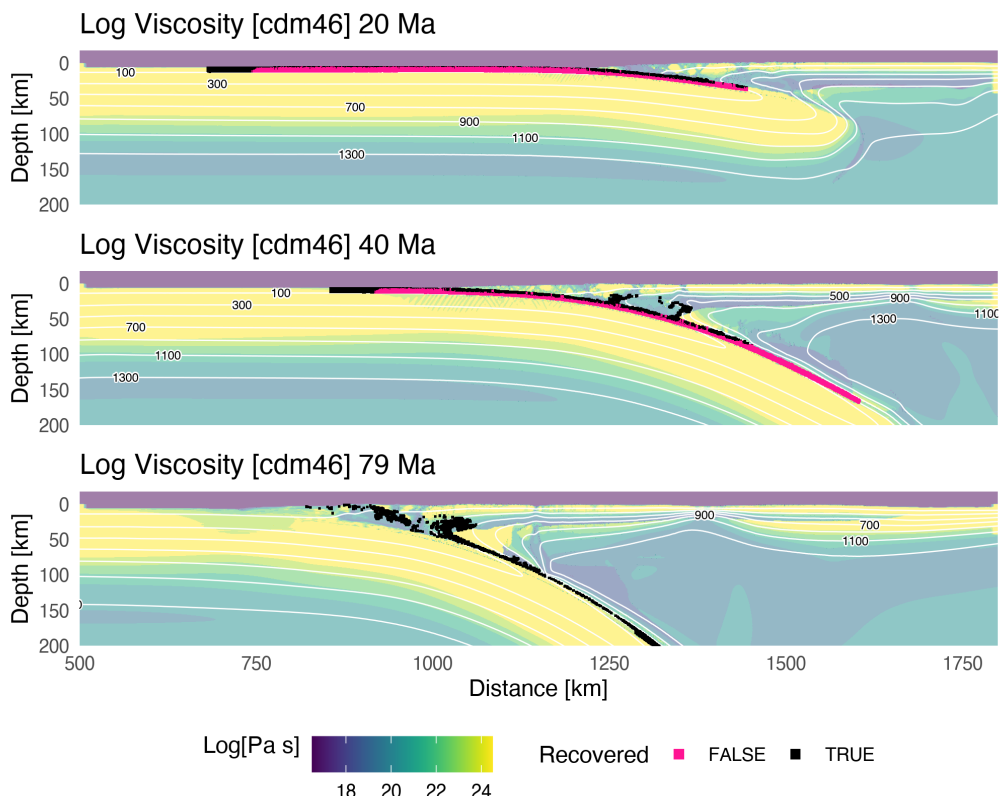


Figure A.147: Geodynamic evolution of model cdm46.

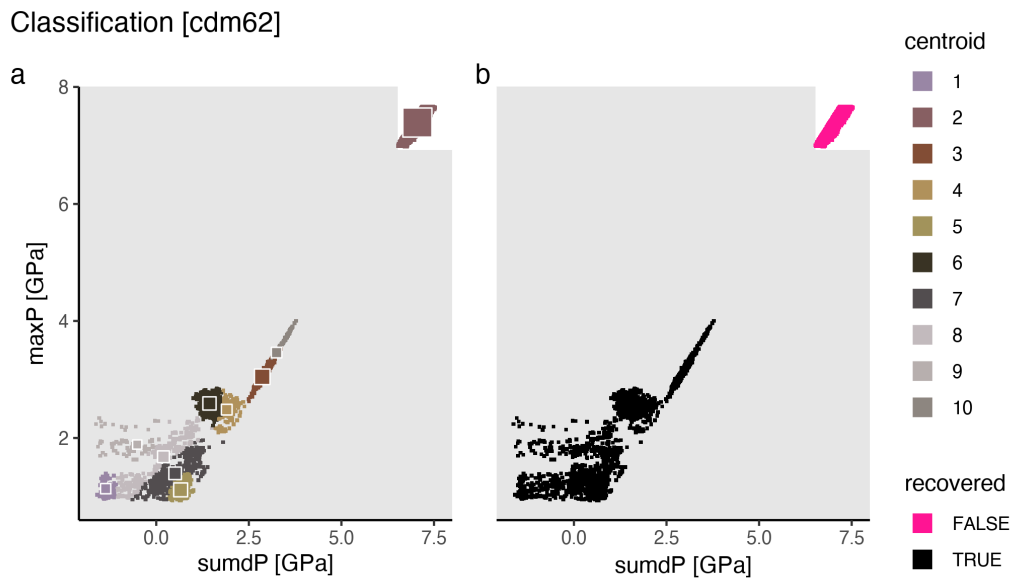


Figure A.148: Marker classification for model cdm62.

Metamorphic conditions [cdm62]

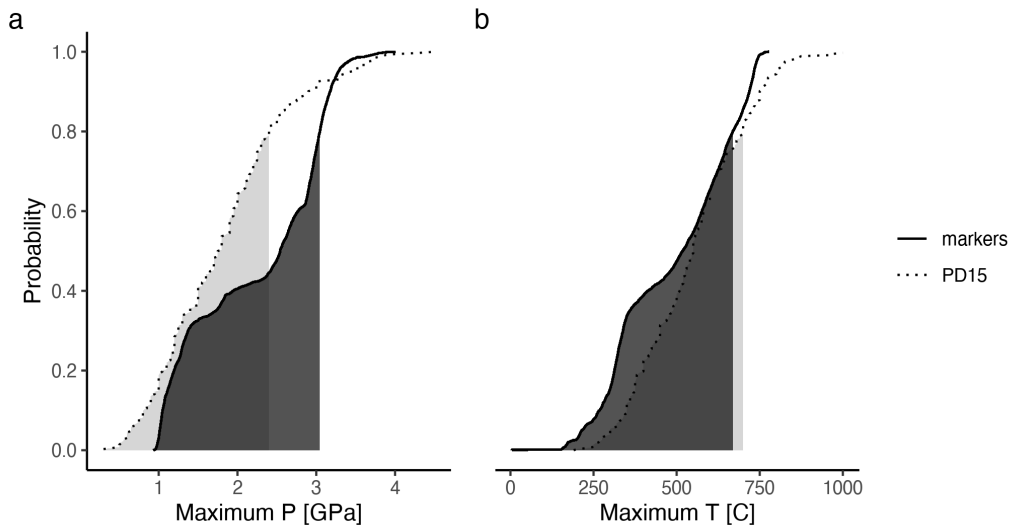


Figure A.149: Metamorphic conditions of markers recovered from model cdm62.

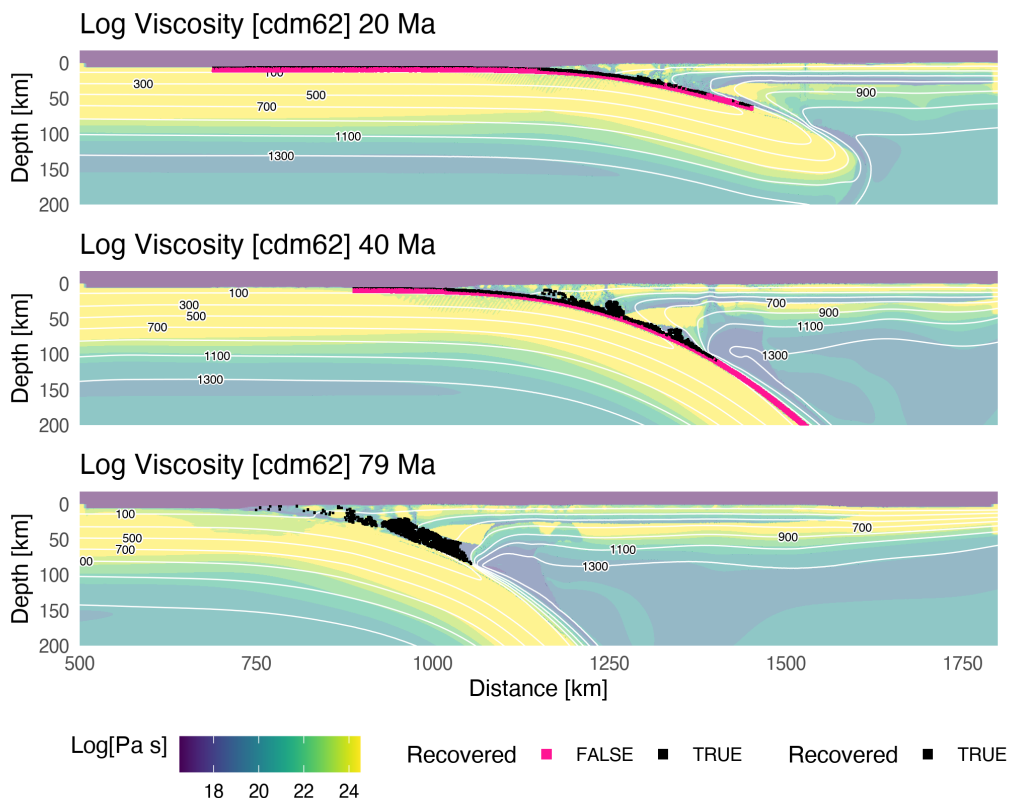


Figure A.150: Geodynamic evolution of model cdm62.

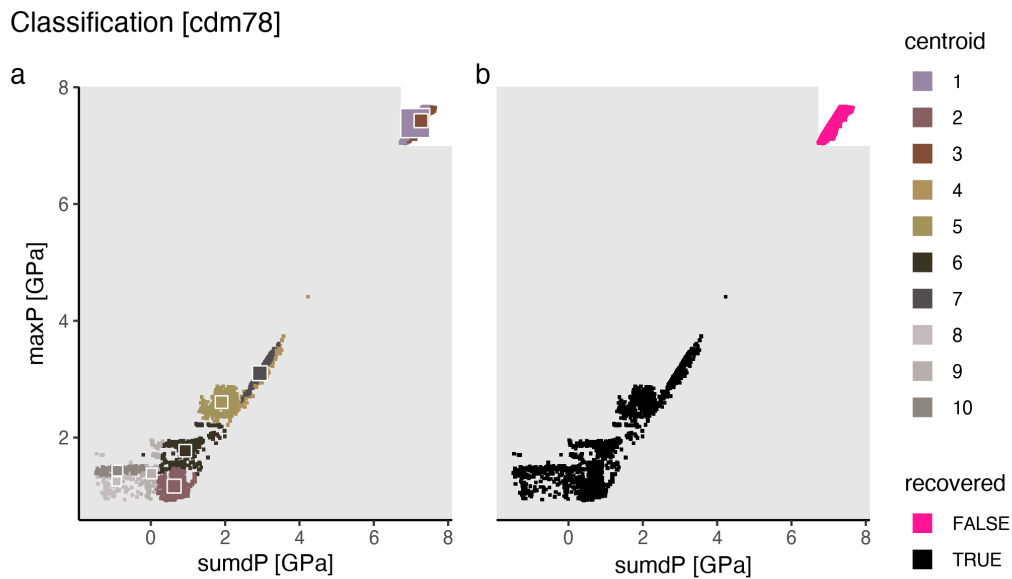


Figure A.151: Marker classification for model cdm78.

Metamorphic conditions [cdm78]

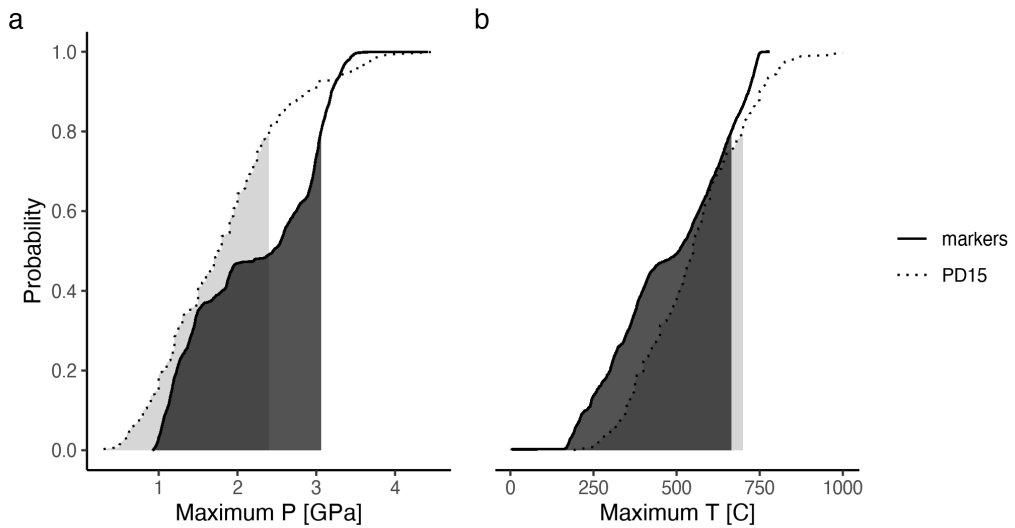


Figure A.152: Metamorphic conditions of markers recovered from model cdm78.

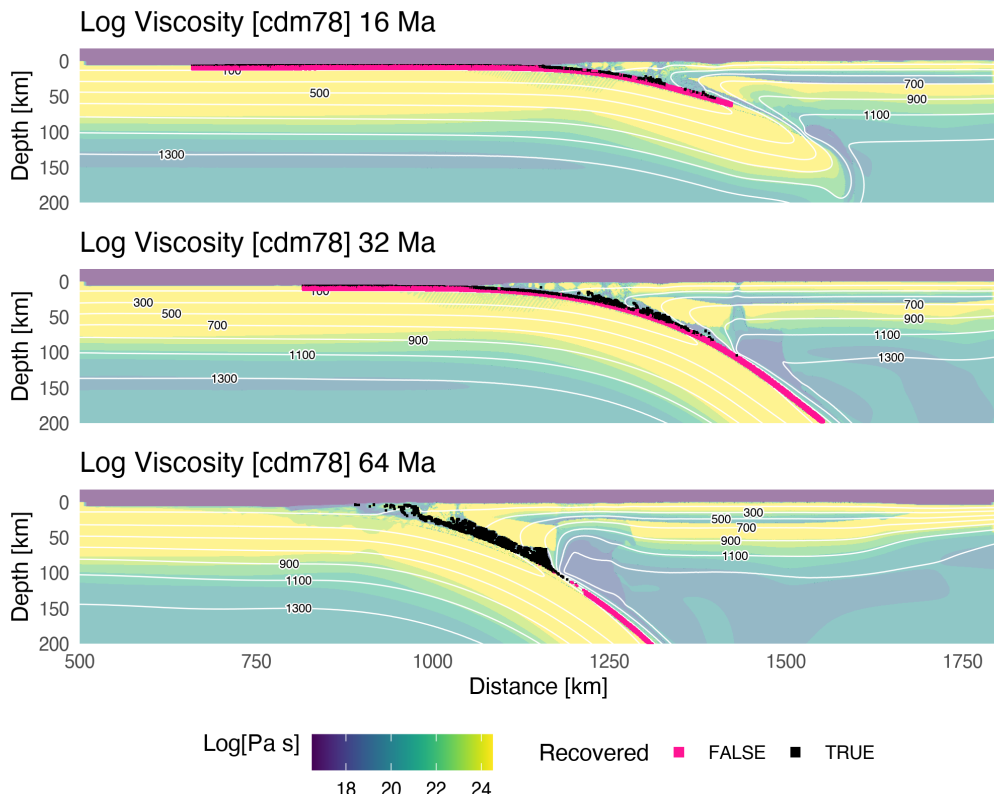


Figure A.153: Geodynamic evolution of model cdm78.

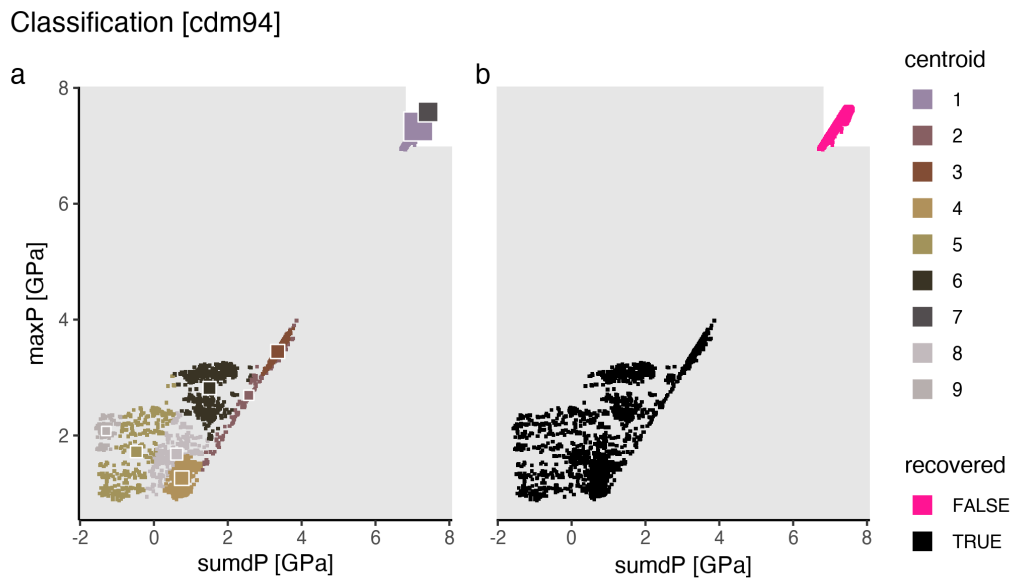


Figure A.154: Marker classification for model cdm94.

Metamorphic conditions [cdm94]

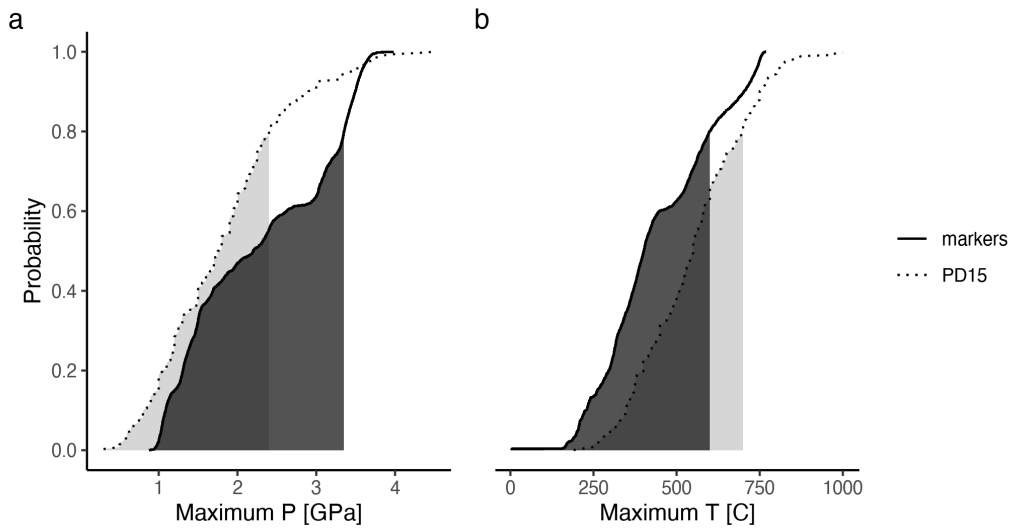


Figure A.155: Metamorphic conditions of markers recovered from model cdm94.

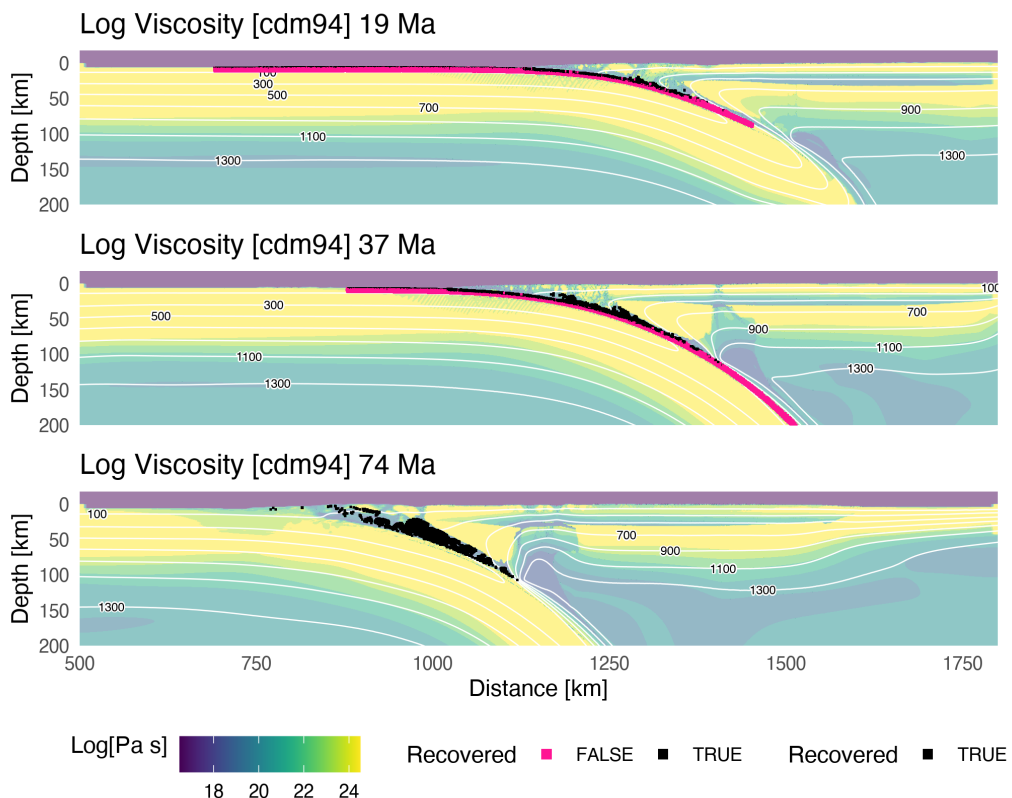


Figure A.156: Geodynamic evolution of model cdm94.

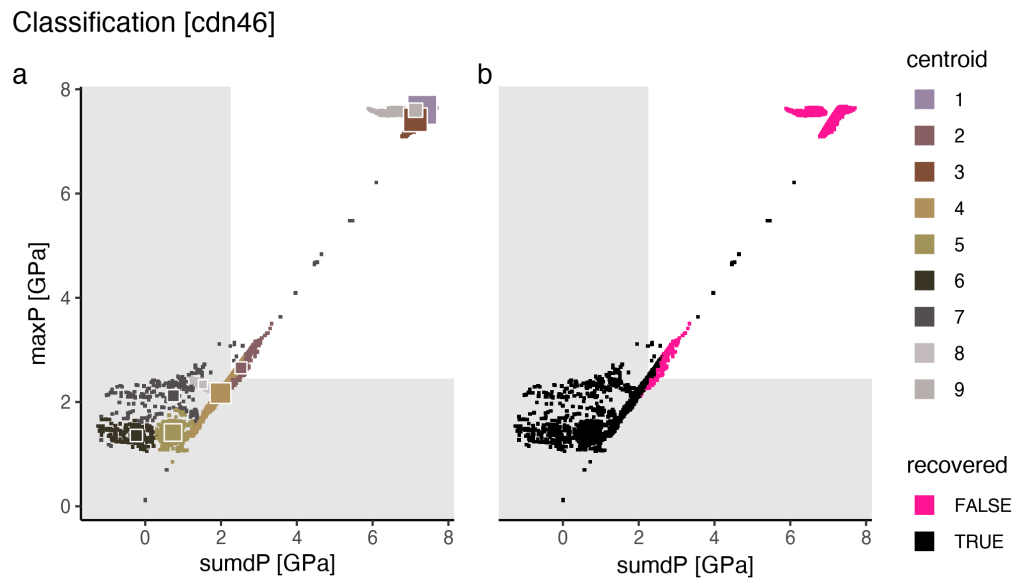


Figure A.157: Marker classification for model cdn46.

Metamorphic conditions [cdn46]

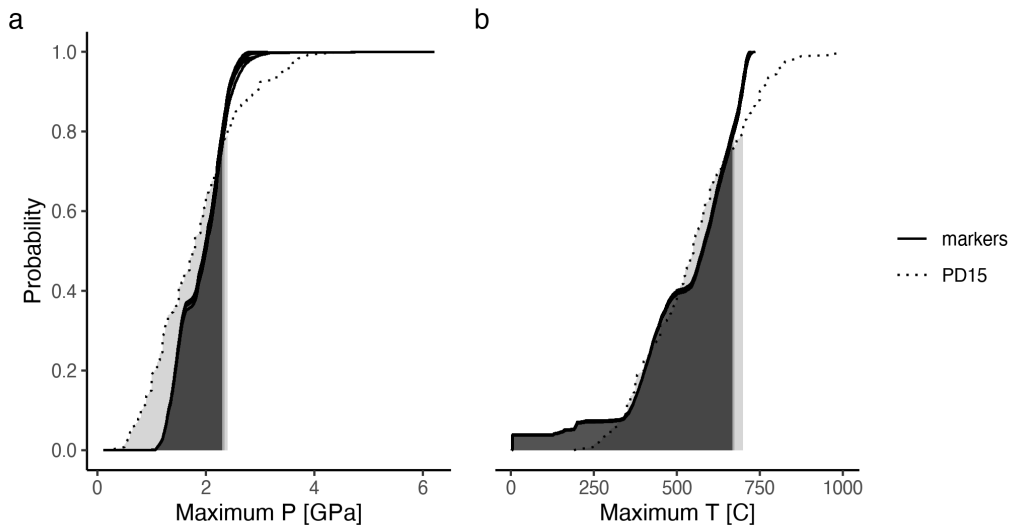


Figure A.158: Metamorphic conditions of markers recovered from model cdn46.

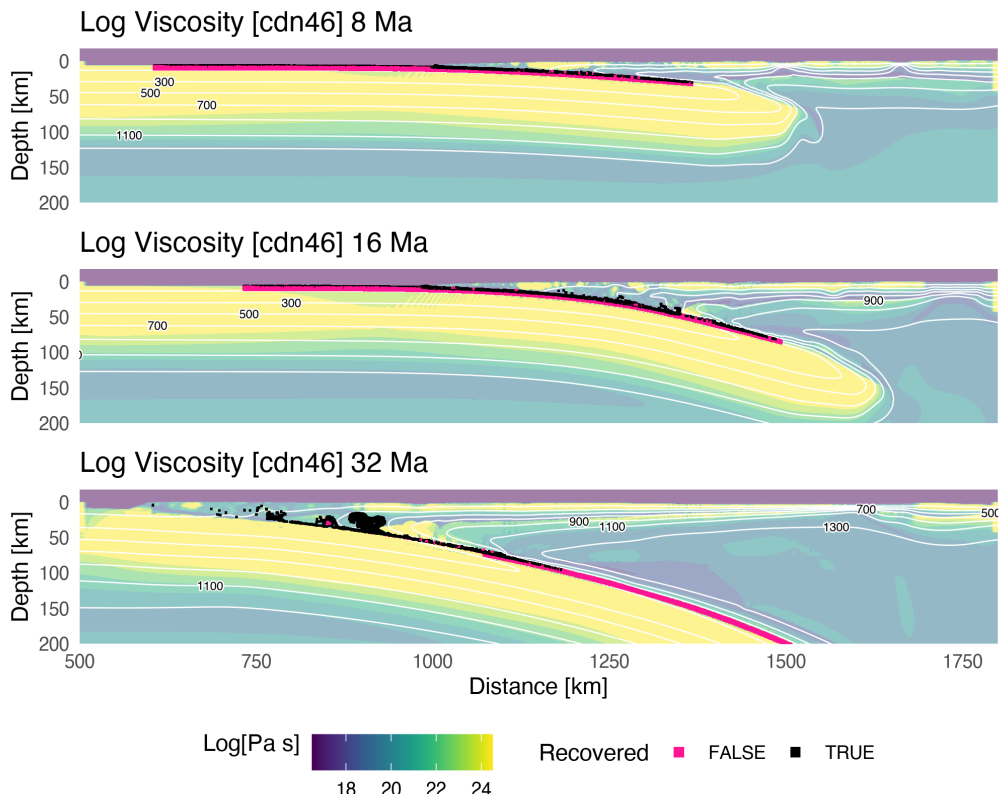


Figure A.159: Geodynamic evolution of model cdn46.

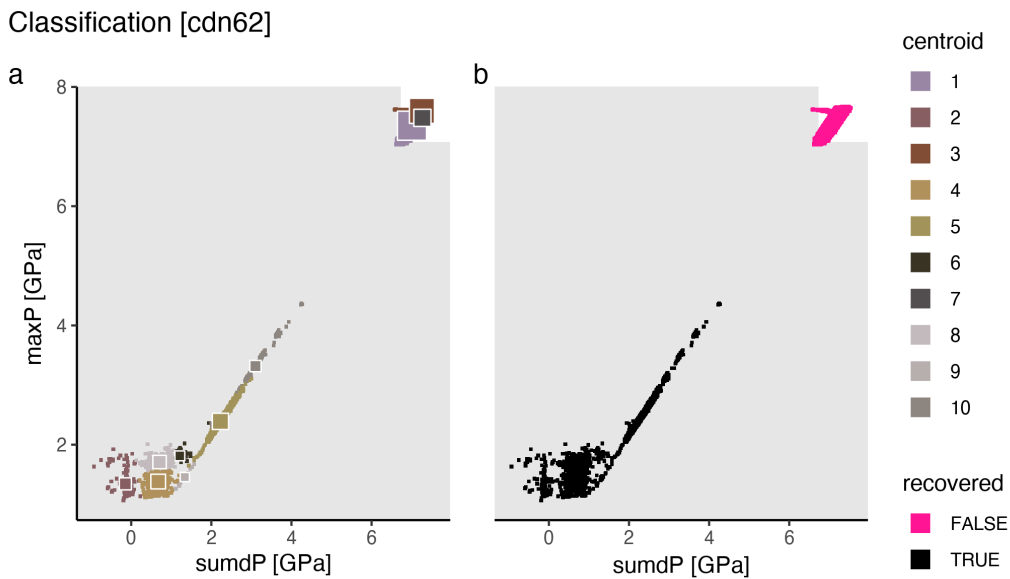


Figure A.160: Marker classification for model cdn62.

Metamorphic conditions [cdn62]

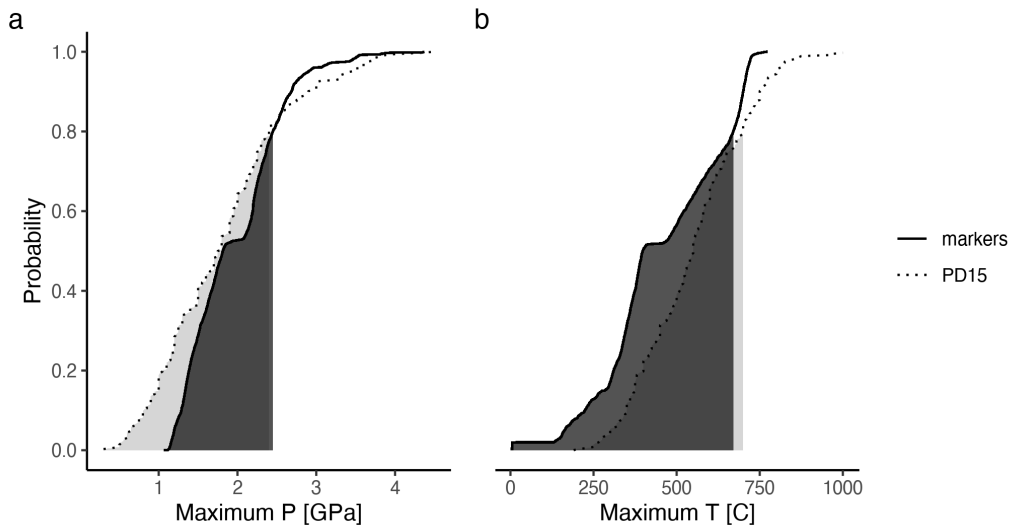


Figure A.161: Metamorphic conditions of markers recovered from model cdn62.

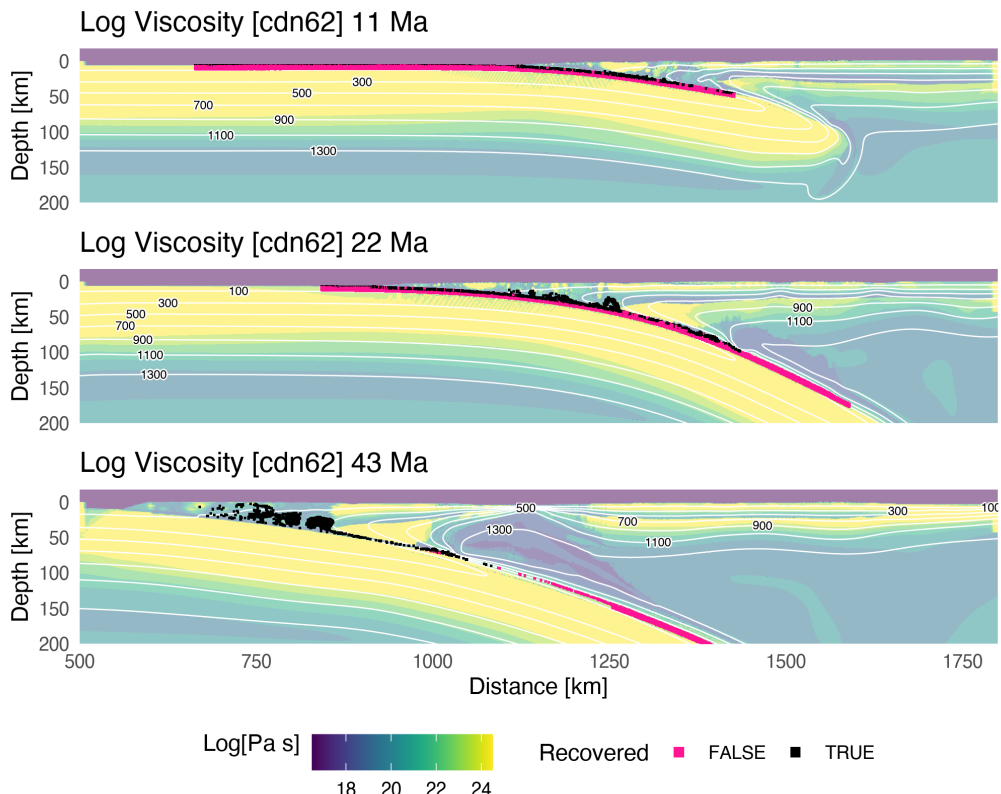


Figure A.162: Geodynamic evolution of model cdn62.

Classification [cdn78]

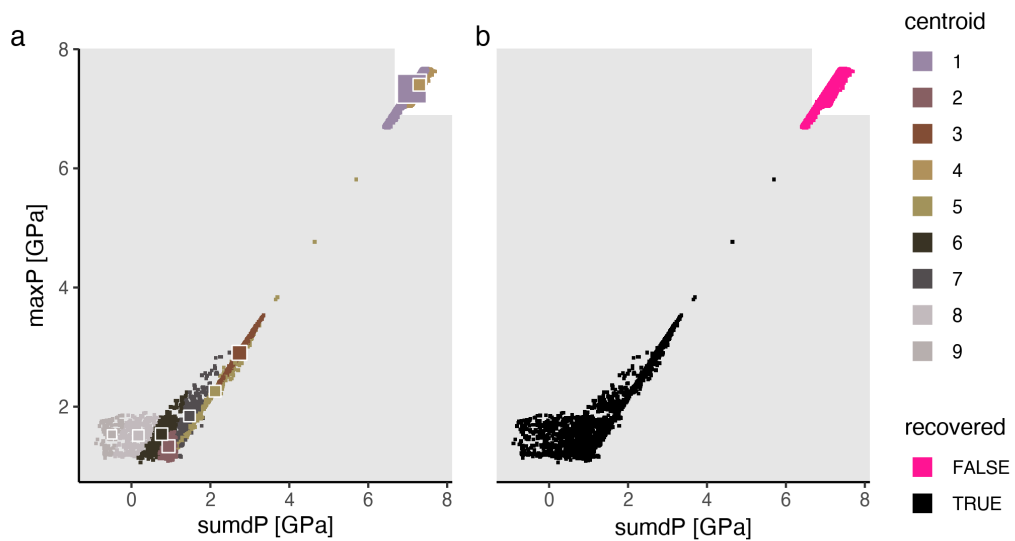


Figure A.163: Marker classification for model cdn78.

Metamorphic conditions [cdn78]

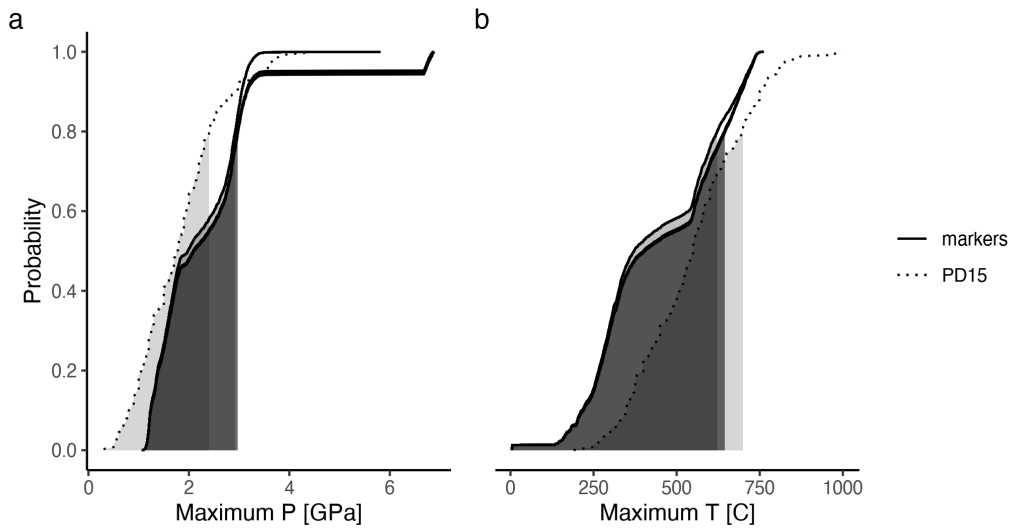


Figure A.164: Metamorphic conditions of markers recovered from model cdn78.

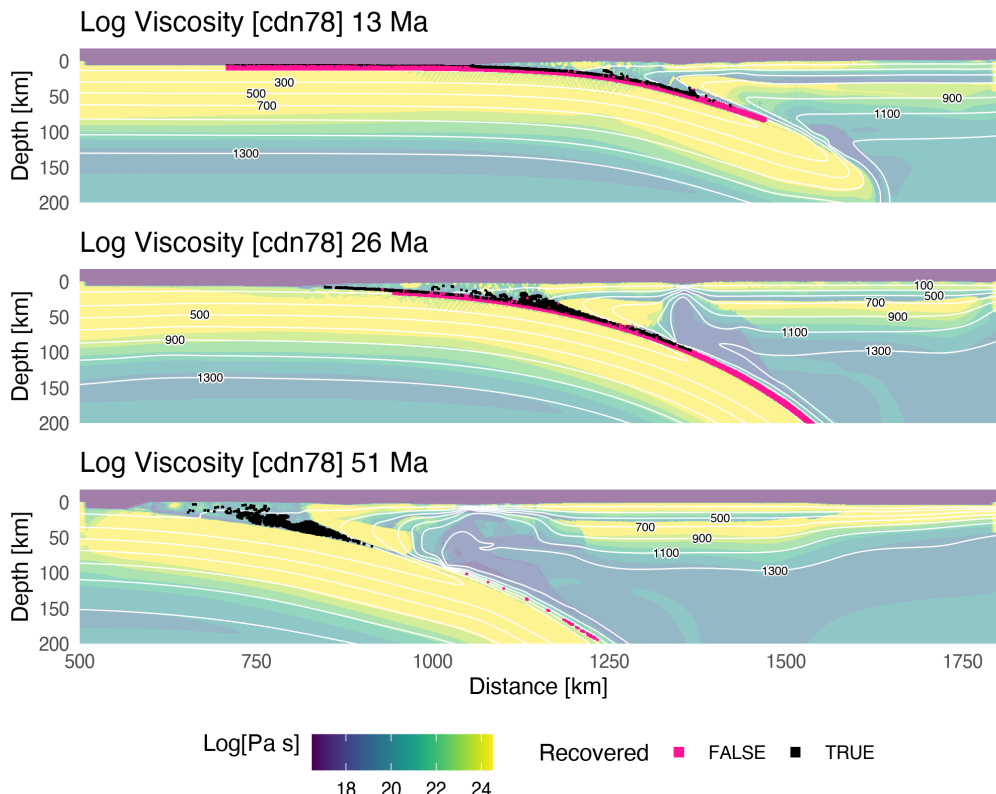


Figure A.165: Geodynamic evolution of model cdn78.

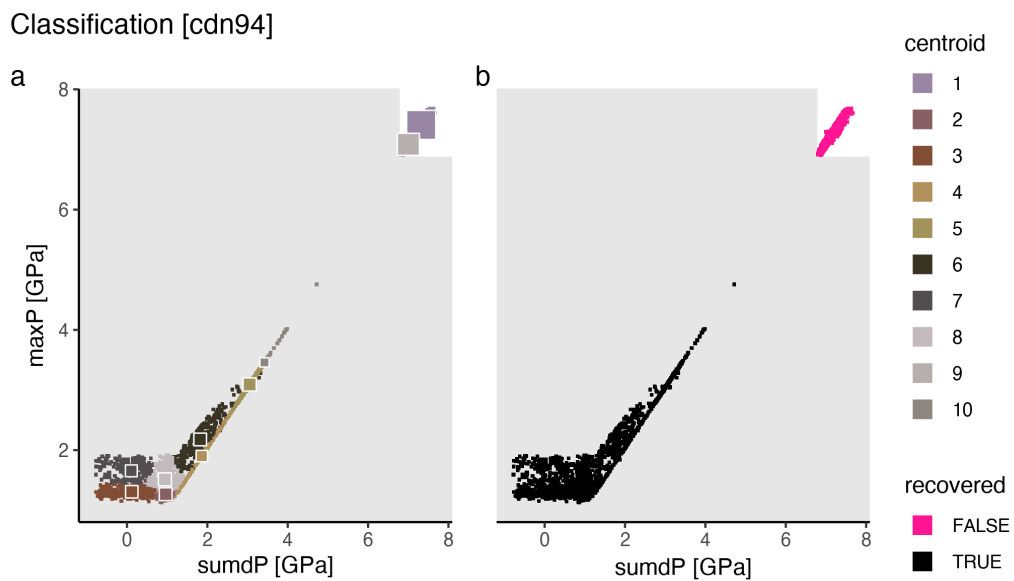


Figure A.166: Marker classification for model cdn94.

Metamorphic conditions [cdn94]

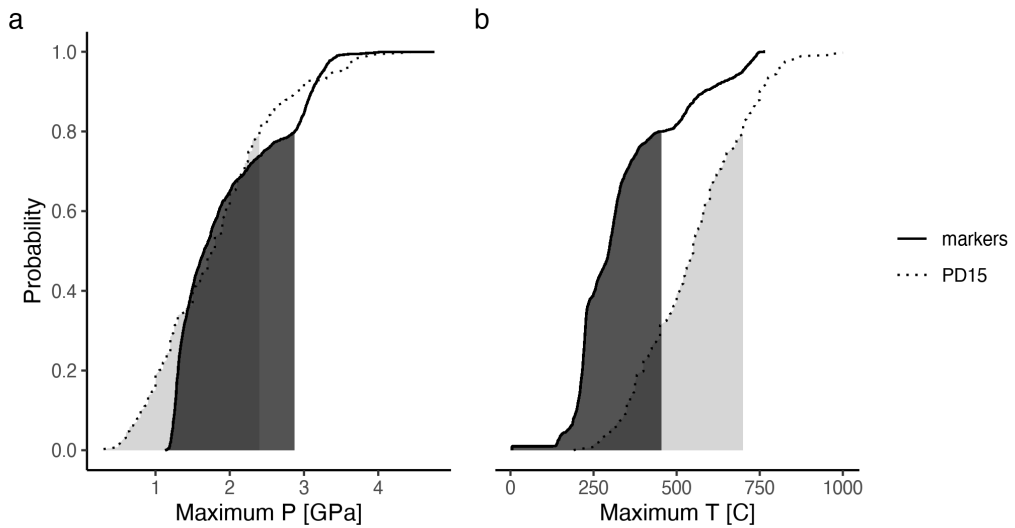


Figure A.167: Metamorphic conditions of markers recovered from model cdn94.

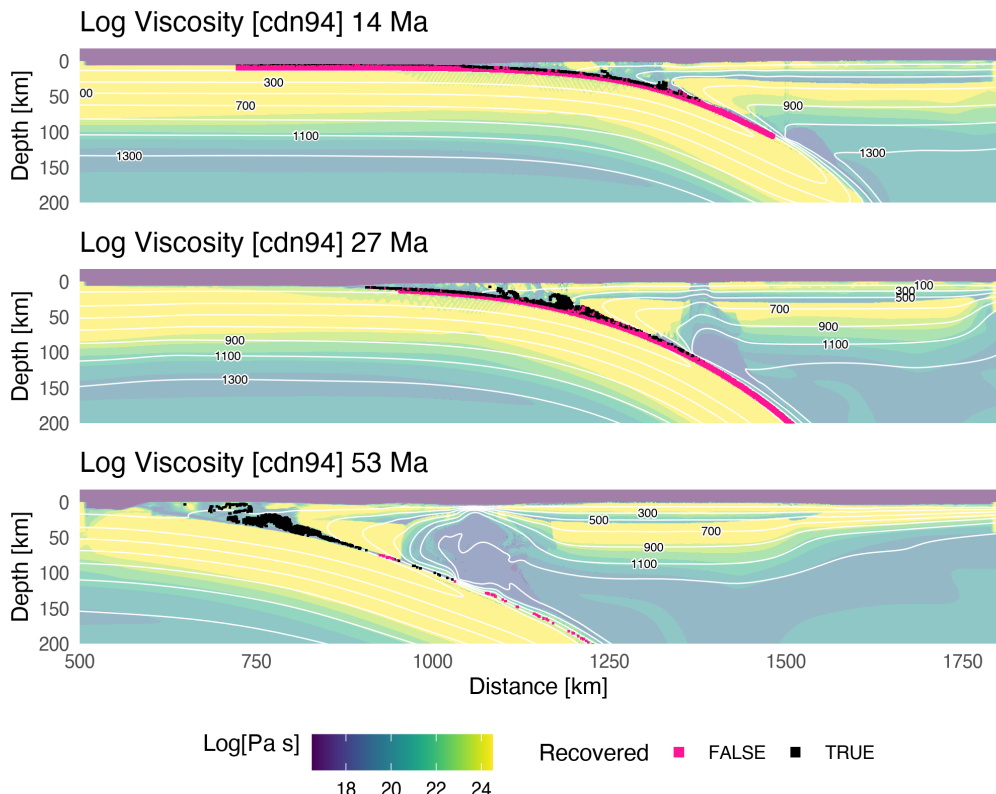


Figure A.168: Geodynamic evolution of model cdn94.

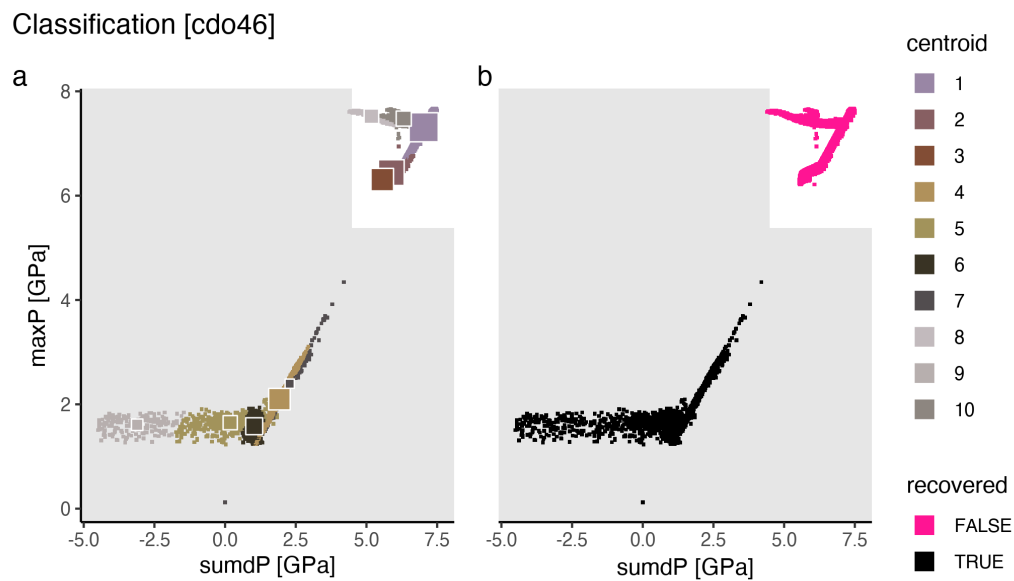


Figure A.169: Marker classification for model cd046.

Metamorphic conditions [cd046]

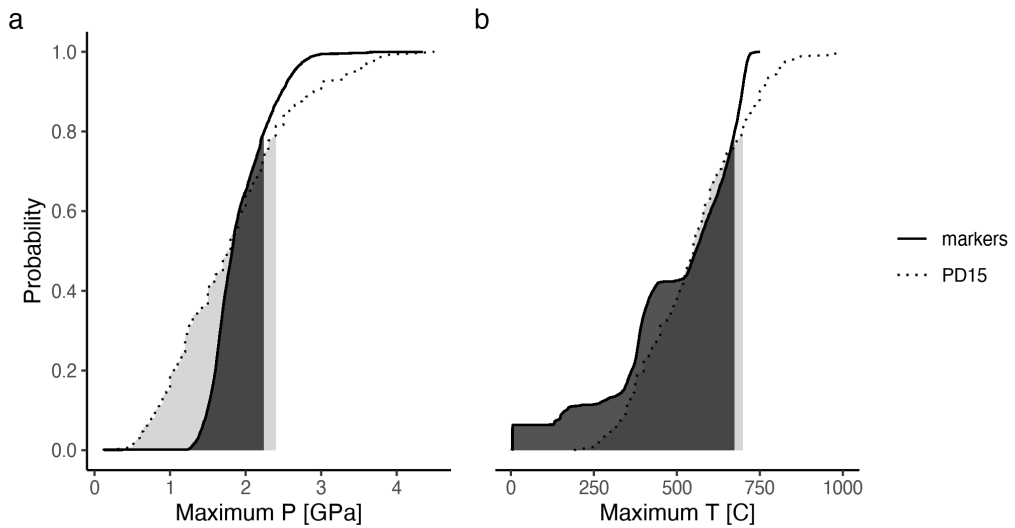


Figure A.170: Metamorphic conditions of markers recovered from model cdo46.

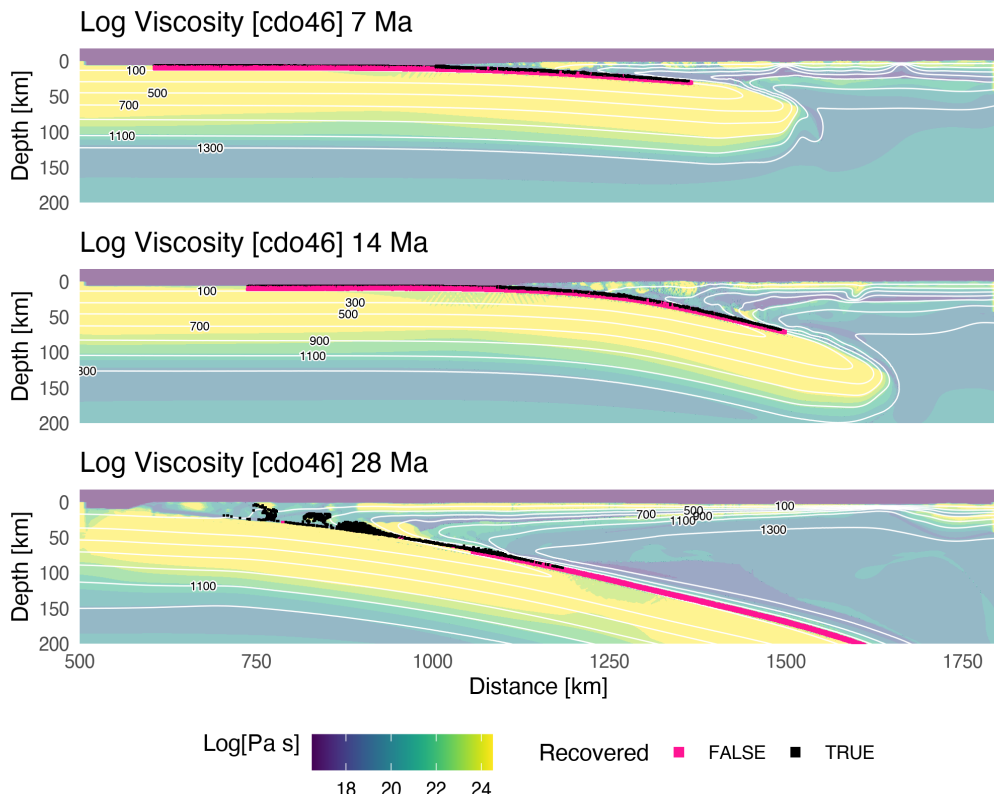


Figure A.171: Geodynamic evolution of model cdo46.

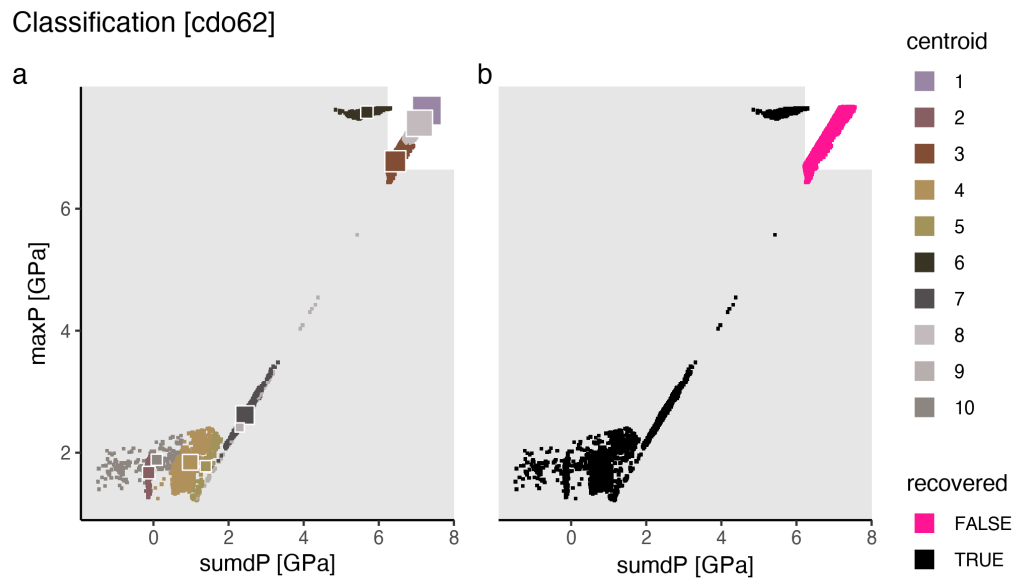


Figure A.172: Marker classification for model cdo62.

Metamorphic conditions [cd062]

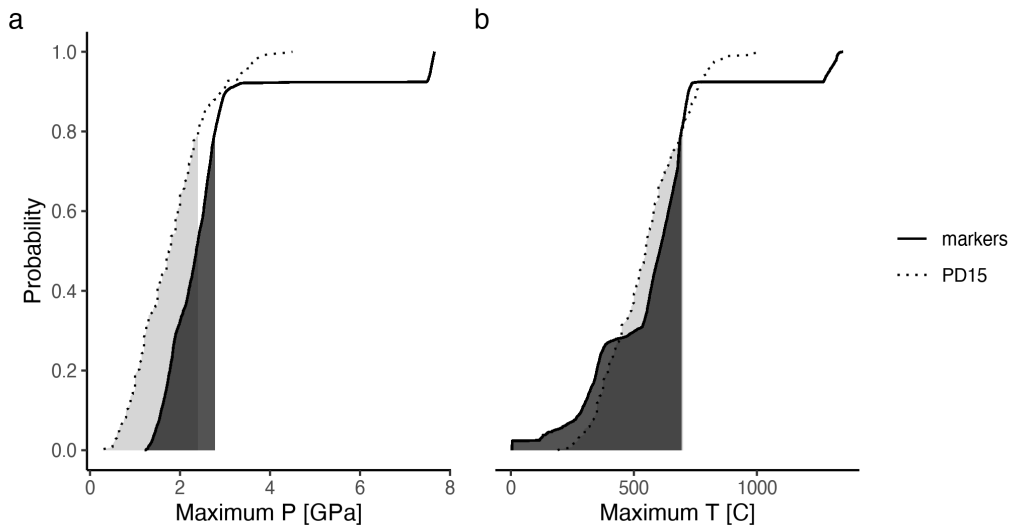


Figure A.173: Metamorphic conditions of markers recovered from model cd062.

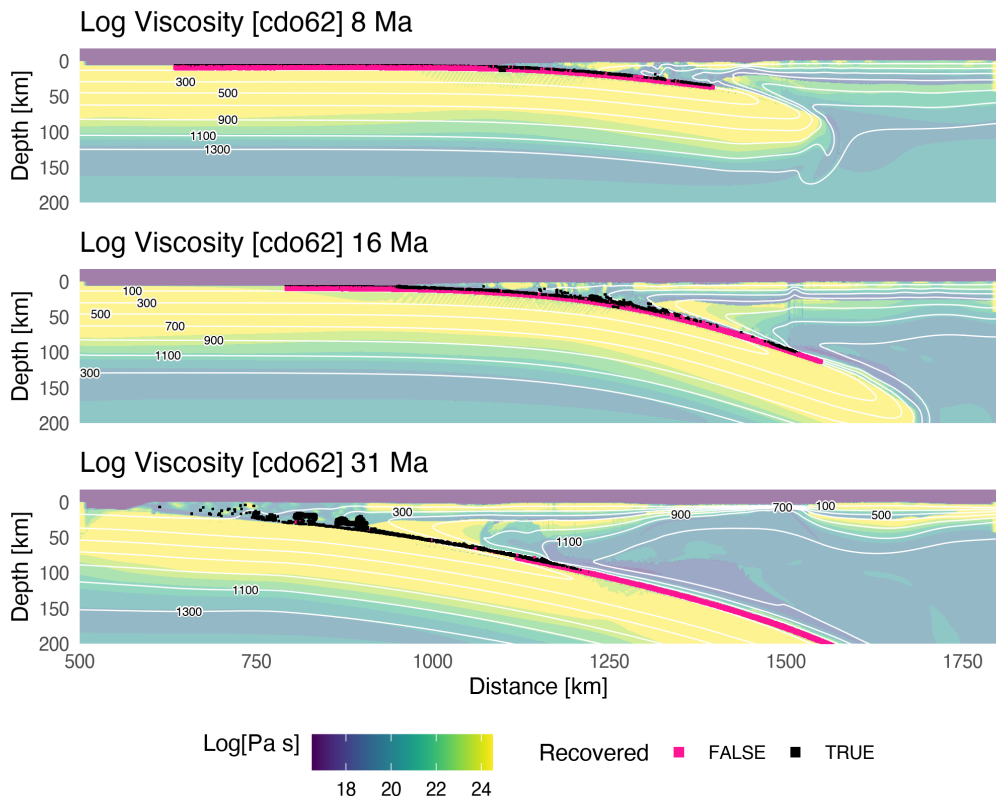


Figure A.174: Geodynamic evolution of model cd062.

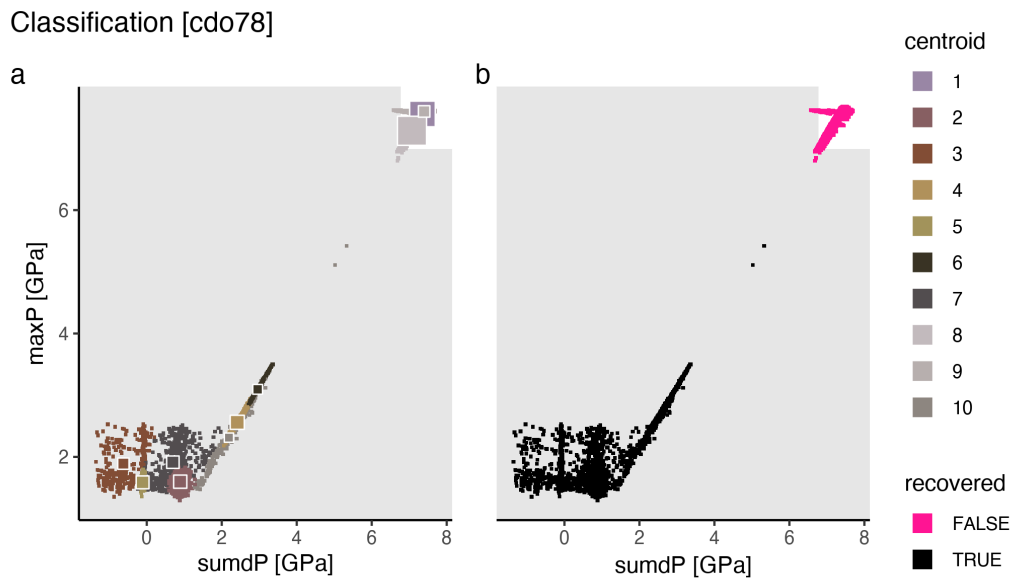


Figure A.175: Marker classification for model cdo78.

Metamorphic conditions [cd078]

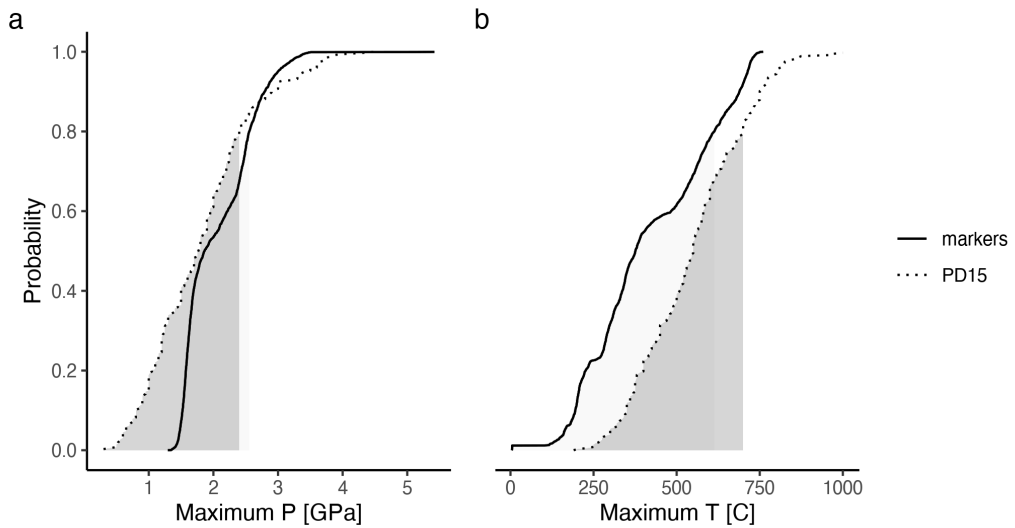


Figure A.176: Metamorphic conditions of markers recovered from model cdo78.

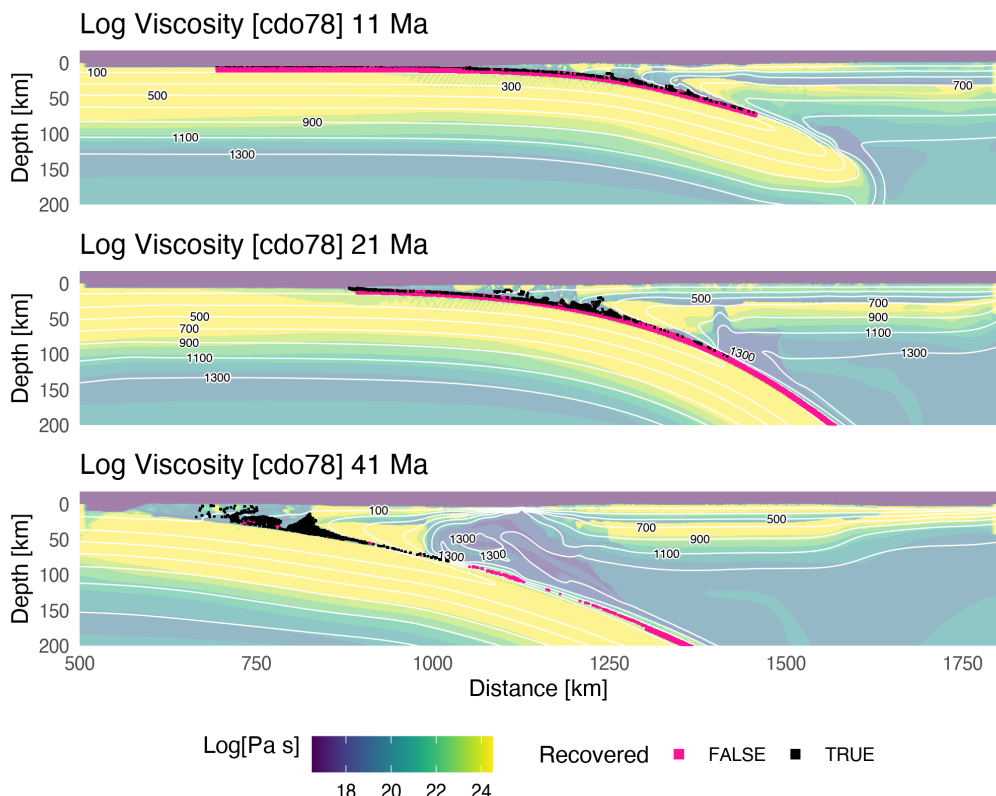


Figure A.177: Geodynamic evolution of model cdo78.

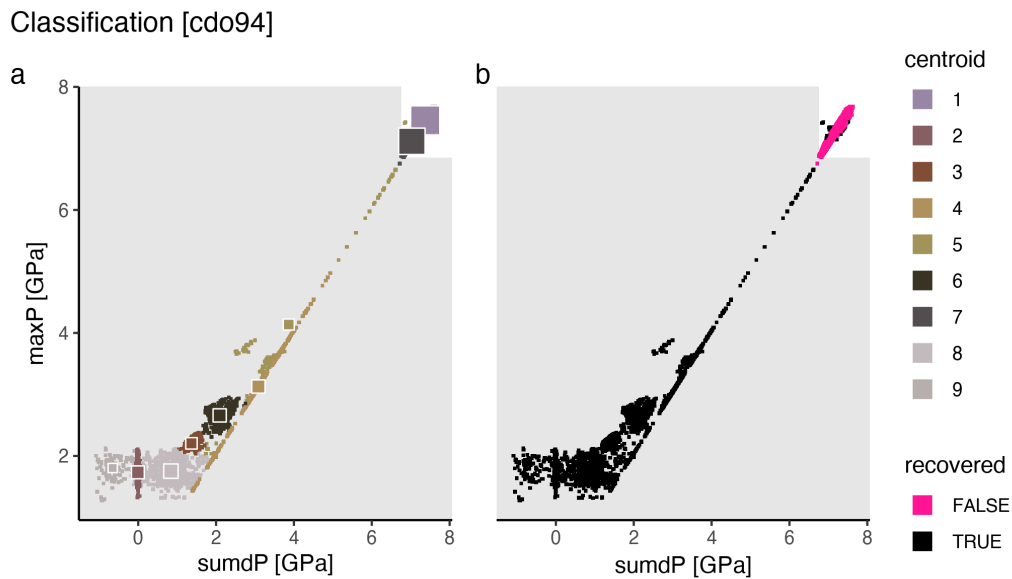


Figure A.178: Marker classification for model cdo94.

Metamorphic conditions [cd094]

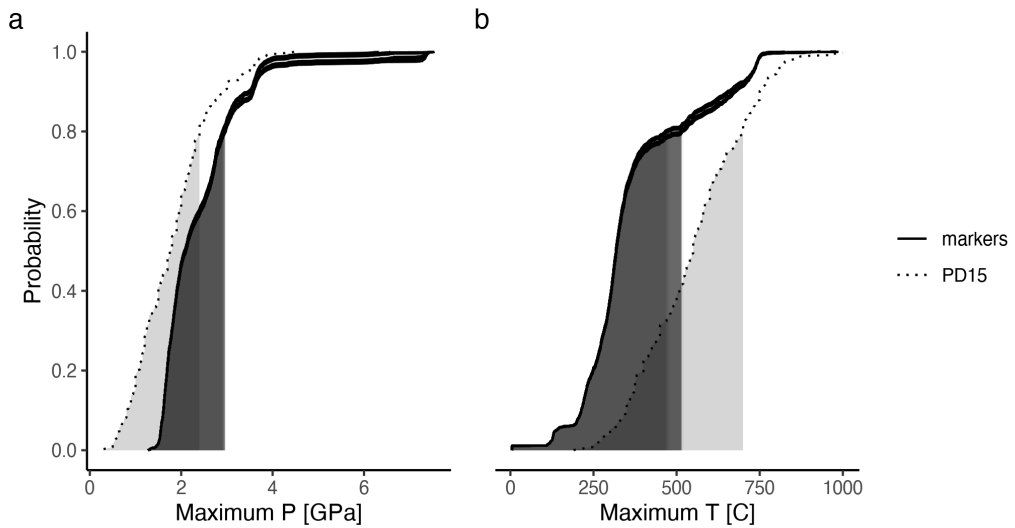


Figure A.179: Metamorphic conditions of markers recovered from model cdo94.

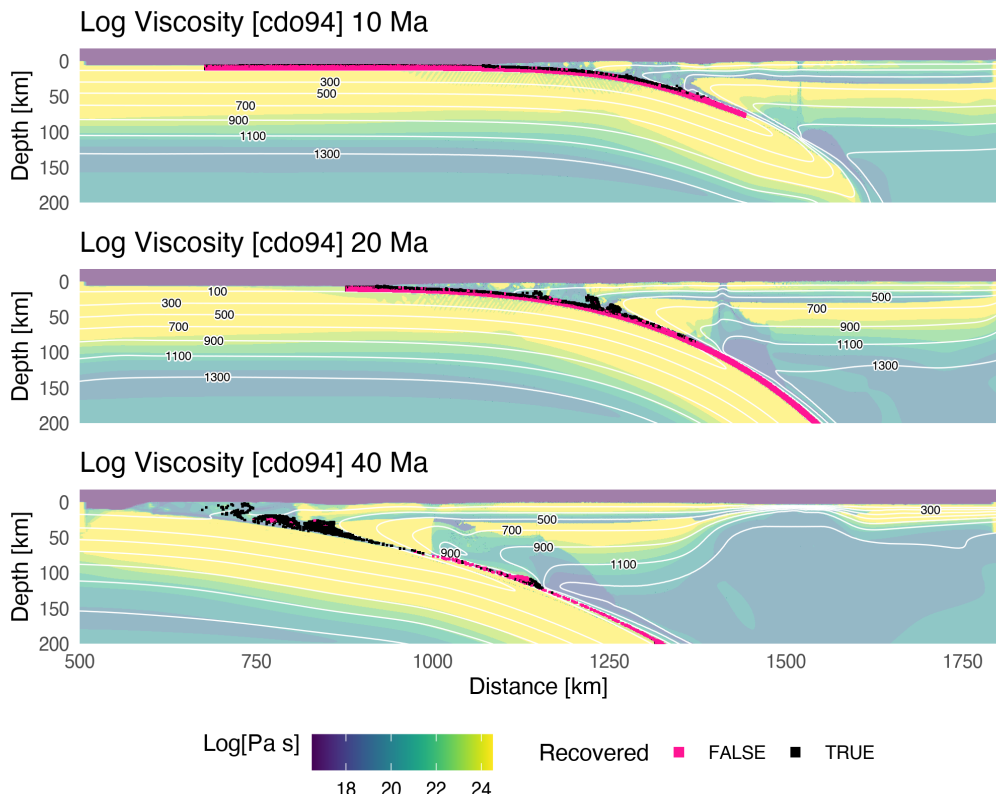


Figure A.180: Geodynamic evolution of model cdo94.

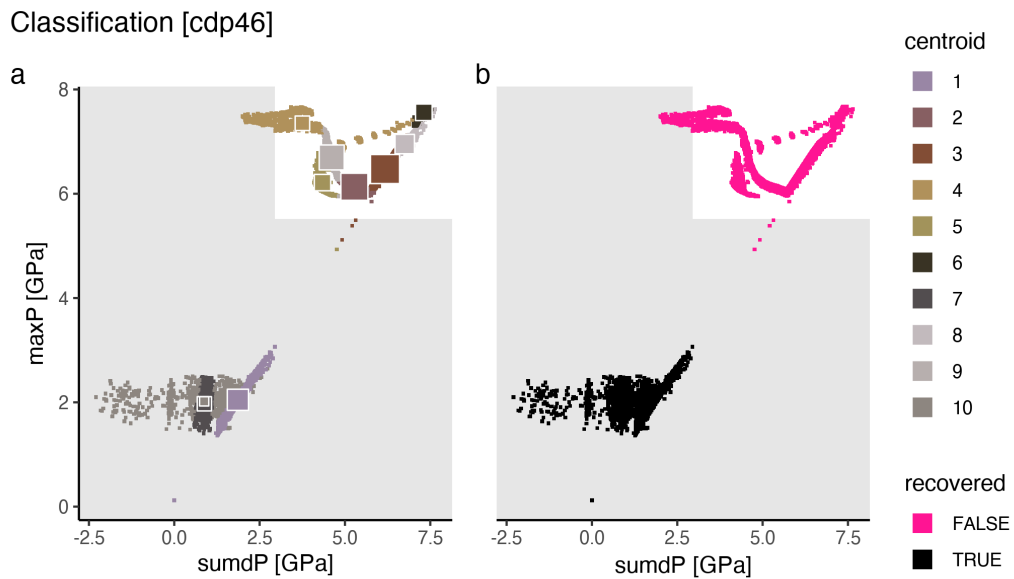


Figure A.181: Marker classification for model cdp46.

Metamorphic conditions [cdp46]

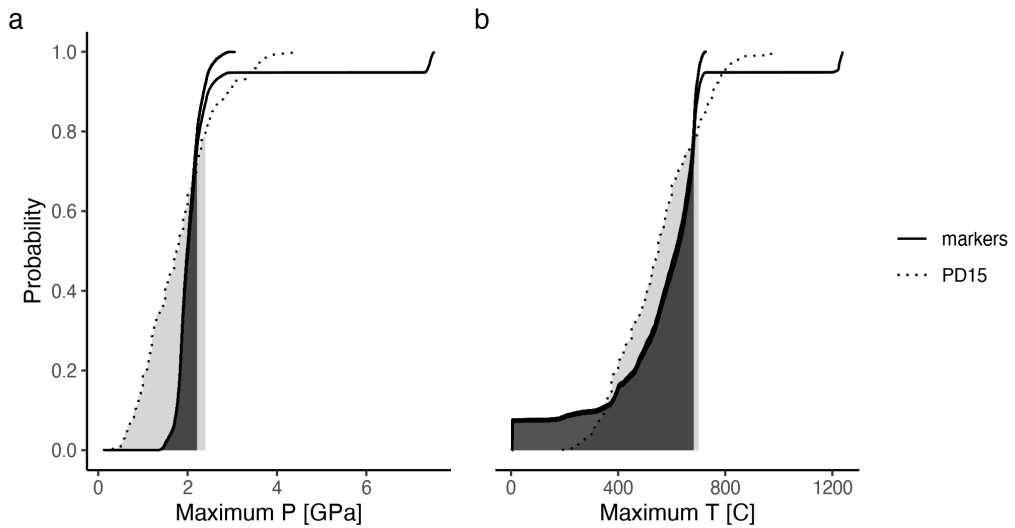


Figure A.182: Metamorphic conditions of markers recovered from model cdp46.

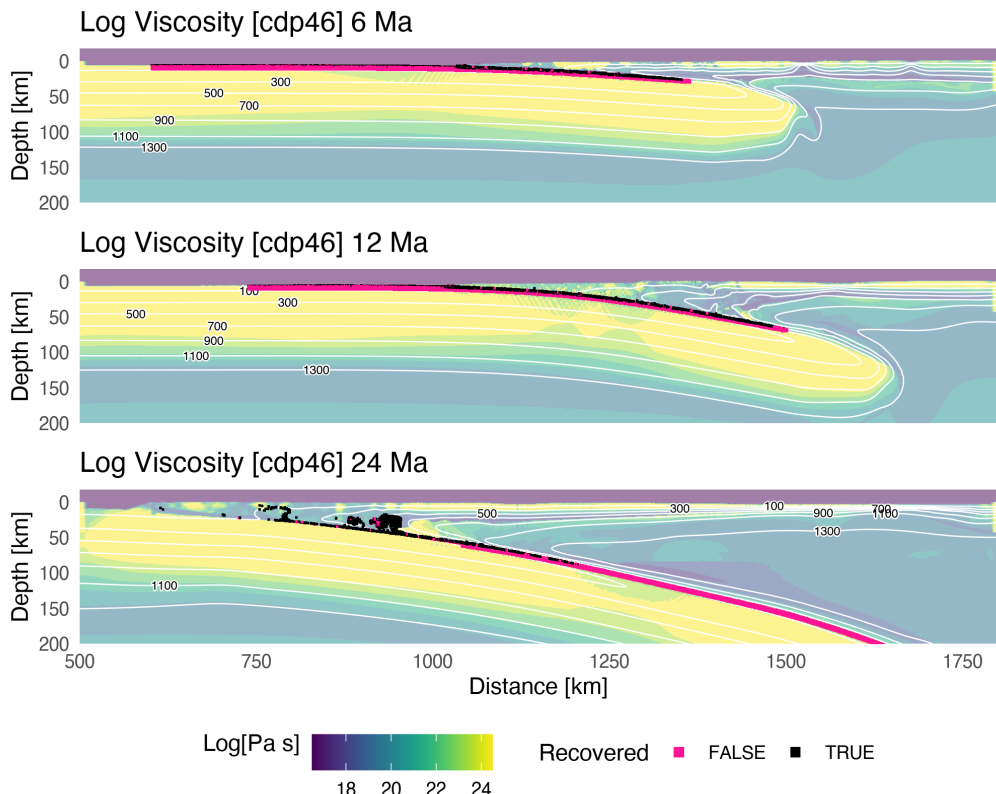


Figure A.183: Geodynamic evolution of model cdp46.

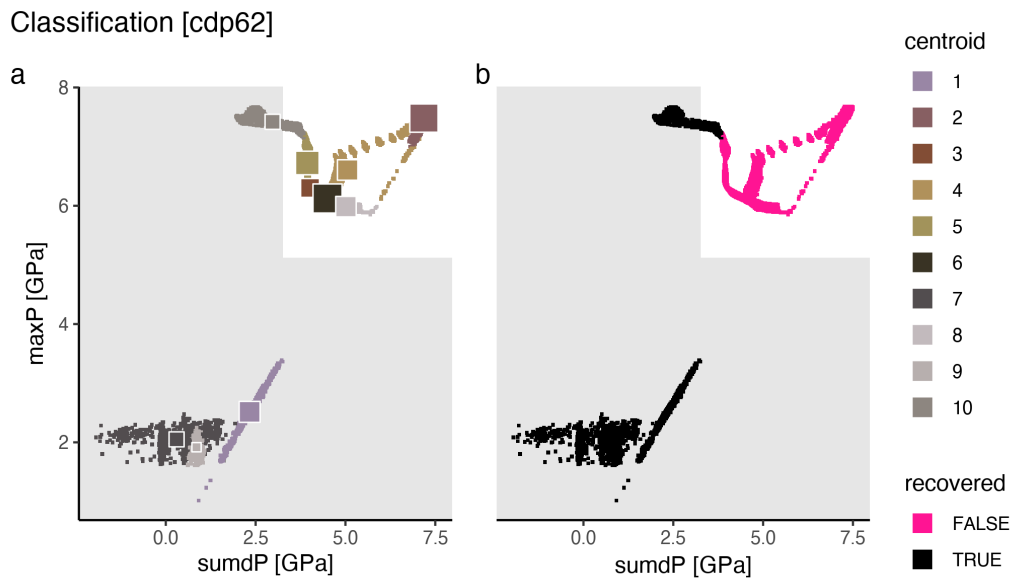


Figure A.184: Marker classification for model cdp62.

Metamorphic conditions [cdp62]

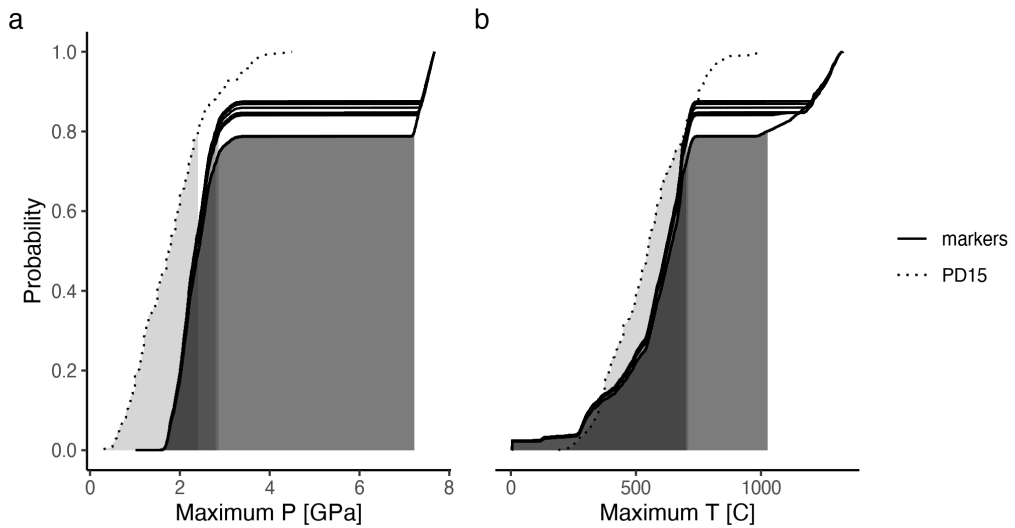


Figure A.185: Metamorphic conditions of markers recovered from model cdp62.

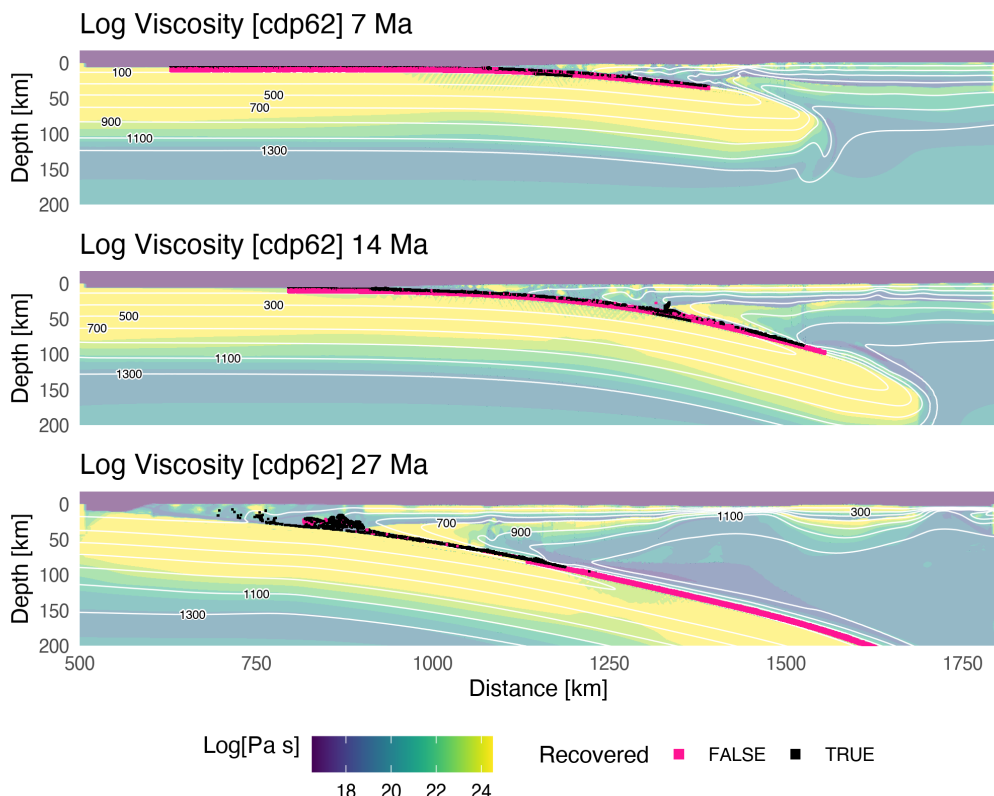


Figure A.186: Geodynamic evolution of model cdp62.

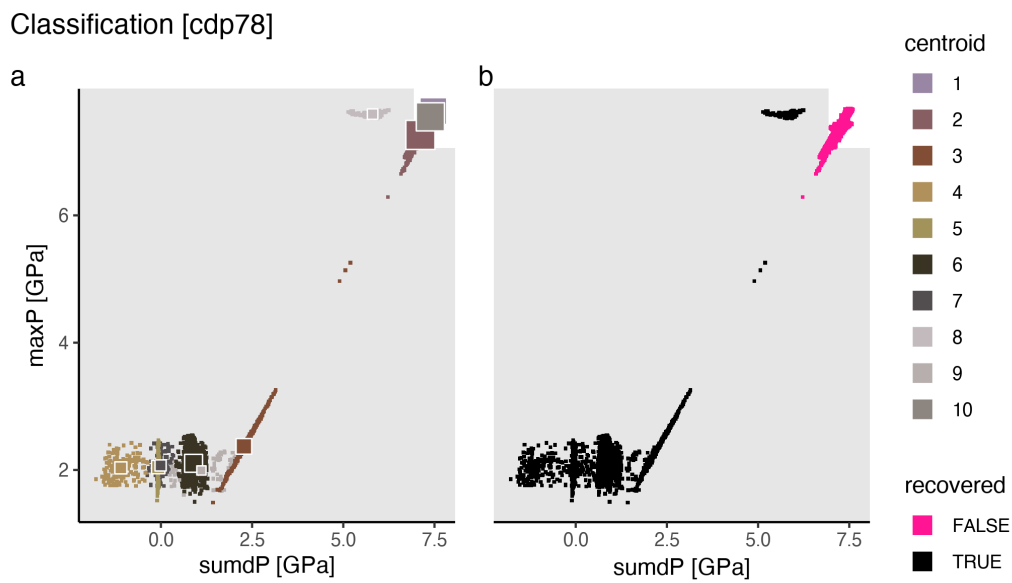


Figure A.187: Marker classification for model cdp78.

Metamorphic conditions [cdp78]

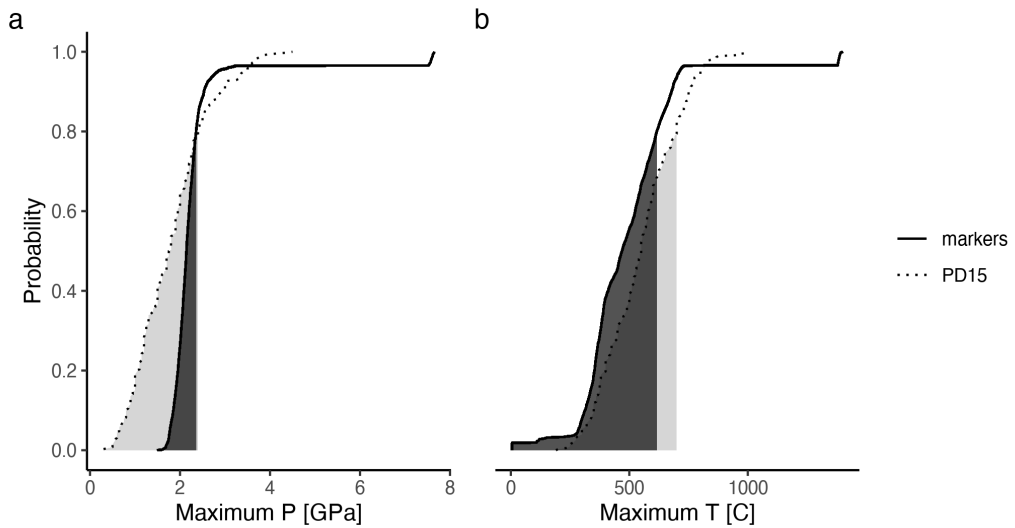


Figure A.188: Metamorphic conditions of markers recovered from model cdp78.

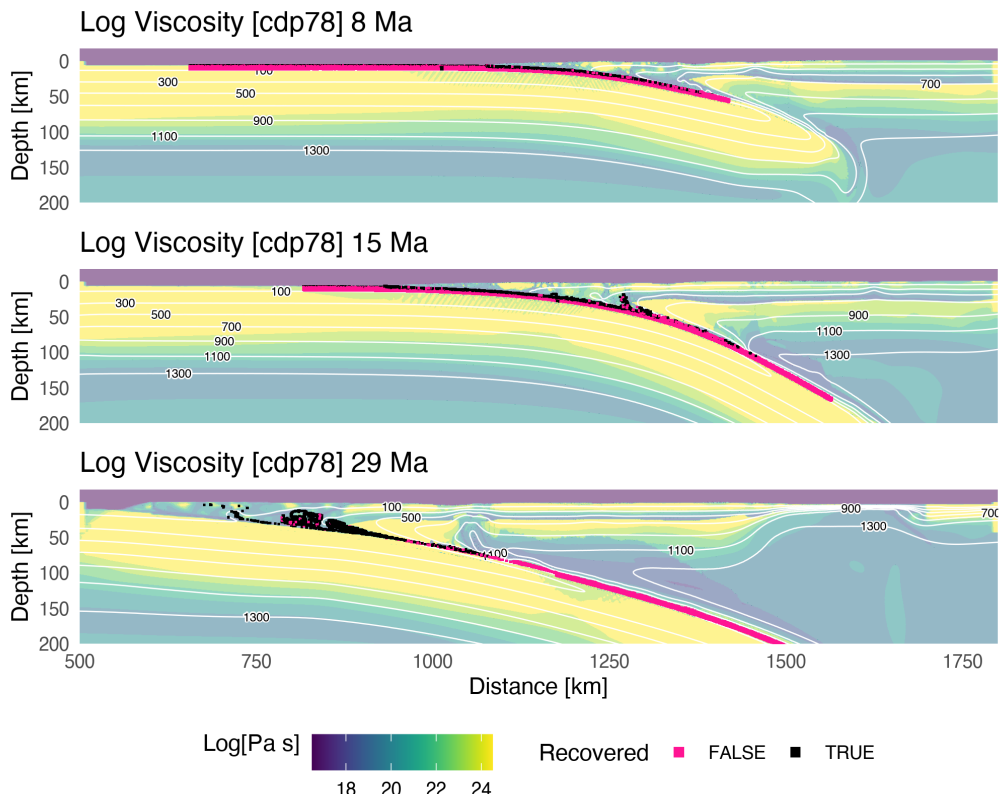


Figure A.189: Geodynamic evolution of model cdp78.

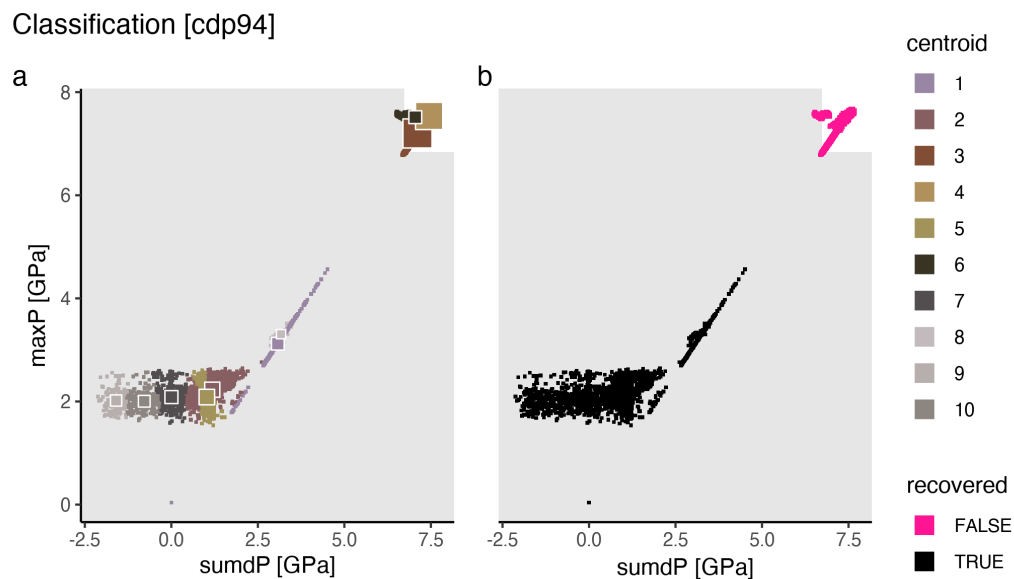


Figure A.190: Marker classification for model cdp94.

Metamorphic conditions [cdp94]

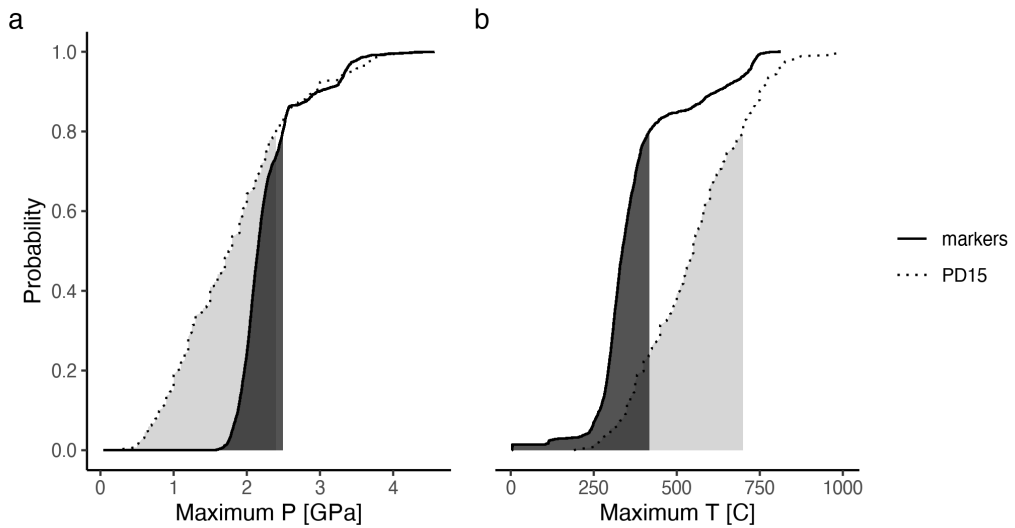


Figure A.191: Metamorphic conditions of markers recovered from model cdp94.

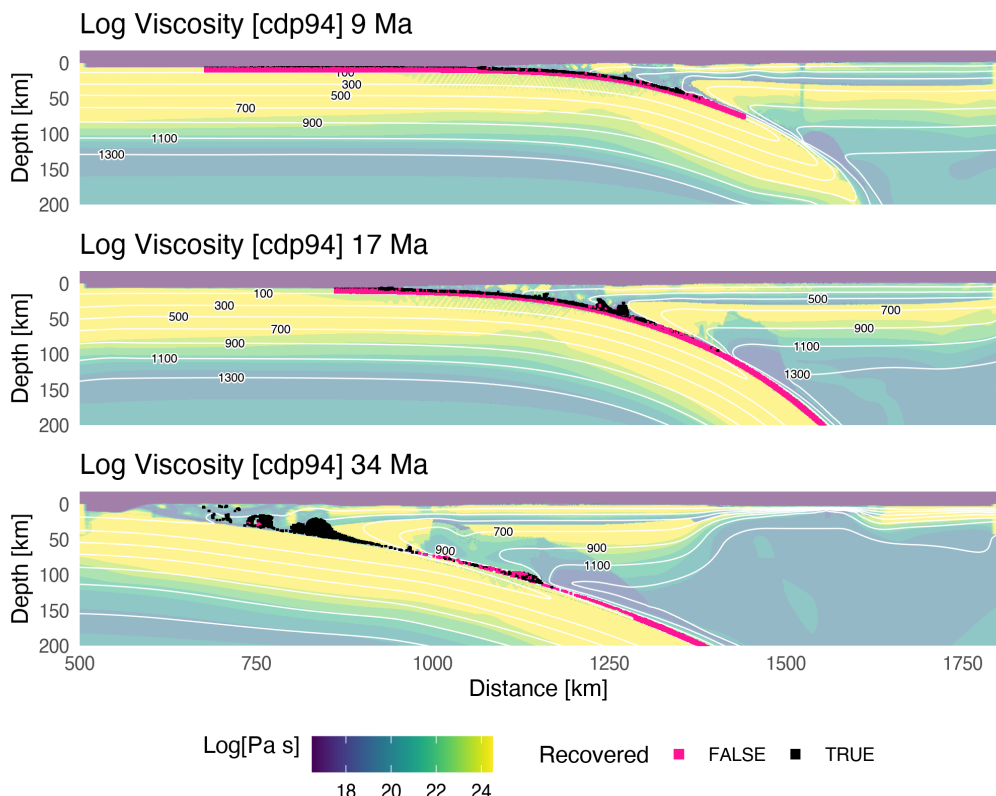


Figure A.192: Geodynamic evolution of model cdp94.

260 **References**

- 261 Abers, G. A., Keken, P. E. van, & Hacker, B. R. (2017). The cold and relatively dry na-
 262 ture of mantle forearcs in subduction zones. *Nature Geoscience*, 10(5), 333–337.
- 263 Agard, P., Yamato, P., Jolivet, L., & Burov, E. (2009). Exhumation of oceanic blueschists
 264 and eclogites in subduction zones: Timing and mechanisms. *Earth-Science Reviews*,
 265 92(1-2), 53–79.
- 266 Agard, P., Yamato, P., Soret, M., Prigent, C., Guillot, S., Plunder, A., et al. (2016). Plate
 267 interface rheological switches during subduction infancy: Control on slab penetra-
 268 tion and metamorphic sole formation. *Earth and Planetary Science Letters*, 451, 208–
 269 220.
- 270 Agard, P., Plunder, A., Angiboust, S., Bonnet, G., & Ruh, J. (2018). The subduction
 271 plate interface: Rock record and mechanical coupling (from long to short timescales).
 272 *Lithos*, 320, 537–566.
- 273 Banfield, J. D., & Raftery, A. E. (1993). Model-based gaussian and non-gaussian clus-
 274 tering. *Biometrics*, 803–821.
- 275 Batchelor, G. K. (1953). *The theory of homogeneous turbulence*. Cambridge university
 276 press.
- 277 Bebout, G. E. (2007). Metamorphic chemical geodynamics of subduction zones. *Earth*
 278 and *Planetary Science Letters*, 260(3-4), 373–393.
- 279 Bebout, G. E., & Barton, M. D. (2002). Tectonic and metasomatic mixing in a high-t,
 280 subduction-zone mélange—insights into the geochemical evolution of the slab–mantle
 281 interface. *Chemical Geology*, 187(1-2), 79–106.
- 282 Boussinesq, J. (1897). *Théorie de l'écoulement tourbillonnant et tumultueux des liquides*
 283 *dans les lits rectilignes a grande section* (Vol. 1). Gauthier-Villars.
- 284 Celeux, G., & Govaert, G. (1995). Gaussian parsimonious clustering models. *Pattern Recog-*
 285 *nition*, 28(5), 781–793.
- 286 Currie, C. A., & Hyndman, R. D. (2006). The thermal structure of subduction zone back
 287 arcs. *Journal of Geophysical Research: Solid Earth*, 111(B8).

- 288 Dempster, A. P., Laird, N. M., & Rubin, D. B. (1977). Maximum likelihood from incom-
289 plete data via the EM algorithm. *Journal of the Royal Statistical Society: Series B*
290 (*Methodological*), 39(1), 1–22.
- 291 Dy, J. G., & Brodley, C. E. (2004). Feature selection for unsupervised learning. *Jour-*
292 *nal of Machine Learning Research*, 5(Aug), 845–889.
- 293 Efron, B., & Tibshirani, R. J. (1994). *An introduction to the bootstrap*. CRC press.
- 294 Ferris, A., Abers, G. A., Christensen, D. H., & Veenstra, E. (2003). High resolution im-
295 age of the subducted pacific (?) Plate beneath central alaska, 50–150 km depth. *Earth*
296 *and Planetary Science Letters*, 214(3-4), 575–588.
- 297 Figueiredo, M. A. T., & Jain, A. K. (2002). Unsupervised learning of finite mixture mod-
298 *els. IEEE Transactions on Pattern Analysis and Machine Intelligence*, 24(3), 381–
299 396.
- 300 Fraley, C., & Raftery, A. E. (2002). Model-based clustering, discriminant analysis, and
301 density estimation. *Journal of the American Statistical Association*, 97(458), 611–
302 631.
- 303 Furukawa, Y. (1993). Depth of the decoupling plate interface and thermal structure un-
304 der arcs. *Journal of Geophysical Research: Solid Earth*, 98(B11), 20005–20013.
- 305 Gao, X., & Wang, K. (2014). Strength of stick-slip and creeping subduction megathrusts
306 from heat flow observations. *Science*, 345(6200), 1038–1041.
- 307 Gerya, T. V. (2019). *Introduction to numerical geodynamic modelling*. Cambridge Uni-
308 versity Press.
- 309 Gerya, T. V., & Stöckhert, B. (2006). Two-dimensional numerical modeling of tectonic
310 and metamorphic histories at active continental margins. *International Journal of*
311 *Earth Sciences*, 95(2), 250–274.
- 312 Gerya, T. V., & Yuen, D. A. (2003). Characteristics-based marker-in-cell method with
313 conservative finite-differences schemes for modeling geological flows with strongly vari-
314 able transport properties. *Physics of the Earth and Planetary Interiors*, 140(4), 293–
315 318.

- 316 Gerya, T. V., Stöckhert, B., & Perchuk, A. L. (2002). Exhumation of high-pressure meta-
317 morphic rocks in a subduction channel: A numerical simulation. *Tectonics*, 21(6),
318 6–1.
- 319 Gerya, T. V., Connolly, J. A., & Yuen, D. A. (2008). Why is terrestrial subduction one-
320 sided? *Geology*, 36(1), 43–46.
- 321 Gorczyk, W., Willner, A. P., Gerya, T. V., Connolly, J. A., & Burg, J.-P. (2007). Phys-
322 ical controls of magmatic productivity at pacific-type convergent margins: Numer-
323 ical modelling. *Physics of the Earth and Planetary Interiors*, 163(1-4), 209–232.
- 324 Hacker, B. R., Abers, G. A., & Peacock, S. M. (2003). Subduction factory 1. Theoret-
325 ical mineralogy, densities, seismic wave speeds, and H₂O contents. *Journal of Geo-*
326 *physical Research: Solid Earth*, 108(B1).
- 327 Harlow, F. H. (1962). *The particle-in-cell method for numerical solution of problems in*
328 *fluid dynamics*. Los Alamos Scientific Lab., N. Mex.
- 329 Harlow, F. H. (1964). The particle-in-cell computing method for fluid dynamics. *Meth-*
330 *ods Comput. Phys.*, 3, 319–343.
- 331 Harlow, F. H., & Welch, J. E. (1965). Numerical calculation of time-dependent viscous
332 incompressible flow of fluid with free surface. *The Physics of Fluids*, 8(12), 2182–2189.
- 333 Hilairet, N., Reynard, B., Wang, Y., Daniel, I., Merkel, S., Nishiyama, N., & Petitgirard,
334 S. (2007). High-pressure creep of serpentine, interseismic deformation, and initiation
335 of subduction. *Science*, 318(5858), 1910–1913.
- 336 Hyndman, R. D., & Peacock, S. M. (2003). Serpentinization of the forearc mantle. *Earth*
337 *and Planetary Science Letters*, 212(3-4), 417–432.
- 338 Hyndman, R. D., Currie, C. A., & Mazzotti, S. P. (2005). Subduction zone backarcs, mo-
339 bile belts, and orogenic heat. *Gsa Today*, 15(2), 4–10.
- 340 Ito, K., & Kennedy, G. C. (1971). An experimental study of the basalt-garnet granulite-
341 eclogite transition. *The Structure and Physical Properties of the Earth's Crust*, 14,
342 303–314.
- 343 Karato, S., & Wu, P. (1993). Rheology of the upper mantle: A synthesis. *Science*, 260(5109),
344 771–778.

- 345 Keken, P. E. van, Wada, I., Sime, N., & Abers, G. A. (2019). Thermal structure of the
346 forearc in subduction zones: A comparison of methodologies. *Geochemistry, Geophysics,
347 Geosystems*, 20(7), 3268–3288.
- 348 Kerswell, B. C., & Kohn, M. J. (2021). *A comparison of heat flow interpolations near
349 subduction zones.*
- 350 Kerswell, B. C., Kohn, M. J., & Gerya, T. V. (2020). Backarc lithospheric thickness and
351 serpentine stability control slab-mantle coupling depths in subduction zones. *Geo-
352 chemistry, Geophysics, Geosystems*, e2020GC009304.
- 353 Kohavi, R., & others. (1995). A study of cross-validation and bootstrap for accuracy es-
354 timation and model selection. In *Ijcai* (Vol. 14, pp. 1137–1145). Montreal, Canada.
- 355 Kohn, M. J., Castro, A. E., Kerswell, B. C., Ranero, C. R., & Spear, F. S. (2018). Shear
356 heating reconciles thermal models with the metamorphic rock record of subduction.
357 *Proceedings of the National Academy of Sciences*, 115(46), 11706–11711.
- 358 McKenzie, D. P. (1969). Speculations on the consequences and causes of plate motions.
359 *Geophysical Journal International*, 18(1), 1–32.
- 360 Moresi, L., Dufour, F., & Mühlhaus, H.-B. (2003). A lagrangian integration point finite
361 element method for large deformation modeling of viscoelastic geomaterials. *Jour-
362 nal of Computational Physics*, 184(2), 476–497.
- 363 Naif, S., Key, K., Constable, S., & Evans, R. L. (2015). Water-rich bending faults at the
364 m iddle a merica t rench. *Geochemistry, Geophysics, Geosystems*, 16(8), 2582–2597.
- 365 Peacock, S. M. (1990). Fluid processes in subduction zones. *Science*, 248(4953), 329–
366 337.
- 367 Peacock, S. M. (1996). Thermal and petrologic structure of subduction zones. *Subduc-
368 tion: Top to Bottom*, 96, 119–133.
- 369 Penniston-Dorland, S. C., Kohn, M. J., & Manning, C. E. (2015). The global range of
370 subduction zone thermal structures from exhumed blueschists and eclogites: Rocks
371 are hotter than models. *Earth and Planetary Science Letters*, 428, 243–254.
- 372 Ranalli, G. (1995). *Rheology of the earth*. Springer Science & Business Media.

- 373 Rondenay, S., Abers, G. A., & Keken, P. E. van. (2008). Seismic imaging of subduction
374 zone metamorphism. *Geology*, 36(4), 275–278.
- 375 Schmidt, M. W., & Poli, S. (1998). Experimentally based water budgets for dehydrat-
376 ing slabs and consequences for arc magma generation. *Earth and Planetary Science
377 Letters*, 163(1-4), 361–379.
- 378 Schwarz, G., & others. (1978). Estimating the dimension of a model. *Annals of Statis-
379 tics*, 6(2), 461–464.
- 380 Scrucca, L., Fop, M., Murphy, T. B., & Raftery, A. E. (2016). Mcclus 5: Clustering, clas-
381 sification and density estimation using gaussian finite mixture models. *The R Jour-
382 nal*, 8(1), 289.
- 383 Sizova, E., Gerya, T. V., Brown, M., & Perchuk, L. (2010). Subduction styles in the pre-
384 cambrian: Insight from numerical experiments. *Lithos*, 116(3-4), 209–229.
- 385 Stehman, S. V. (1997). Selecting and interpreting measures of thematic classification ac-
386 curacy. *Remote Sensing of Environment*, 62(1), 77–89.
- 387 Syracuse, E. M., & Abers, G. A. (2006). Global compilation of variations in slab depth
388 beneath arc volcanoes and implications. *Geochemistry, Geophysics, Geosystems*, 7(5).
- 389 Syracuse, E. M., Keken, P. E. van, & Abers, G. A. (2010). The global range of subduc-
390 tion zone thermal models. *Physics of the Earth and Planetary Interiors*, 183(1-2),
391 73–90.
- 392 Turcotte, D. L., & Schubert, G. (2002). *Geodynamics*. Cambridge university press.
- 393 Vermeesch, P. (2018). IsoplotR: A free and open toolbox for geochronology. *Geoscience
394 Frontiers*, 9(5), 1479–1493.
- 395 Wada, I., & Wang, K. (2009). Common depth of slab-mantle decoupling: Reconciling
396 diversity and uniformity of subduction zones. *Geochemistry, Geophysics, Geosystems*,
397 10(10).
- 398 Yamato, P., Agard, P., Burov, E., Le Pourhiet, L., Jolivet, L., & Tiberi, C. (2007). Burial
399 and exhumation in a subduction wedge: Mutual constraints from thermomechanical
400 modeling and natural p-t-t data (schistes lustrés, western alps). *Journal of Geo-
401 physical Research: Solid Earth*, 112(B7).

- 402 Yamato, P., Burov, E., Agard, P., Le Pourhiet, L., & Jolivet, L. (2008). HP-UHP ex-
403 humation during slow continental subduction: Self-consistent thermodynamically and
404 thermomechanically coupled model with application to the western alps. *Earth and*
405 *Planetary Science Letters*, 271(1-4), 63–74.